THE UNIVERSITY
OF BIRMINGHAM

Terahertz Waveguide Filters

Hao Yang

A thesis submitted to the University of Birmingham for the degree of Doctor of Philosophy

School of Electronic, Electrical and Systems Engineering

The University of Birmingham

March, 2019

Abstract

The waveguide filters are popular choices for transmitting and attenuating signals and the construction of passive circuits. With increasing demands on terahertz systems, waveguide filters with not only excellent performances but also compact size and lightweight are in need. This thesis looks into the design of terahertz waveguide filter while taking advantage of specific micromachining process.

Two waveguide filters operating on WR-3 band (220-325 GHz), one based on high precision computer numerically controlled (CNC) milling and the other using SU-8 photoresist technology, are designed and fabricated in this work to achieve demanding specifications. It is the first demonstration with the best measured performance that a CNC milled filter with a steep rejection characteristic beyond 300 GHz and a SU-8 micromachined filter with novel cross-coupling topology working at WR-3 band. These two filters demonstrate potential replacements of frequency selective surface (FSS) filters used in heterodyne radiometers for unwanted sideband rejection.

Another two WR-3 waveguide filters based on laser micromachining are also presented in the thesis. The filter structures are specially chosen to take advantage of the laser cutting processes and the standard steps of laser micromachining are also optimised accordingly in order to reduce the fabrication errors and achieve better performances. Although the performance of the two filters is not perfect, these works show the potential of the laser micromachining for fabricating terahertz waveguide filters.

Acknowledgement

I would like to thank my supervisor Prof. Mike J. Lancaster for his patient guidance and continuous support and encouragement during my Ph.D. study in the University of Birmingham. I am also grateful to my progress report assessor Dr. Alexandros Feresidis for his precious advices.

My appreciation also goes to my colleagues in the Emerging Device Technology Research Group at the University of Birmingham. In particular, I would like to thank Dr. Xiaobang Shang for his encouragement and many useful discussions on my work, Dr. Cheng Guo for many inspiring suggestions and ideas on the filter design, Dr. Yuvaraj Dhayalan and Dr. Pavel Penchev for fabricating the waveguide filters presented in this thesis. I would also like to thank to Dr. Bo Liu from University of Glyndwr for the cooperation on the work of optimisation for filters and diplexers, Dr. Peter G. Huggard and Dr. Hui Wang from Rutherford Appleton Laboratory for the help on the filter fabrication and measurements.

Finally, I want to express my sincere thanks to my parents and all of my friends for their support and encouragement.

Table of Contents

Chapter 1

Introduction

1.1 Overview of Terahertz Radiation and Applications

Terahertz radiations are electromagnetic waves with a frequency range from about 0.1 THz to 10 THz, or wavelengths between 3 mm and 30 μm, which lie between the microwave and infrared regions of the spectrum [1]. Terahertz frequency range is also the last span within the whole electromagnetic wave spectrum, which has rarely been technologically and commercially developed. From the literature, the terahertz frequency range is often referred to as 'terahertz gap' due to this reason. Meanwhile, this frequency range presents incredibly fascinating prospects for many applications [2].

Terahertz radiation mainly exhibits three attractive properties for applications. The first property is that terahertz radiations are non-ionizing, able to pass through dielectrics such as paper, plastic, cloth and wood, with little attenuation, while metals are highly reflective in this frequency region. Many materials which block visible and infrared (IR) spectra, appear to be transparent in the terahertz region. As compared to microwave radiation, employing terahertz frequency range is able to achieve better spatial resolution required for rendering quality imaging [3]. The next unique property is that terahertz radiations are safe for biological entities due to its relatively low energy. As compared to X-rays which have the risk of creating ionization in biological tissues, terahertz waves have absolutely no ionizing radiation impact, presenting no health hazard to humans and animals being scanned. The third special property is that many substances reveal their unique spectral fingerprints in the far terahertz range (1 - 3 THz), which provides unique information about their structure and allows conducting their chemical analysis [3].

Because of these properties, terahertz radiation has promising applications in areas such as safety monitoring imaging. As introduced preciously, normal covering or packing material (i.e. cloth) are transparent to terahertz radiations while liquid explosives or drugs can be distinguished from their unique spectral characteristics. Metal objects are opaque in the image since they reflect all terahertz radiations. The advantages of low energy, high signal to noise ratio and high sensitivity to the water content in biological tissues [3] present great potential of employing terahertz radiation in medical imaging. As for high frequency communication systems, compared to microwave frequencies, terahertz frequency carriers enable lager available bandwidth as well as smaller size for terahertz components. However, in practice the terahertz radiation suffer from large atmospheric attenuation and can't propagate for long distance in earth's atmosphere. In spite of this drawback, terahertz radiation presents its great potential applications in other area such as quality control, non-destructive testing, astronomy, atmospheric research, short distance wireless communications, networking and military applications [3]. During the last few decades, many studies and researches have been carried out in order to fill the 'terahertz gap', yet not so many really successful breakthroughs have been made, but the unique properties of terahertz sicence and technology suggest that its applications will grow fast [3].

1.2 Overview of Terahertz Waveguide Circuits and Micromachining

Waveguide is one kind of transmission line (usually in the form of a rectangular tube) for the propagation of electromagnetic waves. Compared with other typical transmission lines operating at same frequencies (i.e. microstrip, coaxial cable), waveguide can provide the lowest loss and best power handling capacity [4]. For microwave frequency applications, the bulky size of waveguide

circuits becomes the main drawback. Fortunately, for waveguide components in general, device dimensions decrease as frequency increases. As the operating frequencies of the waveguides go up into terahertz region, the waveguide components become smaller which means the size of waveguide is no longer a drawback. In this case, for terahertz circuits, rectangular waveguide is an ideal low loss medium for interconnectivity and for the construction of passive circuits [4]. However, new challenge comes as tighter dimensional accuracy is required for the fabrication of terahertz waveguide. For example, the cross-sectional dimensions for a WR-3 band (220 - 325 GHz) waveguide is just 864 by 432 μm, and the dimensions of the additional structures inside the waveguide (for example for a filter) can be much smaller than the dimensions of the waveguide itself. The dimensional accuracy required for a waveguide filter based on coupled resonators is even more demanding since the performance of the circuit is very sensitive to the dimensional sizes such as the length of the resonators and width of the coupling iris. From this perspective, more and more researchers have looked into different micromachining techniques to accomplish complex waveguide features with high dimensional accuracy.

Computer Numerical Control (CNC) machining is a traditional way of fabricating metal waveguide components and has been recently utilised for manufacturing devices operating at low terahertz frequencies (0.1-0.3 THz). Waveguide components fabricated by CNC milling with excellent performance have been reported in [5] and [6]. However, researchers are pushing the limit of the CNC micromachining. The structures of the waveguide filter are carefully designed to be achievable by CNC milling process. With the development of high precision CNC machines, CNC milling process remains a good choice for fabricating components operating at terahertz frequencies.

Other alternative micromachining process such as silicon deep reactive ion etching (DRIE) [7-

9], lithographic micromachining technique (LIGA) [10] and SU-8 photoresist technology [11-13], have been developed and employed by the researchers to achieve high-dimensional accuracy in the fabrication of terahertz waveguide filters. In [14], laser micromachining and 3-D printing have also been utilised for waveguide filters using different designs at about 100 GHz. These micromachining processes have shown great potential for the fabrication of terahertz waveguide circuits. However, each micromachining process has its advantages and drawbacks. This will be discussed in Chapter 3 with more details.

1.3 Motivations and Objectives

There has been great potential for the exploiting of terahertz frequency range due to its promising scientific and industrial applications. Many of the existing terahertz instruments are typically very large, difficult to use, intended for specific narrow applications, and prohibitively expensive. The work presented in this thesis focus on reducing the size, weight and cost of terahertz circuit while maintaining its quality of performance. For terahertz systems, the waveguide circuits have become a popular choice of transmission line, due to its lower loss and better power handling capacity. However, the responses of waveguide circuits operating at terahertz frequencies are especially sensitive to the dimensional accuracy, which brings challenges for the fabrication techniques of micro-structures.

Many manufacturing methods have been proposed and modified by the researchers to deal with the fabrication of complex waveguide circuits working at high frequencies. techniques as well as present a number of terahertz waveguide filters showing the advantages of micromachining technologies at terahertz frequencies. The main objectives of this thesis are (1) compare different

micromachining techniques and choose the most suitable processes based on potential performances, costs and available resources; (2) design and fabricate a number of terahertz waveguide filters which take advantage of the fabrication process while pushing the limits of state-of-art for the micromachining process (i.e. SU-8 photoresist technology and laser micromachining in this work).

1.4 Thesis Overview

This thesis is in two major parts: (i) a general review of waveguide filter design techniques and micromachining for terahertz waveguide circuits; (ii) terahertz waveguide circuits based on CNC milling, SU-8 photoresist technology and laser micromachining. Chapters 2-3 focus on the first part and Chapters 4-5 present the latter.

Chapter 1 gives the overview of terahertz radiation and its application, an overview of terahertz waveguide circuits and micromachining, together with the motivations and objectives for the thesis. An overview of the structure for this thesis is also included in this part.

Chapter 2 is intended to provide the general theories which are used to design waveguide filters presented in this thesis. The overview of coupled resonator filters and its coupling matrix representation is presented. This is followed by the overview of the waveguide filter technology and its physical realisation. In the last part of this chapter, a filter design example is given.

Chapter 3 reviews the micromachining techniques for the fabrication of terahertz waveguide circuits (mainly waveguide filters). The process and applications for CNC milling, DRIE process, LIGA process, SU-8 photoresist technology, laser micromachining and 3D-printing are introduced. This is followed by the discussion of the advantages and disadvantages of each process in each

subsection. Then the SU-8 micromachining process, which is developed at University of Birmingham (EDT group) and employed in the filter presented in Chapter 4; it is explained in detail. In the last part, a comparison of these micromachining techniques is provided.

Chapter 4 mainly presents the designs, fabrication and measurements of two micromachined circuits working at WR-3 band (220-325 GHz). One is based high precision CNC machining and another is fabricated using SU-8 photoresist technology. The specification is provided in the first part, followed by the discussion of filter design process. Then the fabrication, measurement and analysis of measured responses are presented. At the end of this chapter, the comparison of these two filters, together with other recently published waveguide filter operating in frequency from WR-10 to WR-1.5 band is given.

Chapter 5 deals with two laser micromachined waveguide filters both composed of four coupled resonators operating in TE_{101} mode working at WR-3 band. The first one uses a novel double-layer design and the second is designed with two H-bends. The design methods, an improved fabrication process of laser cutting and the measurements for both filters are discussed in detail in this chapter. Difference analysis between measured results and designed responses, and further suggestions for employing laser micromachining are presented in the last part of this chapter.

Chapter 6 is the conclusion of the whole thesis. The first part summaries the work that has been done and the main novelties for this work. The second part presents the comparisons between filters described in Chapter 4 and 5. The comparisons contain the measurement responses as well as the discussion of further applications of these processes. The suggestions for future work are also included in this chapter.

References:

[1] J. Hu, S. Liu, Y. Zhang and R. Xu, "Micromachined terahertz waveguide band-pass filters," *2017 IEEE MTT-S International Microwave Symposium (IMS)*, Honololu, HI, pp. 650-653, 2017

[2] X. Shang, "SU-8 Micromachined Terahertz Waveguide Circuits and Coupling Matrix Design of Multiple Passband Filters," Ph.D. dissertation, School Electron., Elect. Syst. Eng., Univ. Birmingham, Birmingham, U.K., 2011.

[3] A. Redo-Sanchez and X. C. Zhang, "Terahertz Science and Technology Trends," *IEEE Journal of Selected Topics in Quantum Electronics*, vol. 14, no. 2, pp. 260-269, Mar. 2008.

[4] H. Yang, Y. Dhayalan, X. Shang, M. J. Lancaster, *et al*, "WR-3 waveguide filter based on high precision CNC milling and SU-8 photoresist technology," *IEEE Trans. THz Sci. Technol*, vol. 8, no. 1, pp. 100-107, Jan. 2018.

[5] C. A. Leal-Sevillano, J. R. Montejo-Garai, J. A. Ruiz-Cruz and J. M. Rebollar, "Low-Loss Elliptical Response Filter at 100 GHz," *IEEE Microw. Wireless Compon. Lett.*, vol. 22, no. 9, pp. 459-461, Sep. 2012.

[6] J. Q. Ding, S. C. Shi, K. Zhou, Y. Zhao, D. Liu and W. Wu, "WR-3 Band Quasi-Elliptical Waveguide Filters Using Higher Order Mode Resonances," *IEEE Trans. THz Sci. Technol.*, vol. 7, no. 3, pp. 302-309, May. 2017.

[7] H. V. Jansen, M. J. de Boer, S. Unnikrishnan, M. C. Louwerse and M. C. Elwenspoek, "Black silicon method X: a review on high speed and selective plasma etching of silicon with profile control: an in-depth comparison between Bosch and cryostat DRIE processes as a roadmap to next generation equipment," *Journal of Micromechanics and Microengineering*, IOP Publishing, Ltd,

Feb. 2009.

[8] J. Y. Li, B. Pan, C. Lugo, M. Tentzeris, and J. Papapolymerou, “Design and characterization of aW-band micromachined cavity filter including a novel integrated transition from CPW feeding lines,” *IEEE Trans. Microw. Theory Tech.*, vol. 55, no. 12, pp. 2902–2910, Dec. 2007.

[9] K. M. K. H. Leong *et al*., "WR1.5 Silicon Micromachined Waveguide Components and Active Circuit Integration Methodology,” *IEEE Trans. Microw. Theory Tech.*, vol. 60, no. 4, pp. 998-1005, Apr. 2012.

[10] J. R. Stanec and N. S. Barker, “Fabrication and integration of micromachined submillimeter-wave circuits,” *IEEE Microw. Wireless Compon. Lett.*, vol. 21, no. 8, pp. 409–411, Aug. 2011.

[11] X. Shang, M. Ke, Y. Wang and M. J. Lancaster, “Micromachined W-band waveguide and filter with two embedded H-plane bends,” *IET Microw., Antennas Propag.*, vol. 5, no. 3, pp. 334-339, Feb. 2011.

[12] Q. Chen, X. Shang, Y. Tian, J. Xu and M. J. Lancaster, "SU-8 micromachined WR-3 band waveguide bandpass filter with low insertion loss," *Electron Lett.*, vol. 49, no. 7, pp. 480-482, March. 2013.

[13] X. Shang, Y. Tian, M. J. Lancaster, S. Singh, “A SU8 micromachined WR-1.5 band waveguide filter,” *IEEE Microw. Wireless Compon. Lett.*, vol. 23, (6), pp. 300-302, Jun. 2013

[14] X. Shang *et al*., “W-Band Waveguide Filters Fabricated by Laser Micromachining and 3-D Printing,” *IEEE Trans. Microw. Theory Tech.*, vol. 64, no. 8, pp. 2572-2580, Aug. 2016.

Chapter 2

General Theory for Resonator Based Filters

2.1 Background of Filters Based on Resonators

A filter is a two-port network commonly utilised for transmitting or attenuating signals for desired frequency bands. The coupled resonator filter is a common type of filter and has been presented in literature for applications in communication system and radar systems [1].

A general synthesis for design filters using coupled resonators can be found in [2]. This technique can be utilised to any kinds of resonators regardless of their physical geometry. Using coupling matrix to represent filter circuits is the key process in such a technique. By modelling the filter in a matrix, each physical element of the final filter circuit can be transferred to a corresponding element in the coupling matrix [3]. Before the introduction of the terahertz filters, the basic knowledge for coupled resonator filter theory related to this work are presented in this chapter.

2.2 Coupling Matrix Representation

The derivation of the representation of general coupling matrix for a coupled resonator filter has been introduced in [2]. The equivalent circuit with magnetically coupled resonators and circuit with electrically coupled resonators are given in Fig. 2.1 (a) and (b) respectively. In Fig. 2.1, R, G, C and L represent the resistance, conductance, capacitance and inductance; *i* and *v* stand for the current and voltage.

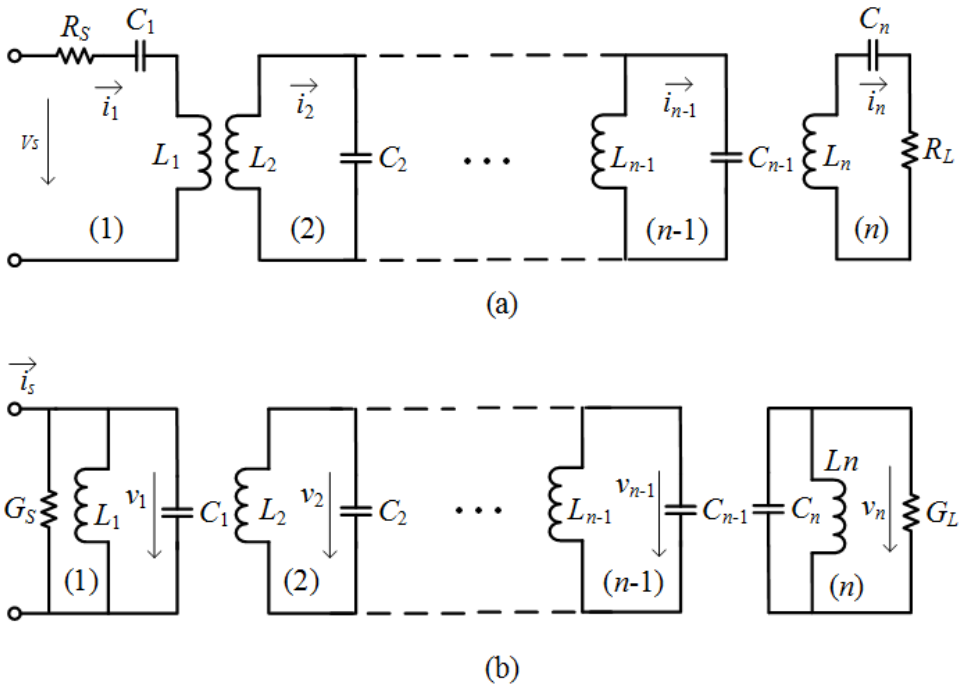

Fig. 2.1 Equivalent circuit of a waveguide filter composed of (a) magnetically *n*-coupled resonators (b) electrically *n*-coupled resonators [2].

By employing Kirchoff's voltage and Kirchoff's current law, the coupling matrix can be derived from an impedance matrix using a set of loop equations or via an admittance matrix calculated using a set of node equations [2]. The derivations present that the normalised admittance matrix and normalised impedance matrix have identical form. We will not reproduce the derivation here, however the result for a general matrix [*A*] in terms of coupling coefficients and external quality factors for both kinds of coupling introduced above is [2]:

$$[A]=[q]+p[U]-j[m]=\begin{bmatrix}\frac{1}{q_{e1}} & 0 & \cdots & 0\\ 0 & 0 & \cdots & 0\\ \vdots & \vdots & \ddots & \vdots\\ 0 & 0 & \cdots & \frac{1}{q_{en}}\end{bmatrix}+p\begin{bmatrix}1 & 0 & \cdots & 0\\ 0 & 1 & \cdots & 0\\ \vdots & \vdots & \ddots & \vdots\\ 0 & 0 & \cdots & 1\end{bmatrix}-j\begin{bmatrix}m_{1,1} & m_{1,2} & \cdots & m_{1,n}\\ m_{2,1} & m_{2,2} & \cdots & m_{2,n}\\ \vdots & \vdots & \ddots & \vdots\\ m_{n,1} & m_{n,2} & \cdots & m_{n,n}\end{bmatrix} \quad (2.1)$$

$$p = j\frac{1}{FBW}\left(\frac{\omega}{\omega_0}-\frac{\omega_0}{\omega}\right) \quad (2.2)$$

where q_{ei} is the normalised external quality factor of resonator i, [q] is the $n\times n$ matrix with all entries zero, except for $q_{11}=1/q_{e1}$ and $q_{nn}=1/q_{en}$, matrix [*U*] is the $n\times n$ unit matrix, *p* is the complex low pass frequency variable, ω_0 is the centre frequency of the resonator, *FBW* represents the fractional bandwidth for the waveguide filter. m_{ij} $(i\neq j)$ is the normalised coupling coefficient between the resonator *i* and *j*, the diagonal entries m_{ii} is the self-coupling coefficient.

As presented in [2], the insertion loss and return loss (*S*-parameters) of this coupled resonator filter can be calculated using the general matrix [*A*] with normalised external quality factors as:

$$\begin{aligned} S_{11} &= \pm\left(1-\frac{2}{q_{e1}}[A]^{-1}_{1,1}\right)\\ S_{21} &= 2\frac{1}{\sqrt{q_{e1}\cdot q_{en}}}[A]^{-1}_{n,1}\end{aligned} \quad (2.3)$$

For filters with Chebyshev, Butterworth and Elliptic or other standard responses, the normalised external quality factors and general coupling matrix [*A*] can be calculated from its low-pass prototype elements g_0, g_1, $\ldots g_{n+1}$, which can be found from tables directly or calculated by formulas shown in equation (2.4) [2].

The low-pass prototype g values for the Chebyshev filter with a passband ripple L_{Ar} dB and the cut-off frequency $\Omega_c = 1$ are calculated using the following formulas given in [2],

$$
\begin{aligned}
g_0 &= 1 \\
g_1 &= \frac{2}{\gamma}\sin\left(\frac{\pi}{2n}\right) \\
g_i &= \frac{1}{g_{i-1}} \frac{4\sin\left(\frac{(2i-1)\pi}{2n}\right)\cdot\sin\left(\frac{(2i-3)\pi}{2n}\right)}{\gamma^2 + \sin^2\left(\frac{(i-1)\pi}{n}\right)} \quad (i = 2 \text{ to } n) \\
g_{n+1} &= \begin{cases} 1 & \text{for } n \text{ odd} \\ \coth^2\left(\frac{\beta}{4}\right) & \text{for } n \text{ even} \end{cases}
\end{aligned}
\tag{2.4}
$$

where

$$
\begin{aligned}
\beta &= \ln\left[\coth\left(\frac{L_{Ar}}{17.37}\right)\right] \\
\gamma &= \sinh\left(\frac{\beta}{2n}\right)
\end{aligned}
$$

Using lumped elements, the normalised external quality factors and the coupling coefficients between adjacent resonators for Chebyshev lowpass prototype filters can be calculated from g values as:

$$
\begin{aligned}
q_{e1} &= g_0 g_1, \quad q_{en} = g_n g_{n+1} \\
m_{i,i+1} &= \frac{1}{\sqrt{g_i g_{i+1}}} \qquad \text{for } i = 1 \text{ to } n-1
\end{aligned}
\tag{2.5}
$$

2.3 Physical Realisation of Waveguide Filter

2.3.1 Rectangular waveguide

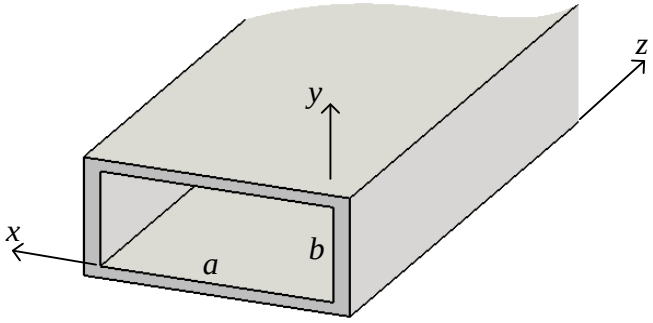

Fig. 2.2 Cross section of a rectangular waveguide [4]

The design of a waveguide filter will be discussed in Section 2.3.4. However, before proceeding this we will discuss the basic principles of a rectangular waveguide as it is so important for the work in this thesis. A waveguide is performed as a circuit which directs the propagation of energy in the form of an electromagnetic wave [4]. The rectangular waveguide, of which the cross section is shown in Fig.2.2, is the most common type of waveguide [4]. The following presents several important properties of a rectangular waveguide. More detailed descriptions of waveguide theory can be found in [4].

In a rectangular waveguide, TE (i.e. transverse electric) and TM (i.e. transverse magnetic) modes are allowed to propagate while a TEM (i.e. transverse electromagnetic) mode is not supported. The cut-off frequency is defined as the lowest frequency each mode can propagate through the waveguide. From the derivation in [4], the cut-off frequency f_{cutoff} of each TE_{mn} mode of TM_{mn} mode is calculated as equation (2.6).

$$f_{cutoff} = \frac{c}{2}\sqrt{(\frac{m}{a})^2 + (\frac{n}{b})^2} \tag{2.6}$$

where *a* and *b* represent the width and height of the rectangular waveguide, *c* is the speed of light in free space, *m* and *n* are the number of half standing waves along the width (*x* axis) and height (*y* axis) of the rectangular waveguide. The mode with the lowest cut-off frequency is called the dominant mode. For common rectangular waveguide which meets the condition of *a=2b*, the TE_{10} mode is the dominant mode as it has the lowest cut-off frequency of $f_{cutoffTE_{10}} = c/2a$. As for TE_{20} mode, it has the second lowest cut-off frequency of $f_{cutoffTE_{20}} = c/a$. In this situation (*a=2b*), in the frequency band between *c/2a* and *c/a* only the TE_{10} mode propagate inside the waveguide, so when using this frequency band, the waveguide is said to be as single mode, the useful bandwidth of this rectangular waveguide is calculated as $f_{cutoffTE_{20}} - f_{cutoffTE_{10}} = c/2a$. To get rid of the influence of higher modes, rectangular waveguides are almost always operated in the band in which they are single-mode [4]. In this case, when designing waveguide filters, the passband of the filter should also be designed within the single-mode frequency band for such waveguide.

For non-standard rectangular waveguide, for example, for $b > a/2$, the cut-off frequency of the TE_{01} mode would be calculated as the second-lowest based on equation (2.6). The actual useful bandwidth of the rectangular waveguide is calculated as $f_{cutoffTE_{01}} - f_{cutoffTE_{10}} = c/b - c/a$, which has relatively smaller single mode bandwidth. Therefore, in order to obtain wider useful bandwidth, *b* is preferred to be no bigger than *a*/2. However, the waveguide attenuation increases as *b* increase [4]. For rectangular waveguide of $b < a/2$, the useful bandwidth is still between the cut-off of TE_{10} mode and TE_{20} mode, however the attenuation would increase [4]. Therefore, for a rectangular

waveguide, the optimum height *b* is exactly half of the width *a*.

2.3.2 Cavity resonator and coupling iris

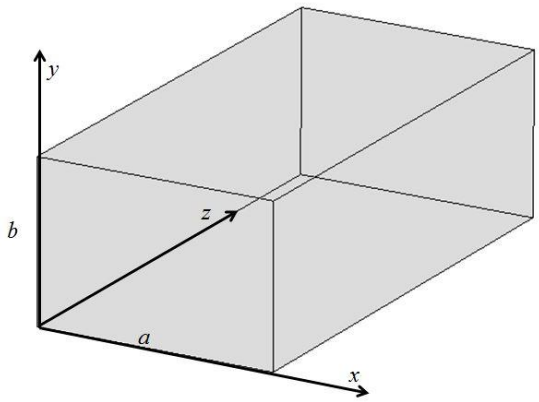

Fig. 2.3 A standard rectangular cavity resonator

Cavity resonators are able to store both electric and magnetic energy [3] and they are the key components in the physical realization of a resonator filter. A cavity resonator is composed by rectangular waveguide ended with two conducting walls at both ends [3]. A standard single cavity resonator is shown in Fig. 2.3. The resonant frequency and the unloaded quality factor are two important parameters for a cavity resonator. The calculation of resonator frequency and unloaded quality factor of a single cavity resonator using the physical dimensions is presented in the following part.

The resonant frequency is the frequency at which the stored electric energy within a single cavity equals the stored magnetic energy [3]. For a rectangular waveguide cavity, the transverse

electric field (E_x, E_y) of the TE$_{mn}$ or TM$_{mn}$ mode can be express as [4]:

$$\overrightarrow{E_t}(x,y,z) = \vec{e}(x,y)[A^+ e^{-j\beta_{mn}z} + A^- e^{-j\beta_{mn}z}] \qquad (2.7)$$

In the above equation (2.7), $\vec{e}(x,y)$ represents the transverse variations in the x and y directions, A^+ and A^- represent the amplitude of the travelling wave in $+z$ and $-z$ (forward and backward) directions. β_{mn} is defined as the propagation constant for the TE$_{mn}$ or TM$_{mn}$ mode and can be found in [4] as:

$$\beta_{mn} = \sqrt{k^2 - (\frac{m\pi}{a})^2 - (\frac{n\pi}{b})^2} \qquad (2.8)$$

where k is the wavenumber which can be calculated as $k = 2\pi f_0\sqrt{\mu\varepsilon}$, μ is the permeability and ε is the permittivity of the material within the waveguide [4]. From equation (2.7), by employing the condition that $\overrightarrow{E_t}(x,y,0) = 0$ and $\overrightarrow{E_t}(x,y,d) = 0$, we can get:

$$l_r = l \cdot \frac{\pi}{\beta_{mn}} = l \cdot \frac{\lambda_g}{2} \qquad for \;\; l = 1,2,3\ldots \qquad (2.9)$$

Equation (2.9) indicates that the length of a cavity resonator l_r should be integer l times of half guided wavelength λ_g of the considered mode at the resonant frequency [4]. The cut-off wavenumber of the rectangular cavity resonator can be calculated as [4]:

$$k_{mnl} = \sqrt{(\frac{m\pi}{a})^2 + (\frac{n\pi}{b})^2 + (\frac{l\pi}{d})^2} \qquad (2.10)$$

where the m, n and l represent the number of half wavelength variations in the x, y, z directions,

respectively. Then the modes existing in the cavity resonator can be expressed as TE_{mnl} and TM_{mnl}, while the resonator frequency f_{mnl} of these modes can be calculated as:

$$f_{mnl} = \frac{ck_{mnl}}{2\pi\sqrt{\mu_r\varepsilon_r}} = \frac{c}{2\pi\sqrt{\mu_r\varepsilon_r}}\sqrt{(\frac{m\pi}{a})^2 + (\frac{n\pi}{b})^2 + (\frac{l\pi}{d})^2} \tag{2.11}$$

where c is the speed of light in free space, μ_r and ε_r stand for the relative permeability and permittivity of the material filling the waveguide, respectively.

The unloaded quality factor Q_{ul} is used to describe the inherent loss in a resonator and is defined as the ratio between the energy stored in the resonator versus power lost per unit time [3]. A low/high unloaded quality factor corresponds to a high/low loss. The unloaded quality factor for a single cavity resonator is calculated using equation (2.12).

$$Q_{ul} = (\frac{1}{Q_c} + \frac{1}{Q_d})^{-1} \tag{2.12}$$

where Q_c stands for the factor of loss caused by lossy conducting walls and Q_d represents the loss caused by dielectric that is filling in the resonator. For the filters designed in this work, air is the filling material within the resonator, therefore $Q_d \to \infty$. In this case, only Q_c is considered and used to calculated the unloaded quality factor. From [1], the Q_c of a single cavity resonator working at TE_{10l} mode is calculated as:

$$Q_c = \frac{(kad)^3 b\eta}{2\pi^2 R_s(2a^3b + 2bd^3 + a^3d + ad^3)} \tag{2.13}$$

where R_s is the surface resistance, the conductivity of the conductive wall for the resonator is σ, R_s is then calculated as $R_s = \sqrt{\omega\mu / 2\sigma}$ [1]. η is the wave impedance and calculated as

$\eta = \sqrt{\mu / \varepsilon}$.

In a waveguide filter design, the cavity resonators are typically coupled by inductive iris or capacitive iris or both, depending on the specification for desired response. Fig. 2.4 shows some standard coupling iris for two rectangular cavity resonators coupled together. The techniques of extracting initial dimensions for the coupling iris from the corresponding elements in coupling matrix will be introduced in the following sections.

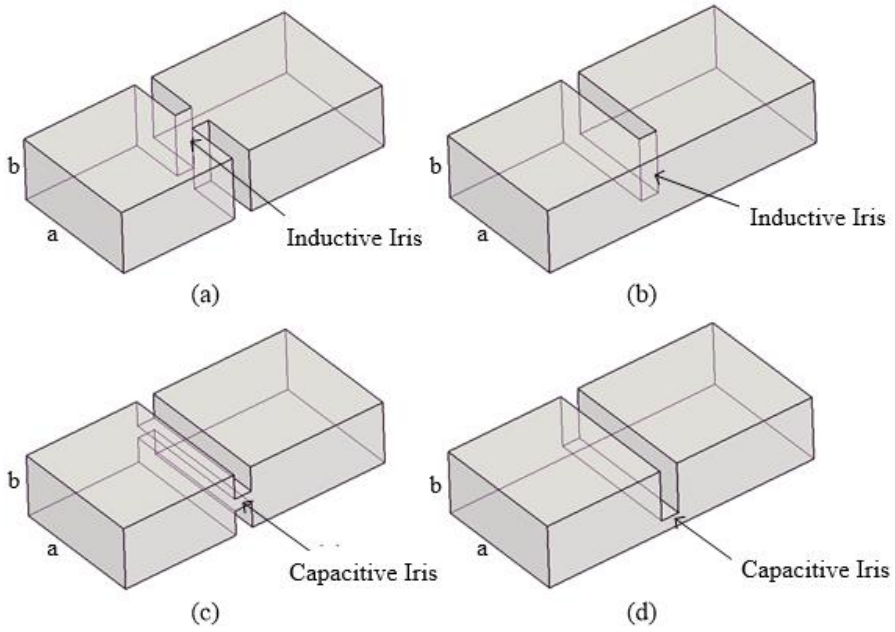

Figure 2.4 Rectangular cavity resonators coupled by different coupling iris: (a)(b) Inductive iris (c)(d) Capacitive iris

2.3.3 Determine external quality factor and coupling coefficients

To convert the elements of coupling matrix into the dimensions of waveguide physical

structures, it is important to figure out the relationship between each matrix entry and its related physical dimension for the waveguide components. As described above, the external quality factors and internal coupling coefficients between resonators can be derived from the filter's specifications. Then the physical dimensions of the filter structures can be determined using the following techniques [1].

The definition of unloaded quality factor Q_{ul} is described in Section 2.3.2. For the cavity coupled with a source and load, the loaded quality factor Q_l is calculated as:

$$Q_l = \left(\frac{1}{Q_{ul}} + \frac{1}{Q_e}\right)^{-1} \tag{2.14}$$

where Q_e is the external quality factor.

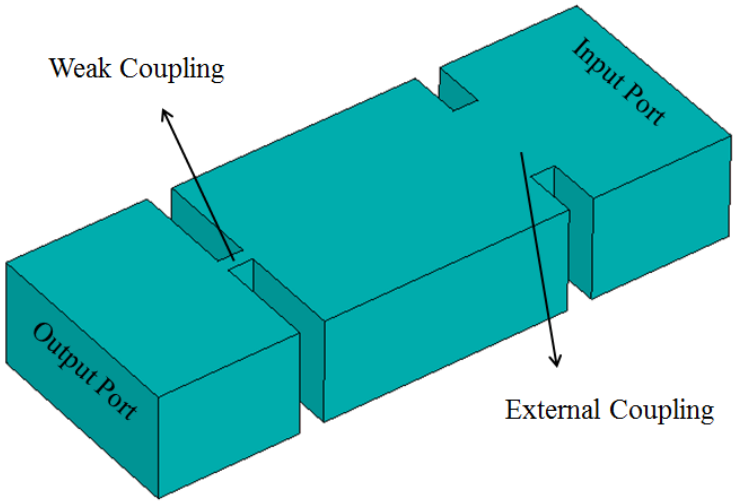

Fig. 2.5 Single resonator cavity externally coupled to one port and weakly coupled to another port

The loaded quality factor can be measured by simulation S_{21} response of the single cavity resonator with one port externally coupled to input port and another port weakly coupled to output

port. Fig. 2.5 shows an example of a resonator cavity that is externally coupled to the input port and weakly coupled to the output port. From the simulated S_{21} response shown in Fig. 2.6, the loaded quality factor Q_l is calculated in equation (2.15) using the resonator frequency f_0 and the 3-dB bandwidth $\Delta f_{3\text{-dB}}$ as:

$$Q_l = \frac{f_0}{\Delta f_{3\text{-}dB}} \tag{2.15}$$

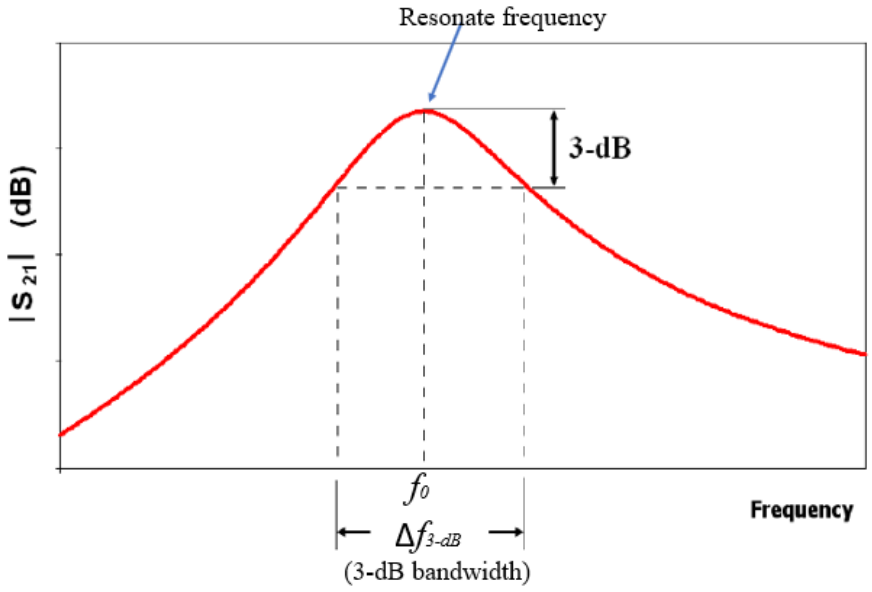

Fig. 2.6 3-dB bandwidth in simulated S_{21} response (Figure reproduced form [3])

It should be noted that Q_l should be calculated when f_0 is equal to resonant frequency of the cavity, otherwise the length l of the resonator should be adjusted to make f_0 equal to the desired resonant frequency. For perfect electric conductor and no radiation to the environment the EM

simulator (i.e. CST Microwave Studio) then the unloaded quality factor $Q_{ul} \to \infty$. From equation (2.7) the external quality factor Q_e can be calculated as:

$$Q_e = Q_l \tag{2.16}$$

To determine the internal coupling coefficient k_c (this is corresponded to m_{ij} in the coupling matrix), the structure shown in Fig. 2.7 is given. The two resonators are identical and internally coupled to each other. The other port of each filter is weakly coupled to input/output port.

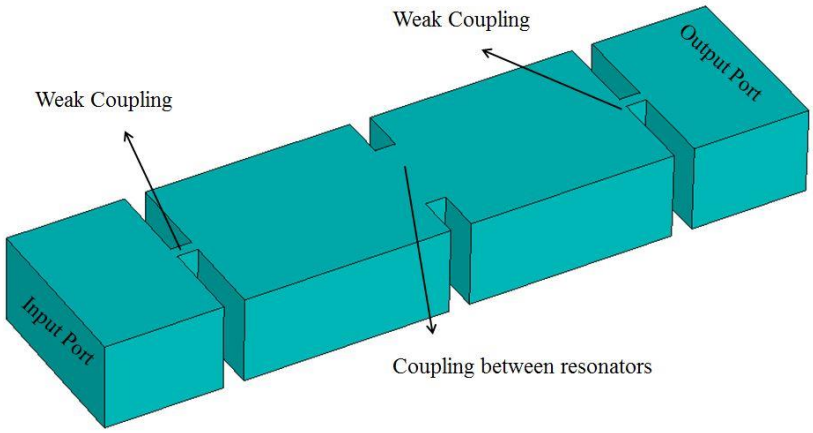

Fig. 2.7 Two coupled resonators with weak external couplings to input/output ports.

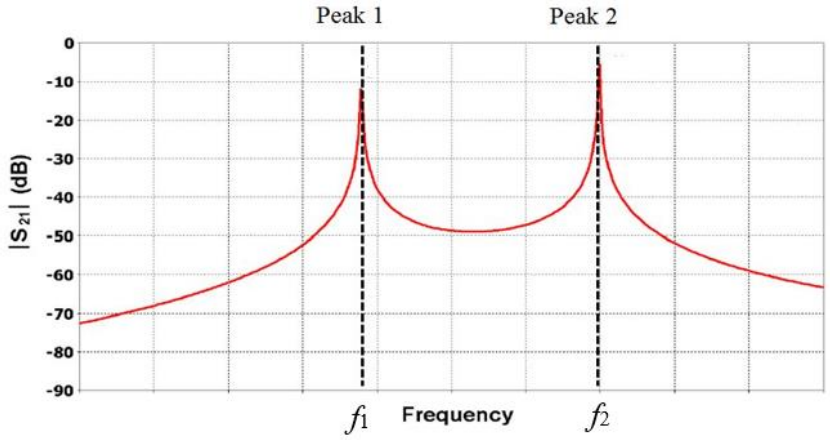

Fig. 2.8 Simulate results of S_{11} and S_{21} for two coupled resonators

Figure 2.8 shows the simulated S_{21} of the two coupled resonators. f_1 and f_2 are the frequencies of two peaks of simulated S_{21}. The coupling coefficient between each two resonators k_c can be calculated from the formulation as [5]:

$$k_c = \pm \frac{1}{2}\left(\frac{f_{02}}{f_{01}} + \frac{f_{01}}{f_{02}}\right)\sqrt{\left(\frac{f_2^2 - f_1^2}{f_2^2 + f_1^2}\right)^2 - \left(\frac{f_{02}^2 - f_{01}^2}{f_{02}^2 + f_{01}^2}\right)^2} \tag{2.17}$$

where, f_{01} and f_{02} are the resonant frequencies of each uncoupled resonator.

When the coupled resonators are synchronously tuned (i.e. $f_{01} = f_{02}$), equation (2.17) is simplified as [2]:

$$k_c = \frac{f_2^2 - f_1^2}{f_2^2 + f_1^2} \tag{2.18}$$

For asynchronously tuned resonators, when the ratio of two resonant frequencies f_{01} and f_{02} is within a small range ($f_{01} / f_{02} < 1.1,\ f_{02} \geq f_{01}$), the asynchronously tuning has very little effect

on the value of the internal coupling coefficient [3]. The topology in Fig. 2.7 can also be applied to extract the internal coupling of the asynchronously tuned resonators. However, for more complicated situations (e.g. $f_{01} / f_{02} > 1.1,\ f_{02} > f_{01}$), we need to apply the full equation of (2.17) to calculate the coupling coefficient between two resonators.

The above techniques give the initial values for the dimensions of the filter design, by connecting resonators in series, the coupled resonator filter is formed. After optimisation process in EM simulators, the response can be optimised to match the filter specification.

2.4 Example of a Standard Coupled Resonator Filter

From the filter's specification, the external quality factors and coupling coefficients between resonators can be obtained in a coupling matrix. The physical dimensions can be extracted from the corresponding elements in the coupling matrix using the method explained in section 2.3.3. Here, the design of a 3rd order Chebyshev filter centred at 300 GHz with 5% fractional bandwidth and 20 dB maximum return loss within passband is presented as an example. As shown in Fig. 2.9, the waveguide filter is composed of three cavity resonators working in the TE_{101} mode. Both the external couplings with input/output port and the internal couplings between resonators are realised by symmetric inductive iris in this example.

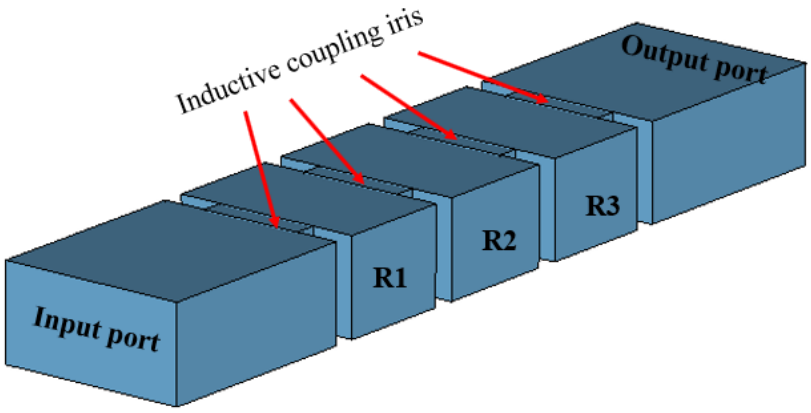

Fig. 2.9 The 3D model for the 3rd order Chebyshev waveguide filter simulated in CST. R1, R2 and R3 represent the resonator 1, 2 and 3. The blue part represents vacuum and the background is set to be perfect electric conductor (PEC).

2.4.1 Calculation of coupling matrix using specifications

By using equation (2.4), the lowpass prototype g values for the of the designed 3rd order Chebyshev filter (n=3, S_{11max}=-20 dB, f_{c0}=300 GHz, FBW=5%) can be calculated as g_0=1, g_1=0.8516, g_2=1.1032, g_3=0.8516 and g_4=1. Applying these g values in equation (2.5), we can figure out the normalised external quality factors and the coupling coefficients between adjacent resonators as: q_{e1}=q_{e3}=0.8516, m_{12}=m_{23}=1.0317.

For the practical waveguide filter, the actual external quality factors and the coupling coefficients can be calculated as:

$$Q_{e1} = \frac{q_{e1}}{FBW} \qquad Q_{en} = \frac{q_{en}}{FBW}$$

$$M_{i,i+1} = FBW \bullet m_{i,i+1} \qquad \text{for } i = 1 \text{ to } n-1 \tag{2.19}$$

From equation (2.19), the required values are calculated to be: $Q_{e1}=Q_{e3}=17.032$, $M_{12}=M_{23}=0.0516$. The actual S parameters can be calculated using these un-normalised values in equation (2.3). The calculated responses using coupling matrix are shown in Fig. 2.10.

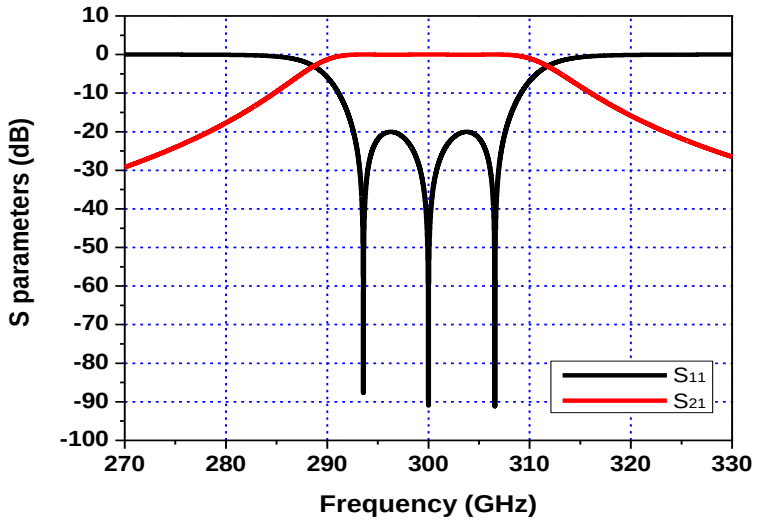

Fig. 2.10 Calculated S-parameters using coupling matrix for the designed 3rd order Chebyshev waveguide filter

2.4.2 Realisation of external quality factors in physical dimensions

Using the method introduced in Section 2.3.3, the dimensions of the coupling iris between input/output ports and resonators can be calculated by simulating the structure shown in Fig. 2.11.

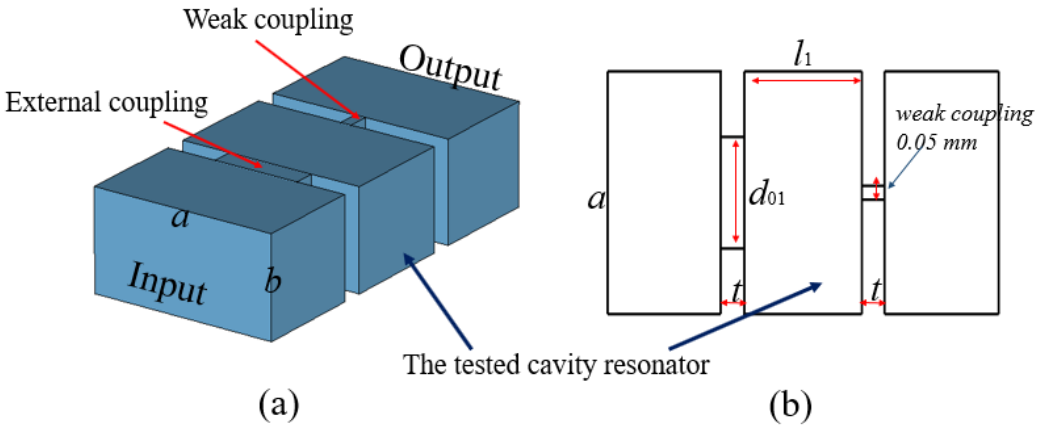

Fig. 2.11 (a) 3D model (a=0.864 mm, b=0.432 mm) simulated in CST to determine the external coupling iris based on external quality factors. (b) The top view of the simulated structure. d_{01} represents the dimension of the external coupling iris between input port and the 1st resonator, l_1 is the length for the 1st resonator. In this example, the thickness t for each iris is set to be 0.1 mm.

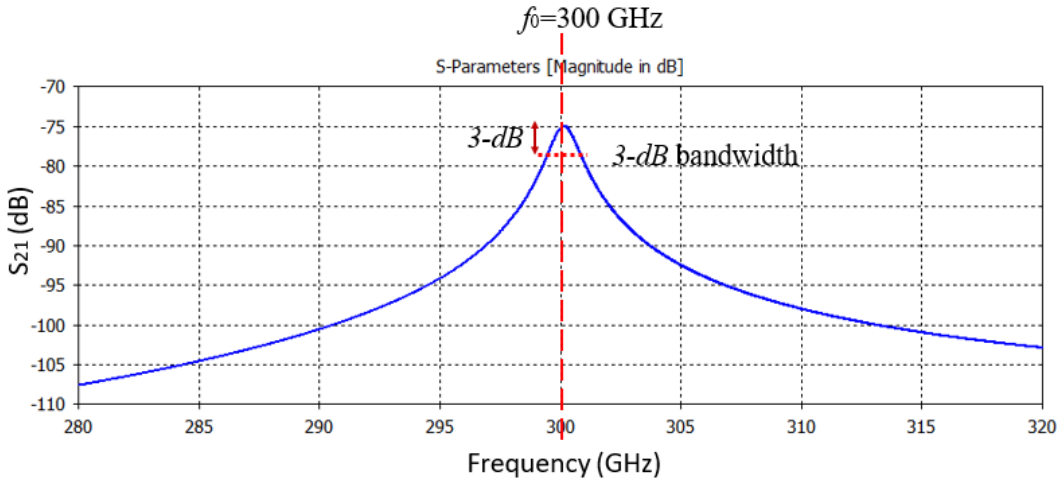

Fig. 2.12 Simulation results of the structure shown in Fig. 2.11. The 3-dB bandwidth can be extracted from the S_{21} response.

Note that the centre frequency for the simulated resonator varies as the length of the resonator (l) changes. In this example, as the dimension for the 1st external coupling iris (d_{01}) changes, the length of the first resonator (l_1) should be adjusted to make sure the centre frequency is still

300 GHz. By repeating these steps for different dimensions of external coupling iris and then substituting the centre frequency (300 GHz) and the 3-dB bandwidth obtained from the simulations into equation (2.15), we can get a series of l_1 and d_{01} with corresponded Q_e values, as shown in Table-2.1.

Table-2.1 Simulated results to extract external quality factor from physical dimensions

f_0=300 GHz					
d_{01} (mm)	0.30	0.35	0.40	0.45	0.50
l_1 (mm)	0.572	0.559	0.530	0.507	0.480
Q_{e1}	245.6	84.1	31.8	15.2	7.1

Seen from Table-2.1, we can figure out that the suitable values for d_{01} is between 0.40-0.45 mm, and the suitable values for l_1 is between 0.507-0.530 mm. Through more detailed simulations (using parameter sweeps in CST), d_{01}=0.438 mm and l_1=0.511 mm are selected as the initial dimensions to achieve the calculated external factor (Q_{e1}=17.032) for this example.

2.4.3 Realisation of coupling coefficients in physical dimensions

As introduced in Section 2.3.3, the dimensions of the coupling iris between resonators can be determined by simulating the structure shown in Fig. 2.13. The simulated results for the structure are given in Fig. 2.14.

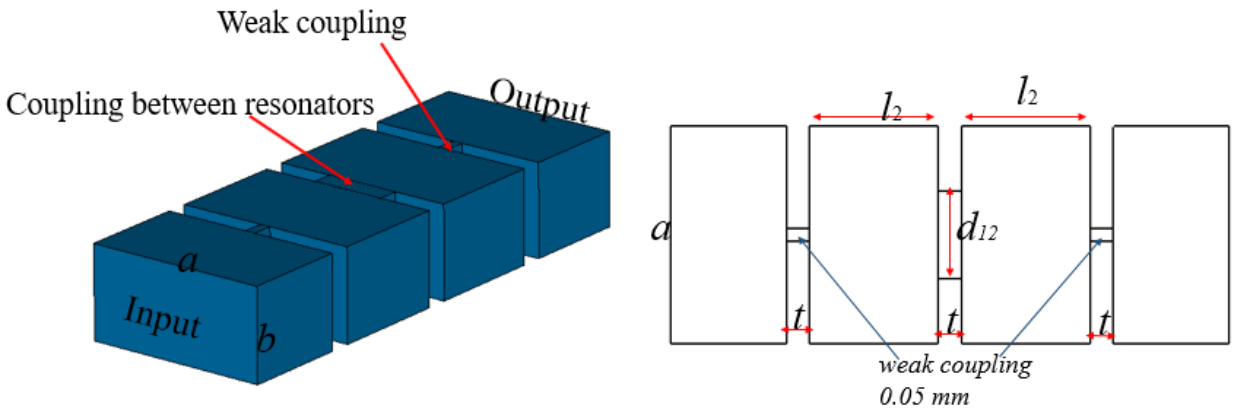

Fig. 2.13 (a) 3D model (a=0.864 mm, b=0.432 mm) simulated in CST to determine the dimensions of coupling iris between resonators. (b) The top view of the simulated structure. d_{12} represents the width of the coupling iris between resonators, l_2 is the length for the 2nd resonator. In this simulation, the thickness t for each iris is also set to be 0.1 mm.

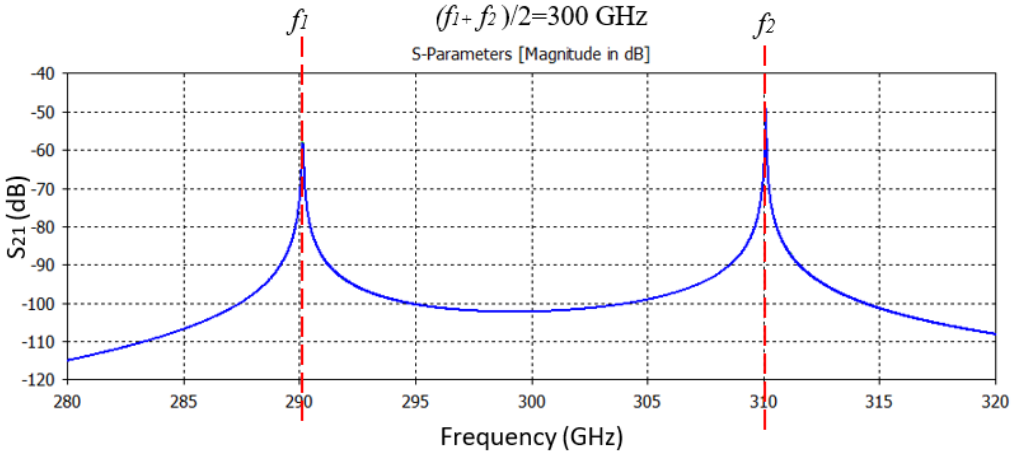

Fig. 2.14 The simulated S_{21} response for the of two coupled resonators shown in Fig. 2.13. f_1 and f_2 are the two resonate frequencies for the structure.

Equation (2.18) gives the relationship between coupling coefficient and two resonate frequency (f_1 and f_2). From the simulations, the coupling coefficients can be controlled by adjusting the width of the coupling iris (d_{12}). Note that the length for the resonator (l_2) should also be adjusted to ensure the middle frequency of two resonate peaks $(f_1 + f_2)/2$ is at centre frequency f_0 of 300 GHz for this example. Using equation (2.18), applying the actual frequencies of two resonate peaks, we can get the actual coupling coefficient M_{12} between resonator 1 and resonator 2. The results for the simulations are given in Table-2.2.

Table 2.2 Simulated results to extract coupling coefficients form physical dimensions

$(f_1 + f_2)/2=f_0$ (300 GHz)					
d_{12} (mm)	0.310	0.320	0.330	0.340	0.350
l_2 (mm)	0.564	0.562	0.560	0.558	0.556
M_{12}	0.0456	0.0498	0.0555	0.0605	0.0663

From Table 2.2, we can figure out that the suitable values for d_{12} is between 0.320-0.330 mm, and the suitable values for l_2 is between 0.560-0.562 mm. After more detailed simulations, to obtain the required coupling coefficients (M_{12}=M_{23}=0.0516), d_{12}=0.322 mm and l_2=0.561 mm are selected as the initial values for the width of the coupling iris.

2.4.4 Final optimisation

After extracting the initial values for the dimensions of the filter structures from coupling matrix elements, three resonators are connected in series and externally coupled with input/output port to establish the 3rd order Chebyshev bandpass filter. The simulation results using the initial values

for the dimensions are shown in Fig. 2.15. Seen from the initial simulated results, the responses can roughly meet the requirements except for the shift in passband frequencies. Then further CST optimisations have been applied to achieve the specifications by adjusting dimensions such as length of the resonators and width of coupling iris. The final responses after optimisations are presented in Fig. 2.15 and the optimised dimensions are given in Fig. 2.16.

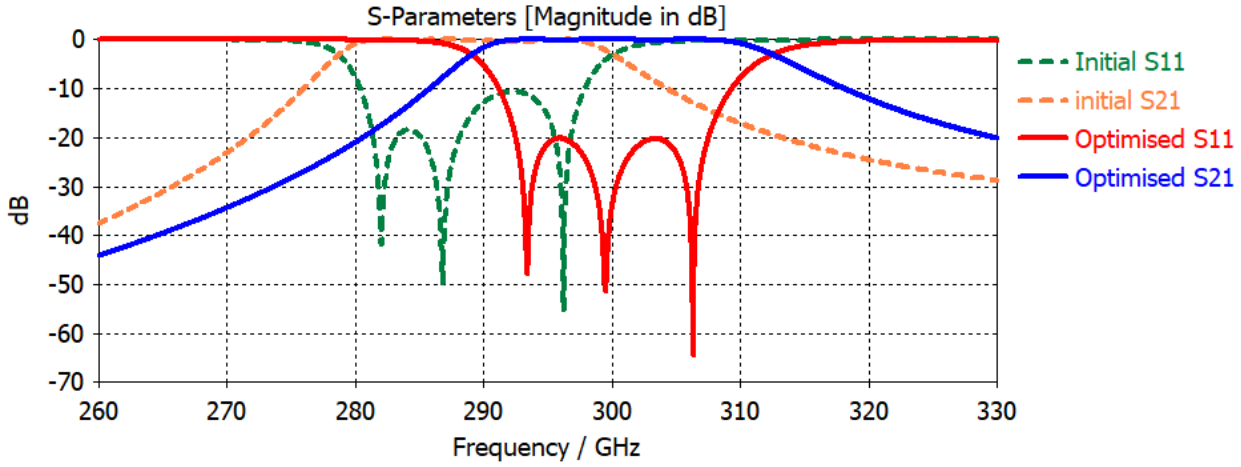

Fig. 2.15 CST simulated S-parameters responses using initial values (dash lines) and responses after optimisations (solid lines).

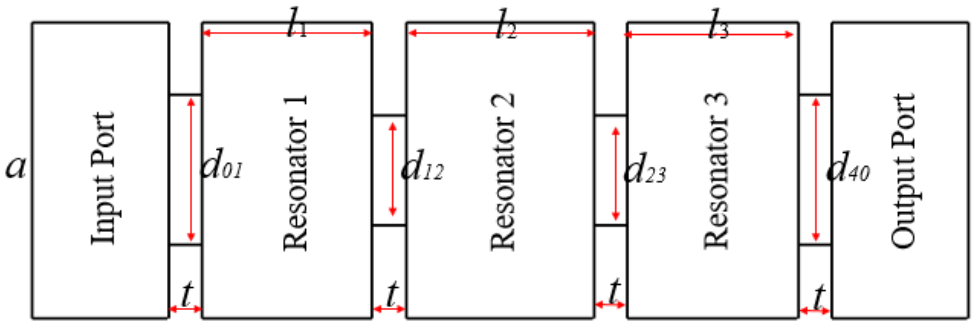

Fig. 2.16 The top view of the 3rd order Chebyshev filter with optimised dimensions. The optimised dimensions for the filter structures are: l_1=l_3=0.460 mm, l_2=0.517 mm, d_{01}=d_{40}=0.442 mm, d_{12}=d_{23}=0.318mm, t=0.1 mm,

2.5 Conclusions

The background theories for the filter based on coupled resonators have been presented in this chapter. It starts with the introduction of coupling matrix representation for the resonator-based filters. This is followed by the discussion of characteristic for the rectangular waveguides, cavity resonators and coupling iris. Then the methods of realisation of physical dimensions based on coupling matrix are explained in detail. Finally, the design process of a 3rd order Chebyshev waveguide filter is given as an example. Note that it is very important to obtain a relatively accurate initial values since the optimisation process may fail to achieve the specification if the initial values are too far from the solution results.

Reference:

[1] D. M. Pozar, *Microwave Engineering*. Third edition, John Wiley & Sons, Inc, 2005

[2] J. Hong and M. J. Lancaster, *Microstrip Filters for RF/Microwave Applications*. New York, USA: Wiley, 2001.

[3] R. J. Cameron, C. M. Kudsia, R.R. Mansour, *Microwave Filters for Communication Systems: Fundamentals, Design and Applications.* Hoboken, NJ, USA: Wiley, 2007.

[4] N. J. Cronin, *Microwave and Optical Waveguides.* IOP Publishing Ltd, 1995.

[5] J. Hong, "Couplings of asynchronously tuned coupled microwave resonators," *IET Microw., Antennas Propag.*, vol.147, no.5, pp.354-358, Oct. 2000.

Chapter 3

Micromachining for Terahertz Waveguide Circuits

As introduced in Chapter 1, the waveguide, usually in the form of a rectangular metal or metallised tube, is an ideal low loss medium for the connection and construction of passive circuits compared with other types of transmission lines operating at the same frequencies [1]. Due to its low loss characteristics, the waveguide becomes more and more popular, especially for circuits operating at frequencies at about 0.1 THz and beyond. However, as frequency goes up, the size of the waveguide decreases and the tolerance on dimensions become more stringent, which bring huge challenges and high cost to the conventional fabrication techniques such as CNC (Computer Numerical Controlled) machining. From the review of Chapter 2, for waveguide filters based on coupled cavity resonators, the dimensional accuracy is the primal challenge since their resonant frequencies depend on the accuracy of dimensions of the length of resonator cavities (primarily the length but other dimensions also) and external quality factor and coupling coefficients are sensitive to the dimensions of the coupling iris. Researchers have been actively studying this and different manufacturing techniques have been proposed and developed for the fabrication of complex terahertz circuits with improved dimensional accuracy and reduced cost [2]. The current states of these micromachining techniques will be reviewed and presented in Section 3.1.

The SU-8 photoresist technology and laser micromachining are the two emerging micromachining techniques which are employed in this work to fabricate the waveguide devices working at WR-3 band (220-325 GHz). The detailed process of SU-8 photoresist technique [3] is presented in Section 3.2 and a novel multi-stage process for laser micromachining is discussed in Section 5.2.2, while the micromachined terahertz circuits using those two techniques are described

in Chapter 4 and Chapter 5.

3.1 Overview of Micromachining Techniques for Terahertz Waveguide Circuits

Fabricating terahertz circuits using traditional process, such as CNC milling, can be extremely expensive and hard to achieve demanding dimensional accuracy at high frequency. Different micromachining techniques such as silicon deep reactive ion etching (DRIE) [4-5], lithographic micromachining technique (LIGA) [6] and SU-8 photoresist technology [7-8], have been developed and utilised in fabricating terahertz waveguide filters with high-dimensional accuracy. Laser micromachining [9] and 3-D printing [10] have also been utilised for high frequency filters by the authors using different designs at about 0.1 THz [3]. The general introduction for these different fabrication techniques is presented in the following subsections.

3.1.1 CNC milling

Traditionally, for geometrically simple metal waveguide circuits operating at lower frequency, the main fabricating process is by milling on a high precision CNC machine, usually using a split-block technique [2]. Recently, for waveguide components operating around 100 GHz, the CNC milled waveguide filters with excellent performance have been reported. Two 4^{th} order Chebyshev waveguide filters operating on W-band are presented in references [11] and [12]. The first filter is centred at 92.6 GHz and measured to have 0.5 dB insertion loss with fractional bandwidth (FBW) of 4.53%. In [12], the filter is centred at 100 GHz with 10 GHz bandwidth and measured to have 0.6 dB insertion loss within passband. For the 220 to 325 GHz WR-3 band, waveguide features

and tolerances decrease by a factor of around three. Fabricating waveguide filters at such a frequency requires an expensive, high precision CNC mill [3]. Filter design flexibility is also limited by tool sizes and depth to diameter aspect ratios [12]. However, researchers are still pushing the limits of conventional CNC milling: two fourth order CNC milled waveguide filters working on WR-3 band are presented in [13], one with measured 0.7 dB insertion loss and 8.77% (22.6 GHz) bandwidth and another with measured 0.5 dB insertion loss and 9.83% (25.2 GHz) bandwidth. High frequency CNC machined waveguide circuits are reported by Jet Propulsion Laboratory (JPL). The CNC milling process is successfully developed and employed to fabricate several waveguide circuits operating at terahertz frequencies (up to 1.5 THz), with a high dimensional accuracy [14] (typically within 2 μm deviation from designed value). Figure 3.1 shows the two terahertz waveguide circuits reported in [14], fabricated by the JPL using high precision end-mil machining technique. For fabricating complex terahertz waveguide circuits, further improvements are being made with CNC milling process. An example of a purpose-built ultra-high precision CNC micromachining platform as shown in Fig. 3.2 is developed and reported in [15]. This represents the current state-of-the-art CNC machining technique, with typical measured dimensional accuracies of 2-3 μm, surface roughness of 75 nm and tools of sizes available between 25 μm and 10 mm (with aspect ratio greater than 5:1). Several waveguide circuits including highly integrated blocks operating at frequencies ranging from W-band to 2.7 THz were successfully produced via this platform [15].

Although these good examples show that CNC milling method is still capable for the terahertz waveguide circuits fabrication, the drawbacks of this technique is obvious: (i) As frequency increases, the feature size decreases, and the unit cost will increase dramatically due to the requirement of feasible high precision CNC mill. (ii) To fulfil the strength requirements of the

milling cutter, the depth to diameter ratio usually needs to be less than about 3:1, which means some narrow trenches or iris are not possible for CNC milling process to fabricate. (iii) Round internal corners are almost inevitable due to the chosen milling cutter in the fabrication process. (iv) It is not a good choice for large scale production since it is a serial processing method [14] (v) expensive, specialist CNC machine tools are required.

In this work, a CNC milled extracted pole filter operating at WR-3 band (220-325 GHz) with an improved performance is presented in Chapter 4.

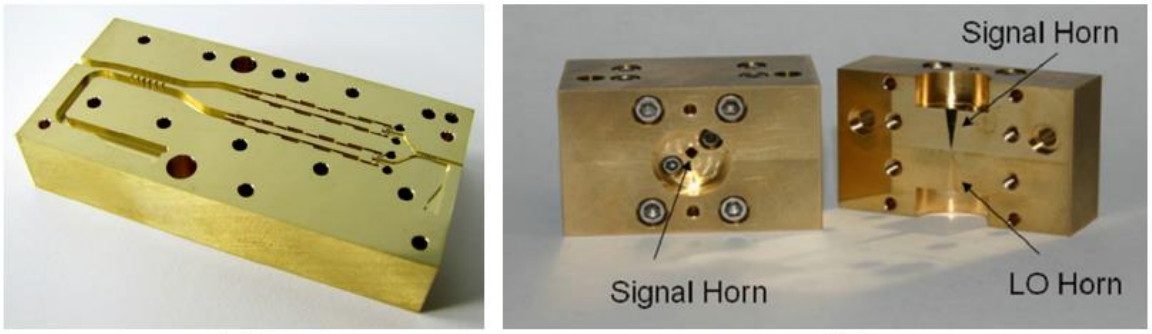

Figure 3.1 State-of-art terahertz waveguide circuits using CNC milling by JPL (a) A quad-chip tripler operating at 260-360 GHz (b) A balanced HEB mixer with integrated feed horns working at 1.5 THz. (Figure reproduced from [14])

Fig. 3.2 The Kern Model 44 (left) and Kern MMP (right) high precision CNC milling platform used at Arizona State University and the University of Arizona [15].

3.1.2 Si deep reactive ion etching (DRIE)

DRIE is a popular micromachining technique. This process can be basically categorized into bulk micromachining.

Bulk micromachining is a method that fabricates structures by selectively etching material from a bulk substrate [16]. Although various different materials can be used as the substrate for bulk micromachining, silicon is being used for that purpose in most cases because of the greater level of experience with this material, achieved through the production of semiconductor devices [15]. Ceramic, plastic or glass materials could be the potential alternate materials to Si [17]. However, according to the state-of-art techniques, silicon provides the best characteristics in terms of cost,

machinability and metallisation.

DRIE of bulk silicon wafers is a fabrication technique that can produce deep structures, typically with high aspect ratios, in a silicon substrate [18]. This is an attractive technique for the fabrication of terahertz waveguide circuits. Examples of waveguide filters using DRIE process working on W-2.2 band, W-1.5 band and W-1 band can be found in literature [19-21]. This lithography-based process is ideally suited for large size batch production, and is capable of offering uniformity between batches [2]. Fig. 3.3 presents the six key steps for the DRIE process and these steps can be summarised as:

(i) Silicon oxide (i.e. SiO_2) is deposited on both side of the substrate wafer as a SiO_2 mask layer and a SiO_2 stop layer;

(ii) Apply photoresist on top of the SiO_2 mask layer;

(iii) After patterning and developing the photoresist layer, the exposed SiO_2 mask layer is etched to form the oxide mask;

(iv) Remove the photoresist layer then etch the silicon substrate to form the desired structures;

(v) Remove the SiO_2 mask layer and SiO_2 stop layer by using buffered oxide etch (BOE) solution;

(vi) Metallise the fabricated silicon layer with Ti layer and Cu layer.

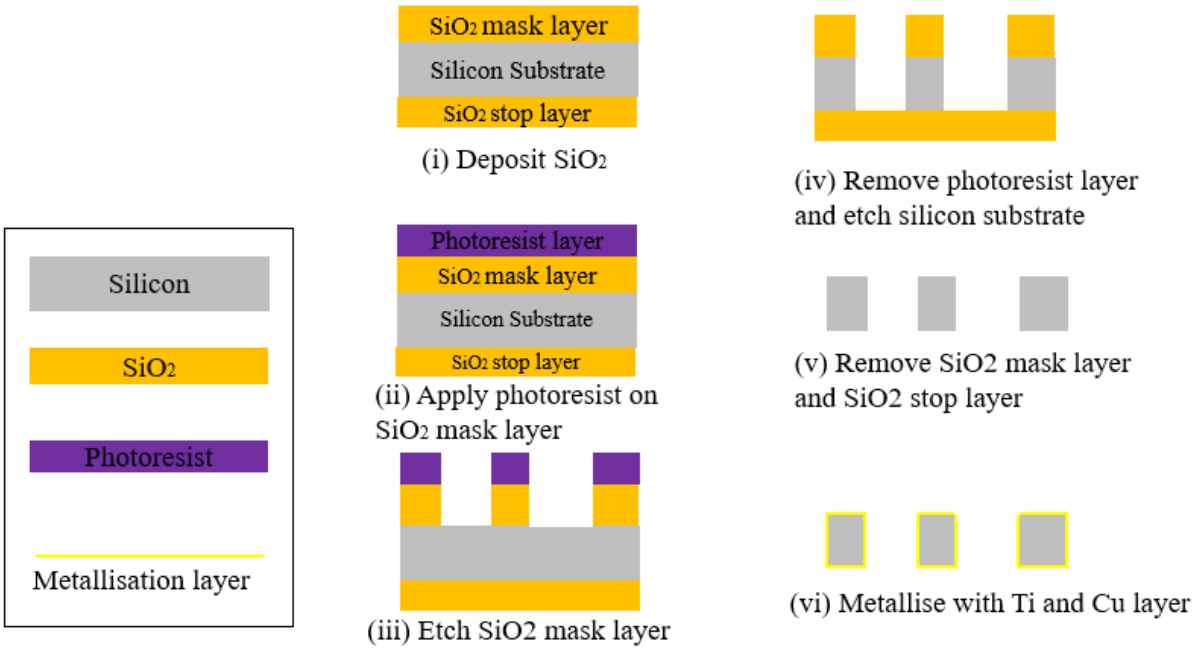

Fig. 3.3 Key steps for DRIE process [22]

Compared with CNC machining, DRIE can be utilised in high frequencies applications and has drawn more attention due to its shorter fabrication time, higher aspect ratios (>30:1) and excellent critical dimension control [22]. However, DRIE process for micromachining suffers from four main problems: (i) hard to achieve vertical (~90°) sidewalls; (ii) difficult to obtain uniform depth across the wafer for each etch depth [23]; (iii) relatively poor surface roughness on the sidewalls [24]; (iv) the height of structure is limited by commercially available silicon wafer thickness [25]. More efforts have been put onto DRIE process in order to address these problems to a certain extent [24]. Typically, the dimension deviations within 2 μm and less than 3° sidewall draft angles have been achieved for a well-established DRIE process [26]. Note that these tolerances vary with wafer thickness. As for draft angles on side walls, reference [22] reports improved

etching angles as low as 0.5°, measured on a WR-1 waveguide filter. This filter also has the best reported surface roughness of 100 *n*m [22]. Normally, for waveguide circuits built using DRIE process, they are formed by two etched silicon pieces and within each piece only features of the same depth are allowed. Recently, a further advancement on the technique is reported in [26], in which presents a multistep DRIE process that can fabricate different depths for arbitrary waveguide features within same silicon piece with ±2% tolerance. This additional flexibility allows more complex waveguide devices to be constructed and enables the possibility of integration of multiple components onto a single silicon package.

3.1.3 LIGA process [28]

LIGA is an acronym of German terms **Li**thographie, **G**alvanoformung and **A**bformung, which correspond to the three English words as Lithography, Electroforming and Moulding that describe the three key steps for this fabrication technique. Fig. 3.4 presents the standard steps that have been utilised in LIGA process. The first thing for the LIGA process is coating the substrate (normally a silicon wafer) with X-ray sensitive resist. Typically, Poly (methyl methacrylate) (PMMA) is chosen as the resist and applied to the substrate by a glue-down process [27]. Then the resist is patterned by exposure to the X-ray through an X-ray mask with high resolution features. During the development process, for structures with high aspect-ratios, the ratio of dissolution rates for the resist-developer system in the exposed and unexposed areas should be 1000:1. The empirically optimised developer which provides the required ratio of dissolution rates can reduce stress-related cracking from swelling compared with conventional PMMA developers [28]. In the next step, the substrate is rinsed with deionized water and the resist (PMMA) microstructures can be released as

the final product (e.g., optical components) or can be used as an electroplating template to produce the metal master mould. This metal mould is with high dimensional accuracy and can be utilised for mass production of desired plastic microstructures with injection moulding, as shown in Fig. 3.4.

The light source of LIGA, the synchrotron generated X-rays, have a deeply penetrating capability. With high energy X-rays, it is able to pattern resist (e.g. PMMA) with thicknesses of millimetre scale and achieve better than 100:1 aspect ratio [27]. In addition, in the lithography process, the using of X-ray gives the advantage that diffraction effects can be reduced due to its short wavelength [27], thus provide high accuracy of sub-micrometre dimensional control. Moreover, X-rays are able penetrate thick resists with less than 0.1 μm horizontal run-out per 100 μm thickness. This provides extremely vertical sidewalls with very small surface roughness (rms (root mean squared) roughness is better than 20 nm) [28].

Compared with typical DRIE process, the LIGA process is able to fabricate nearly perfect geometries in terms of aspect ratio, vertical sidewalls, pattern precisions and achievable thickness. However, the biggest drawback for this micromachining technique is that the cost is very high (e.g. X-ray sources and X-ray masks) for research purpose or small-scale production. For mass production purposes, it is believed that LIGA process is a good choice for fabricating microstructure [10].

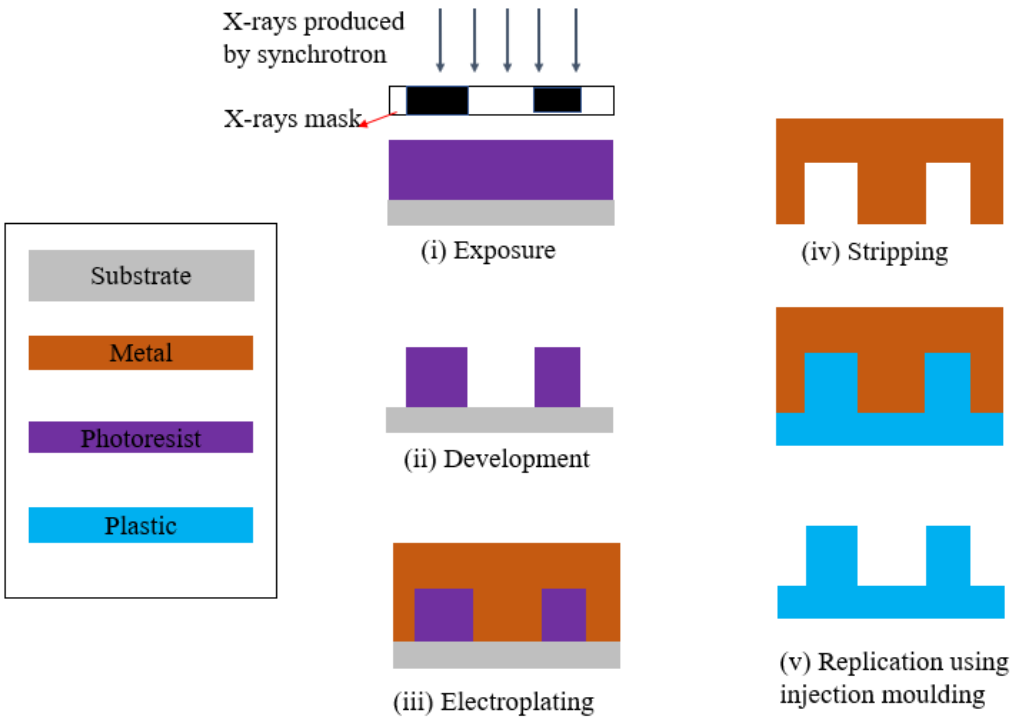

Fig. 3.4 Key steps for the LIGA process [28]

3.1.4 SU-8 photoresist technology for micromachining

SU-8 micromachining is a photolithographically-based process, which is another promising technology for manufacturing millimetre-wave and terahertz waveguide components [3]. SU-8 is capable of constructing three-dimensional (3D) terahertz waveguide structures with high aspect ratios (greater than 50:1), high dimensional accuracy (tolerance within 2 μm), and excellent surface roughness (better than 50 *n*m of rms roughness) [30].

Compared with CNC machining, SU-8 micromachining has several advantages. For example, SU-8 can achieve a similar high dimensional accuracy with potentially lower cost. It may also allow sharper internal corners and higher corner radius to depth ratios [3]. Meanwhile, SU-8

process is a batch fabrication which allows repeatability between devices as well as production of several devices in a single fabrication run [31]. Compared with DRIE, standard photolithography processes are used with SU-8 with better surface roughness on the sidewalls of waveguide structures [31].

The SU-8 process has been widely employed in terahertz circuits, such as W-band filters in [7], WR-3 band waveguide filters in [8], and WR-1.5 in [32].

At the EDT group of the University of Birmingham, the SU-8 process has been developed over the past decade, and successfully applied to a series of passive circuits [7-8, 30, 32]. In Section 3.2, the detailed process of SU-8 micromachining is described and in Chapter 4, a novel WR-3 band waveguide filter, designed to meet a required specification, fabricated using the SU-8 photolithography process, will be given as an example.

3.1.5 Laser micromachining

Laser micromachining is another attractive alternative for the fabrication of microstructures and has the potential of manufacturing terahertz waveguide components [2]. The laser light, which has high power density and low angle divergence, can also be employed in micromachining. The laser micromachining is a fabrication technique that directs the output of a high-power laser through an optic system and then uses the laser beam to remove materials [33]. By directing the focused beam at the material, it is able to melt, burn or vaporize away a part of the material, producing microstructures with high-quality surfaces [33].

Three main types of lasers are utilised in laser micromachining: carbon dioxide (CO_2) lasers,

the neodymium YAG (Nd-YAG) lasers and excimer lasers. The carbon dioxide lasers are typically employed in industry cutting of many materials such as metal, plastic and fabrics. The Nd-YAG lasers are used where very high power is needed and are commonly used for cutting and scribing metals and ceramics [33]. Both CO_2 and Nd-YAG lasers are infrared (IR) lasers, which make use of localized heating by a laser beam spot. IR lasers are suited for three main micromachining applications: drilling and cutting, welding, or heat treatment [34]. The biggest drawback of IR lasers is that, with high power beam directing at the cutting area, the material adjacent to the fabricated surfaces will be affected by the relatively high temperature [33].

An excimer laser is a form of ultraviolet (UV) laser and are commonly used for the fabrication of industrial microstructures with 0.05–1000 μm feature sizes [34]. This kind of laser affects the chemical bond within the material and transfer the material from solid to gas. In order to selectively remove the material and pattern the structures, a mask similar to that utilised in photolithography-based process is applied [34]. Different from typical silicon-etching-based process or photolithography-based process, the cutting depth can be controlled by adjusting the number of pulses. Depth of several hundred microns and vertical or tapered (by tuning the angle of the incident laser beam) sidewalls can be achieved. The excimer laser is usually utilised in the cutting for polymer or silicon materials, or sometimes can be employed in fabricating thin metal layers if the system supports sufficient laser power densities.

Laser micromachining has some very appealing advantages compared with existing processes. Compared to CNC machining, laser micromachining is able to achieve high dimensional and geometrical accuracy for tiny features (as small as 10-20 μm). Since laser micromachining is a non-contact process, which gets rid of the generation of defects and cracks due to mechanical stresses [2]. Compared with DRIE process, LIGA-based electroplating process and SU-8

photoresist techniques, laser micromachining is another great choice since it is capable of producing complex features with multiple depths and it offers relatively high accuracy (<10 um) and repeatability. It can be applied to different materials (including metal) as well. Laser micromachining is reported to be employed for the fabrication of various optical or quasi-optical components, such as terahertz metal mesh filters [35]. However, from the literature, laser cutting is rarely utilised to produce terahertz waveguide components, except for a W-band waveguide filter presented in [9] and a 2-THz horn antenna laser cut from silicon [35].

In general, the main advantages that laser micromachining provides over other micromachining techniques are: (i) It can be applied to different materials including metal. Almost all metal devices are allowed to be fabricated, and this offers an attractive choice to scenarios where a higher thermal stability of the devices is required [2]. (ii) It is capable of producing complex 3-D waveguide structures with varying depths (or heights) from one workpiece and thus eliminates the need for splitting the device into several layers and then assembling them with a high accuracy [7]. (iii) Laser cutting system are highly flexible and can be configured to cut, drill, weld, engrave and deposit materials, which is cost effectively and allowing modification in the design. Therefore, laser micromachining is an excellent choice for the small to medium batch size production of terahertz waveguide devices.

In Chapter 5, a novel hybrid manufacturing approach combining CNC milling with laser micromachining is introduced. Two WR-3 band waveguide filters, which are specifically designed to take advantage of the laser micromachining fabrication process, are presented in Chapter 5.

3.1.6 3-D printing

3-D printing, or additive manufacturing, is another promising technique to produce low terahertz frequency waveguide circuits. One of the potential advantages of using 3-D printing for millimetre-wave and terahertz applications is the potential weight reduction by replacing the conventional metals with metallised polymer materials. The filter can also be specially designed and appropriately fabricated to reduce its mass by removing material at current nulls in the resonator structure [38]. Another advantage is that 3-D printing enables complex geometry designs compared to CNC milling or silicon etching process. For example, filters based on spherical resonators working on X-band shown in [38] which have ultra-high unloaded quality factors can be easily made using 3-D printing and this design can be scaled to operate in low terahertz frequencies. There are basically three additive manufacturing techniques, stereolithography apparatus (SLA), selective laser sintering (SLS) and fused deposited modelling (FDM), which are most commonly used for micromachining. From the latest literature, SLA process offers the highest resolution and the best surface integrity [38]. For the state-of-the-art SLA process presented in [39], the tolerance of dimensional accuracy is within 25 μm and the surface roughness is better than 1 μm. Good results of waveguide filters fabricated using SLA can be found in [39], with the highest reported frequencies operating at W-band [39]. SLS process is suited for the fabrication of all-metal waveguide structures, at the penalty of relatively lower dimensional accuracy and worse surface roughness [2]. Two examples of waveguide filters using SLS process (printed using copper) operating at E-band (60-90 GHz) can be found in [40] with relatively poor performance. According to the research in [40], there are mainly two reasons that attribute to the deviation between simulated and measured response. The first is that the surface roughness of the filter is measured to be 6 μm which can have significant influence to the response. The other reason

is that the fabricated dimensions shrink by around 2-3% compared to the designed values [40]. Further research has been done in [41]. Two fifth order filters operating at W-band, one made from stainless steel and the other made from stainless steel coated with copper, are fabricated and tested. The insertion loss within passband are measured to be 1.9 dB and 1.0 dB for the stainless-steel filter and copper coted filter respectively. The filters presented in [41] are currently the highest frequency waveguide filters fabricated using SLS process with the best performance.

Note that the 3-D printing technique is new and not able to achieve terahertz specifications at the moment. However, the development of this novel micromachining process is fast and the dimensional accuracy for this technique is expected to improve significantly over time. This is a promising technique with the potential for terahertz circuit to be fabricated using 3-D printing technique soon.

3.2 Fabrication Process for SU-8 Photoresist Technology

SU-8 photoresist technology for micromachining have been employed for fabricating a range of waveguide circuits. The SU-8 resist is sensitive to ultraviolet (UV) light, which means that employing the relatively cheaper UV-lithography process is possible. Since SU-8 is a photosensitive material, standard photolithography process can be utilised to define prescribed micro-patterns accurately by selective exposure to UV radiation through a mask [42]. These outstanding characteristics of SU-8 make it an attractive choice as the material for micromachining.

There are two different process to fabricating waveguide filters. One is SU-8 single layer lithography which mainly employed for fabricating microstructures with relatively simple

geometries. The other is SU-8 two-layer lithography processes which is developed for more complex waveguide devices [2]. The key steps of the typical SU-8 process include [43]: (i) spin coating, (ii) soft bake, (iii) exposure, (iv) post-exposure baking, (v) development, (vi) hard baking, (vii) substrate removal, and (viii) metallization. Figure 3.5 illustrates these basic steps for SU-8 single-layer and two-layer processing. The general fabrication process utilised in the waveguide circuit presented in this thesis is described with a schematic in the following part.

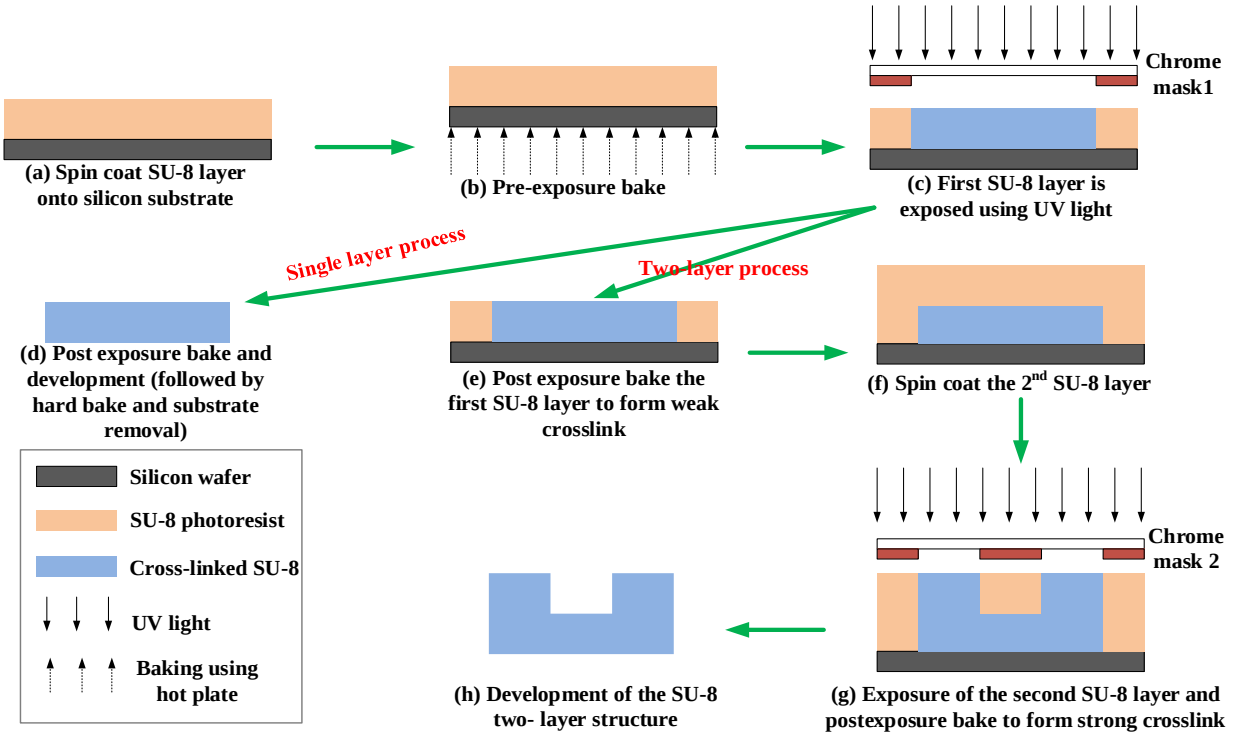

Fig. 3.5 Basic steps for SU-8 single-layer and two-layer processes. (Figure reproduced from [2])

3.2.1 Spin coating

The SU-8 photoresist is commonly stored as liquid form. In the first step, the liquid SU-8 is well spread on a flat silicon substrate with a desired thickness via spin coating process [43]. As

shown in Figure 3.4 (a), a measured amount of the SU-8 photoresist is added to the top of a cleaned silicon wafer (using H_2SO_4 and H_2O_2, then rinsing with de-ionized water and drying in air) which is fixed on a spinner. After the wafer spun around with appropriate speed, the SU-8 photoresist will be distributed uniformly over the surface of silicon wafer due to the effect of centrifugal forces. The spin speed is typically depended on the resist type and required resist thickness [15]. Normally to fabricate devices with thinner layer thickness required higher spin speed. For the SU-8 micromachined waveguide filter operating on WR-3 band presented in this work, the designed layer thickness is 432 μm. Precision weight control for the SU-8 photoresist has been employed in order to accurately control the layer thickness.

3.2.2 Soft bake

The soft bake process, or can be called as pre-exposure bake, is aimed at drying out the solvents from the SU-8 resist. This process is typically carried on with an infrared oven, a microwave oven or a level hot plate [43]. Among these choices, the level hot plate offers the best thermal control. In this work, as shown in Figure 3.4 (b), the soft bake is performed on a hot plate, which is precision levelled to ensure the uniform thickness for each SU-8 layer [43]. The resist is first baked at 65° C for 20 minutes, and then baked at 95° C for usually 4-6 hours (depending on the required thickness). The first 65°C baking step is to assist self-planarization of the SU-8 photoresist and produces better thickness uniformity for each fabricated SU-8 layer [42], while the main purpose of the second step of soft baking at 95°C is driving off the solvent.

3.2.3 Exposure

As shown in Figure 3.4 (c), after pre-bake, the SU-8 photoresist is exposed under UV light through a designed mask to define patterns of the waveguide structures. The mask is usually made by a piece of transparent glass covered by patterned chromium [43]. The parts on the glass that covered by chromium correspond to the filter features that are selectively removed. By projecting UV light onto the mask, the pattern is transformed from mask to the photoresist, since glass is transparent to UV light, whereas the parts covered by chromium are non-transparent.

Usually an UV lamp with proper incident energy (J/cm^2) is used to produce the incident light on the photoresist through the mask. The choice of incident energy is mainly decided by the required photoresist thickness. According to the reaction when exposed to light, the photoresists can be basically grouped into two categories: positive resists and negative resists. For positive/negative resists, the chemical bonds are weakened/strengthened while exposing to light and the exposed parts become more soluble/insoluble [16]. In this case, positive resists will obtain same patterns with the mask after the development process, while negative resists will gain opposite patterns with the mask. For this work, SU-8 is a typical negative photoresist. After exposure under UV light, the SU-8 resist will produce a photoacid which can perform as a catalyst in the cross-linking reactions during the post exposure bake process [15].

3.2.4 Post exposure bake

Since SU-8 is a negative resist, the post exposure bake is a necessary step for producing the cross-linking reactions [33]. Figure 3.4 (d) and (e) present the post exposure bake process for

single-layer and two-layer SU-8 process. By post exposure bake at 60-100°C, the rates of cross-linking reactions increase and the exposed areas will become insoluble in the developer. To ensure the quality of the final products and avoid the cracking of the SU-8 samples, the bake time should be precisely controlled. Longer post-bake time can increase the stress within the resist and cause bending of the final structures while shorter bake time may result in some exposed areas not fully cross-linked (i.e. soluble to solvents in the development step). Generally, the post exposure bake process is firstly carried out on a conventional oven or a hot plate at 65° C for 2 minutes, and then ramped up to 95° C for 30 minutes. After switching off the heater, the wafer is left on the oven or the hot plate to gradually cool down to room temperature [42].

3.2.5 Development

The development process, as shown in Figure 3.4 (d) for single layer-process and (h) for two-layer process, is usually employed after post exposure bake to remove the unwanted SU-8 resist (non-cross-linked area). This process is performed by immersing the exposed and baked resist together with the silicon wafer into the developer solution at room temperature for about 30 mins. The immersing time can be different according to the designed thickness and required aspect ratio of the SU-8 layer [44]. In order to increase the development rate, a strong agitation, which can enhance diffusion of developer molecules with the non-cross-linked SU-8 resist, is usually required during the process [44]. Then the developed sample is rinsed using Isopropyl Alcohol (IPA) and drying with a nitrogen gun. After completing this step, filter structures are formed corresponding to the negative image of the designed mask.

3.2.6 Hard bake and substrate removal

After the development process, a hard bake process is recommended to enhance the cross-linking bonds, which makes sure that the final structures of SU-8 resist is strong and can endure common acids and alkalis, and also resilient to following process such as metal evaporation which puts the SU-8 layers into environment with higher than 100° C temperature. The hard bake is usually carried out on a hot plate at 150° C for 30 minutes. Without hard bake process, the SU-8 structures are susceptible to bending during metallisation process [45].

Due to strong bond associated with the cross-linking, it is usually difficult to separate the patterned SU-8 layer from the silicon substrate. There are two ways to remove the substrate. The first one is to put a layer of soluble resist below the SU-8 during the spin coating process and then the patterned SU-8 layer is released by dissolving the sacrificial layer in tetramethylammonium-hydroxide-based solution at room temperature for about 5 hours [44]. The second method is by immersing the SU-8 layer together with the substrate in a 10% sodium hydroxide solution (i.e. NaOH) [42]. This method requires immersing with temperature of 60° C for more than 7 hours to fully etch the silicon away.

3.2.7 Metallisation

Sputtering and evaporation are commonly utilised for the metallisation process with the SU-8 layers [16]. To enhance the chemical bond between the SU-8 layers with the typical coating metal such as silver or goad, a thin adhesive layer (i.e. 5 nm of Chromium (Cr) or Titanium (Ti) layer) is firstly sputtered onto the surface of the SU-8 layers. The samples are then put in an evaporation

metal coater, in which silver or gold is vaporised by heating and then transported in vacuum to condense on the surface of the SU-8 layers to be coated [42]. During sputtering and evaporation process, the SU-8 layer is fixed on a tuneable sample holder which can rotate continuously in different angles to ensure good coverage of coating on all the surfaces of the SU-8 pieces, including the sidewalls [42].

3.2.8 Fabrication process for SU-8 two-layer processing

The SU-8 two-layer process is an optimised method developed for complex structures based on the general SU-8 single-layer process. The difference between two method happens after the resist exposed to UV light (i.e. after step shown in Fig. 3.5 (c)). For the general single layer process, the structure is baked after exposure to form cross-link, developed in solution and then hard baked, finally released from silicon wafer, as shown in Fig. 3.5 (d). However, for the SU-8 two-layer process, the post exposure bake process would be carried out under relatively low temperature for the first SU-8 layer to form weak crosslink. Then the SU-8 resist for the second layer is spin coated on top of the first SU-8 layer, as shown in step (e) and (f). As presented in Fig. 3.5 (g)-(h), same process utilised in single-layer process such as an exposure of UV light, post-exposure bake and development are repeated for the second layer. The final product is a fully cross-linked and joined two layered SU-8 structure, without internal joints [2].

Compared with the single layer process, in which the isolated islands structures (i.e. features that can't stand along without support) are not permitted, the two-layer process address the problem of this restriction and allows standalone regions on the top layer [2]. This enables the realisation of some complex waveguide filter designs. One example can be found in [46], in which

a WR-3 band cross-coupled dual-band filter is fabricated and measured. In addition, the two-layer process is an efficient solution since it can eliminate the inner joints between layers and avoid localized air gaps [2]. This is a significant improvement for waveguide devices based on SU-8 photoresist technology since this would reduce the energy loss through the gaps.

3.3 Conclusions

This chapter has given an overview of micromachining techniques for terahertz waveguide circuits as well as general process of some recently developed micromachining techniques such as DRIE process, LIGA process, SU-8 photoresist technology, laser micromachining and 3-D printing. Table-3.1 shows the comparison of the maximum aspect ratio, dimensional accuracy and achievable surface roughness for different micromachining techniques. This table presents the state-of-art reported in literature for different micromachining techniques. Regardless of the cost, devices and technicians that are required to accomplish the waveguide circuits, this comparison only takes the best performances achieved by the researchers into account. Another table that summaries the recent published waveguide filters (including the filters described in this thesis) operating in frequency from the WR-10 to WR-1.5 band will be given in Chapter 4.

As introduced in this chapter, DRIE is relatively a mature technique utilised in micromachining. Many researchers have already looked into this process to dig its potential in the fabrication of terahertz circuits. However, to achieve high dimensional accuracy and low draft angles on sidewalls, an extremely well-established DRIE process are required [22][26], which means that experienced technicians and expensive machines with high accuracy are indispensable for the research. Seen from the comparison in Table-3.1, LIGA process is the technique with best

achievable performances. However, the great cost and limited resources for this technique (e.g. X-ray sources and X-ray masks) makes LIGA process not a good choice for research purpose or small-scale production. Compared from reported micromachined circuits, 3D printing didn't provide any obvious advantages in performances, but 3D printing is definitely a promising micromachining technique applied in terahertz circuits once the fabrication process for this technique have been fully developed. Researchers in EDT group in University of Birmingham have already successfully designed, fabricated and measured several waveguide circuits operating at around 100 GHz with reasonable performances.

The choice of the micromachining techniques utilised in this work is mainly based on three factors: (i) the potential of the technique utilised in machining terahertz circuits; (ii) the resources that are available during the research process; (iii) the cost for research purpose. Balancing between these factors, SU-8 photoresist technology is a promising micromachining process and our EDT group in University of Birmingham has sufficient technical devices and experience for fabricating SU-8 waveguide circuits operating at 100-300 GHz. From Table-3.1, laser micromachining is not an attractive micromachining process since it is not able to achieve demanding specifications of terahertz circuits at the moment. However, with the advantages of repeatable at the micro-scale relatively high accuracy and able to fabricate a wide range of materials with complex features, laser micromachining is a novel and promising technique for fabricating terahertz waveguide circuits. More importantly, the School of Mechanical Engineering in University of Birmingham provides us with resources such as instruments with high accuracy and experienced technicians to investigate the application of laser micromachining in terahertz circuits. From above reasons, SU-8 photoresist technology and laser micromachining have been chosen and applied in the fabrication of terahertz filters in this work.

As SU-8 photoresist process is employed to fabricate some of the micromachined waveguide circuits presented in this thesis, the detailed steps of the SU-8 fabrication process are also presented in this chapter. The examples of the fabricated filter using SU-8 photoresist technology will be presented in the following Chapter. The novel multi-stage process for laser micromachining will be introduced and explained together with the designing of laser micromachined filters in Chapter 5.

Table-3.1 Comparison of best performance of different micromachining techniques

Techniques	Achievable aspect ratio	Dimensional accuracy (μm)	Surface roughness	Reference
CNC machining	>5:1	<2	75 nm	[14]
DRIE process	>30:1	<2	100 nm	[22]
LIGA process	>100:1	<1	10 nm	[28]
SU-8 process	>20:1	<2	40 nm	[32]
Laser machining	>3:1	<10	1.25 μm	[9]
3D printing (SLA)	>100:1	<25	1 μm	[39]
3D printing (SLS)	>15:1	<50	2 μm	[41]

References:

[1] N. J. Cronin: “Microwave and Optical Waveguides,” (Iop Publishing Ltd, 1995)

[2] X. Shang, H. Yang, D. Glynn, M. J. Lancaster. “Submillimeter-wave waveguide filters fabricated by SU-8 process and laser micromachining” *IET Microw., Antennas Propag.*, vol. 11, no. 14, pp. 2027-2034, Nov. 2017.

[3] H. Yang, Y. Dhayalan, X. Shang, M. J. Lancaster, *et al.*, “WR-3 waveguide filter based on high precision CNC milling and SU-8 photoresist technology,” *IEEE Trans. THz Sci. Technol.*, vol. 8, no. 1, pp. 100-107, Jan. 2018.

[4] J. Y. Li, B. Pan, C. Lugo, M. Tentzeris, and J. Papapolymerou, “Design and characterization of aW-band micromachined cavity filter including a novel integrated transition from CPW feeding lines,” *IEEE Trans. Microw. Theory Tech.*, vol. 55, no. 12, pp. 2902–2910, Dec. 2007.

[5] K. M., K. H. Leong *et al.*, “WR1.5 Silicon Micromachined Waveguide Components and Active Circuit Integration Methodology,” *IEEE Trans. Microw. Theory Tech.*, vol. 60, no. 4, pp. 998-1005, Apr. 2012.

[6] J. R. Stanec and N. S. Barker, “Fabrication and integration of micromachined submillimeter-wave circuits,” *IEEE Microw. Wireless Compon. Lett.*, vol. 21, no. 8, pp. 409–411, Aug. 2011.

[7] X. Shang, M. Ke, Y. Wang and M. J. Lancaster, “Micromachined W-band waveguide and filter with two embedded H-plane bends,” *IET Microw., Antennas Propag.*, vol. 5, no. 3, pp. 334-339, Feb. 2011.

[8] Q. Chen, X. Shang, Y. Tian, J. Xu and M. J. Lancaster, “SU-8 micromachined

WR-3 band waveguide bandpass filter with low insertion loss," *Electron Lett.*, vol. 49, no. 7, pp. 480-482, March. 2013.

[9] X. Shang et al., "W-Band Waveguide Filters Fabricated by Laser Micromachining and 3-D Printing," *IEEE Trans. Microw. Theory Tech.*, vol. 64, no. 8, pp. 2572-2580, Aug. 2016.

[10] C. Guo, J. Li, D. D. Dinh, X. Shang, M. J. Lancaster and J. Xu, "Ceramic filled resin-based 3D printed X-band dual-mode bandpass filter with enhanced thermal handling capability," *Electronics Letters*, vol. 52, no. 23, pp. 1929-1931, 11 10 2016.

[11] X. Liao, L. Wan, Y. Yin and Y. Zhang, "W-band low-loss bandpass filter using rectangular resonant cavities," *IET Microw., Antennas Propag.*, vol. 8, no. 15, pp. 1440-1444, Sep. 2014.

[12] C. A. Leal-Sevillano, J. R. Montejo-Garai, J. A. Ruiz-Cruz and J. M. Rebollar, "Low-Loss Elliptical Response Filter at 100 GHz," *IEEE Microw. Wireless Compon. Lett.*, vol. 22, no. 9, pp. 459-461, Sep. 2012.

[13] J. Q. Ding, S. C. Shi, K. Zhou, Y. Zhao, D. Liu and W. Wu, "WR-3 Band Quasi-Elliptical Waveguide Filters Using Higher Order Mode Resonances," *IEEE Trans. THz Sci. Technol.*, vol. 7, no. 3, pp. 302-309, May. 2017.

[14] P. J. Bruneau, H. D. Janzen, J. S. Ward, "Machining of Terahertz Split-Block Waveguides with Micrometer Precision," *33rd International conference on IRMMW-Terahertz*, 2008.

[15] C. E. Groppi, B. Love, M. Underhill, *et al.*: "Automated CNC micromachining for integrated THz waveguide circuits," *Proc. 21th Int. Symp. Space THz Technolo*, Oxford, 23-25 March 2010

[16] H. T. Ran, “MEMS and Microsystems: Design, Manufacture, and Nanoscale Engineering” (2nd edition, Wiley)

[17] Bulk micromachining from University of Maryland [online], available at http://terpconnect.umd.edu/~sandborn/research/JPL_MEMS/microeng_bulk.html

[18] J. L. Yeh, A. H. Jiang, and N. C. Tien. “Integrated polysilicon and DRIE bulk silicon micromachining for an electrostatic torsional actuator.” *Journal of Microelectromechanical Systems*, 1999, pp.456-465.

[19] S. Biber, J. Schur, L.P. Schmidt, “Technological Issues for Micromachining of New Passive THz Components Based on Deep Trench Silicon Etching,” *Infrared and Millimeter Waves, 12th International Conference on Terahertz Electronics*, 2004, pp. 145 – 146.

[20] J. P. Becker, J. R. East, and L. P. B. Katehi, “Performance of silicon micromachined waveguide at W-band,” *Electron. Lett*., vol. 38, no. 13, pp. 638–639, Jun. 2002.

[21] W. R. McGrath, C. Walker, M. Yap, and Y. Tai, “Silicon micromachined waveguides for millimeter-wave and submillimeter-wave frequencies,” *IEEE Microw. Guided Wave Lett.*, vol. 3, no. 3, pp. 61–63, Mar. 1993.

[22] T. Reck, C. Jung-Kubiak, C. Leal-Sevillano, *et al*.: “Silicon micromachined waveguide components at 0.75 to 1.1 THz”. *39th Int. Conf. Infrared, Millimetre, and Terahertz waves (IRMMW-THz)*, Tucson, AZ, 2014, pp. 1-2.

[23] N. Kouma, O. Tsuboi, Y. Mizuno, H. Okuda, X. Mi, M. Iwaki, H. Soneda, S. Ueda, and I. Sawaki, “A multi-step DRIE process for a 128×128 micromirror array,” *IEEE Opt. MEMS LEOS Int. Conf*., 2003, pp. 53–54.

[24] T. J. Reck, C. Jung-Kubiak, J. Gill, *et al*: "Measurement of silicon micromachined waveguide components at 500-750 GHz", *IEEE Trans. Terahertz. Science and Technology*, 2014, 4, (1), pp. 33-38

[25] H. Tai-Ran, "MEMS and Microsystems: Design, Manufacture, and Nanoscale Engineering" (2nd edition, Wiley)

[26] C. Jung-Kubiak, T. J. Reck, J. V. Siles, *et al.*, "A multistep DRIE process for complex terahertz waveguide components", *IEEE Trans. Microw. Theory Tech.*, 2016, 6, (5), pp. 690-695

[27] M. A. Forman, "Low-loss LIGA-fabricated coplanar waveguide and filter," 2006 *Asia-Pacific Microwave Conference*, Yokohama, 2006, pp. 1905-1907.

[28] C. K. Malek, V. Saile, "Applications of LIGA technology to precision manufacturing of high aspect-ratio micro-components and systems: a review," *Microelectronics Journal*, 2004, 35, pp. 131 -143.

[29] E. H. Conradie, D. F. Moore, "SU-8 Thick Photoresist Processing as A Functional Material for MEMS Applications," *Journal of Microw. and Microenginnering*, 2002, 12, pp. 368-374

[30] Y. Tian, X. Shang, Y. Wang, *et al.*, "Investigation of SU8 as a structural material for fabricating passive millimeter-wave and terahertz components", J. Micro/Nanolith. MEMS MOEMS, 2015, 14, (4), p. 044507

[31] C. H. Smith, A. Sklavonuos and N. S. Barker, "SU-8 micromachining of millimeter and submillimeter waveguide circuits," *2009 IEEE MTT-S International Microwave Symposium Digest*, Boston, MA, 2009, pp. 961-964.

[32] X. Shang, Y. Tian, M. J. Lancaster, S. Singh, "A SU8 micromachined WR-1.5 band

waveguide filter," *IEEE Microw. Wireless Compon. Lett*., vol. 23, (6), pp. 300-302, Jun. 2013.

[33] D. Banks, Microengineering, MEMS, and Interfacing, a practical guide (2006, CRC Press)

[34] Gower, Malcolm. Excimer laser microfabrication and micromachining. *Proceedings of SPIE - The International Society for Optical Engineering*. 4088.

[35] B. Voisiat, A. Bičiūnas, I. Kašalynas, *et al.*: "Band-pass filters for THz spectral range fabricated by laser ablation", *Appl. Phys. A*, 2011, 104, (3), pp. 953-958

[36] C. K. Walker, H. Knoepfle, J. Capara, et al.: "Laser micromachining of silicon: a new technique for fabricating high quality terahertz waveguide components", *Proc. 8th Int. Symp. Space THz Technolo.*, Cambridge, MA, USA, Mar 1997, pp. 358-376

[37] C. Guo, X. Shang, M. J. Lancaster, et al: "A 3-D printed lightweight X-band waveguide filter based on spherical resonator", *IEEE Microw. Wireless Compon. Lett*., 2015, 25, (7), pp.442-444

[38] M. D. Auria, W. J. Otter, J. Hazell, *et al.*: "3-D printed metal-pipe rectangular waveguides", *IEEE Trans. Compon. Packag. Manuf. Techn*., 2015, 5, (9), pp.1339-1349

[39] "Swissto12, Lausanne, Switzerland", http://www.swissto12.com, accessed 7 October 2016

[40] B. Zhang, H. Zirath: "3D printed iris bandpass filters for millimetre-wave applications", *Electronics Letters*., 2015, 51, (22), pp. 1791-1793

[41] M. Salek *et al*., "W-Band Waveguide Bandpass Filters Fabricated by Micro Laser Sintering," *IEEE Transactions on Circuits and Systems II: Express Briefs*, vol. 66, no. 1, pp. 61-65, Jan. 2019.

[42] M. Ke, Y. Wang, and M. J. Lancaster, “Design and realisation of low loss air-filled rectangular coaxial cable with bent quarter-wavelength supporting stubs,” *Microw. Opt. Technol. Lett*., vol. 50, pp. 1443–1446, May 2008.

[43] H. J. Levinson, Principles of Lithography (second edition, 2005, SPIE the International Society for Optical Engineering)

[44] A. Del Campo and C. Greiner, “SU-8: a photoresist for high-aspect ratio and 3D submicron lithography,” *J. Micromech. Microeng*., vol.17, no.6, pp. 81–95, 2007.

[45] S. Roberstson, L. Katehi and G. Rebeiz: “Micromachined W-band Filters,” *IEEE Trans. Microw. Theory Tech.,* 1996, 44, (4), pp. 598-606.

[46] X. Shang, M. Ke, Y. Wang, et al.: “WR-3 band waveguide and filters fabricated using SU8 photoresist micromachining technology”, *IEEE Trans. Terahertz. Science and Technology*., 2012, 2, (6), pp. 629-637

Chapter 4

Micromachined Waveguide Circuits Using High Precision CNC Machining and SU-8 Photoresist Technology

This chapter presents two waveguide filters operating on WR-3 band (220-325 GHz). One is fabricated in copper alloy (plated with gold for the waveguide structures) using high precision computer numerically controlled (CNC) milling and the other is produced using SU-8 photoresist technology and then coated with silver. This work is in a cooperation project with Rutherford Appleton Laboratory. These two devices have been published in an IEEE Transactions on Terahertz Science and Technology paper [1].

Both filters are based on coupled resonators with same Chebyshev response. The first filter is a CNC milled extracted pole filter utilising split-block approach. The second filter is a cross coupled third order filter made with metallised SU-8 photoresist technology. These two filters are designed as an efficient alternative to frequency selective surface (FSS) filters used in heterodyne radiometers for unwanted sideband rejection [1]. Section 4.1 provides the introduction for the design motivation and filter design specifications. Section 4.2 describes the analysis for the design of the waveguide circuits based on coupling matrix synthesis [2]. The design, fabrication process, assembling and measurement process for CNC milled extracted pole filter and SU-8 micromachining filter are given in Section 4.3 and Section 4.4, respectively. In the final part of this chapter, Section 4.5 presents the comparison between these two filters and recently published terahertz micromachined waveguide circuits.

4.1 Background

Multichannel air and spaceborne sounders have been wildly used in analysing spectroscopic characterization of the Earth's atmosphere [3]. Molecular spectroscopy is performed by these instruments at millimetre wavelengths in relatively narrow frequency channels. Within the instrument, linearly polarized signals are frequency de-multiplexed by a quasi-optical feed chain. Frequency selective surfaces (FSSs) are used to demultiplex linearly polarized signals and to prevent the signals in the unwanted sideband from reaching the double sideband heterodyne mixers [4]. As the atmospheric signals are weak, the sideband rejecting FSS needs to have a very low insertion loss and a high isolation between two adjacent channels which are close to each other in frequency [5]. From the real application reported in [5], the FSS used in the system has the specification:

- Passband: 316.5-325.5 GHz, FBW=2.8% (maximum insertion loss < 0.6 dB)
- Unwanted sideband: 349.5-358.5 GHz (rejection better than 30 dB)

The Quasi-optical FSS transmission measurement test bench used in [5] is reproduced in Fig. 4.1. The filter device was constructed of two FSS screens with a diameter of 50 mm separated by a distance 475 μm. To utilise the FSS filter in the measurement system, two FSS layers were mounted in a 10 mm thick 100 mm × 100 mm invar holders [5].

Waveguide technology, as introduced in Chapter 3, can be a potential alternative to FSS to achieve loss insertion loss within passband and sideband rejection. For rectangular waveguide filters working on WR-3 band (220 – 330 GHz), the dimensions of the cross-section (width a and height b) are only 864 μm by 432 μm and the total length are usually within several millimetres. Compared to FSS, waveguide technology is giving the advantage of considerable reduction in size

and mass of components.

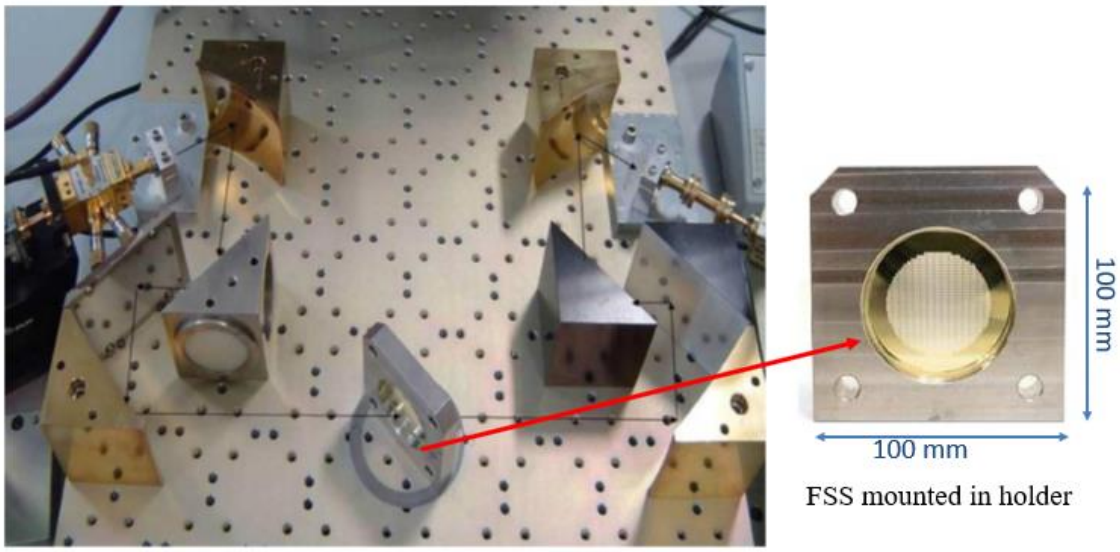

Fig. 4.1 Quasi-optical FSS transmission measurement test bench and photograph of the two-layer dual polar FSS mounted in an invar holder. (Figure reproduced from [5])

In this work, in order to meet available measurement capability (WR-3 band: 220-330 GHz), the specification in [5] and above was scaled by a factor of 1.1 giving:

- Passband: 287.7-295.9 GHz, FBW=2.8% (maximum insertion loss < 0.6 dB)
- Unwanted sideband: 317.7-325.9 GHz (rejection better than 30 dB)

In this work, CNC milling and SU-8 photoresist technology are employed in the fabrication of terahertz waveguide filters. In order to minimize the influence of the fabrication error, the filter structures are specially designed to take advantage of the fabrication processes. The design processes are discussed in the following sections.

4.2 Design of the Waveguide Filters

To design the waveguide circuit which meets the specification, the first thing we need to figure out is how many resonators are needed. Using the general theory for resonator filters introduced in Chapter 2, Fig. 4.2 shows the S_{21} responses for a set of Chebyshev filters plotted using coupling matrix. *n* stands for the order of the filter (i.e. number of resonators). All filters have the same centre frequency (291.8 GHz), BW (8.2 GHz) and passband return loss (20 dB). The passband and unwanted sideband specification are shown in grey and red section in Fig. 4.2. Ideally S_{21} should be smaller than 30 dB at frequencies above the reference line. Seen from the figure, the 3rd, 4th and 5th order filters are all fine in terms of providing sufficient attenuation at unwanted sideband.

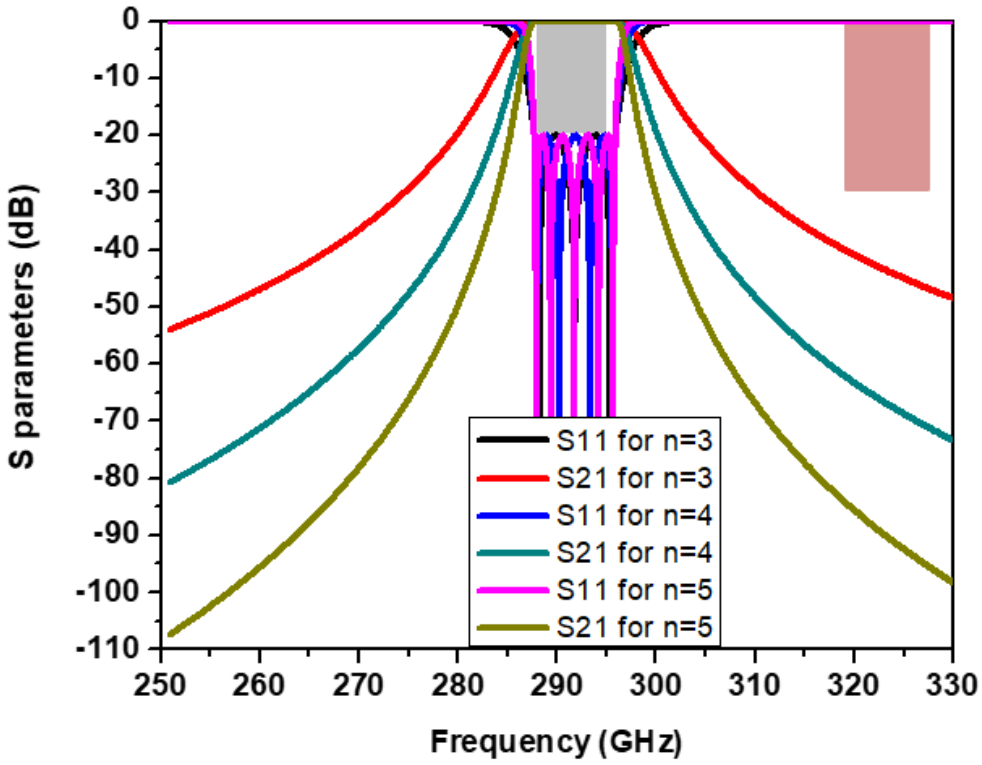

Fig. 4.2 The calculated responses based on same *g* values for 3rd, 4th and 5th order filter plotted using coupling matrix. Passband and stopband specifications are shown in grey and red section respectively.

However, the practical waveguide filters usually suffer from poor upper stopband response due to the influence of higher order modes and the resonances at higher harmonic frequencies, which occur at frequencies of 1.6 to 1.7 times the centre frequency [7]. Fig. 4.3 shows the model of the physical realization of a third order filter centred at 291.8 GHz with 8.2 GHz bandwidth. The simulation results of the filter are shown in Fig. 4.4. Compared with the calculated results using coupling matrix synthesis, the rejection for upper stopband (317.7 – 325.9 GHz) is increased by around 15 dB due to the appearance of the higher order mode (i.e. TE_{201} mode in this example).

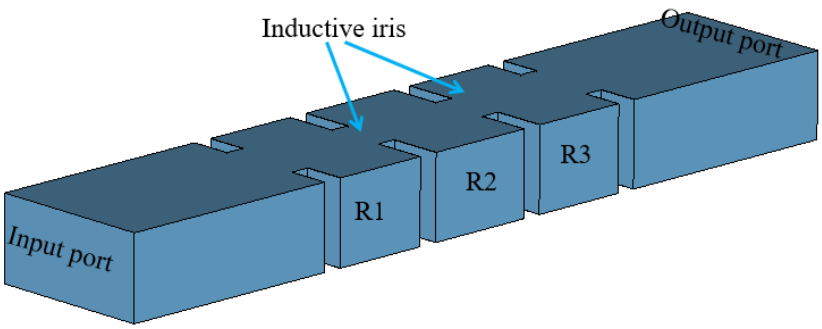

Fig. 4.3 The design of a third order filer centred at 291.8 GHz with 8.2 GHz bandwidth using inductive iris

In the next step, the passband insertion loss is calculated and compared with the specification. The passband insertion loss of a Chebyshev passband filter designed from its low-pass prototype can be calculated using the equation [2]:

$$\Delta L_A = 4.343 \sum_{i=1}^{n} \frac{\Omega_c}{FBW \bullet Q_{ui}} g_i \quad dB \qquad (4.1)$$

where ΔL_A is the insertion loss at the centre frequency of the filter, *FBW* is the fractional bandwidth

of the filter, Ω_c (typically 1 rad/s) is the cut-off frequency of the low-pass prototype, g_i are the low-pass element values and Q_{ui} is the unload quality factor for the i th resonator. All coupled resonators are operating at the TE_{101} mode. The calculations assume the filter has the following specifications: centre frequency 291.8 GHz, bandwidth 8.2 GHz and passband return loss 20 dB. By employing the conductivity for silver block which is 6.17×10^7 S/m in equation (2.12), Q_{ui} of each resonator can be calculated to be 1525. Substitute these data in equation (4.1), the calculated passband insertion loss for 3rd, 4th and 5th order waveguide filters made of pure silver are presented in the black line in Fig. 4.5.

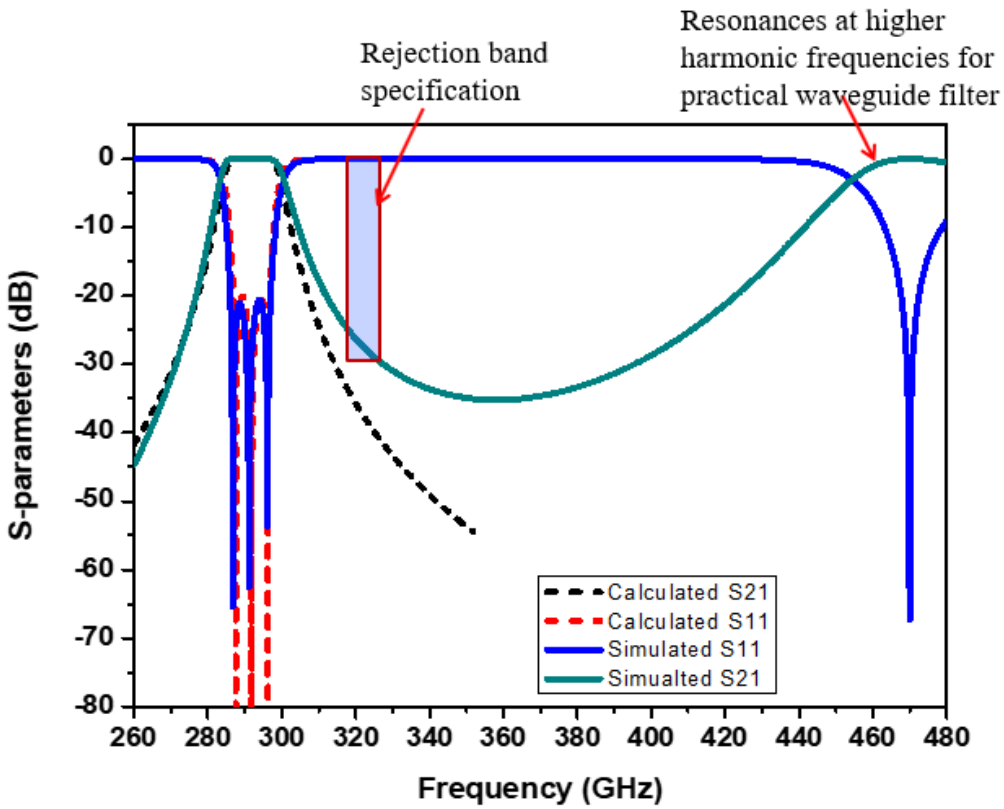

Fig. 4.4 Comparison for calculated results of third order Chebyshev filter using coupling matrix synthesis and simulated results for practical third order waveguide filter

In practice the effective conductivity of thin-film-silver has been found to be around 45.5% (i.e. 2.81×10^7 S/m) of the pure silver block [6]. The red line in Fig. 4.5 may be more realistic as its Q_{ui} is calculated to be 1029 using a conductivity 45.5% of that of silver block. From previous experiments in [6], this effective conductivity has a good agreement with measured results. Therefore, in Fig. 4.5 the passband insertion loss for 45.5% of the bulk conductivities of bulk silver (practical model) and bulk silver (ideal model) have been considered and calculated. The blue dash line in Fig. 4.5 shows the acceptable insertion loss.

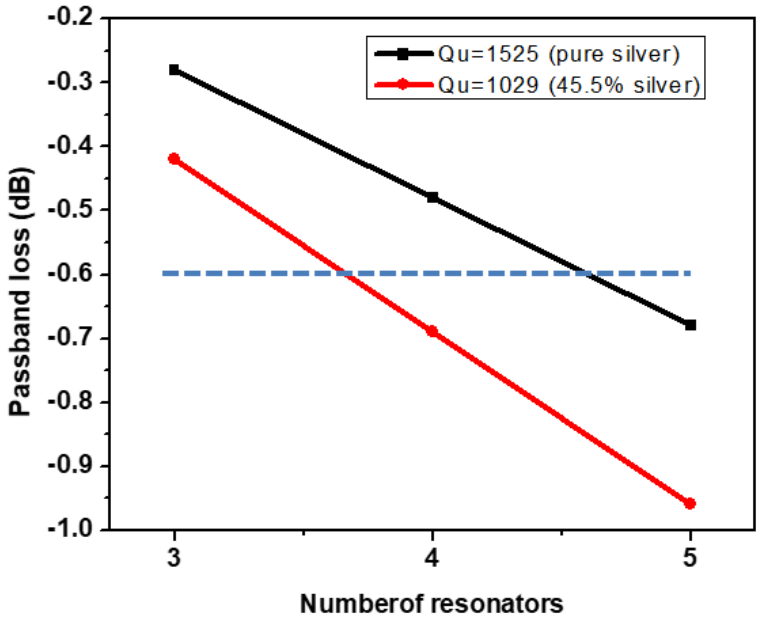

Fig. 4.5 Calculated passband insertion loss vs. number of resonators (based on same *g* values)

As shown in Fig. 4.5, the calculation of insertion loss for practical situation (red line) gives the conclusion that, in order to fulfil the passband insertion loss specification, the filter should have no more than four resonators.

The design difficulty is to achieve low insertion loss within passband and high rejection of the

close higher stop band. Based on the above analysis, to achieve the specification, both filters are designed to have only three resonators. Meanwhile, transmission zeros are introduced between the passband and unwanted upper sideband to prevent poor rejection caused by higher mode for practical waveguide filter.

As described in Section 4.3, the CNC filter obtains the transmission zero using a conventional extracted pole design, and in Section 4.4, the SU8 filter has a completely new design topology to produce the transmission zero. These are the first waveguide filters to achieve this at these high frequencies.

4.3 CNC Milled Extracted Pole filter

4.3.1 Design process of extracted pole filter

The 3D model of the CNC filter is shown in Fig. 4.6. It is composed of three coupled resonators operating at TE_{101} mode and an extracted pole resonator [8]. It has been shown in the literature that the selectivity of conventional E-plane filter can be improved by using inductively coupled cavities mounted on the top of waveguide housing [9]. The extracted pole resonator utilised in this work is designed to achieve a transmission zero between the passband the upper stopband to prevent poor rejection caused by higher mode (i.e. TE_{201} mode in this case).

At the first step, a third order Chebyshev waveguide cavity filter was designed based on the specification of 291.8 GHz centre frequency, 3% (8.2 GHz) bandwidth, and a 20 dB return loss in the passband. To meet this specification, the external quality factor and coupling coefficients are calculated to be $Q_{e1} = Q_{e3} = 28.87$, $k_{12} = k_{23} = 0.030$. The synthesis of designing such a standard Chebyshev filter based on resonators was described in Chapter 2. For this structure, an inductive

iris between the test ports and the first/last resonators controls the external coupling (Q_e), the iris between resonator 1 and 2 (or resonator 2 and 3) controls the coupling coefficient k_{12} (or k_{23}). In order to be compatible with CNC milling process, the corners of the resonators are designed to have a radius of 0.10 mm (see Fig. 4.6) to permit fabrication with a 0.20 mm end mill. In this case, the minimum structures should be designed no smaller than 0.20 mm due to the limitation of the drill.

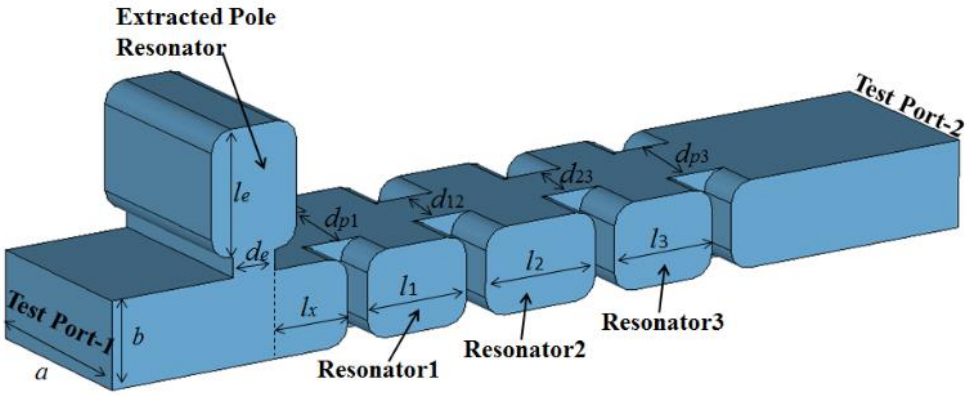

Fig. 4.6 Diagram of third order extracted pole filter structure. a = 864, b = 432, l_1 = l_3 = 510, l_2 = 517, l_e = 619, l_x = 383, d_e = 205, d_{p1} = d_{p3} = 432, d_{12} = d_{23} = 309. (Unit: μm)

To meet the upper stopband specification, a steep roll-off is needed on the high frequency side of the passband. Using extracted pole resonator [8] (i.e. inductively coupled cavity connected to the broad wall of the waveguide) is a good solution for improving the selectivity of a conventional waveguide filter. In this work, an extracted pole resonator with same width and height (a and b as shown in Fig. 4.6) is inductively coupled to the third order waveguide filter using the method of reference [10] and [11], provides a transmission zero in the rejection band and achieves a very

high cut-off rate into the upper sideband. As described in [9], one of the advantages for the extracted-pole technique is that each real frequency transmission zero is independently tunable, which means we can control the response of the rejection band by adjusting the parameters of the extracted pole resonator (i.e. distance of the extracted pole resonator away from the filter l_x and the length of the extracted pole resonator l_e, as shown in Fig. 4.6) to meet the specification without having much influence to the passband response.

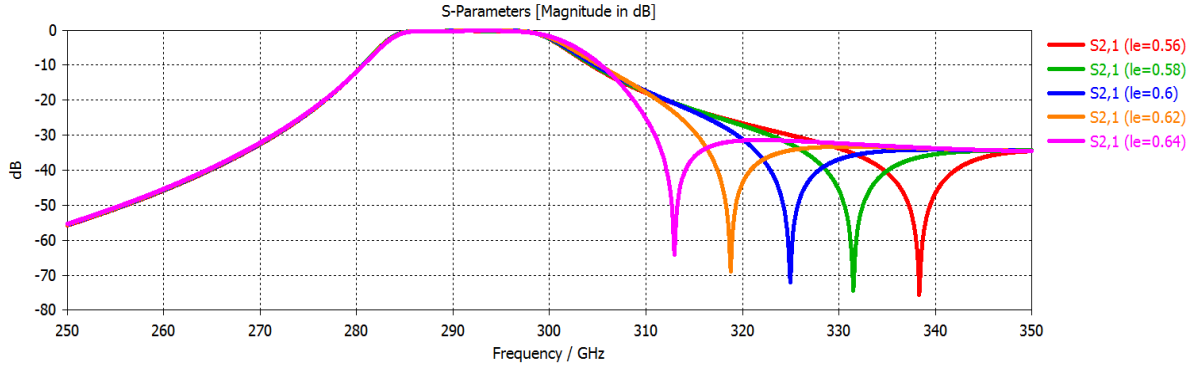

Fig. 4.7 S_{21} responses for different extracted pole resonator lengths (l_e=0.56, 0.58, 0.60, 0.62, 0.64 mm) and same distance of the extracted pole resonator away from the filter (l_x=0.5 mm)

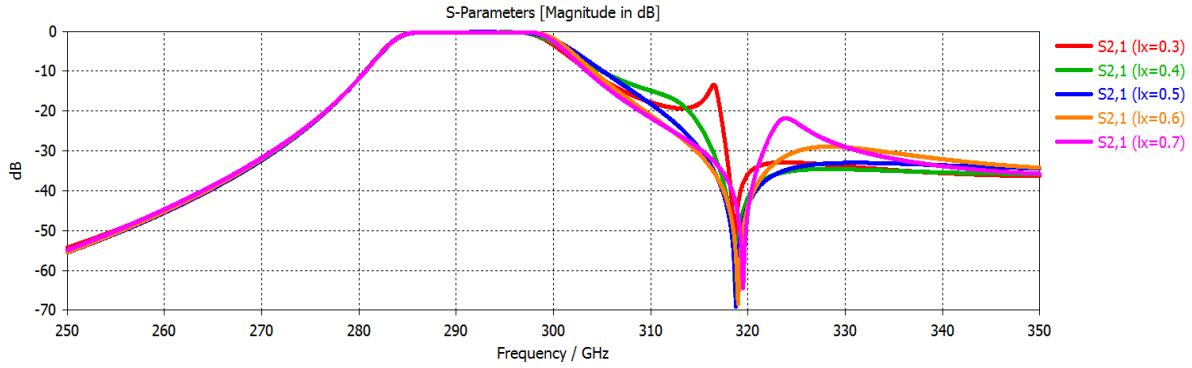

Fig. 4.8 S_{21} responses for distance of the extracted pole resonator away from the filter (l_x=0.3, 0.4,

0.5, 0.6, 0.7 mm) and same length for extracted pole filter (l_e=0.62 mm).

In the next step, the dimensions of the initial design for the waveguide structure are first calculated and tested using the coupling matrix approach [12], then the parameter sweeps are carried out for the dimensions of the extracted resonator (i.e. l_e and l_x shown in Fig. 4.6) to find out the best upper stopband response to meet the specification.

To investigate the relationship between filter response and the parameters of the extracted pole resonator (i.e. l_e and l_x shown in Fig. 4.6), parameter sweep simulations for l_e are carried out in Fig. 4.7. For same l_x, the frequency of the transmission zero decreases as the length of the extracted pole resonator l_e increases. From the simulation results in Fig. 4.8, the shape of the S_{21} response near the transmission zero can be changed by distance l_x of the extracted pole resonator away from the filter. From those simulations we can find out that the length of the extracted pole resonator l_e controls the frequency of the transmission zero, the distance between the extracted pole resonator and the waveguide filter (i.e. l_x shown in Fig. 4.6) controls the shape of the response near the transmission zero.

Finally, full-wave simulation and optimisation for the designed filter are carried out by CST Microwave Studio (version 2016). The filter material is assumed to be gold (conductivity = 4.10×10^7 S/m). The total length of the filter structure shown in Fig. 4.6 is 4 mm. The cavity dimensions achieved after optimisations are also shown in Fig. 4.6. The S-parameters simulation results after optimisations are shown in Fig. 4.9. The predicted passband insertion loss for the extracted pole filter (4 mm filter structure) is below 0.35 dB and the rejection in the unwanted sideband is above 30 dB. The passband reflectivity, S_{11}, is below -20 dB.

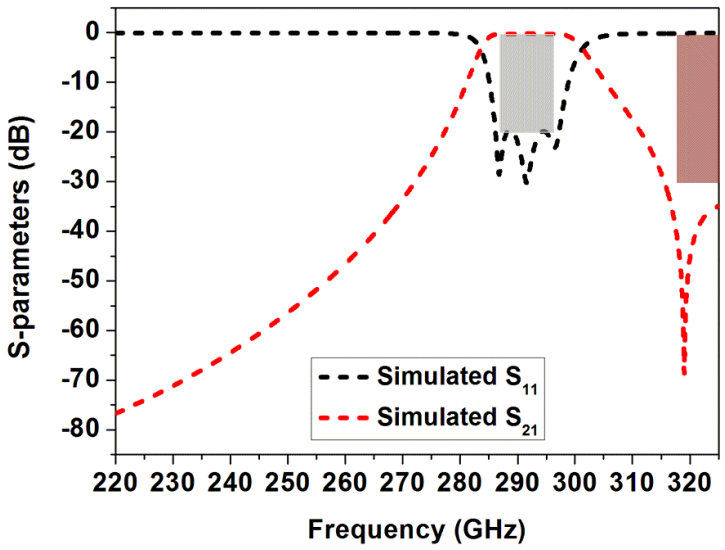

Fig. 4.9 Simulated *S*-parameters for the CNC milled extracted pole filter. Passband and stopband specifications are shown in grey and red respectively.

4.3.2 Fabrication and measurement details for CNC milled filter

In order to test the filter, a CNC machined block which contains the filter is designed and is shown in Fig. 4.10. The input and output waveguides have both been extended by 8 mm in order to accommodate standard waveguide flanges and screws. A 20 mm length of straight WR-3 waveguide is included as a measurement reference in the same block as the waveguide filter. Standard UG-387 waveguide flanges were machined in the block. By utilising an E-plane split-block technique, the transmission loss is minimized as no surface current flows across the contact plane.

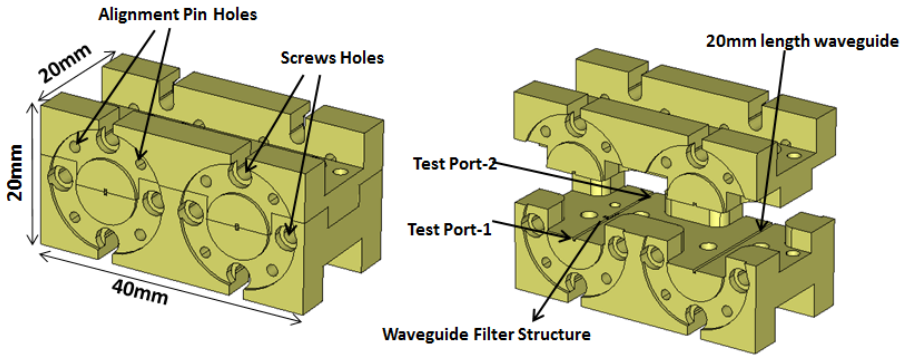

Fig. 4.10 Split block design for CNC milled extracted pole filter

The extracted pole waveguide filter was fabricated at the Rutherford Appleton Laboratory using a high precision Kern milling machine and tungsten carbide cutters with diameters down to 0.20 mm. The block material was copper alloy which was then coated with a thin film of gold (around 3 μm) by electroplating. As mentioned above, the internal corners of the filter had a radius of 0.2 mm. Fig. 4.10 shows the 3D model of the split block design with alignment pin holes and screws holes and Fig. 4.11 shows the photograph of the split plane of the CNC machined block with its four resonators. The fabricated waveguide filter with blocks is shown in Fig. 4.12(a).

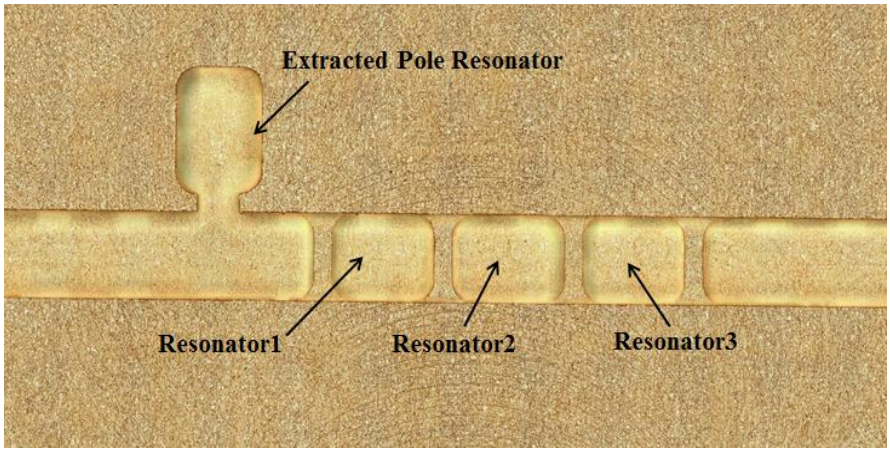

Fig. 4.11 Photograph of the internal cavities of the fabricated CNC milled extracted pole filter.

The *S*-parameter measurements for the CNC milled extracted pole filter were carried out using a Keysight PNA network analyser with a pair of VDI (Virginia Diodes Inc.) WR-3.4 extension heads. For the measurement, the CNC machined block was fixed between the waveguide flanges of two frequency extension heads, as shown in Fig. 4.12 (b) and (c). The insertion loss for the 20 mm length of WR-3 waveguide in the same block was also measured. The results are shown in Fig. 4.13. The filter with the additional waveguide has an average passband insertion loss of around 0.65 dB and greater than 30 dB rejection in the upper stopband. As shown in Fig. 4.14 (a), the insertion loss for 20 mm of waveguide is measured to be 0.3 dB for the passband, giving the waveguide a loss of 0.015 dB/mm. Allowing for a total of 16 mm of waveguide connecting the filter to the flanges, the passband insertion loss of the 4 mm long filter structure is thus 0.41 dB. Fig. 4.14 (b) shows the comparison of measured and simulated passband S_{21} response for the 4 mm long filter structure that is with the effect of the additional waveguide removed.

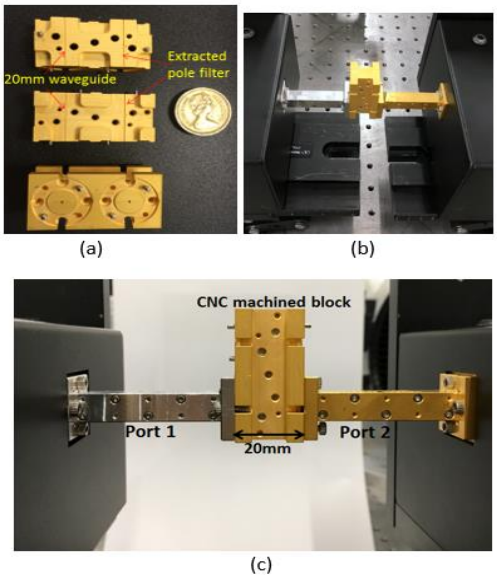

Fig. 4.12 Measurement set up for CNC milled extracted pole filter: (a) Photograph of the filter blocks fabricated by CNC milling (20×20mm×40mm). (b) (c) Test setup for the CNC milled extracted pole filter and 20mm length waveguide.

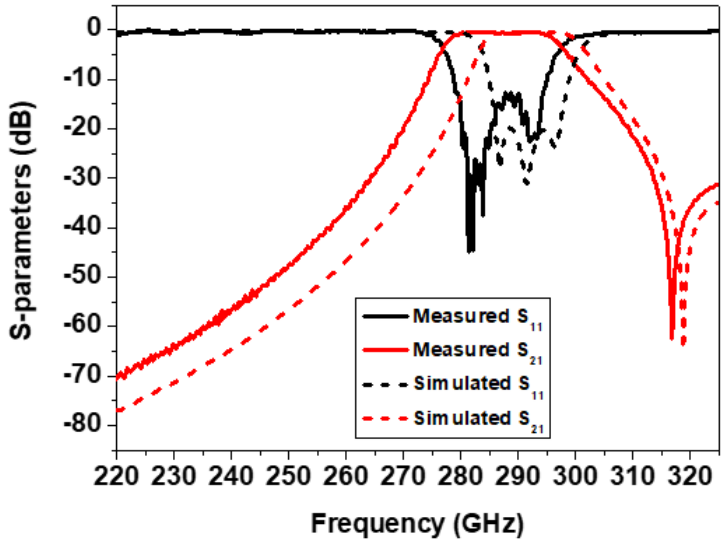

Fig. 4.13 S-parameters response over whole WR-3 band for simulated and measured results of the CNC extracted pole filter.

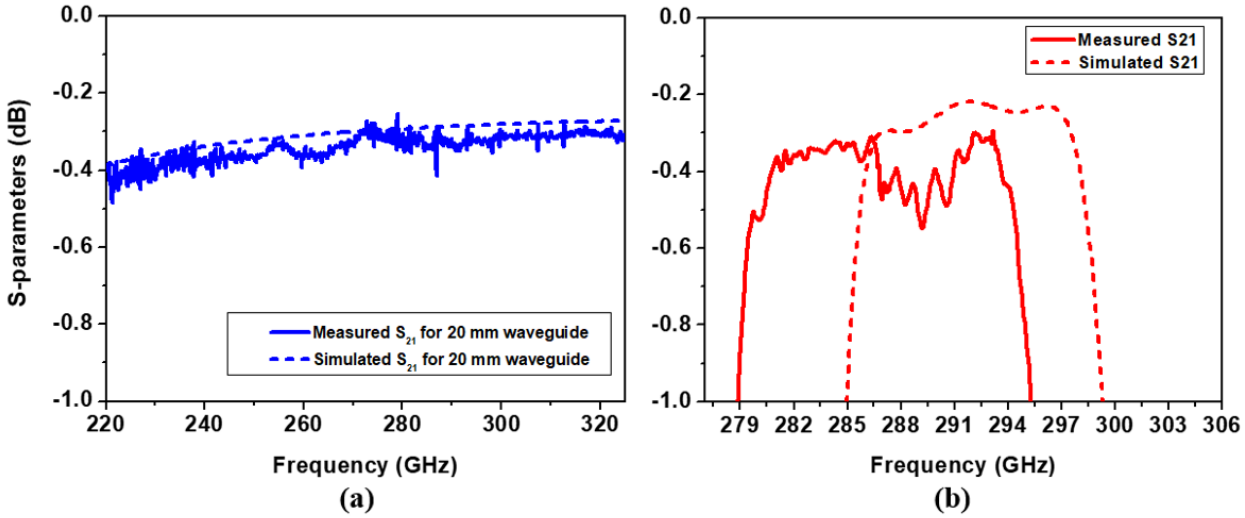

Fig. 4.14 (a) Measured and simulated S_{21} for 20 mm straight waveguide (b) Expanded view of S_{21} for the extracted pole filter showing the measured and simulated passband response with the effect

of the connecting waveguide removed. The simulations are performed assuming a material conductivity corresponding to that of bulk gold.

4.3.3 Difference analysis

Table-4.1 Comparison between designed and measured resonator dimensions for CNC extracted pole filter

	Designed (μm)	Measured (μm)	Errors (μm)
Cavity #	$a \times b \times l$	$a \times b \times l$	$E_a \times E_b \times E_l$
Resonator 1	864×432×510	874×438×521	10×6×11
Resonator 2	864×432×567	874×438×574	10×6×7
Resonator 3	864×432×510	874×438×519	10×6×9
Extracted Pole Resonator	864×432×619	877×439×629	13×7×10

The measurements are in very good agreement with simulations except that centre frequency of the filter is shifted downwards by around 5 GHz. After the S-parameter measurements, the devices are sent back to RAL in order to make accurate dimension measurements. Table-4.1 shows the measured dimensions and the designed dimensions. Comparing the measured dimensions and the designed values, it can be seen that the main reason of the frequency shift is probably the larger-than-designed dimensions of resonators. Generally, dimensions are within a few microns of designed values, except for the lengths of the resonators and the width of the waveguide (i.e. the dimension of *a* shown in Fig. 4.6) which are about 10-15 μm larger than assumed in the simulations. Using the measured dimensions and re-simulating the filter in CST, excellent agreement with measurements is obtained as shown in Fig. 4.15.

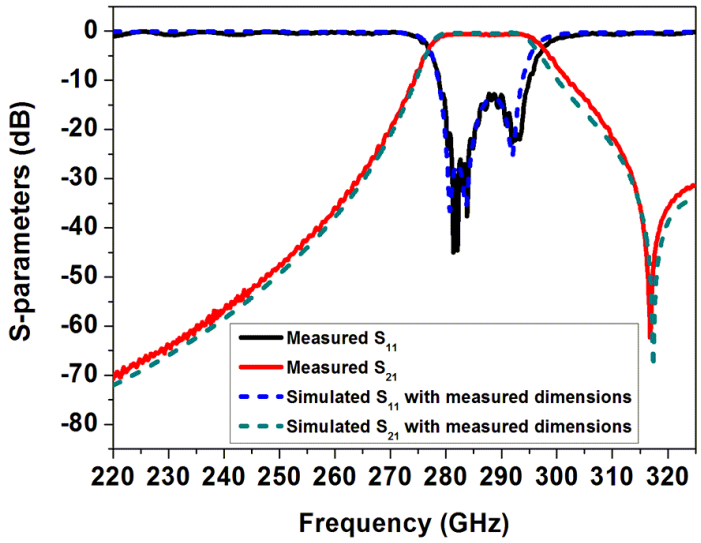

Fig. 4.15 Simulated response of the CNC milled extracted pole filter with measured dimensions

4.4 SU-8 Micromachined Filter

4.4.1 Design process of SU-8 micromachined filter

The configuration of the designed SU-8 photoresist filter to meet the same specifications is shown in Fig. 4.16 (a). The layout of the cavities is specially designed to take the advantage of the single-layer SU-8 process described in Section 3.2. The filter has three coupled resonators and a cross-coupling between the first and third resonators and is shown in Fig. 4.16 (a) and (b). With this topology and by setting the frequency of the transmission zero at 317.7 GHz, which is the lower boundary of the upper stopband, external Q and coupling coefficients are calculated using coupling matrix synthesis [2] introduced in chapter 2 as: $Q_{e1} = Q_{e3} = 27.65$, $k_{12} = k_{23} = 0.031$, $k_{13} =$

0.006, k_{11} = k_{33} = 0.002, k_{22}= -0.006. Fig. 4.17 shows the calculation result for the designed coupling matrix.

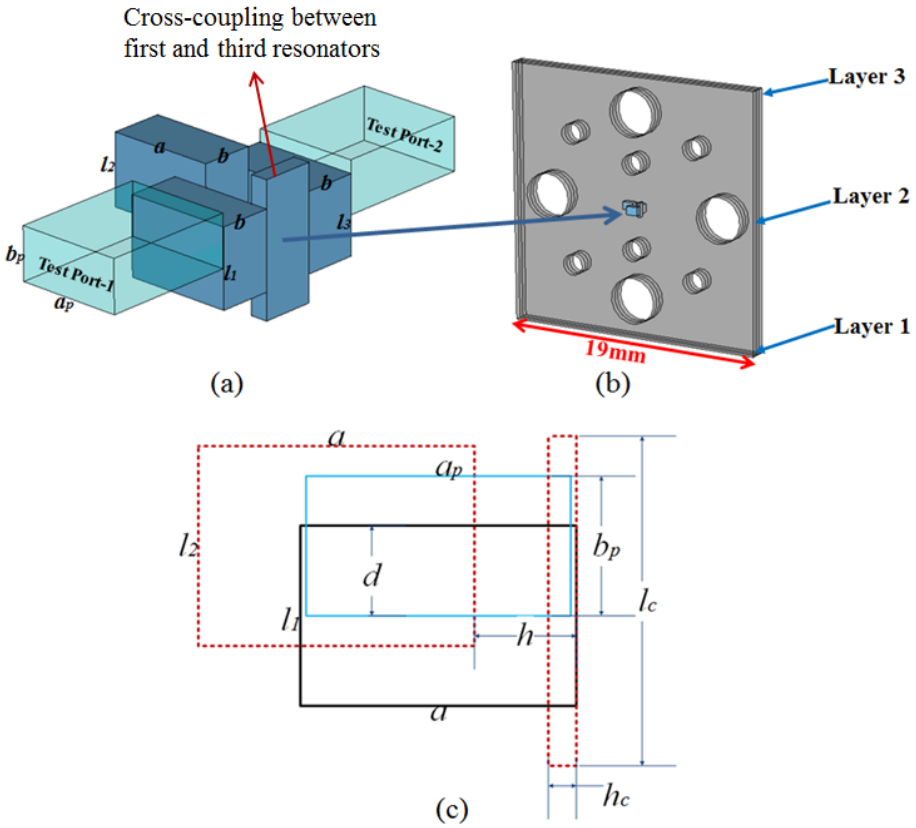

Fig. 4.16 Diagram of WR-3 band filter formed of three SU-8 layers with same thickness of 432 µm. (a) Diagram of the filter structure. Dimensions of the test ports are: a_p = 864 µm, b_p = 432 µm. Dimensions of the resonators are: a = 876 µm, b = 432 µm, l_1 = l_3 = 647 µm, l_2 = 589 µm. (b) Illustration of the whole filter device including dowel holes and screw clearance holes designed to match the UG-387 waveguide flange. (c) A perspective front-view of the filter structure. The blue rectangle represents the input/output of test port. The black rectangle represents the first (or third) resonator, whereas the cavities in the second layer are represented by red rectangles. d = 327 µm, h = 578 µm, l_c = 1100 µm, h_c = 143 µm.

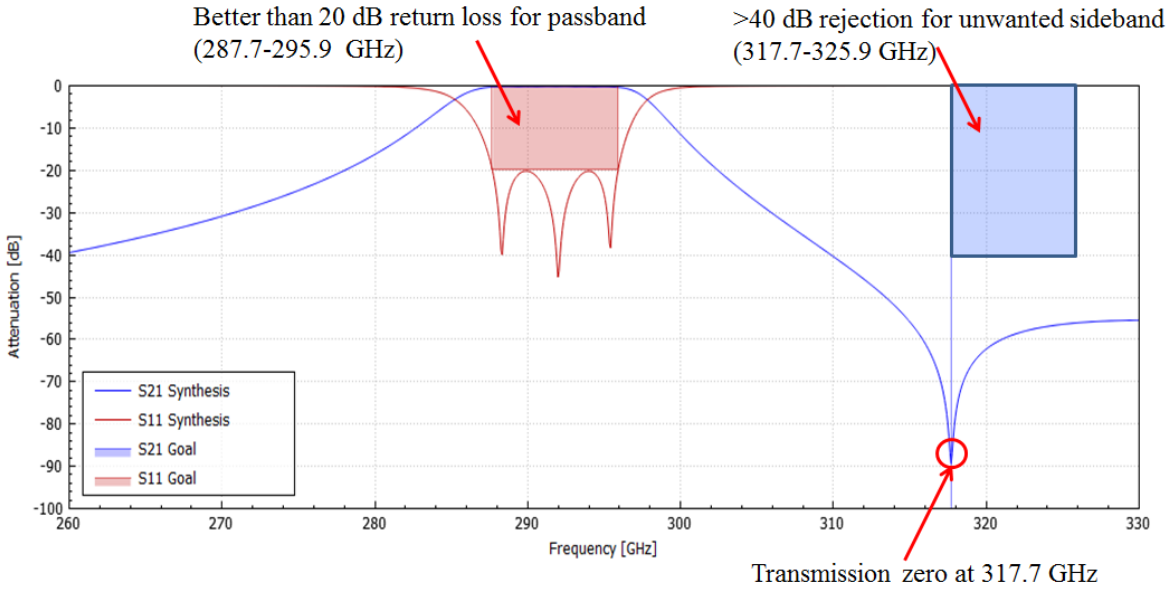

Fig. 4.17 Calculation of cross-coupling based response from the coupling matrix

As shown in Fig. 4.16(b), the device is composed of three SU-8 layers. Each of the silver-coated SU-8 layers has a thickness of 432 μm and contains one resonator. Seen from Fig. 4.16(a), the SU-8 layer thickness determines the WR-3 waveguide resonator height, *b*. Since the central resonator couplings k_{12} and k_{23} are equal, layers 1 and 3 are identical and the whole structure is symmetrical. Rather than controlling the coupling through a conventional iris, the relative positions of the resonators are shifted to obtain the desired coupling coefficients. In other words, the horizontal displacement *h*, shown in Fig. 4.16 (c), determinates k_{12} and k_{23}, whereas the offset *d* between the test port and first/third resonators controls the external coupling. The cross-coupling between first and third resonators is accomplished by a slot in the middle layer. The frequency of the resulting transmission zero is controlled by the width of this cross-coupling slot, h_c. The above

geometric design parameters, shown in Fig. 4.16, are optimised by the SMEAFO method [13] using CST Microwave Studio (version 2016). Fig. 4.16(c) provides the detailed dimensions of this filter after optimisation.

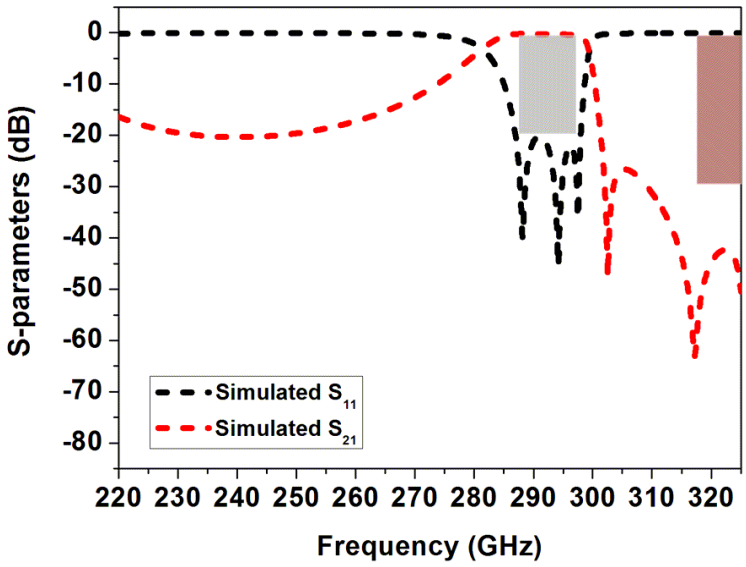

Fig. 4.18 Simulated *S*-parameters for the SU-8 micromachined filter. Passband and stopband specifications are shown in grey and red respectively.

The optimised *S*-parameter response of the filter is shown in Fig. 4.18. The predicted passband insertion loss is below 0.4 dB and the rejection in the unwanted sideband is better than 35 dB. Passband reflectivity, S_{11}, is below -20 dB. The simulations predict two unexpected transmission zeros, one located between passband and upper stopband at 302.5 GHz and another at 326.2 GHz, just above the waveguide band's upper edge. These zeros are caused by unwanted cancellation effect of the signals transmitted by different paths from the input to the output due to the special structure of the design. That is in addition to the cross-coupling accomplished by the slot on the middle layer, there is an additional coupling path between resonators 1 and 3.

4.4.2 Fabrication and Measurement Details for SU-8 Micromachined Filter

The filter is designed to be inserted between standard UG-387 waveguide flanges for measurement. As shown in Fig. 4.16 (b) and Fig. 4.19 (a), six alignment pin holes which accommodate the flange dowels as well as aligning the different SU-8 layers, are incorporated in the design. Larger clearance holes for the waveguide flange screws are also introduced.

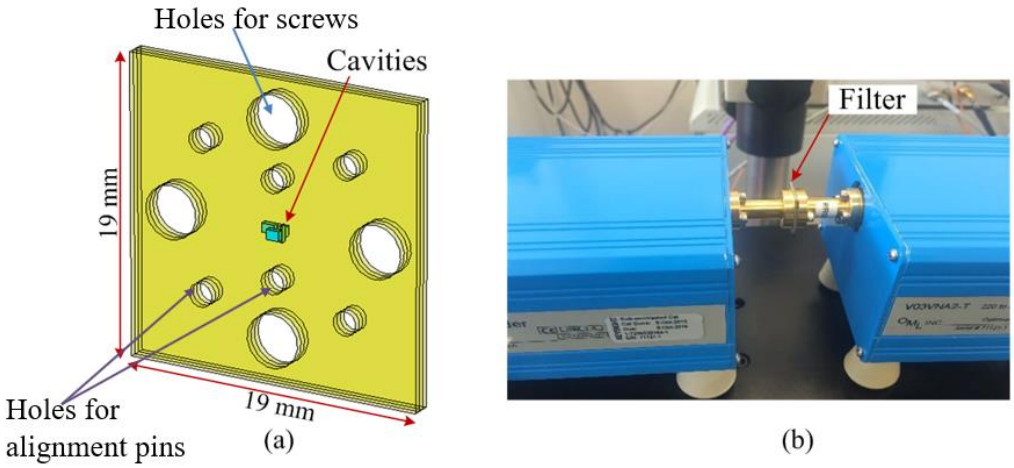

Fig. 4.19 (a) Designed SU-8 filter composed of three SU-8 layers. (b) Testing process for SU-8 micromachined filter

As introduced in Section 3.3, a photomask is need during exposure process. The mask designed for the SU-8 photoresist process is shown in Fig. 4.20. In this work, the mask feature is designed on a 125 mm ×125 mm glass that is transparent to UV light. The black area in Fig. 4.19 represents the chromium pattern which prevent the SU-8 from UV exposure so that the alignment pin holes and cavity structures are produced. In this work, each SU-8 layer only takes 19 mm ×19 mm area, five groups of samples with same dimensions for filter structure but different dimensions for

alignment pin holes are developed on the single mask for better efficiency. Such design of mask increases the chance that the fabricated SU-8 layers are perfectly matched to the flange dowels. Table-4.2 presents the comparison of alignment pin holes dimensions for different sample groups.

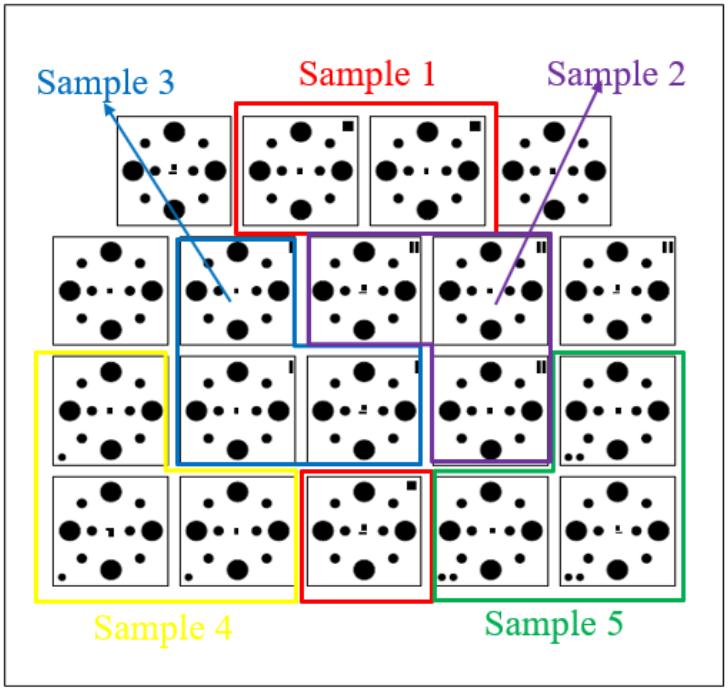

Fig. 4.20 Designed mask for the SU-8 photoresist process

Table-4.2 Designed alignment pin holes dimensions for different sample groups on the mask

Sample Group	1	2	3	4	5	Specification for pins on waveguide flange
Key holes dimensions (mm)	1.60	1.64	1.68	1.72	1.76	1.60
Alignment pin holes dimensions (mm)	1.70	1.74	1.78	1.84	1.88	1.70

The fabricated layers of the SU-8 filter are shown in Fig. 4.21 (a). The process detail for the SU-8 filter fabrication is described in Section 3.2. In this work, the SU-8 base is a single side polished silicon wafer with dimensions of 100 mm diameter and 1 mm thick. The sacrificial layer between SU-8 and silicon is 1.5 μm thick Omni Coat [14]. The coating was soft baked by placing the wafer on a hot plate at 200^{o} C for 120 seconds. It was then cooled on a flat copper plate at room temperature for 300 seconds.

To fabricate desired thickness of SU-8 layers, we measure the mass of the SU-8 liquid [14]. A mass of 5.20 g on a 100 mm diameter wafer corresponds to a thickness of 432 μm. The coated wafer is left on a levelled copper plate at room temperature for 1 hour for self-planarization. Then it was soft baked at 65 and 85^{o} C for 40 and 240 minutes respectively [1].

UV exposure process was carried out in Cannon PLA-510 mask aligner. The wafer base was aligned to the desired samples shown on the mask. The resist was exposed for 4 cycles of 40 s, with a 2 minutes interval between each cycle to allow the resist to stabilize. A PL 360 filter was placed over the chrome mask during UV exposure, which effectively blocked UV radiation with a wavelength below the 365 nm i-line [15]. The exposed wafers were baked at 70^{o} C for 30 minutes, which helps the acid assisted cross-linking of the exposed structures. After this bake, the SU-8/Si wafer was developed for 15 minutes in MicroChem EC at room temperature with constant magnetic stirring. The patterned SU-8 layers were released by dissolving the sacrificial layer in tetramethylammonium hydroxide based MFCD26 solution from MicroChem at room temperature for 5 hours. The released SU-8 pieces were cleaned with propan-2-ol and dried by nitrogen gas. Layers of 30 nm of chromium, and subsequently 1500 nm of silver, were deposited by sputtering and thermal evaporation respectively. This was done on both sides of the patterned SU-8 layers without breaking the vacuum. The evaporator was continuously rotated by the substrate holder at

all angles to make sure the walls of the waveguide structure were well coated.

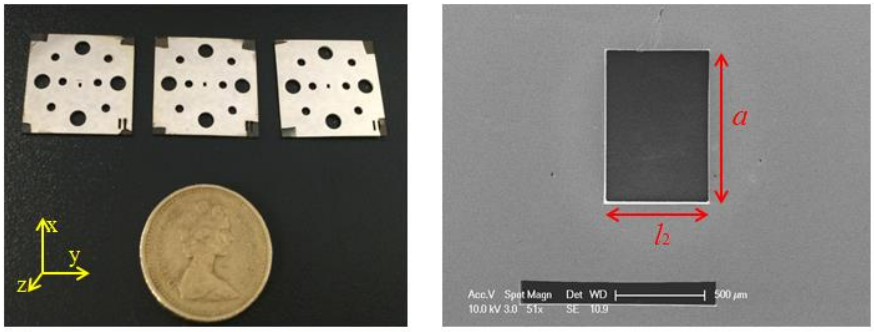

(a) (b)

Fig. 4.21 (a) Photograph of the 3 silver-coated SU-8 layers, 20 × 20 mm for each layer with a thickness of 0.432 mm. (b) Scanning electron microscope image of the cavity structure for the second SU-8 layer.

For the SU-8 filter, the measurement is performed on an Agilent E8361A network analyser using a short-open-load-thru calibration. As shown in Fig. 4.19 (b), the SU-8 filter is placed between two waveguide flanges of the network analyser and the layers aligned by the high precision dowels on the waveguide flanges.

The measurement process has been carried out for all sample groups (sample groups 1-5) of SU-8 filters. The comparison of measured results is given in Table-4.3. Seen from the table, the best results are from Sample 3. One reason is that it provides best match between the SU-8 layers and waveguide flanges. The S-parameters responses for this filter are shown in Fig. 4.22. It can be observed from Fig. 4.22(b) that there are significant ripples in the measured S_{21} response. A different network analyser was used in these measurements from those of the CNC filter and the ripple is attributed to a poor match in the receiver head which has a transmit-only module at Port

2. This problem is discussed in detail in [16]. The measured insertion loss is around 0.45 dB in the passband and a larger than 30 dB rejection within the upper stopband.

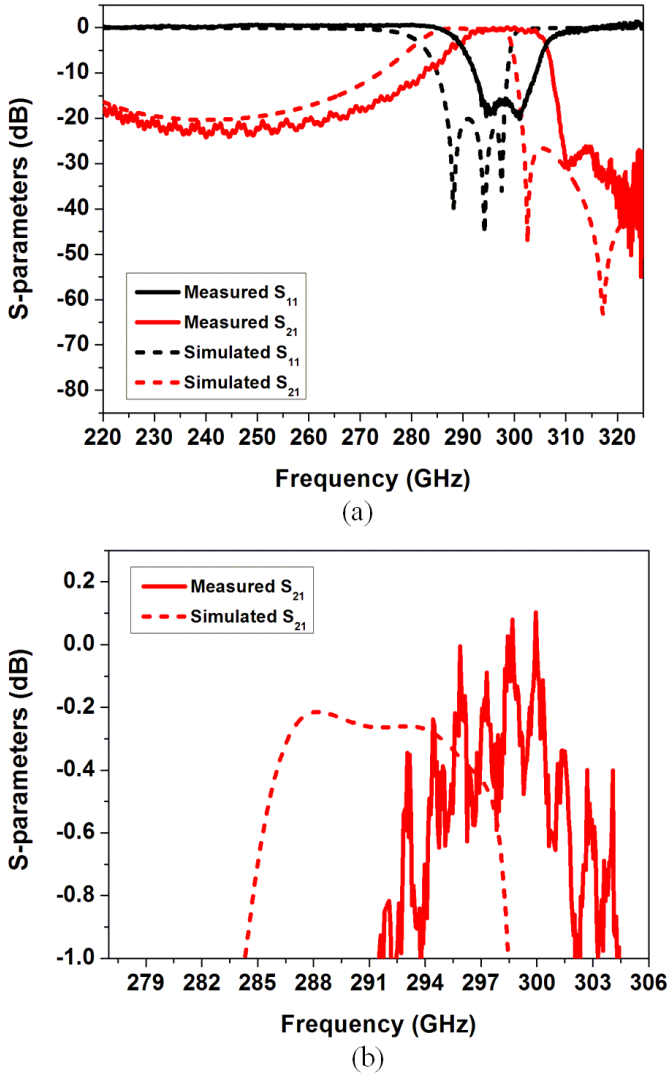

Fig. 4.22 Comparison of the simulated results and measured results of the filter based on SU-8 photoresist technology. (a) Response over whole WR-3 band. (b) Expanded view of S_{21} over passband. The simulations are performed in CST assuming a material conductivity equal to that of silver.

Table-4.3 Measured results for different sample groups of SU-8 filter

	Frequency shift	Passband loss	Rejection for unwanted sideband	Poles within passband (S_{11})
Simulated Results	0	0.3 dB	>35 dB	3
Sample group 1 measured	Can't fit into the waveguide flanges			
Sample group 2 measured	+8	1.4 dB	>24 dB	3
Sample group 3 measured	+7	0.5 dB	>33 dB	3
Sample group 4 measured	+7	2.2 dB	>24 dB	2
Sample group 5 measured	+9	3 dB	>12 dB	2

4.4.3 Difference analysis

From the results shown in Fig. 4.22, the measured centre frequency of this filter is shifted upward by around 7 GHz from the simulation. Because the layer thickness determines the resonator height *b*, simulations show that the centre frequency of the filter does not strongly depend on the layer thickness. So, the difference in centre frequency of the filter between measurement and simulation may be due to inaccurate dimensions in the layer plane. The dimensions of the SU-8 filter cavities were measured using a scanning electron microscope. Fig. 4.21(b) shows the cavity within the second layer and Table-4.4 shows the measured resonator dimensions. Measured dimensions in the plane are around 1% smaller than designed values on one side of the SU-8 layer and 3% smaller on the other side. After inserting the measured dimensions in CST simulations, a much-improved agreement with measurements is obtained, as shown in Fig. 4.23.

Table-4.4 Comparison of designed and measured resonator dimensions for SU-8 filter

	Designed (μm)	Measured (μm)			
		Side 1		Side 2	
Cavity #	*a* × *l*	*a* × *l*	*errors*	*a* × *l*	*errors*
Resonator 1	876×647	863×623	13×24	869×638	7×9
Resonator 2	876×589	861×576	15×13	874×584	2×5
Resonator 3	876×647	855×630	11×17	873×641	3×6

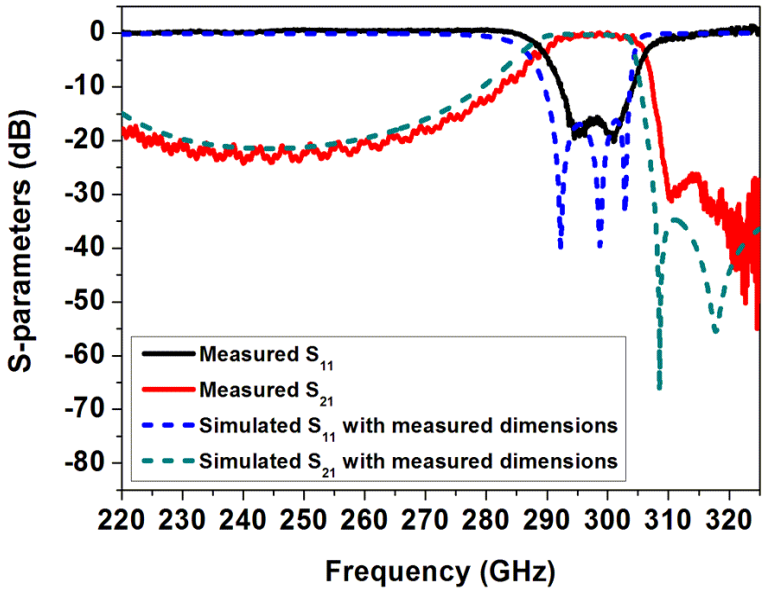

Fig. 4.23 Simulated response of the SU-8 filter with measured dimensions.

4.5 Comparison and Discussion

Table-4.5 Comparison of simulations and measurements between CNC milled extracted pole filter, SU-8 micromachined filter and FSS filter

	CNC extracted pole filter	SU-8 filter	FSS filter
Passband Insertion loss	0.41 dB	0.45 dB	0.6 dB
Centre Frequency and Bandwidth	286.5 GHz BW=9.5 GHz	299 GHz BW=9 GHz	291.8 GHz BW=8.2
Centre Frequency Shift	-5.3 GHz	7.2 GHz	0 GHz
Stopband Attenuation	>32 dB	>33 dB	>30 dB
Size of Filter Device	20 mm × 20 mm × 4 mm (split block)	19 mm × 19 mm × 0.432 mm (three layers)	100 mm × 100 mm × 10 mm (invar holder)

Table-4.5 is a comparison of the measurement results of the CNC extracted pole filer, the SU-8 micromachined filter and the FSS filter. Both the CNC milled and SU-8 filters comfortably achieve the requirements of a lower than 0.6 dB passband insertion loss, with measured values of 0.41 dB and 0.45 dB for the metal and SU-8 devices respectively. The requirements for over 30 dB stopband attenuation are also achieved. The CNC milled extracted pole filter offers a better low frequency rejection, whereas the SU-8 device provides a steeper roll-off on this high frequency side of the passband. As discussed in the Section 4.3.3 and Section 4.4.3, these two filters suffer from -5.3 GHz and +7.2 GHz frequency shift due to inaccurate dimensions. Noticed that both fabricated filters have lager bandwidth than the specification, such results are allowed (or even

better) as long as low insertion loss within passband and high isolation between passband and unwanted sideband are achieved. Compared with the FSS filter, both the CNC milled filter and SU-8 filter presented in this Chapter provide better passband responses and steeper roll-offs for the stopband attenuation with smaller overall volumes.

Table-4.6 shows the comparison between waveguide filters reported in open literature and two filters described here. These filters operate in the frequency range from WR-10 band to WR-1.5 band. All of the filters summarised in Table-4.6 are based on coupled rectangular resonant cavities but fabricated using different micromachining techniques. References [17] and [18] describe fourth order W-band filters based on CNC fabrication process. In [17], the filter is measured to have 0.5 dB insertion loss and a 4.53% (4.20 GHz) bandwidth, and in [18], the filter is measured to have 0.6 dB insertion loss and a 10% (10 GHz) bandwidth. For the 220 to 325 GHz WR-3 band, waveguide features and tolerances decrease by a factor of around three. The examples of WR-3 band CNC milled filter can be found in [19], where two fourth order bandpass filters are presented, one with measured 0.7 dB insertion loss and 8.77% (22.6 GHz) bandwidth and another with measured 0.5 dB insertion loss and 9.83% (25.2 GHz) bandwidth. As for DIRE process, which is another popular micromachining process, WR-3 band waveguide filter example can be found in [20], where a dual mode filter with 7.52% FBW centred at 395.05 GHz is presented. For the utilisation in filter fabrication process, compared with CNC process, SU-8 can achieve a similar high dimensional accuracy with potentially lower cost. It may also allow sharper internal corners and higher corner radius to depth ratios. Meanwhile, SU-8 process is a batch fabrication which allows repeatability between devices as well as production of several devices in a single fabrication run [21]. Compared with DRIE, SU-8 photoresist technology offers better surface roughness on the sidewalls of waveguide structures [21]. SU-8 micromachining process has been employed to

demonstrate filters in the WR-10 [22], WR-3 [23], and WR-1.5 bands [24]. Emerging micromachining process such as laser micromachining and 3-D printing were utilised in [25] for filters using different designs at about 100 GHz (WR-10 band). Two laser micromachined filters are discussed in chapter 5.

In this work, a CNC milled extracted pole waveguide filter and a SU-8 micromachined filter working in WR-3 band have been designed and made to best exploit the characteristics of the fabrication processes. From the comparison shown above, this work presents the first demonstration that a CNC milled filter with a steep rejection characteristic beyond 300 GHz and a SU-8 micromachined filter with novel cross-coupling topology working at WR-3 band. The measured performance of the filters is in very good agreement with the numerical predictions once the latter have been corrected for the small errors in manufacturing. The two filters show no significant difference in performance despite the two alternative fabrication processes and designs. Both filters achieve less than 0.5 dB insertion loss for a designed ~10 GHz wide passband and a rejection of more than 30 dB in the upper stopband. Either of these two micromachined waveguide filters can be potential replacements of FSS filters used in spaceborne radiometers with desired responses and a more compact size.

Table-4.6 Comparison of published waveguide filters operating in frequency from WR-10 to WR-1.5 band

Waveguide band	f_0 (GHz)	FBW	Filter type	Micromachining techniques	n	IL (dB)	RL (dB)	Reference (year)
WR-10	92.6	4.53%	Chebyshev response filter	CNC	4	0.5	>14	[17] (2014)
WR-10	100	10%	Extracted pole filter with pseudo-elliptical response	CNC	4	0.6	>18	[18] (2012)
WR-10	88.47	9.73%	Chebyshev filter	SU-8	4	0.97 ~1.1	>15	[20] (2011)
WR-10	100	4%	Chebyshev filter	Laser micromachining	4	0.5~ 0.8	>15	[25] (2016)
WR-10	87.5	11.5%	Chebyshev filter	3-D printing	4	0.3~ 0.5	>18	[23] (2016)
WR-3	257.7	8.77%	Quasi-elliptical filter	CNC	4	0.7	>14	[19] (2017)
WR-3	256.3	9.83%	Quasi-elliptical filter	CNC	4	0.5	>15	[17] (2017)
WR-3	300	3.3%	Chebyshev filter	SU-8	3	0.4	>15	[23] (2013)
WR-3	395.05	7.52%	Dual mode filter with elliptical response	DIRE	4	2.84	>16	[20] (2015)
WR-3	286.6	5.58%	Extracted pole filter with Chebyshev response	CNC	3	0.41	>14	This work [1]
WR-3	298.6	5.36%	Cross-coupled Chebyshev filter	SU-8	3	0.45	>16	This work [1]
WR-1.5	671	7.91%	Chebyshev filter	SU-8	3	0.65	>11	[24] (2013)

Note: f_0: centre frequency of the filter; FBW: fractional bandwidth; n: filter order; IL: passband insertion loss; RL: passband return loss.

References:

[1] H. Yang, Y. Dhayalan, X. Shang, M. J. Lancaster, *et al,* "WR-3 waveguide filter based on high precision CNC milling and SU-8 photoresist technology," *IEEE Transactions on Terahertz Science and Technology*, vol. 8, no. 1, pp. 100-107, Jan. 2018.

[2] J. Hong and M. J. Lancaster, *Microstrip Filters for RF/Microwave Applications.* New York: Wiley, 2001.

[3] R. J. Martin and D. H. Martin, "Quasi-optical antennas for radiometric remote sensing," *Electron. Comm. Eng. J.*, vol. 8, pp. 37–48, Feb. 1996.

[4] R. Cahill, *et al.*, "Low loss FSS for channel demultiplexing and image band rejection filtering," in *Proc 24th ESTEC AntennaWorkshop on Innovative Periodic Antennas: Photonic Bandgap, Fractal and Freq. Sel. Surfaces*, The Netherlands, May. 2001, pp. 103–108, European Space Agency.

[5] R. Dickie *et al*., "Submillimeter Wave Frequency Selective Surface with Polarization Independent Spectral Responses," *IET Microw., Antennas Propag.*, vol. 57, no. 7, pp. 1985-1994, July. 2009.

[6] R.J. Batt, G.D. Jones, D.J. Harris, "The Measurement of the Surface Resistivity of Evaporated Gold at 890 GHz, " *IEEE Trans. Microw. Theory Tech.,* vol. 25, no. 6, pp. 488-491, Jun. 1977.

[7] G. F. Craven, R. F. Skedd: 'Evanescent Mode Microwave Components' (Artech House Inc., 1987)

[8] J. Bornemann, "A new class of E-plane integrated millimeter-wave filters," *IEEE MTT-S International Microwave Symposium Digest*, Long Beach, CA, USA, 1989, vol.2, pp. 599-602

[9] R. R. Mansour and G. Woods, "Design of millimeter-wave extracted-pole filters with asymmetrical frequency characteristics," *1991 IEEE MTT-S Int. Microw. Symp. Dig.*, Boston, MA, 1991, vol.2, pp. 659-663.

[10] Y. Yang, M. Yu and Q. Wu, "Advanced Synthesis Technique for Unified Extracted Pole Filters," *IEEE Trans. Microw. Theory Tech.*, vol. 64, no. 12, pp. 4463-4472, Dec. 2016.

[11] J. R. Montejo-Garai, J. A. Ruiz-Cruz, C. A. Leal-Sevillano, J. M. Rebollar, L. Rogla, and S. Sobrino, "Compact Low-Cost Diplexer with Elliptic Filter Response for Ka-Band Satellite Applications," in *Proc. 2015 Int. Workshop on Microw. Filters CNES-ESA*, 2015.

[12] H. V. Jansen, M. J. de Boer, S. Unnikrishnan, M. C. Louwerse and M. C. Elwenspoek, "Black silicon method X: a review on high speed and selective plasma etching of silicon with profile control: an in-depth comparison between Bosch and cryostat DRIE processes as a roadmap to next generation equipment," *Journal of Micromechanics and Microengineering*, IOP Publishing, Ltd, Feb. 2009.

[13] J. D. Williams and W. Wang, "Study on the postbaking process and the effects on UV lithography of high aspect ratio SU-8 microstructures," *J. Microlitho., Microfab., Microsyst.*, vol. 3, pp. 563–568, 2004.

[14] X. Shang, Y. Tian, M. J. Lancaster, S. Singh, "A SU8 micromachined WR-1.5 band waveguide filter," *IEEE Microw. Wireless Compon. Lett.*, vol. 23, (6), pp. 300-302, Jun. 2013

[15] D. Glynn, T. He, J. Powell, Y. Tian, X. Shang and M. J. Lancaster, "Submillimetre rectangular waveguides based on SU-8 photoresist micromachining technology," *2016 46th Eur. Microw. Conf.*, London, 2016, pp. 1346-1349

[16] Y. Wang, M. J. Lancaster, M. Ke and X. Shang, "Measurements of micromachined

waveguide devices at WR-3 band using a T/R-T module-based network analyzer," *77th ARFTG Microw. Measurement Conf.*, Baltimore, MD, 2011, pp. 1-4.

[17] X. Liao, L. Wan, Y. Yin and Y. Zhang, "W-band low-loss bandpass filter using rectangular resonant cavities," *IET Microw., Antennas Propag.*, vol. 8, no. 15, pp. 1440-1444, Sep. 2014.

[18] C. A. Leal-Sevillano, J. R. Montejo-Garai, J. A. Ruiz-Cruz and J. M. Rebollar, "Low-Loss Elliptical Response Filter at 100 GHz," *IEEE Microw. Wireless Compon. Lett.*, vol. 22, no. 9, pp. 459-461, Sep. 2012.

[19] J. Q. Ding, S. C. Shi, K. Zhou, Y. Zhao, D. Liu and W. Wu, "WR-3 Band Quasi-Elliptical Waveguide Filters Using Higher Order Mode Resonances," *IEEE Trans. THz Sci. Technol.*, vol. 7, no. 3, pp. 302-309, May. 2017.

[20] J. Y. Li, B. Pan, C. Lugo, M. Tentzeris, and J. Papapolymerou, "Design and characterization of a W-band micromachined cavity filter including a novel integrated transition from CPW feeding lines," *IEEE Trans. Microw. Theory Tech.*, vol. 55, no. 12, pp. 2902–2910, Dec. 2007.

[21] C. H. Smith, A. Sklavonuos and N. S. Barker, "SU-8 micromachining of millimeter and submillimeter waveguide circuits," *2009 IEEE MTT-S International Microwave Symposium Digest*, Boston, MA, 2009, pp. 961-964.

[22] X. Shang, M. Ke, Y. Wang and M. J. Lancaster, "Micromachined W-band waveguide and filter with two embedded H-plane bends," *IET Microw., Antennas Propag.*, vol. 5, no. 3, pp. 334-339, Feb. 2011.

[23] Q. Chen, X. Shang, Y. Tian, J. Xu and M. J. Lancaster, "SU-8 micromachined WR-3 band waveguide bandpass filter with low insertion loss," *Electron Lett.*, vol. 49, no. 7, pp. 480-

482, March. 2013.

[24] X. Shang, Y. Tian, M. J. Lancaster, S. Singh, "A SU8 micromachined WR-1.5 band waveguide filter," *IEEE Microw. Wireless Compon. Lett.*, vol. 23, (6), pp. 300-302, Jun. 2013

[25] X. Shang *et al*., "W-Band Waveguide Filters Fabricated by Laser Micromachining and 3-D Printing," *IEEE Trans. Microw. Theory Tech.*, vol. 64, no. 8, pp. 2572-2580, Aug. 2016.

Chapter 5

Micromachined Waveguide Circuits Fabricated by Laser Micromachining

This chapter describes two laser micromachined filters working at WR-3 band (220 – 325 GHz). The first filter is based on a novel double layer design with non-vertical walls, i.e. draft angles on side walls. The second filter is a standard 4th order Chebyshev waveguide filter measured with two H-plane bends.

Section 5.1 gives the review of previous work on laser micromachining and design motivation. Section 5.2 introduces the design, fabrication and measurement of a laser micromachined WR-3 band 4th order filter. A laser micromachined filter design with two H-plane bends is presented in Section 5.3. In the final part of this chapter, a conclusion is given in Section 5.4.

5.1 Background

As discussed in Chapter 3, with the advantages of repeatable at the micro-scale with relatively high accuracy and able to fabricate a wide range of materials with complex features, laser micromachining is another attractive fabrication technique for terahertz waveguide circuits. With the support from School of Mechanical Engineering in University of Birmingham, we are able to investigate the application of laser micromachining. However, from the literature, laser cutting is rarely utilised to fabricate terahertz waveguide components, except for a W-band waveguide filter presented in [1] and a horn antenna (laser cut from silicon) operating on 2 THz [2]. This brings extra challenges since that very limited successful experiences can be learned from the previous works from other researchers.

In [1], a 4th order Chebyshev bandpass filter fabricated using laser micromachining, with centre

frequency of 100 GHz and fractional bandwidth (FBW) of 4%, is presented by EDT group from University of Birmingham. The filter was designed to achieve less than 0.3 dB insertion loss and better than 20 dB return loss across the passband. It should be noticed that in order to take the advantage of the laser micromachining process, the filter is designed to have a special double layer structure, as shown in Fig. 5.1. The measurement and simulation results of the filter described in [1] is shown in Fig. 5.2. From the measured results in [1], the insertion loss and return loss across the passband is 0.65 dB, 15 dB respectively, which is close to designed value of 0.3 dB insertion loss and 20 dB return loss obtained from simulations with brass. Overall the measurement results of this filter have good agreement with simulations.

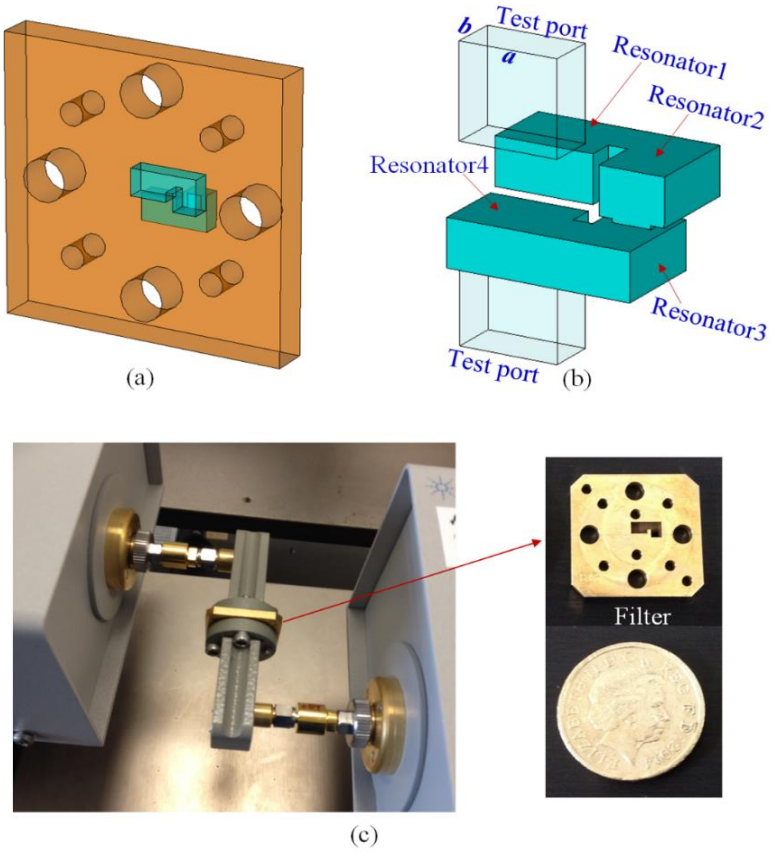

Fig. 5.1. W-band filter fabricated using laser micromachining [1]. (a) Diagram of the filter (blue part) and flange (brown part) based on a single piece. (b) Diagram of the filter features. (c)

Measurement setup and photograph of the filter.

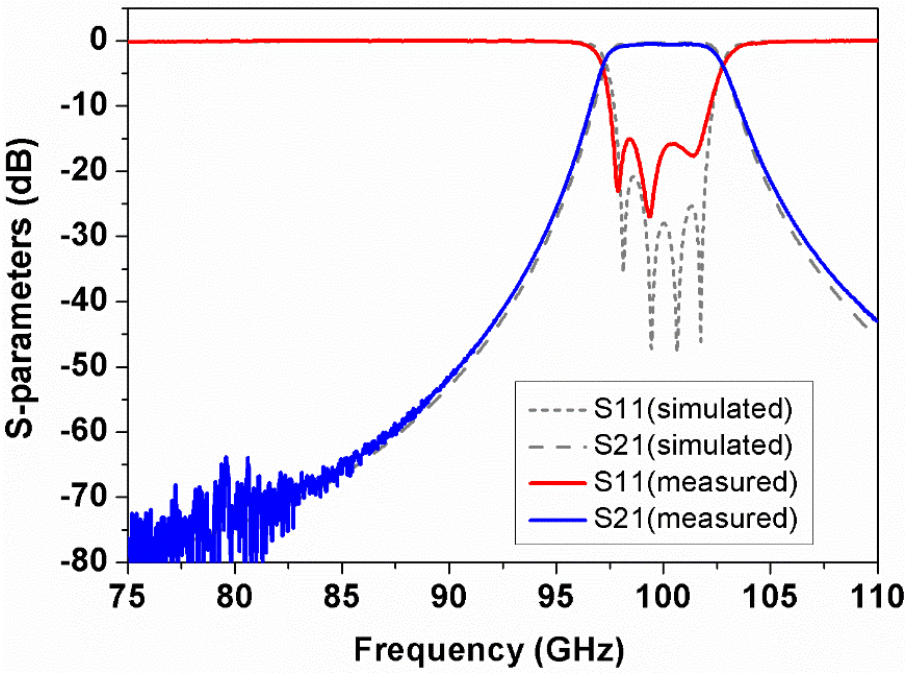

Fig. 5.2. Measurement and simulation results of the laser machined W-band waveguide filter. [1]

One of the drawbacks when applying laser cutting at terahertz frequencies is that laser micromachining is only a good choice when small features are to be fabricated. This is because laser micromachining has relatively low removal rates in comparison to the conventional milling process [3]. To avoid this, a novel multi-stage process technique [4] integrates CNC milling process with laser micromachining is proposed in [1] to solve the problem. Meanwhile, the fabrication process is specially designed in [1] to get rid of draft angles on side walls. These details are discussed in Section 5.2.2. Furthermore, as the frequency goes higher (i.e. WR-3 band), the laser machined structures can have larger draft angles (up to 10°) on their side walls [3], which can have a significant influence on the performance of terahertz devices due to their high sensitivity to variation in geometrical accuracy. Due to these limitations, the waveguide filters in

this work have to be specially designed, in order to take the advantage of laser micromachining process for producing terahertz devices and compensate for the draft angle. Two possible designs are presented in Section 5.2 and 5.3 utilising laser micromachining for WR-3 band filters.

5.2 Laser Machined Double Layer Filter

5.2.1 Design Process of Double Layer Filter

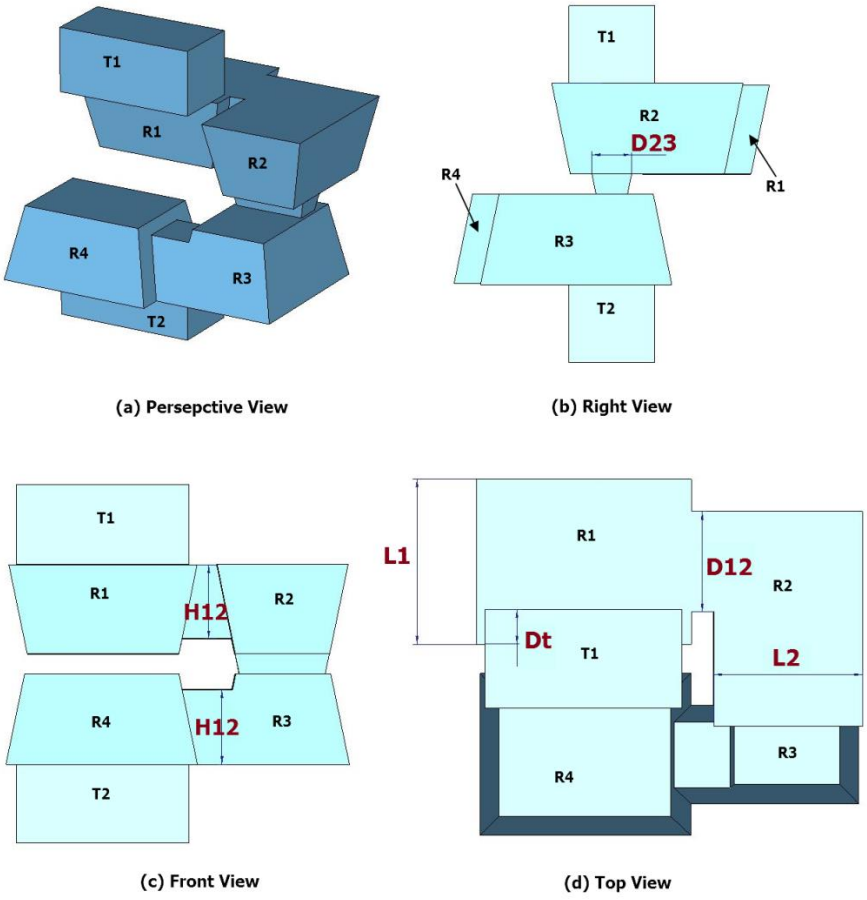

Fig. 5.3 Diagram of the laser micromachined double layer filter. T1 and T2 are input/output test

port, R1–R4 are resonators that have draft angles on side walls.

In this work, the filter is designed to operate at WR-3 band (220 – 325 GHz) with centre frequency of 300 GHz and fractional bandwidth of 5%. The objective is to achieve less than 0.5 dB insertion loss and better than 20 dB return loss.

The 3D model of the laser micromachined double layer filter is shown in Fig. 5.3, note the sloping walls which are at the draft angles produced by the laser. It is composed of four coupled resonators operating at TE_{101} mode and has a Chebyshev response. The filter is designed using the synthesis technique introduced in Chapter 2. To achieve the specifications, the coupling coefficients between resonators and external quality factor are calculated to be*:* $m_{12}= m_{34} = 0.0456$, $m_{23}= 0.035$, $Q_{e1}= Q_{e4}= 18.628$. In order to be compatible with the laser micromachining process, the filter utilises a similar structure with filter presented in [1], as shown in Fig. 5.3(a). For the designed structure, the displacements (D_t) between the test port (i.e. T1/T2 shown in Fig. 5.3) and the first/fourth resonator (i.e. R1/R4 shown in Fig. 5.3) control the external coupling (Q_e). The 1st and 2nd resonators (or the 3rd and 4th resonators) are coupled through an inductive iris which also has draft angles on its side walls. The coupling between the 2nd and 3rd resonators is via a capacitive slot. The coupling coefficients between resonator 1 and 2 are controlled by the height and width of the inductive iris (i.e. H_{12} and D_{12} shown in the Fig. 5.3) while the coupling coefficient between 2nd and 3rd resonator is controlled by the width of the capacitive iris (i.e. D_{23} shown in the Fig. 5.3). Instead of using symmetric structure in the design, the four resonators are specially positioned so that the first and forth resonators are not aligned with the test port. Such design provides two advantages: (i) the 1st and 4th resonators are directly externally coupled to the input/output test ports (without the need to have extra coupling iris and connection waveguides at both filter ends); (ii) the first and last resonators do not directly face to each other in *z* direction, which provides

more tolerance for depth dimensions (the space between resonator 1 and 4 may be cut through and become an aperture during the fabrication process if using symmetric design). The draft angles of 7.5 degrees on side walls that caused by laser cutting process [5] are taken into account in the model. The filter is designed to fabricated on a 20 mm × 20 mm and 1 mm thickness brass plate, as shown in Fig. 5.4, the holes are designed to match the screws and alignment pin holes of UG-387 flange. Full-wave modelling and simulations for this filter are carried out using CST Microwave Studio (version 2015) and optimised by the SMEAFO method [6]. Fig. 5.5 shows the simulation results of the filter. In order to be compatible with the process of laser machining, the filter is designed to be a one-piece component without any internal joints, which usually cause extra loss or requires assembling with high precision for split block filter designs such as filters reported in [7] and [8]. Furthermore, this is a compact design which provides a reduction in size compared to standard waveguide filter.

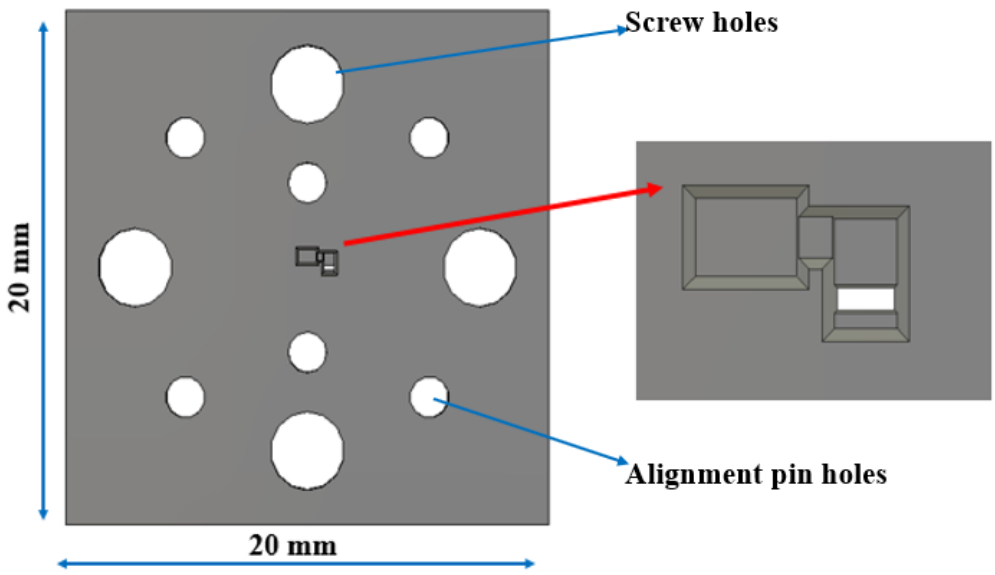

Fig. 5.4 Diagram of the filter including screw holes and alignment pin holes for UG-387 flange.

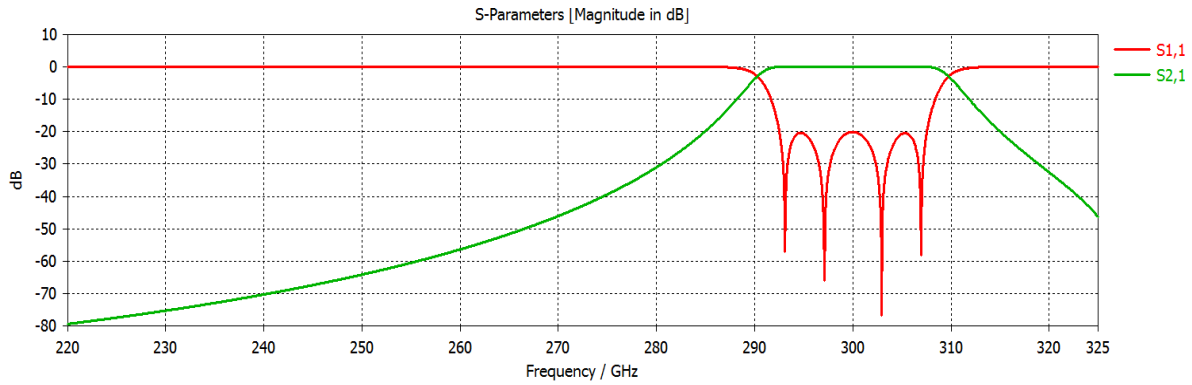

Fig. 5.5 Simulation results for the S-parameters of the laser micromachined double layer filter.

5.2.2 Fabrication Details

Compared to CNC milling, laser micromachining is only a better choice when small features are required to be fabricated due to its relatively low removal rates [3]. To increase the fabricating efficiency, a novel multi-stage process [4], as shown in Fig. 5.6, is proposed and employed to solve this problem. This process chain combines CNC milling process with laser micromachining process. Features with dimensions larger than 2 mm, such as alignment pin holes and screw holes for alignment and fixing to flanges are fabricated using CNC milling in order to achieve a higher material removal rate. Laser micromachining is utilised for fabricating the functional features (i.e. resonators and coupling irises) for a higher dimensional accuracy. Fig. 5.6 shows the key steps of the laser machining fabrication process that has been applied in the W-band waveguide filter fabricating [1] and other terahertz components [3]. These steps can also be summarized as follows [4]:

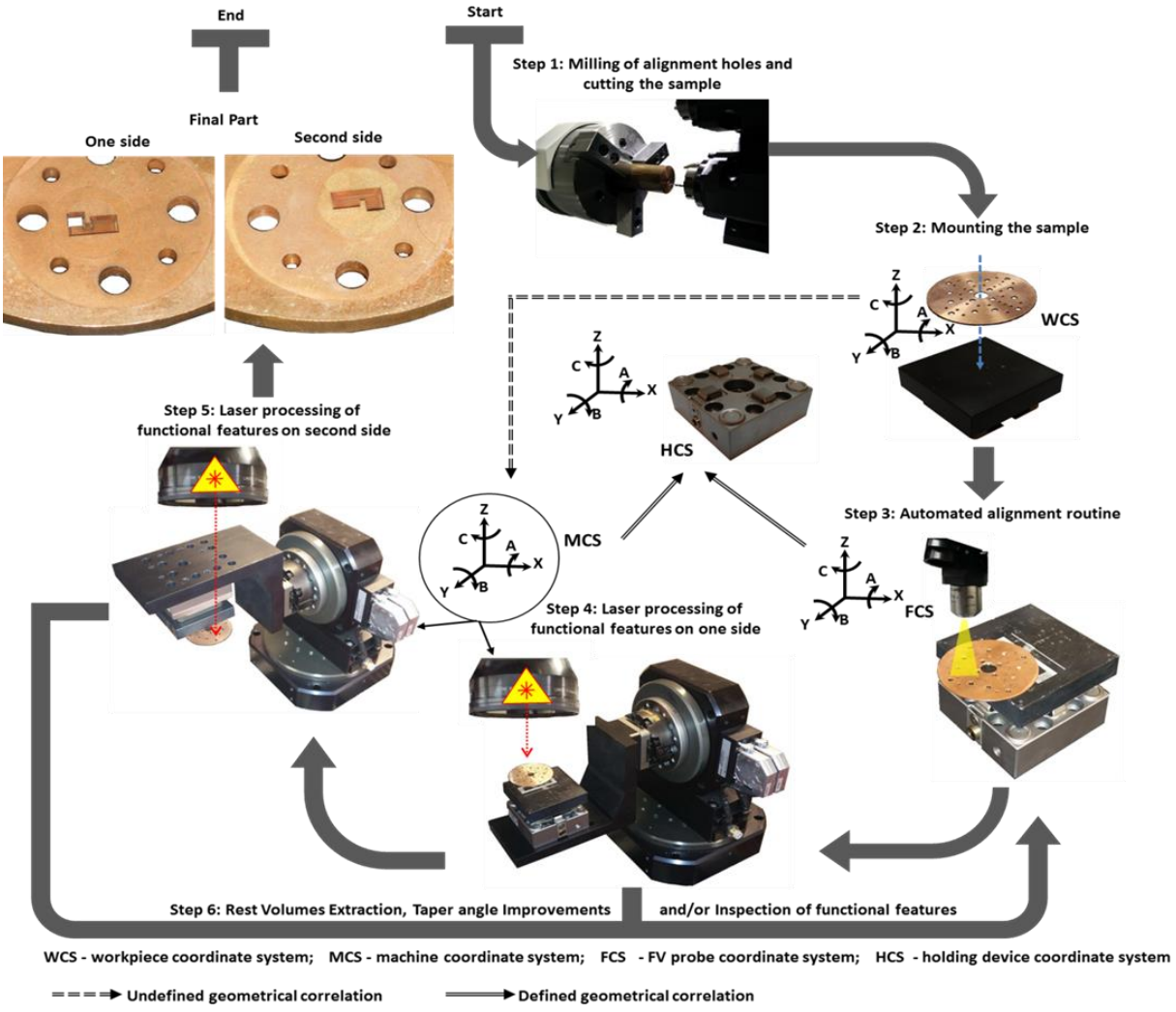

Fig. 5.6 Diagram presenting key fabrication steps of laser micromachining. [4]

(1) Milling of the alignment holes and screw holes and cutting the edge of the sample (using CNC process) on a brass plate. Furthermore, an alignment mark (a cross) is also machined on the sample for follow up processing in the laser micromachining system;

(2) Mounting the sample on a workpiece holding pallet, which is then placed in the laser micromachining module, where the functional features of the terahertz filter are fabricated;

(3) Input the CAD model of the design and calculating the necessary offsets of the laser beam on the workpiece to compensate the misalignments [3];

(4) Laser machining of functional filter structures on one side of the CNC milled sample;

(5) Removing and fixing the sample again on the workpiece holding pallet for laser processing of its second side;

(6) Inspecting the dimensions of the produced functional filter features using Alicona Infinite Focus microscope system [9]. Comparing with the designed CAD model and achieving the dimensional deviations from the designed values. Applying further laser machining operations to optimise if there are any deviations from the designed dimensions of the filter features.

The laser machining parameters are: an average power of 4.2 W, pulse repetition frequency of 125 kHz, beam scanning speed of 0.5-2 m/s [3]. For the filter designed in this work, the process has been optimised due to the symmetric double-layer design. For Step (5), the optimised process eliminates the error caused by misalignment while fixing samples. For the new process, to fabricate on the other side, instead of removing and fixing the sample again, we keep the sample on the holding pallet and rotate it 180° employing a rotary stage, thus gain access to the opposite side of the waveguide and then repeat the steps (3) and (4). The rotations of the stage have an estimated accuracy, repeatability and reproducibility better than 10 μm [10]. By carefully optimising the laser processing parameters, laser micromachining operations can achieve very good repeatability and step (6) can thus be eliminated from the process chain. More details about the laser machining process can be found in [3], [4] and [9].

As reported in [1], in order to deal with the draft angles on side walls, multi-axis machining employing the rotary stages is utilised between step (4) and step (5) to achieve vertical sidewalls (~90°). Since the draft angles of sidewalls are already considered in this work, no multi-axis machining is required during the process. Such a design can be an effective solution to eliminate the potential dimensional deviations caused by these extra steps.

5.2.3 Measurement Results and Discussion

The *S*-parameter measurements of the filter is carried on an Agilent E8361A network analyser subject to a short–open–load–thru calibration. For the measurement, the laser machined filter is fixed between two waveguide flanges of the network analyser. The high precision dowels on the waveguide flanges ensure the accuracy to which the laser micromachined filter is aligned to flanges of the network analyser. The screws are utilised for an intimate contact between the filter and test ports.

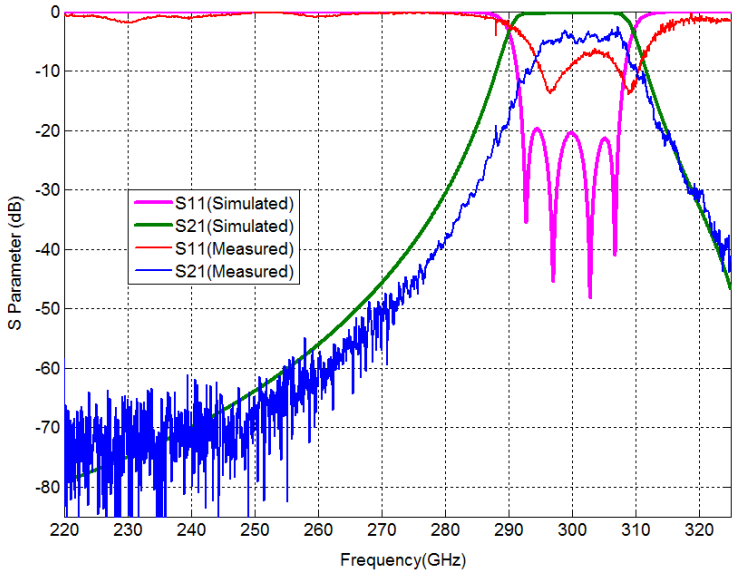

Fig. 5.7 S-parameters response over whole WR-3 band for simulated and measured results of the laser micromachined double layer filter.

The *S*-parameter measurement results of the laser machined double layer filter are shown in Fig. 5.7. The average passband insertion loss is measured to be around 5 dB, which is much larger than the expected value of 0.3 dB obtained from CST simulations using the conductivity of brass

(i.e. 2.74 × 10^7 S/m). From the measurement using the Alicona InfiniteFocus microscope, the surface roughness values of of laser process area in this work are on the order of 1.25 µm [4]. The actual effective conductivity for the filter is thus reduced to 7.04×10^6 S/m [1]. Using the value of the effective conductivity in the simulation, this gives a result of 0.55 dB insertion loss within passband. The maximum passband return loss is measured to be 8 dB, whereas the simulated result using effective conductivity is 16 dB. This difference of return loss within passband provides around 0.7 dB of the loss in the S_{21} result. The rest 4.3 dB loss, is believed to be caused by the small gap at the interface between filter and test flanges. As shown in Fig. 5.8, the input/output port is directly coupled to the first/fourth resonator, which means the energy would leak through the gap shown in Fig. 5.8 if there is poor alignment between the filter and UG-387 flange or non-flat surfaces of the waveguide filter.

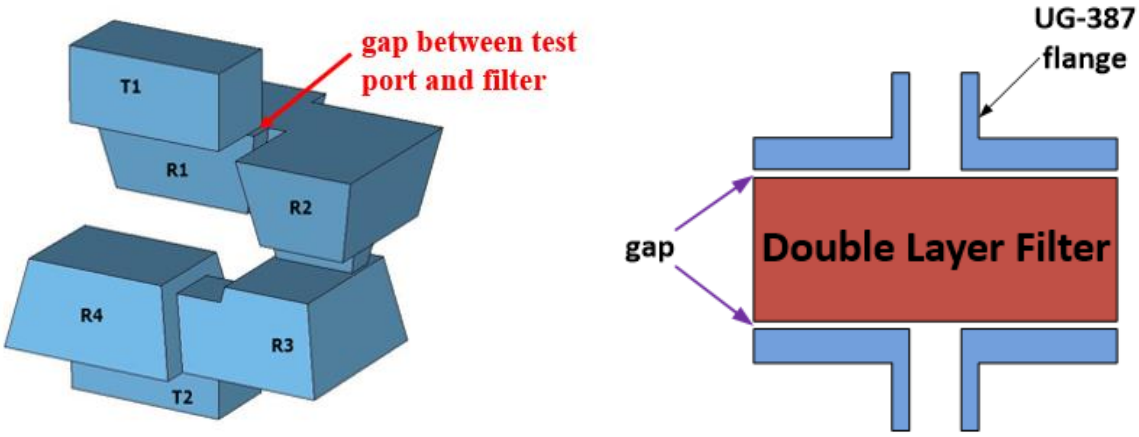

Fig. 5.8 The potential gaps existing between input/output port and 1st/4th resonator.

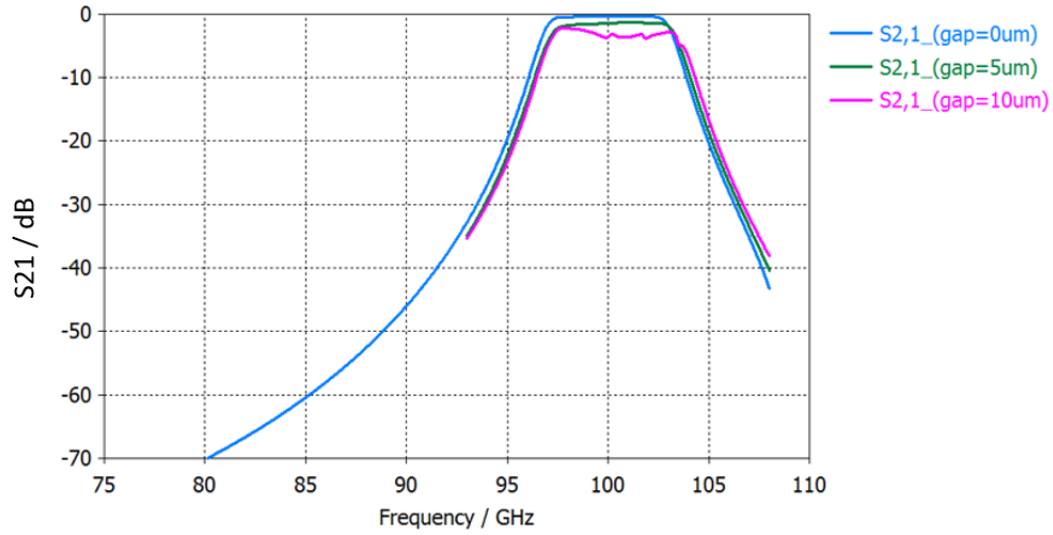

(a)

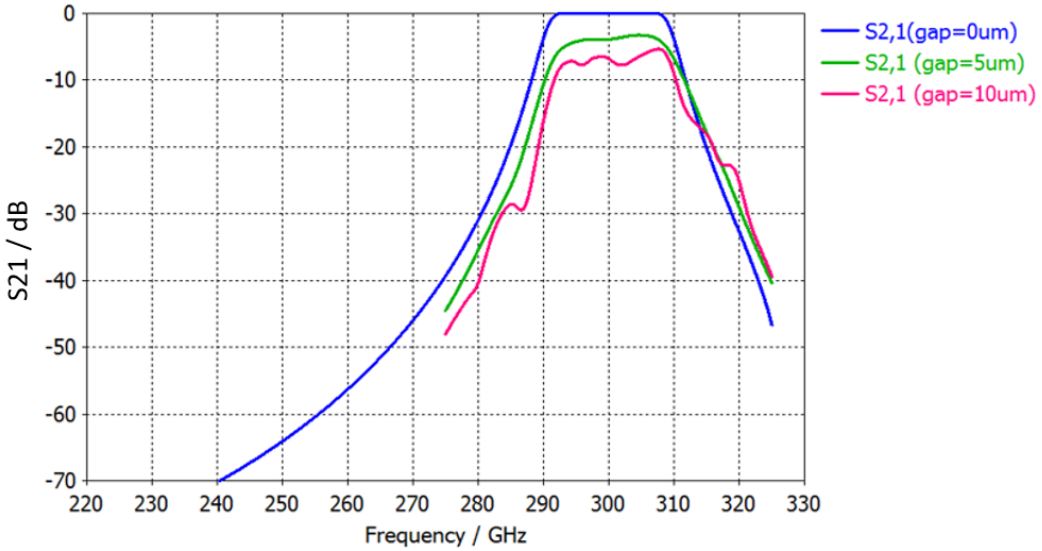

(b)

Fig. 5.9 Simulation of insertion loss for 0 μm, 5 μm and 10 μm gap dimensions for (a) filter operating at W-band; (b) filter operating at WR-3 band.

As shown in Fig. 5.9(a), for W-band waveguide filter simulations, the simulation results show that small gaps (5 and10 μm) at the interface between filter and test flanges provide about 1.5 dB

and 3.5 dB of average insertion loss within passband. When applying same dimensions of gaps in WR-3 band filter design, the simulation results show that this could result in significant loss (5 dB and 9 dB insertion loss within passband). The comparison of the simulation results shows that the designed WR-3 band filter is much more sensitive than the W-band filter for the gaps between test port and 1st/4th resonators.

As for the deviation in S_{11} responses, as shown in Fig.5.7, these differences can be caused by dimensional inaccuracies for filter structures or misalignments between test ports and filter flange. From the dimensional measurement using Alicona InfiniteFocus microscope [9], the dimensions of features on the top surface are measured to be within 5 μm deviations of designed values. From simulations shown in Fig. 5.10, these dimensional deviations can bring up to 0.2 dB difference for insertion loss within passband and ±1 GHz frequency shift for centre frequencies.

Another reason for the deviation of S_{11} is the misalignment during measurement process. As shown in Fig. 5.11, alignment pins go through the 'Key' holes on filter flange and provide precise alignment between filter and test port. However, the diameters for the alignment pins are measured to be 1.56 mm while the CNC milled 'Key' holes on the filter flange are measured to be 1.60 mm. Such dimensional difference gives up to 40 μm misalignment between test port and the filter. Fig. 5.12 shows the comparison of simulation results for 20 μm, 40 μm misalignment and designed values. These simulations show that the maximum 40 μm misalignment that caused by difference between 'Key' holes and alignment pins can bring up to 0.3 dB insertion loss and no frequency shift.

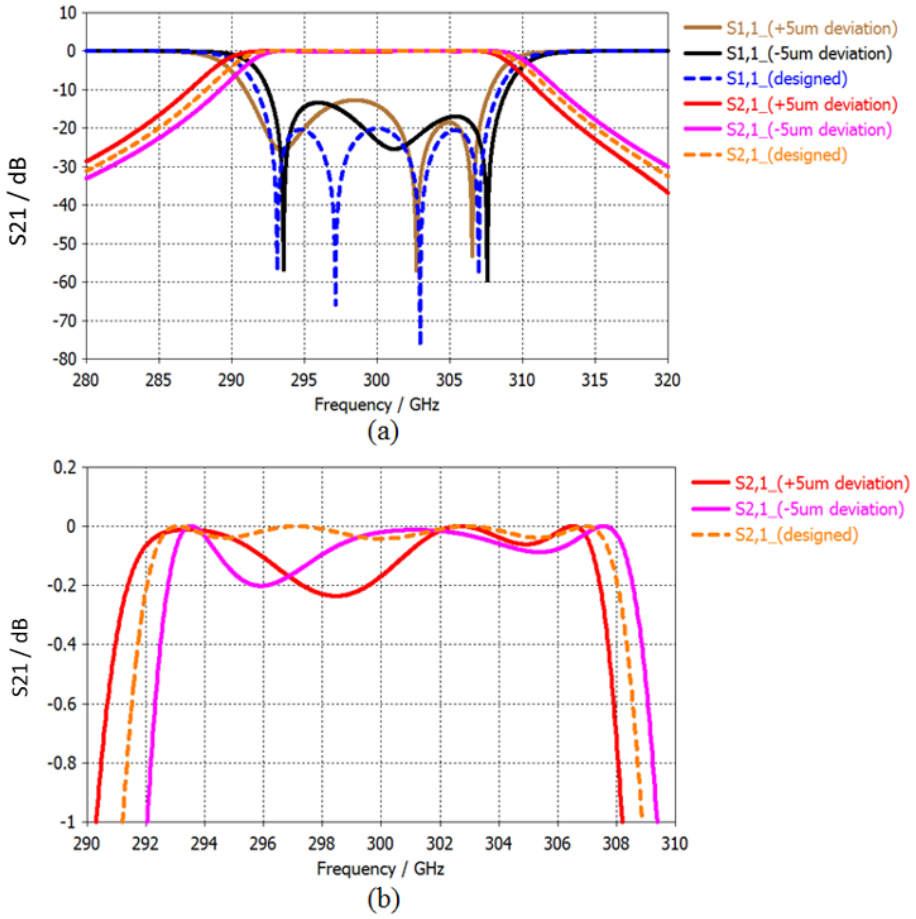

Fig. 5.10 Comparison of simulation results for 5 μm dimensional deviations and designed values

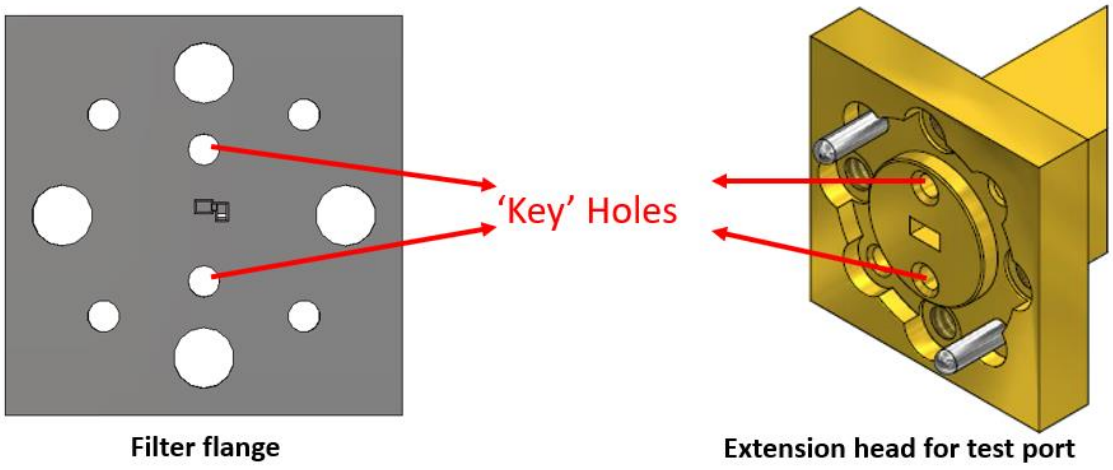

Fig. 5.11 'Key' holes that are used for alignment during measurement process

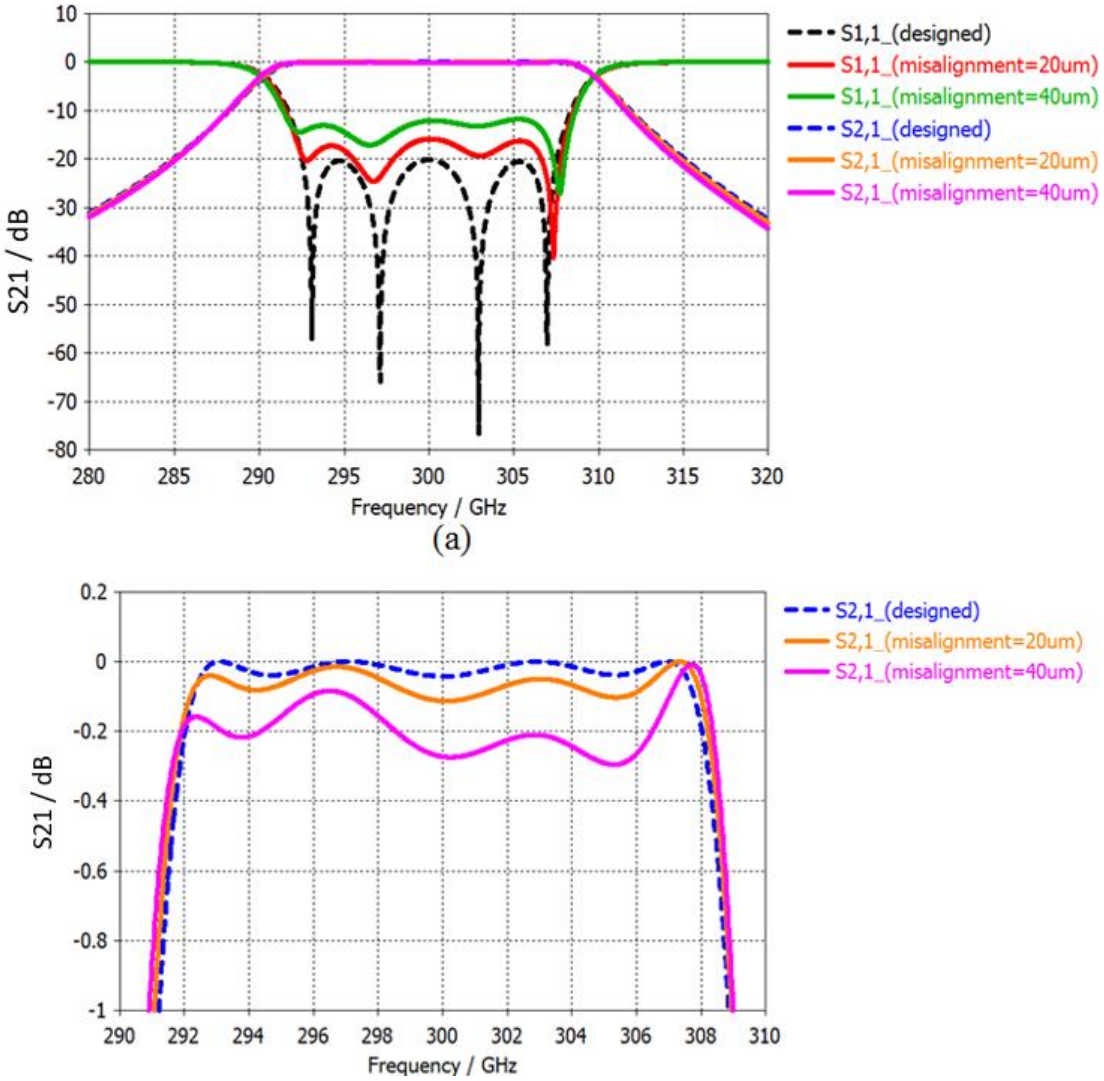

Fig. 5.12 Comparison of simulation results for 20 μm, 40 μm misalignments and designed values

5.3 Laser Machined Filter with Bends

5.3.1 Design process of filter with two H-bends

As discussed in Section 5.2.3, to reduce the energy loss, the design needs to avoid having one wall of the resonators directly connecting to the flange face. The standard rectangular waveguide filter with two H-plane bends is proposed here as an alternative. This waveguide filter designed for laser micromachining is shown in Fig.5.13. The whole structure is composed of four coupled resonators operating in TE_{101} mode and two H-bends. The design method of the filter is based on [11], and it has a Chebyshev response. The filter is designed to have a centre frequency of 300 GHz and a fractional bandwidth of 5%. To meet the specifications, the coupling coefficients between resonators and external Q are calculated to be: $m_{12}= m_{34} = 0.0456$, $m_{23}= 0.035$, $Q_{e1}= Q_{e4}= 18.628$.

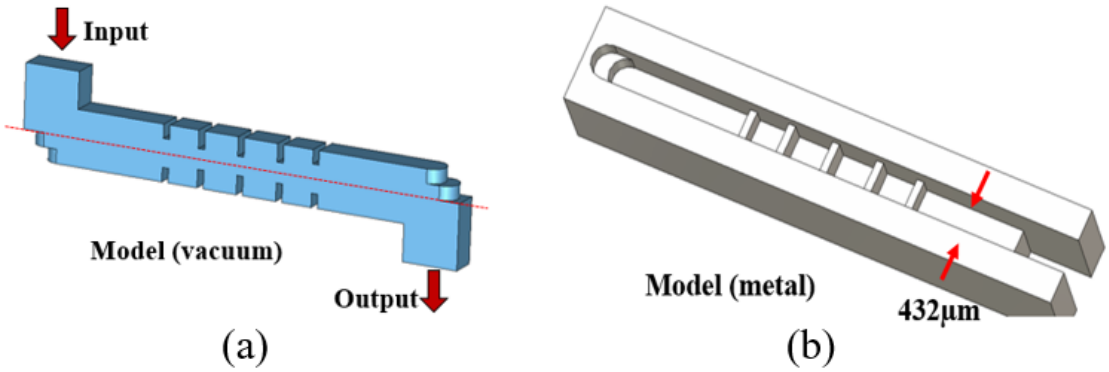

Fig. 5.13 3D model of the WR-3 band waveguide filter using laser micromachining. (a) The vacuum model of the filter device based on four resonators in the middle and two embedded bends directly connected to the first and fourth resonators. The whole structure is split across the red dash line (E-plane). (b) The illustrate of half of the actual metal model of the filter device.

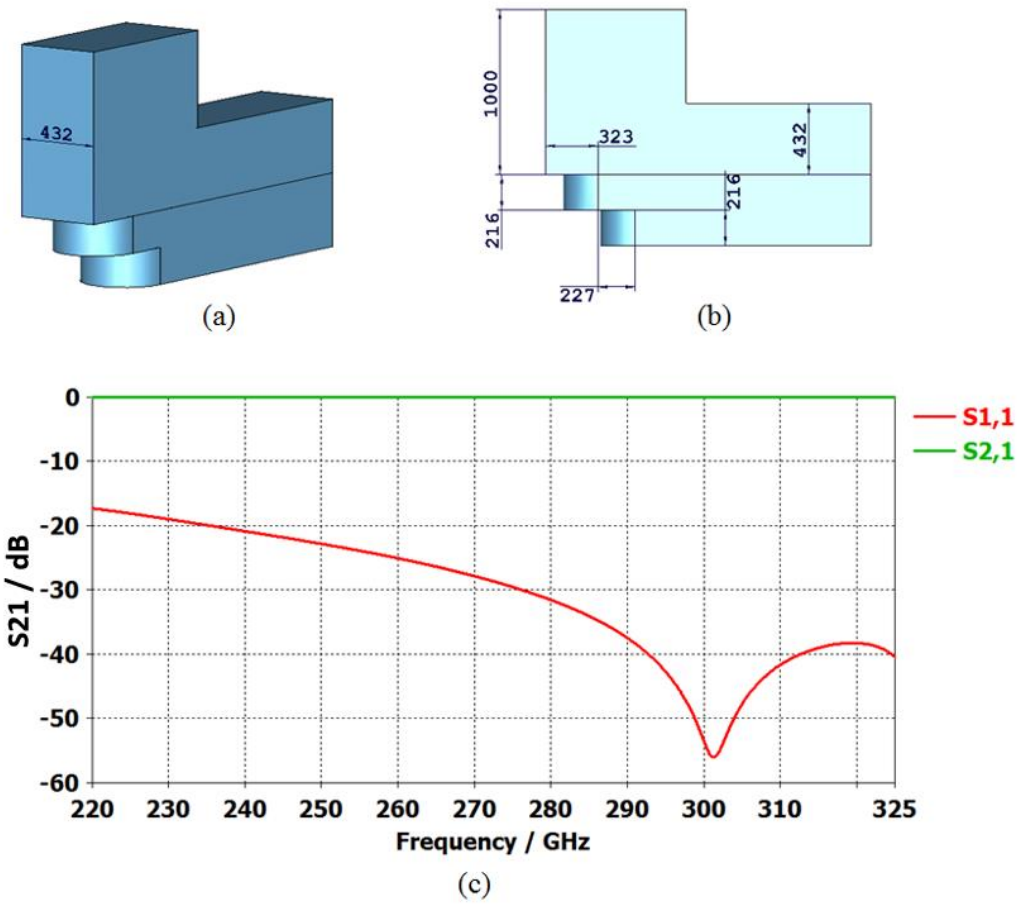

Fig. 5.14 H-bend design for laser micromachining and simulation results. (a) Perspective view of the H-bend (dimensions are in micrometres); (b) Front view and dimensions of the H-bend. (c) Simulation results of the H-bend working at WR-3 band.

Different from the conventional 90º H-bend designs such as multi-stepped corners reported in [12], a specially designed H-plane bend which is compatible with the laser micromachining process is shown in Fig. 5.14. The bend features are designed to achieve a good match across the whole WR-3 band. Similar bend designs have been reported in [13]. The differences are that in [13], the bend is composed of 5 layers using SU-8 technology. But in this work, the bend is only

composed of 2 pieces thanks to that laser micromachining is capable of producing waveguide structures with varying depths (or heights) from one workpiece [10]. The dimensions and features of one bend simulated in CST are shown in Fig. 5.14(a) and (b). One of the bends is added to both the input and output of the standard fourth order Chebyshev waveguide filter to achieve a precise connection with the network analyser. Fig. 5.14 (c) shows the model of the single H-bend and simulated results by CST (version 2016). The simulation results turn out that the design can achieve over 40 dB return loss at passband (292.5-307.5GHz).

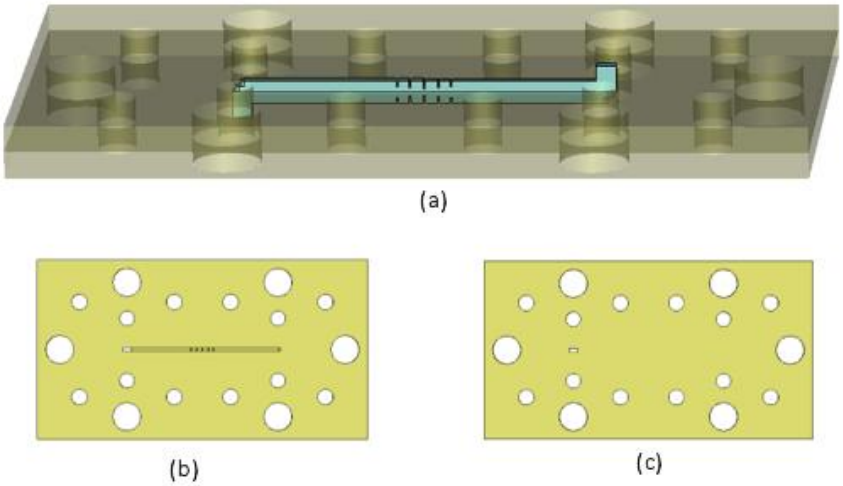

Fig. 5.15 Diagram of the WR-3 band filter based on laser micromachining. (a) Illustration of the filter formed of two 1 mm thick brass plates. The blue structure in the diagram represents the vacuum inside the device. (b) Top view of one brass plate (half of the filter device). (c) Bottom view of one brass plate.

The waveguide is split across E-plane, since the whole structure is symmetrical, each half of the device is fabricated on a 1mm thickness brass plate. As shown in Fig. 5.15 (a), two pieces of the plates consist of the filter structure. In order to provide repeatable connection between the flange and the input/output of the filter and accurate alignment between two micromachined brass plates, alignment pin holes and screw holes are added on the brass plate. The same fabrication process is carried as introduced in Section 5.2.2. The final design of the filter device is shown in Fig. 5.15 and the simulation results of the whole structure including bends are given in Fig. 5.16. The material conductivity is assumed to be the conductivity of brass (i.e. 2.74×10^7 S/m). The simulation of the designed filter gives 0.4 dB average insertion loss and better than 20 dB return loss within the passband.

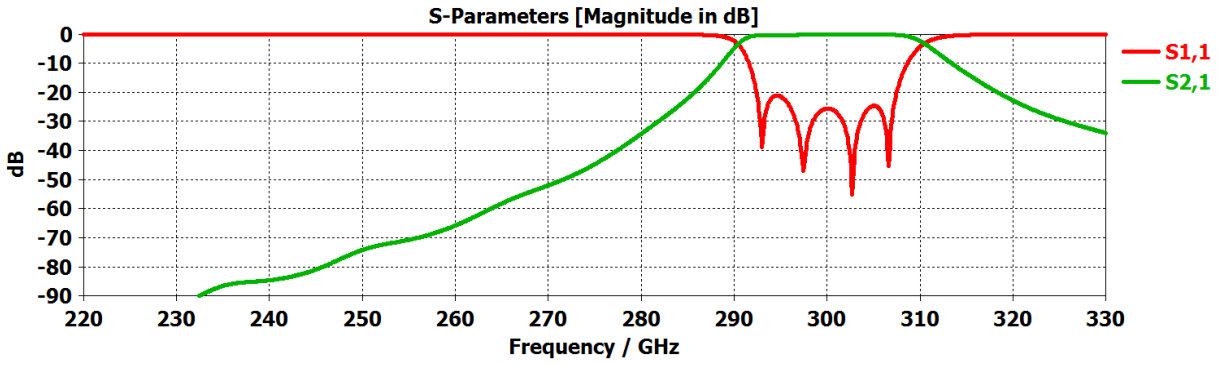

Fig. 5.16 Simulated results of the laser micromachined filter with two H-plane bends.

As a comparison to the double-layer waveguide filter introduced in Section 5.2, simulations for the influence of gaps between test port and filter are also carried on this filter with two H-bends. Fig. 5.17(a) shows the possible gaps that can exist during measurement process. The simulation results of insertion loss for 0 μm, 5 μm and 10 μm gaps are shown in Fig. 5.17(b) and Fig. 5.17 (c). These simulation results show that, by using H-bends to avoid direct coupling between test port and resonators, 10 μm gaps can only bring up to 0.45 dB insertion loss within passband.

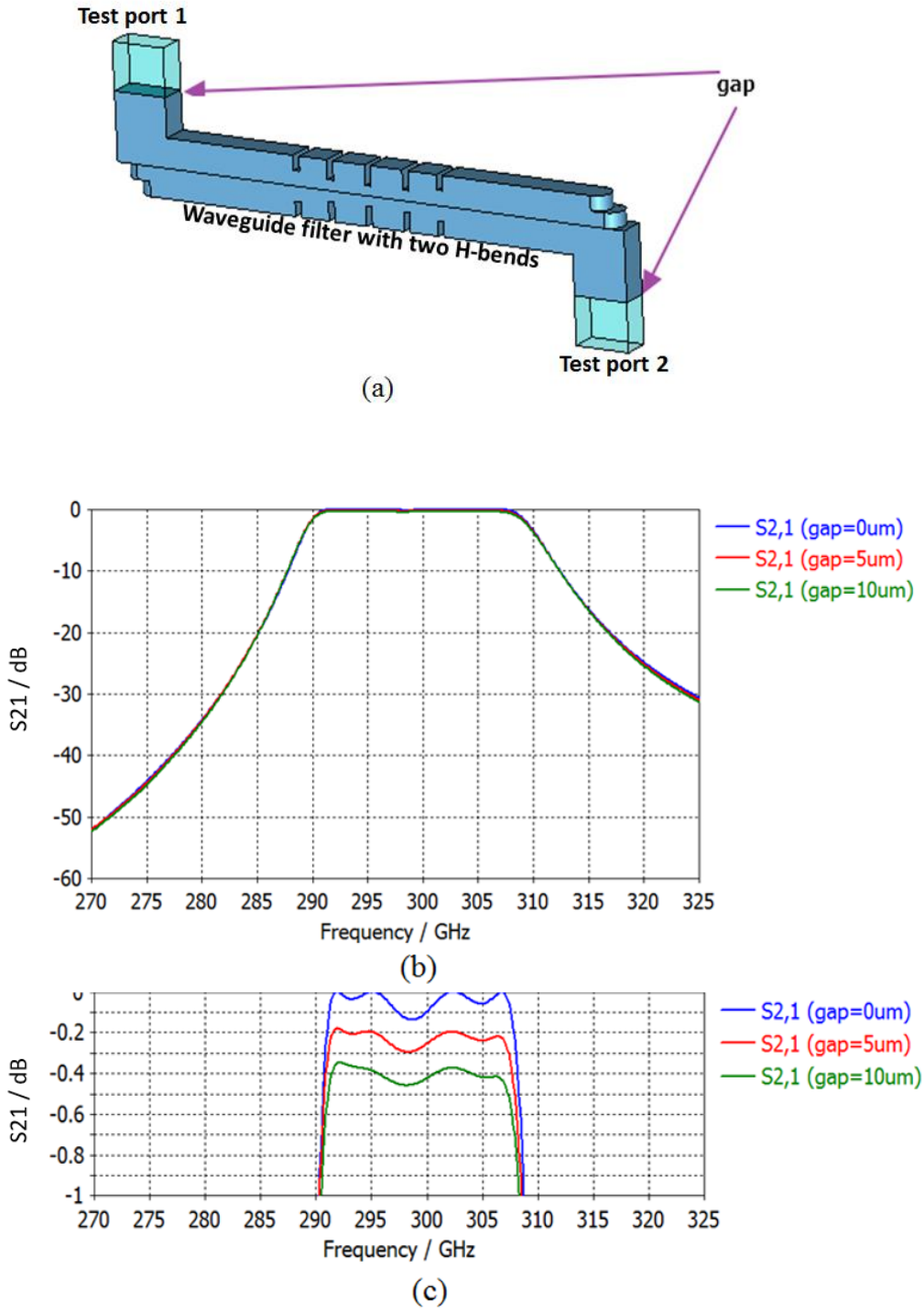

Fig. 5.17 (a) The gaps exist between input/output port and waveguide filter with two H-bends; (b)simulation results of insertion loss for 0 μm, 5 μm and 10 μm gaps; (c) zoom in of the insertion loss within passband (292.5 – 307.5 GHz).

5.3.2 Measurement and Discussion

(a) (b)

Fig. 5.18 (a) Photograph of the laser micromachined filter with two H-plane bends. (b) Measurement setup.

The S-parameter measurements of the filter with bends are performed on an Agilent E8361 Network Analyzer with OML extension modules V03VNA2-T/R and V03VNA2-T (220-325GHz). The return loss at one port has been measured with the other port connected to a load [10]. A short-open-load calibration was performed first. Then the laser micromachined filter, aligned by the alignment pins, and connected to the test ports. Fig. 5.18(a) shows the photograph of laser micromachined filter and the measurement setup is shown in Fig. 5.18(b).

The S-parameter measurement results and simulated results of the laser micromachined filter are shown in Fig. 5.19. There are big deviations between measured results and simulated results: the insertion loss at passband is measured to be around 7 dB and the bandwidth is larger than expected. Moreover, an unexpected peak is shown in S_{21} at 320 GHz, which cause the poor rejection at upper part of the band. As for S_{11} response, the return loss is below 7 dB (while the designed one is below 20 dB). 6 poles are shown within passband as compared with the designed

4 poles. Although laser micromachining utilised in this work gives surface roughness on the order of 1.25 μm, which reduces the effective conductivity to 7.04×10^6 S/m, this only provides around extra 0.3 dB insertion loss within passband according to the simulations. 7 dB return loss within passband corresponds to around 0.8 dB insertation loss. As the simulation results show in Fig. 5.17(c), gaps between filter device and test ports only provide up to 0.45 dB insrtion loss. It is believed the extra 4.5 dB insertion loss are mainly due to the energy loss through the air gap between two brass plates and. Fig. 5.20 shows the simulated S_{21} results for different dimensions of gaps. This simulation indicates that about 10 μm gaps between two brass plates can cause larger than 7 dB insertion loss within passband, meanwhile, as simulated gaps increase to more than 15 μm, the upper stopband response becomes worse.

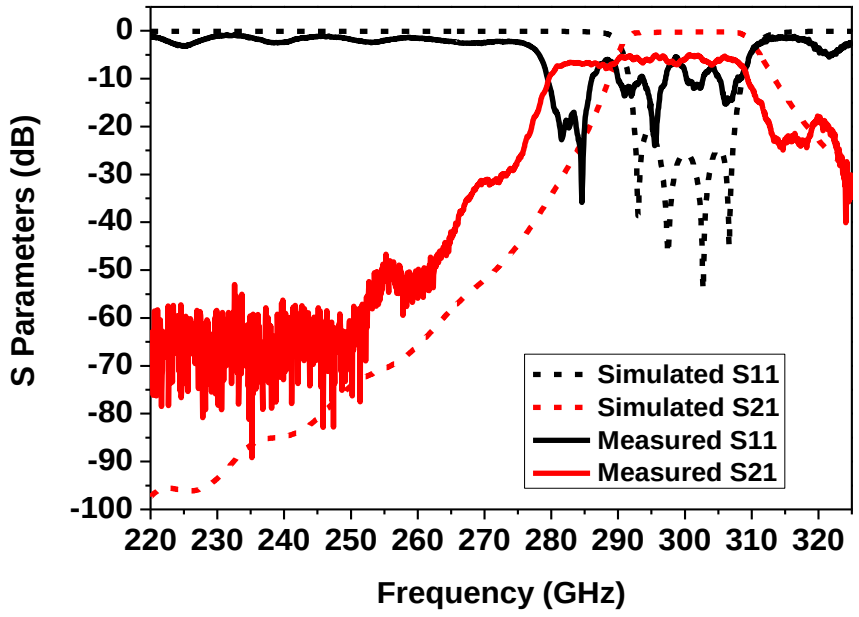

Fig. 5.19 Measurement and simulation results of S-parameters for laser cutting filter with two H-bends

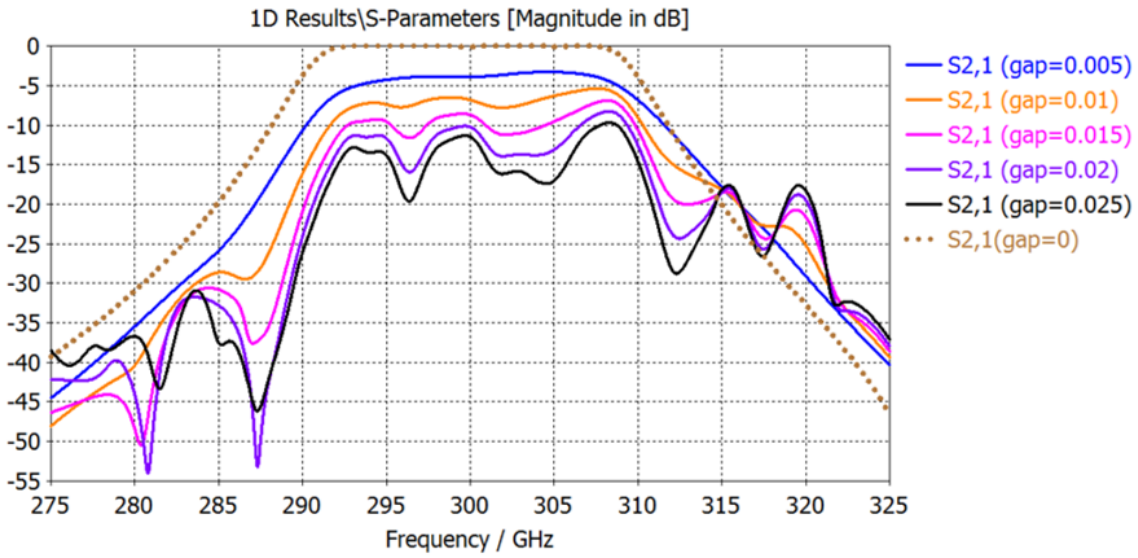

Fig. 5.20 Simulated S_{21} response for gaps ranging from 0 μm to 25 μm

As for the extra poles response in S_{11}, based on further simulations as shown in Fig. 5.21(b), they are considered to be caused by the misalignment, especially rotation of two brass plates. Fig.5.21(a) shows the model that two parts of the filter can have a rotation of certain degrees across the joint face. Fig.5.21(b) presents the simulation results of the filter with 0º, 0.5º and 1º rotation. This simulation shows that such misalignment can result in extra poles for S_{11} within passband and also poor response of rejection for upper stopband.

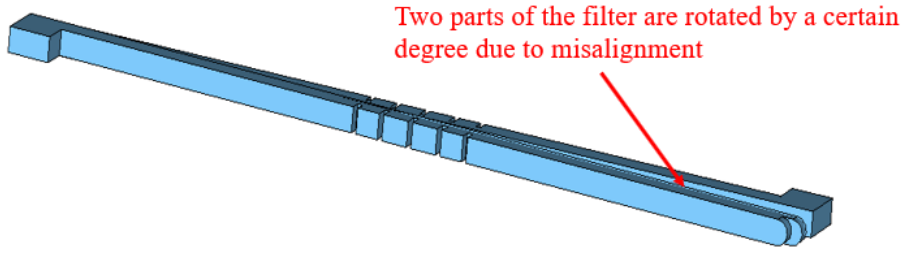

(a)

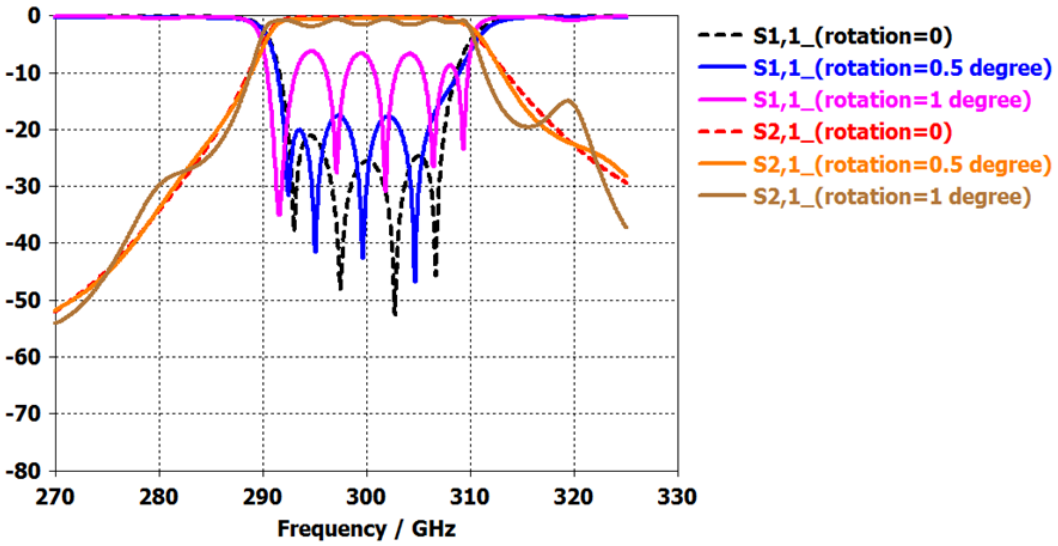

(b)

Fig. 5.21 (a) The rotation of two parts of the filter caused by misalignment during fabricating process. (b) Simulated results of different rotations between two parts of the filter.

To further investigate the deviation between the measurement and simulation results, the 1mm thick brass plate sample is scanned in 3D and then a contour is extracted at different height levels (z level) from the top surface of the plate using Alicona InfiniteFocus microscope [9]. Dimensions for the waveguide filter features are then carefully measured. Fig. 5.22 shows the cross-section of the features that are measured. The designed dimensions and measured dimensions are shown in Table 5.1.

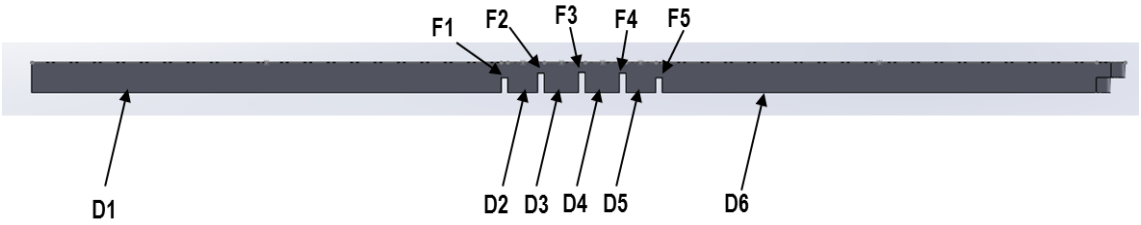

Fig. 5.22 Cross-section of the waveguide filter and features that are measured

Table-5.1 Measured and actual dimensions for the filter features

Parameter	Designed dimensions (mm)	Actual dimensions for Part 1 (mm)	Actual dimensions for Part 2 (mm)
F1 – Height	0.21208	0.209	0.207
F1 – Width	0.1	0.102	0.098
F2 – Height	0.27783	0.27197	0.2695
F2 – Width	0.1	0.134	0.116
F3 – Height	0.28886	0.28023	0.2825
F3 – Width	0.1	0.113	0.111
F4 – Height	0.27783	0.27197	0.2695
F4 – Width	0.1	0.116	0.110
F5 – Height	0.21208	0.209	0.207
F5 – Width	0.1	0.1007	0.085
D1	7.24089	7.2426	7.253
D2	0.46089	0.4433	0.4554
D3	0.53013	0.506	0.517
D4	0.53013	0.5112	0.517
D5	0.46089	0.4521	0.4557
D6	7.13396	7.1519	7.1687
Width of channel (1)	0.432	0.426	0.423
Width of channel (2)	0.432	0.428	0.426
Depth of channel (1)	0.432	0.426	0.424
Depth of channel (2)	0.432	0.432	0.430
Port- Length	0.864	0.891	0.88
Port- Width	0.432	0.422	0.431
Volume (mm^3)	3.06	2.86	2.87

To work out the rotational error during the fabraction process, the top surface of the sample is inspected. By using the position of the alignment holes, the rotation of the waveguide filter feature is defined. Fig. 5.23 shows the results for the positional accuracy of the waveguide channel in respect to the four alignment holes. From the measurement, the angle differences are 0.851º and

0.058º in respect to the alignment holes for the two plates respectively. From these results we can calculate the rotation exist between two parts of the filter to be: 0.851-0.058=0.793 degrees.

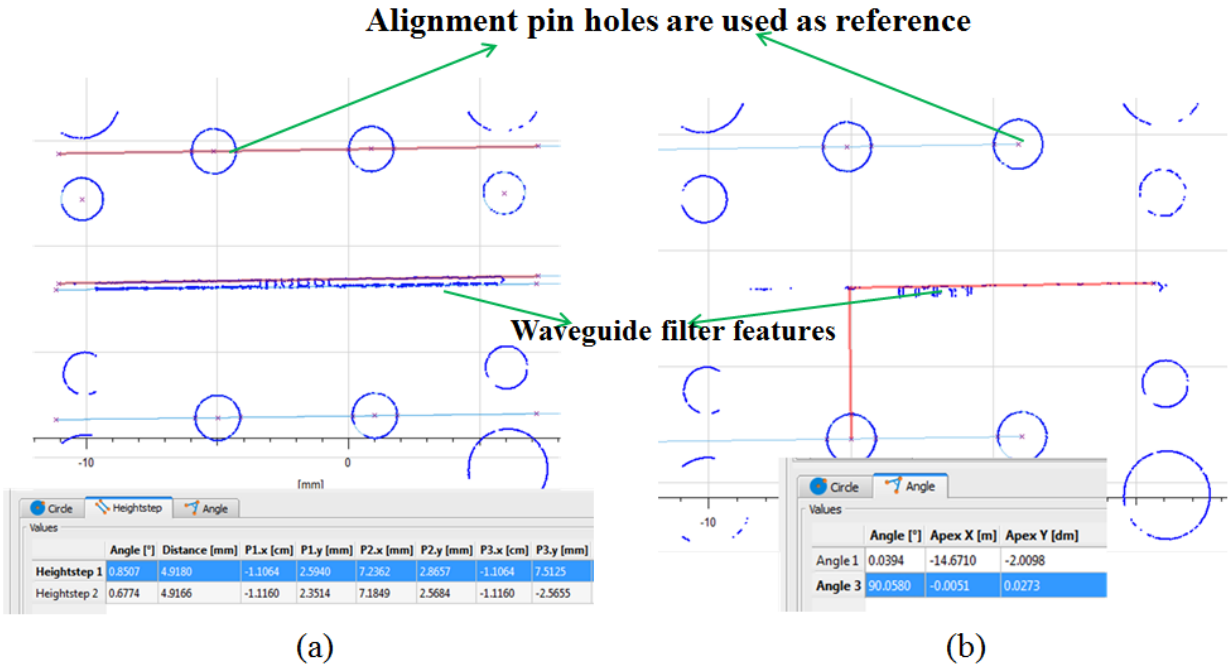

(a) (b)

Fig. 5.23 Results for the positional accuracy of the waveguide channel in respect to the four alignment holes on (a) brass plate 1 and (b) brass plate 2.

By using the actual measured dimensions and rotation in the simulation from the comparison of measurements and simulations shown in Fig.5.18, regardless of energy loss within passband, we can see that the S_{21} response shape of simulation with dimensional error and rotation can roughly match the measured results.

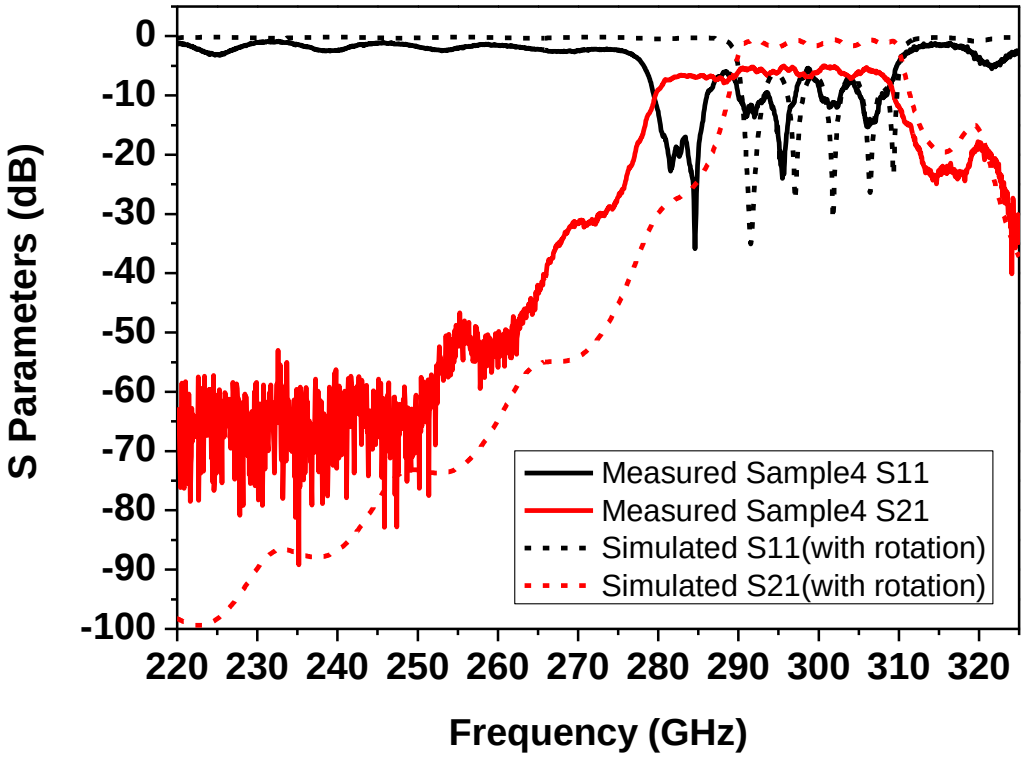

Fig. 5.24. Comparison between simulated results using measured dimensions with rotation and actual measured results of the sample

5.3.3 Improvements for the process

From the analysis presented in Section 5.3.2, two things can be done to improve the performance of the filter: (i) optimising the alignment during fabricating process to get rid of rotation between two plates; (ii) increasing the flatness for the joint surface of two brass plates to reduce the gaps between two halves.

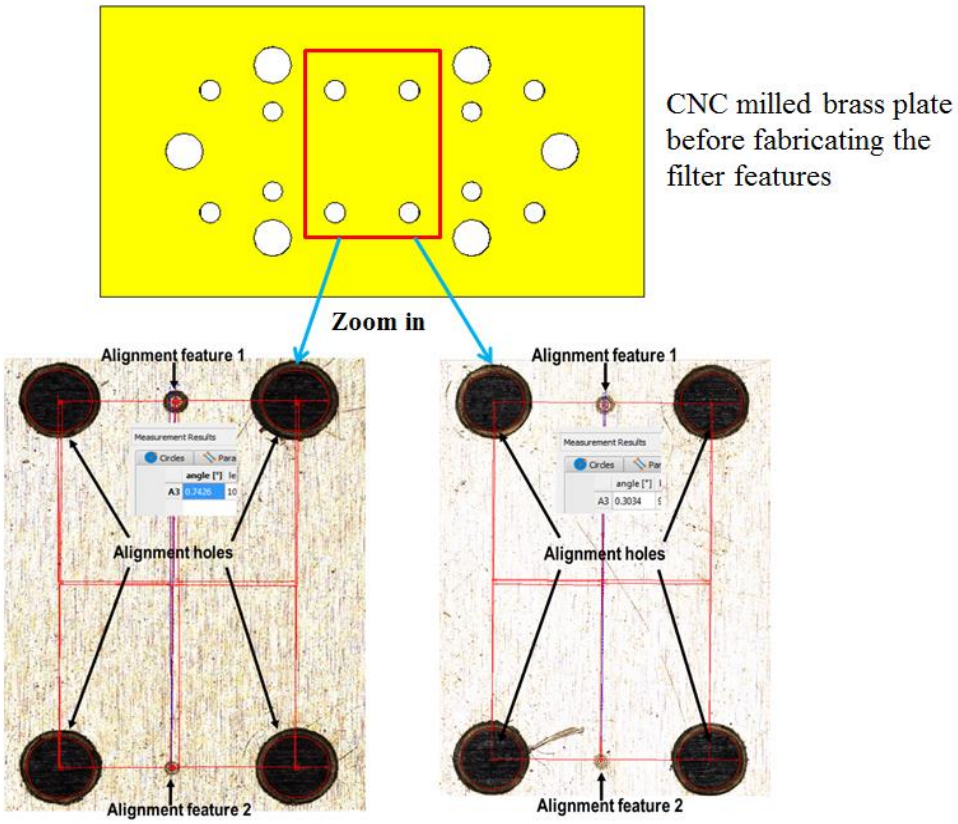

Fig. 5.25. Rotational deviation of the two alignment features in respect to the four alignment holes on two brass plate.

Before fabricating the operating features of the filter, inspections are carried on the CNC milled brass plates using Alicona Infinite Focus microscope system. This time two extra alignment features were added as during CNC process for better alignment in later steps. A photograph of the new CNC milled brass plates is shown in Fig. 5.25.

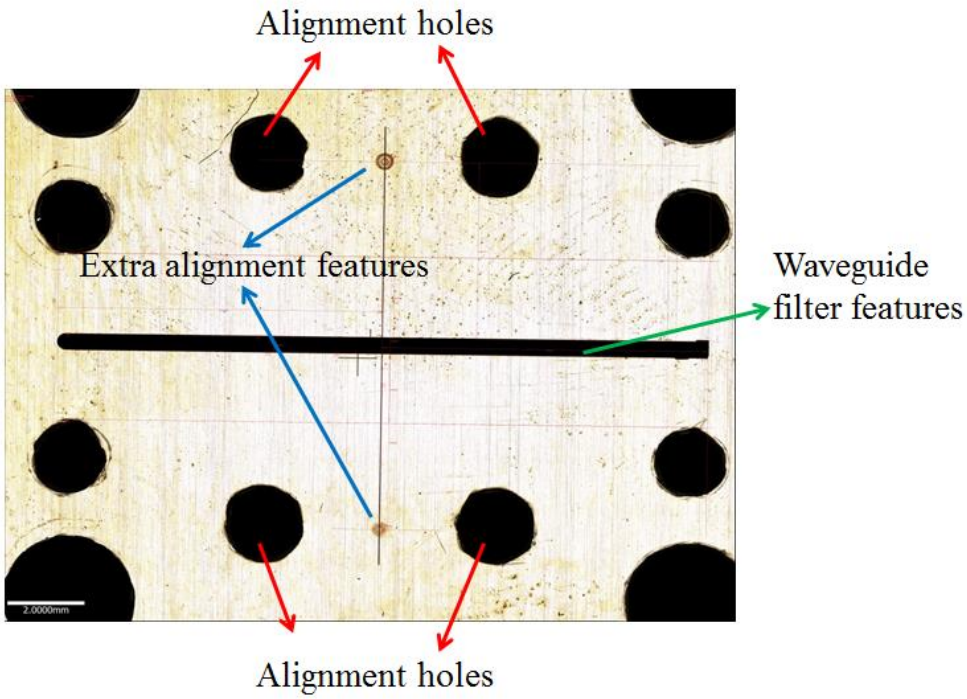

Fig. 5.26 Functional filter features fabricated after re-alignment using alignment features.

From Fig. 5.25, the poor CNC process gives 0.75 and 0.3 degree deviations on two plates between alignment pin holes and alignment features. Obviously, this gives misalignment during fabrication affecting the filter features. So during the fabrication of the next sample, the alignment for each plate is adjusted in order to compensate the deviations caused by CNC milling process. The fabricated filter is shown in Fig. 5.26, from the measurement it still present around 0.2 degree rotation between two plates. This is still due to the alignment error caused by poor positioning of alignment holes fabricated by CNC milling even with the extra effort and is a limitation of the workshop.

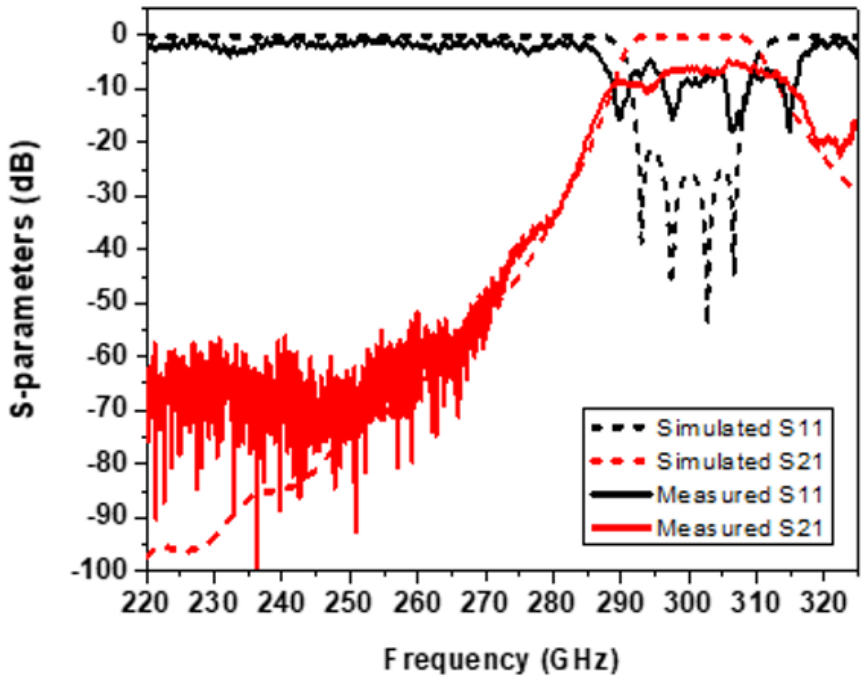

Fig. 5.27 Measurement results of S-parameters for laser cutting filter with two H-bends after re-alignment and polishing vs. simulated results.

To increase the flatness of the interface between two brass plates, the surface of the sample is polished and then the whole device is assembled and measured again. The results is shown in Fig. 5.27. Compared with previous sample, the problems of frequency shift and extra poles within passband have been solved. However, the insertion loss within passband is still around 7 dB, which means the energy loss between two brass plates is still the problem. As shown in Fig. 5.28, the loss factor is included to compare the measurement results of two samples and it can be calculated using equation (5.1) [14]

$$\text{loss factor(dB)} = 20 \cdot \log_{10}(\sqrt{|S_{11}|^2 + |S_{12}|^2}) \qquad (5.1)$$

For a lossless circuit the loss factor is 0 dB. Compared with insertion loss, the loss factor is able

to show the loss of the circuit more accurately since it also contains the effect of the return loss [14]. By comparing the loss factors before and after re-alignment and polishing process with the simulation results of the designed model, we can work out if the performance has been improved by correcting the error in alignment and polishing the surfaces of the interface. From the calculated loss factors shown in Fig. 5.28, the average loss has been improved by about 0.5 dB and the frequency shift has been corrected after re-alignment and polishing process. However, compared to simulation results of the designed filter, these works didn't have significant improvements on reducing the energy loss.

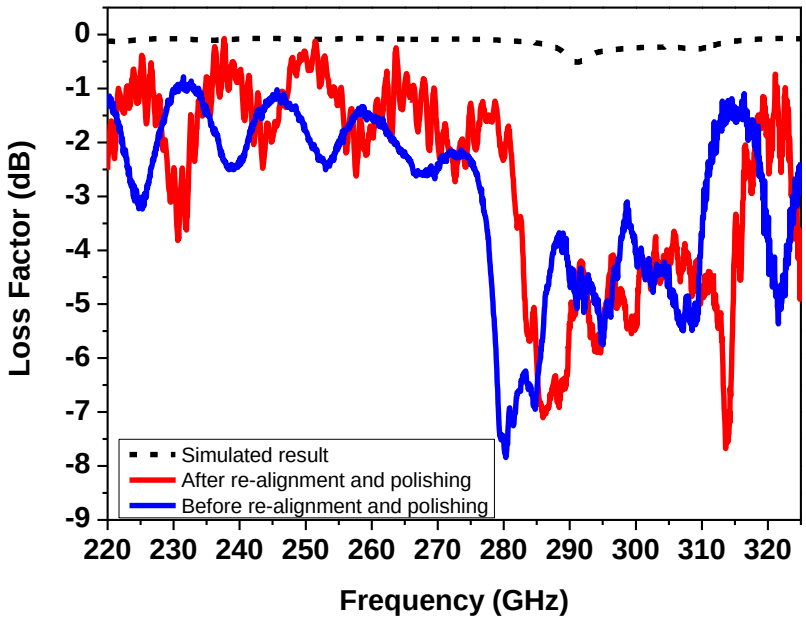

Fig. 5.28 Loss factor calculation for two samples before and after re-alignment and polishing.

5.4 Conclusions

This chapter has described the details of the laser micromachining process and presents two laser cutting waveguide filters with Chebyshev response. Both filters were specially designed to take the advantage of the laser micromachining process. The standard steps of laser micromachining were also optimised accordingly in order to reduce the fabrication errors and improve the performance of the filters. Although the performance of the two filters is not very good (i.e. 5 dB insertion loss within passband for the double-layer filter and 7 dB insertion loss for the filter with two H-bends), these works show the potential of the laser micromachining for WR-3 band or higher frequency waveguide circuits.

According to the state of art on laser micromachining process, it is capable of achieving a tolerance within 10 μm [10]. As laser micromachining process developing, the tolerance can be improved considerably over time. This is a novel technology with great potential for the fabrication of terahertz devices. State-of-the-art high precision CNC milling (e.g. Kern milling machine from Rutherford Appleton Laboratory) can achieve slightly tighter tolerance; however, it also has drawbacks such as very expensive milling machines, as well as the abrasion of cutters, limitations of small cuter size, and generation of defects and cracks due to mechanical stresses [10]. From this point of view, laser micromachining can be a promising alternative.

In the future work for laser micromachined waveguide filters, there are a few things that could be done to improve the performance. Firstly, better alignment can be achieved by using laser cutting instead of CNC milling to fabricate the key alignment holes, although this may increase the total time spent on laser cutting process. Secondly, for both filters presented in this chapter, brass plate (conductivity = 1.59×10^7 S/m) with 1mm thickness is selected as the fabrication

material due to its good CNC machinability. In the future experiments, fabricating the same design using copper (conductivity = 5.81×10^7 S/m) workpieces on the proposed manufacturing platform or plating silver (conductivity = 6.30×10^7 S/m) on the surface of the operating structures can improve the performance in terms of insertion loss. The only difference is that for the first solution the laser parameters will need to be adjusted slightly in order to deal with a different material. For the second solution, a specially designed coating process is required. In addition, the surface roughness for laser cutting features can be further improved by optimising laser parameters settings, such as pulse repetition rates and beam spot diameters. By using proper laser parameters, silicon can also be an alternative fabricating material and achieving roughness on the order of 200 nm [15] after optimised process. For the filter with two H-bends, in order to further investigate the energy loss between two plates, a straight-through waveguide with same total length with the filter and same H-bends can be fabricated as a comparison. Another improvement that could be done is on the CNC milled brass plates. Creating high pressure area between interfaces (e.g. between test ports and first/forth resonators for double-layer filter) could be a good potential solution for reducing gaps which are the main reason for the energy loss.

References:

[1] X. Shang *et al*., "W-Band Waveguide Filters Fabricated by Laser Micromachining and 3-D Printing," *IEEE Transactions on Microwave Theory and Techniques*, vol. 64, no. 8, pp. 2572-2580, Aug. 2016.

[2] C. K. Walker, G. Narayanan, H. Knoepfle, J. Capara, J. Glenn, and A. Hungerford, "Laser micromachining of silicon: A new technique for fabricating high quality terahertz waveguide components," *Proc. 8th Int. Symp. Space THz Technol.*, Cambridge, MA, USA, Mar. 1997, pp. 358–376.

[3] P. Penchev, S. Dimov, D. Bhaduri, *et al*, "Generic integration tools for reconfigurable laser micromachining systems," *J. Manuf. Syst*., 2016, **38**, pp. 27-45.

[4]P. Penchev, X. Shang, S. Dimov, *et al*., "Novel manufacturing route for scale up production of terahertz technology devices," *ASME Journal of Micro- and Nano-Manufacturing*, 2016, **4**, pp. 021002-021002-14

[5] S. Dimov, *et al.*, "Micro- and nanomanufacturing: challenges and opportunities," *Proc IMechE Part C: J Mech Eng Sci.* 2012, 226: pp. 3–15.

[6] B. Liu, H. Yang, and M. J. Lancaster. "Global Optimisation of Microwave Filters Based on a Surrogate Model-Assisted Evolutionary Algorithm." *IEEE Trans. Microw. Theory Techn.*, vol. 65, no. 6, pp. 1976-1985, Jun. 2017.

[7]X. Liao, L. Wan, Y. Yin, *et al*., "W-band low-loss bandpass filter using rectangular resonant cavities', *IET Microw. Antennas Propag.*, 2014, **8**, (15), pp.1440-1444

[8]X. Shang, M. Ke, Y. Wang, *et al*., "Micromachined W-band waveguide and filter with two embedded H-plane bends," *IET Microw. Antennas Propag.*, 2011, **5**, (3), pp.334-339

[9] Laser Processing Group, Mech Eng, University of Birmingham. "The description of the laser

micro processing platform in the Mech Eng Laser Lab".

[10] X. Shang, H. Yang, D. Glynn and M. J. Lancaster, "Submillimeter-wave waveguide filters fabricated by SU-8 process and laser micromachining," in *IET Microwaves, Antennas & Propagation*, vol. 11, no. 14, pp. 2027-2034, Nov. 2017. (SCI)

[11] J. Hong and M. J. Lancaster, *Microstrip Filters for RF/Microwave Applications.* New York: Wiley, 2001.

[12] A. R. Kerr, "Elements for E-plane Split-Block Waveguide Circuits," ALMA Memo 381

[13] X. Shang, M. Ke, Y. Wang and M. J. Lancaster, "WR-3 Band Waveguides and Filters Fabricated Using SU8 Photoresist Micromachining Technology," *IEEE Transactions on Terahertz Science and Technology*, vol. 2, no. 6, pp. 629-637, Nov. 2012.

[14] D. M. Pozar, *Microwave Engineering*, New York, USA: Wiley, 2005

[15]B. Voisiat, A. Bičiūnas, I. Kašalynas, *et al.*, "Band-pass filters for THz spectral range fabricated by laser ablation," *Appl. Phys. A*, 2011, **104**, (3), pp.953–958

Chapter 6

Conclusions and Future Work

6.1 Conclusions

This thesis has looked into the design and fabrication of terahertz waveguide filters. Micromachining techniques employed for the fabrication of terahertz circuits, especially waveguide filters, have been reviewed. A series of terahertz waveguide devices have been specially designed to take advantage of their fabrication process and presented as examples.

Coupling matrix representation for the resonator-based filters and the characteristic for the rectangular waveguides, cavity resonators and coupling iris are introduced as the background theories for waveguide filter design [1]. The methods of extracting physical dimensions from coupling matrix elements [2] are explained and a 3rd order Chebyshev waveguide filter design example is given.

A general review of micromachining techniques for terahertz waveguide circuits such as CNC machining, DRIE process, LIGA process, SU-8 photoresist technology, laser micromachining and 3-D printing, has been presented. The current state-of-the-art of fabrication process for these micromachining techniques have been discussed and compared. Among these techniques, CNC machining is a conventional fabrication process employed in relatively low terahertz (0.1-0.3 THz) applications. DRIE process and LIGA process are mature processes which have been looked into by many researchers and already been applied in the fabrication of high frequencies (up to 1 THz) waveguide circuits. The 3-D printing, is a promising technique to fabricate low terahertz circuits. With the further development of this novel manufacturing process, 3-D printing has great potential of applications at higher frequencies. With great potential of employed in terahertz applications

and achievable resources, the SU-8 photoresist technology and laser micromachining processes have been researched in the University of Birmingham for many years, and have been utilised to produce a series of waveguide devices in EDT group for terahertz applications [3]. One SU-8 made filter and two laser machined filters operating at WR-3 band have been described as examples presented in Chapter 4 and Chapter 5.

A CNC milled waveguide filter and a SU-8 micromachined filter working in WR-3 band have been successfully designed to fulfill demanding specification of low insertion loss within passband and high rejection of upper stopband. This is achieved by using extracted pole design for the CNC machined filter and employing cross-coupling structures for the SU-8 based filter. Both filter designs have taken the advantages of the characteristics of the machining processes to minimize the fabrication errors. It is the first demonstration with the best measured performance that a CNC milled filter with a steep rejection characteristic beyond 300 GHz and a SU-8 micromachined filter with novel cross-coupling topology working at WR-3 band [4]. Apart from the frequency shift of passband, the measured performance of the filters is in good agreement with the simulations of the designed models. By measuring the dimensions of the fabricated filters using a scanning electron microscope (SEM), it is found that the deviation between measurements and simulations are caused by small errors in manufacturing. The two filters show no significant difference in performance despite the two alternative fabrication processes and designs. Either of these two micromachined waveguide filters can be potential replacements of FSS filters used in spaceborne radiometers for unwanted sideband rejection with more compact size and less weight [4].These two terahertz waveguide filters with reasonable performances presented in this work give one solution of employing high precision CNC milling process and SU-8 photoresist techniques in the fabrication of terahertz circuits with demanding specifications.

Two 4th order Chebyshev waveguide filter operating at WR-3 band based on laser micromachining with novel topologies are designed, fabricated and measured. This work is an extend of researches reported in [5]. Both filters are specially designed to take the advantage of the laser micromachining process. In return, the laser micromachining process is also adjusted and optimised accordingly in order to reduce the fabrication errors and improve the performance of the filters. For the measurement results, the double layer filter gives 5 dB insertion loss within passband while the filter with two H-bends provides 7 dB insertion loss. The lower insertion loss for the first filter is mainly contributed by the gaps between the filter and waveguide flanges, whereas for the second filter, the gaps between the joints of two pieces of the filter is the main reason of the energy loss. Note that laser cutting is currently a novel process utilised in the fabrication of microstructures, the dimensional accuracy of this technique is expected to grow fast over time. This work shows the potential of applying laser micromachining in the fabrication of waveguide circuits operating at WR-3 band or higher frequency.

Table-6.1 summarises the comparison of these three micromachining processes in terms of accuracy, the assembling and measurement process, cost and major difficulties encountered in the application of fabricating terahertz waveguide filters.

Among these three techniques, the SU-8 process is more mature in terahertz applications and has demonstrated filters up to 700 GHz [3]. The CNC milling is a conventional method of fabricating waveguide components with relatively low frequencies, but the limits of this technique have been pushed by the researchers. The laser micromachining process is relatively new but the expectation of it producing viable circuits is high. The potential of all these techniques for the production of terahertz waveguide components has been demonstrated.

Table-6.1 Comparison of CNC machining, SU-8 process and laser micromachining

Micromachining process	Best accuracy can achieve	Assembling & measurement	Major difficulties	Cost
High precision CNC milling	1-2μm (minimum structures can be no smaller than the diameter of the driller)	Flange can be designed freely	1. Design should consider the miller 2. Alignment of split block 3. High frequency applications requires small miller with high precision 4. Depth of cut is limited to about 3 times of the cutter diameter	Depends on the process, high frequency device may cost a lot due to the requirement to expensive millers
SU-8 photoresist technology	2μm accuracy has been reported in literature. Accuracy of 5μm can be achieved in the lab at University of Birmingham.	Can be tested directly	1. Alignment 2. Thickness need optimisation	1.Mask cost over 200 pounds 2. Process is time consuming
Laser micromachining	Tolerance within 10 μm	Need to cut on CNC fabricated plate to feed the flange	1. Alignment (horizon& rotation) 2. Dimensions with curves are inaccurate 3. The bottom of waveguide are rough due to the process	1. Fabricated materials cost Low (brass plate) 2. High precision laser cutting system may cost a lot, but the fabrication process doesn't cost too much

6.2 Future Work

The work on CNC milled filters can be further pushed to higher frequencies. More effort could be put on the investigation of the design of waveguide structures with reduced aspect ratio and other kinds of extracted pole topologies which can provide stronger rejection for unwanted

sideband. As for the work of filters based on SU-8 technology, further work could be carried out on: (i) investigation of improvements on the fabricating process (e.g. precisely control of UV exposure time) to provide SU-8 devices with better dimensional accuracy; (ii) research of possible mechanically tuning method for SU-8 terahertz waveguide circuits; (iii) investigation of multi-layer process for SU-8 process to get rid of the problem of misalignment and reduce the energy loss through gaps between different layers; (iv) metallisation process could be further optimised to improve the coverage of coated material on the sidewalls.

For the work of terahertz waveguide filters based on laser micromachining, there are a few things that could be done to improve the device performance. Firstly, to improve the alignment during measurement, the flange needs to be machined with high precision CNC drilling process, otherwise the alignment pin holes should be fabricated using same process with the filter features in the same coordinate axis. Secondly, to reduce the energy loss through gaps, high pressure area should be created on the filter flanges to ensure better contact and less gaps between operating filter structures. This could be also realised by employing choke-ring designs on the filter flange. Finally, research could be carried out to employing laser cutting in different materials such as copper (which provide with better conductivity) or silicon (with potential of higher dimensional accuracy). Note that to fabricate different materials using laser cutting, laser systems with different frequencies and power densities may be required [6].

Reference:

[1] R. J. Cameron, C. M. Kudsia, R.R. Mansour, *Microwave Filters for Communication Systems: Fundamentals, Design and Applications.* Hoboken, NJ, USA: Wiley, 2007.

[2] J. Hong and M. J. Lancaster, *Microstrip Filters for RF/Microwave Applications*. New York: Wiley, 2001.

[3] X. Shang, H. Yang, D. Glynn, M. J. Lancaster. "Submillimeter-wave waveguide filters fabricated by SU-8 process and laser micromachining" *IET Microw., Antennas Propag.*, vol. 11, no. 14, pp. 2027-2034, Nov. 2017.

[4] H. Yang, Y. Dhayalan, X. Shang, M. J. Lancaster, *et al*, "WR-3 waveguide filter based on high precision CNC milling and SU-8 photoresist technology," *IEEE Trans. THz Sci. Technol*., vol. 8, no. 1, pp. 100-107, Jan. 2018.

[5] X. Shang *et al*., "W-Band Waveguide Filters Fabricated by Laser Micromachining and 3-D Printing," *IEEE Transactions on Microwave Theory and Techniques*, vol. 64, no. 8, pp. 2572-2580, Aug. 2016.

[6] P. Penchev, S. Dimov, D. Bhaduri, *et al*., "Generic integration tools for reconfigurable laser micromachining systems," *J. Manuf. Syst*., 2016, **38**, pp. 27-45.

Appendix I

Optimisation for Filters and Diplexers

One of the key steps for the design of millimetre-wave or terahertz waveguide filters is the model-based optimisation process. To simulate the responses of a candidate filter design, the equivalent circuit model and the full-wave electromagnetic (EM) model are often employed [1]. Fig. A.1 illstrates the model-based optimisation process. For the equivalent circuit model, it is often computationally cheap but with insufficient accuracy, while the full-wave EM model is often accurate but computationally expensive [2]. Since millimetre-wave or terahertz waveguide circuits are very sensitive to the physical dimensions (e.g. resonator length, dimensions for coupling iris), high accuracy results are often required for the simulations [3]. In this appendix we discuss optimisation based on full-wave EM model simulations it is based on collaborative work with Dr Bo Liu at the University of Glyndwr and has resulted in joint publications [2].

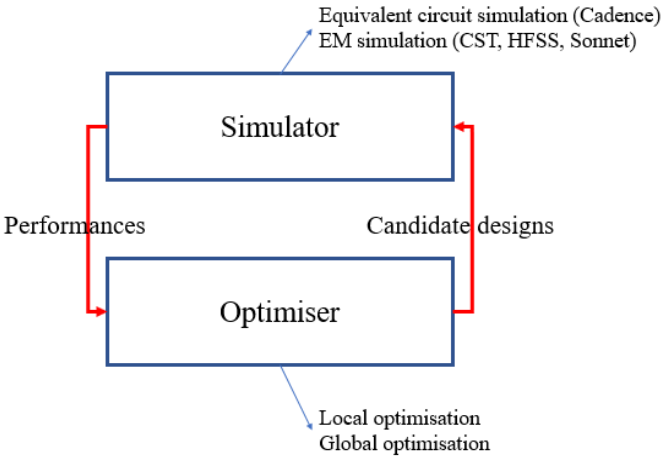

Fig. A.1 Model-based optimisation process

Local optimisation is a routine approach for full wave optimisation of microwave or terahertz waveguide filters. This method can be a good choice where the initial dimensions of the candidate

design is near to the optimal region. For the filters with simple topology and less variables, such as the laser micromachined filter with two H-bends and the CNC milled extracted pole filter presented in this thesis, the routine design process is: (i) calculate the coupling matrix representation from filter specifications; (ii) extract initial physical dimensions from coupling matrix elements; (iii) apply initial dimensions in full-wave EM model; (iv) final optimise the dimensions using local optimisation.

However, for more complex filter designs (i.e. complex topology and more variables), the local optimisation process can meet insoluble problems such as numerous local optima or the initial design is not near to the optimal region. Under such situations, the success rate of the local optimisation may not be high. Traditional global optimisation techniques are able to achieve a high success rate for such problems, but are often time consuming and computationally expensive considering the cost of full-wave electromagnetic simulations [2].

To address the above challenges, a new method, called surrogate model-assisted evolutionary algorithm for filter optimisation (SMEAFO), has been proposed by Bo Liu in [2]. In SMEAFO, considering the characteristics of filter design landscapes, Gaussian process surrogate modelling, differential evolution operators, and Gaussian local search are organised in a particular way to balance the exploration ability and the surrogate model quality, so as to obtain high-quality results in an efficient manner [2]. Experiments show that SMEAFO is able to obtain designs with high accuracy comparable with global optimisation techniques but within a reasonable amount of time. Two practical filter examples and one diplexer example, which do not appear to be solvable by popular local optimisation techniques are solved efficiently by the SMEAFO. These examples are given in the following sections. The SMEAFO-based filter design optimisation tool can be downloaded from http://fde.cadescenter.com.

Example 1: A 3rd order Chebyshev filter with cross-coupling

As shown in Fig. A.2, this example is a cross-coupled waveguide filter operating at WR-3 band, which is presented in Chapter 4 and optimised using SMEAFO method. This filter has demanding specifications for the insertion loss within passband and rejection for unwanted sideband. Local optimisation failed with the optimisation for this filter. One possible reason for the failure can be the extremely narrow optimal region.

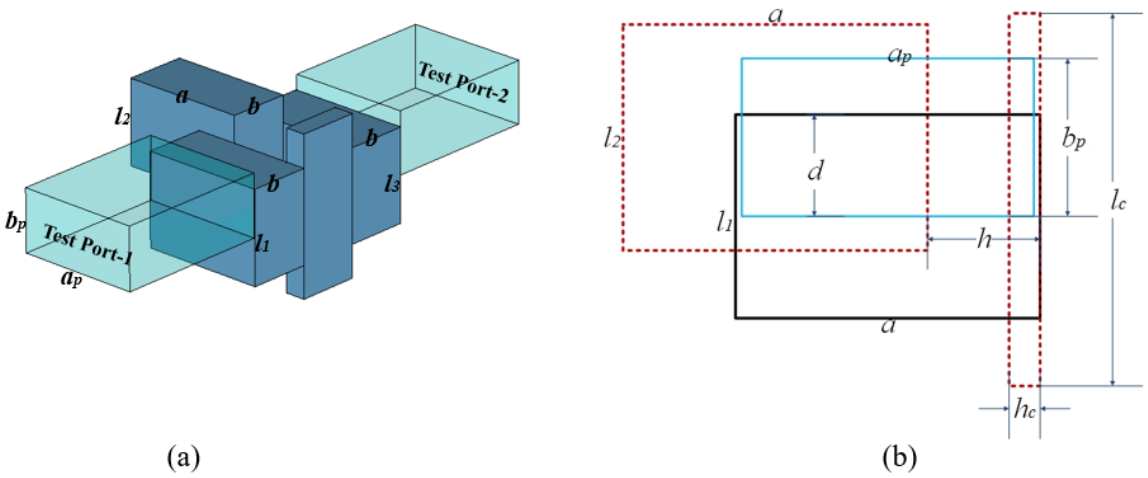

Fig. A.2 A 3rd order Chebyshev filter with cross-coupling. (a) 3-D model of the filter simulated in CST. (b) Perspective front-view of the filter structure with important dimensions. a_p=0.864 mm, b_p=0.432 mm (dimensions for input/output ports).

The design specifications are that the passband is 287.7-295.9 GHz (8.2 GHz passband centred at 291.8 GHz) with maximum return loss of - 20 dB (max|S_{11}| within the passband should be at least less than -20 dB and is as smaller as possible). The unwanted sideband is 317.7-325 GHz with better than 30 dB rejection (max|S_{21}| should be less than -30 dB). Therefore, the optimisation problem is formulated as:

$\max(|S_{11}|) \leq$ -20 dB, 287.7-295.9 GHz

$\max(|S_{21}|) \leq$ -30 dB, 317.7-325 GHz

The ranges of design variables are in Table-A.1. From the filter topology and 3-D structures, we need to define the upper and lower boundaries for the filter dimensions (variables). This is very important since wrong boundaries for parameters can lead to no physical realisation for the 3-D model and may ruin the whole optimisation process. The initial dimensions for the filter are given in Table-A.2. Note that the initial dimensions are from the calculation of coupling matrix, but this calculation does not need to be very accurate since SMEAFO is a global-optimisation-based method. However, with more accurate initial dimensions, it is easier for this method to find the global optima, especially for the optimisation of circuits with more variables [3].

The filter is simulated in CST (2015 version) using full-wave EM model. The simulated responses using the initial values is given in Fig. A.3. It can be seen that the performance of the initial design is far from the specifications. The filter is then optimised using SMEAFO method. The examples are run on a PC with Intel 3.5-GHz Core i7 CPU and 8-GB RAM under Windows operating system. CST is used as the EM simulator. No parallel computation is applied in these experiments [2]. Each EM simulation costs around 3 min and the convergence of SMEAFO method happens before 800 EM simulations. The optimised results are given in Fig. A.4 with all specifications achieved.

Table-A.1 Ranges of the variables for example 1 (all dimensions are in millimetres)

Variables	a	$l_1(l_3)$	l_2	l_c	d	h	h_c
Lower bound	0.8	0.4	0.4	0.4	0.01	0.01	0.01
Upper bound	0.95	0.8	0.8	1.8	0.43	0.86	$<h$

Table-A.2 Initial dimensions and optimised dimension for example 1 (all dimensions are in millimetres)

Variables	a	$l_1(l_3)$	l_2	l_c	d	h	h_c
Initial dimensions	0.864	0.616	0.561	1.212	0.353	0.537	0.122
Optimised dimensions (SMEAFO method)	0.876	0.674	0.589	1.100	0.327	0.578	0.143

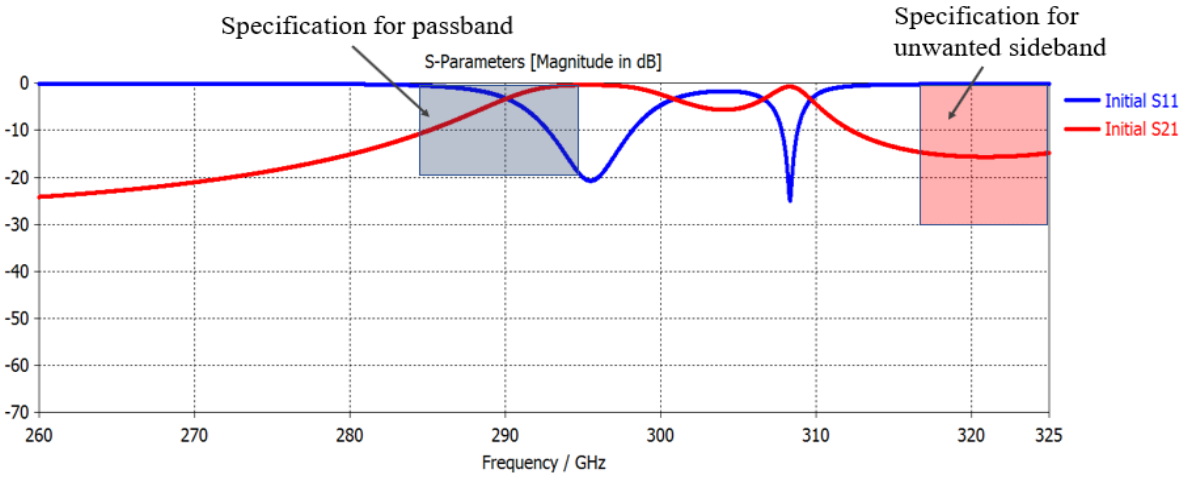

Fig. A.3 S-parameters simulated results for the filter using initial values. Passband and rejection band specifications are shown in grey and red.

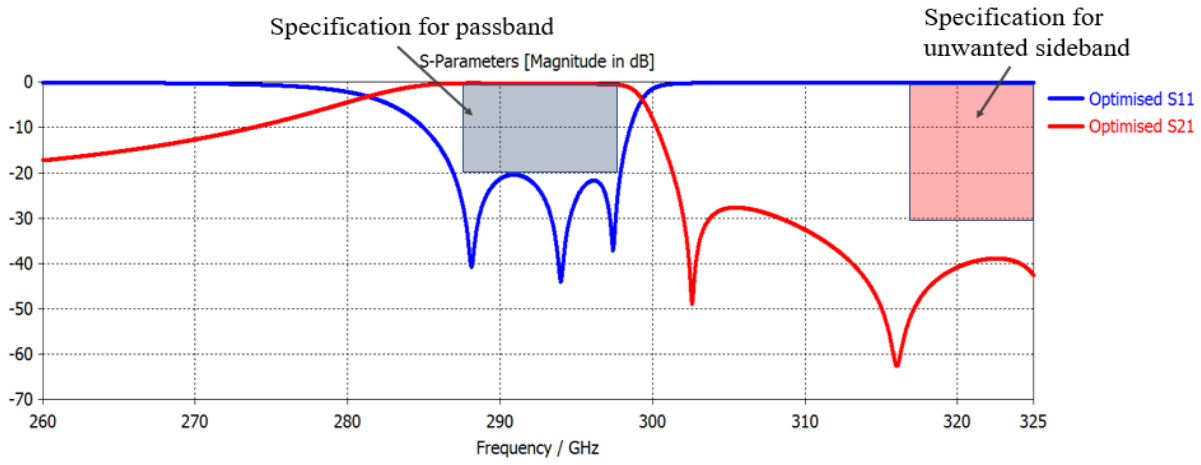

Fig. A.4 Optimised responses for the filter using SMEAFO method. Passband and rejection band specifications are shown in grey and red.

Example 2: a 7th order waveguide filter

This example is a waveguide filter composed of 7 coupled rectangular waveguide cavities operating at TE101 mode. The coupling is achieved by capacitive iris. This filter is designed to be used as one branch of a diplexer. The design specifications are that the passband is 10.7-12.75 GHz with maximum return loss of - 20 dB ($\max|S_{11}|$ within the passband should be at least less than -20 dB and is as smaller as possible). The rejection band is 13-14.5 GHz with better than 20 dB rejection ($\max|S_{21}|$ should be less than -20 dB). Seen from the specifications, the filter has very wide passband (FBW=17.1%) and the passband and rejection band are very close. The optimisation problem is formulated as:

$$\max(|S_{11}|) \leq \text{-20 dB, 10.7-12.75 GHz}$$

$$\max(|S_{21}|) \leq \text{-20 dB, 13-14.5 GHz}$$

The initial calculation of initial dimensions using coupling matrix synthesis are given in Table III. The filter is simulated in CST (2015 version) using full-wave EM model. The simulated

responses using the initial values is given in Fig. A.6. Seen from the performance of the initial design, poles for S_{11} within passband are clear, but the passband is much narrower than the designed value. This is because coupling matrix calculation has the assumption of all resonators working on the centre frequency, and initial dimensions calculated from this method is not accurate for the wide band filters. For high-order filters, the number of variables increases and numerous local optima often exist in the landscape [3]. Under such circumstances, the successful rate for local optimisation is very low. After the using Trust Region Framework method in CST (a common local optimisation algorithm), the optimisation fails to achieve the specifications after 3000 EM simulations.

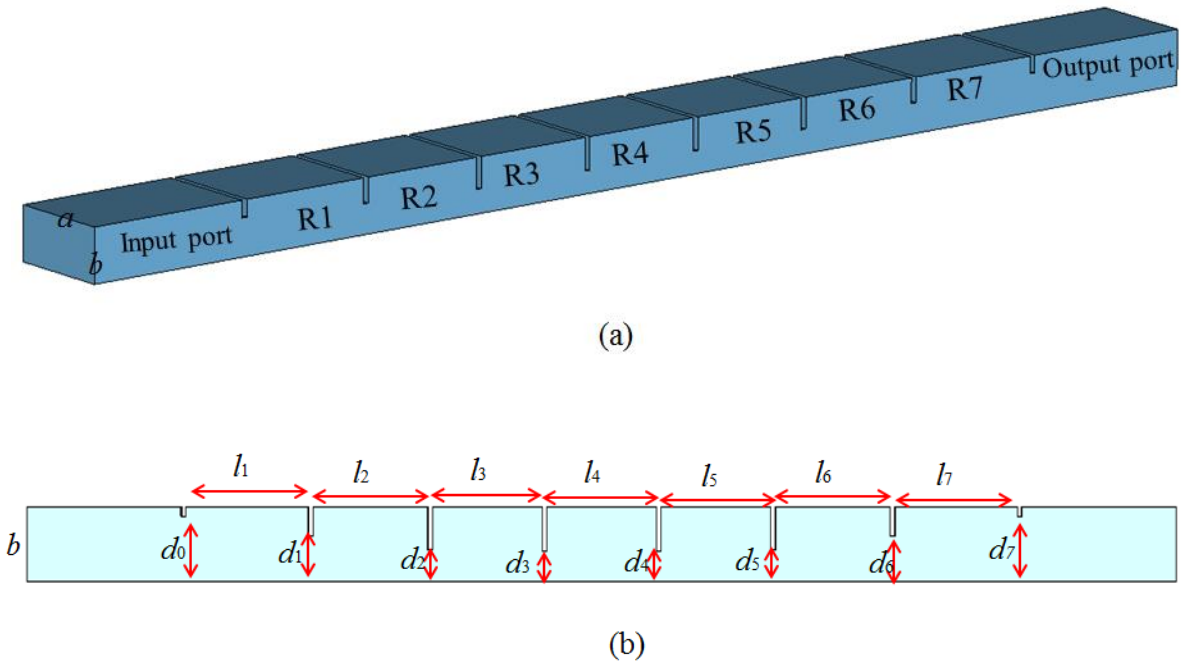

Figure A.5 A 7th order Chebyshev waveguide filter using capacitive iris (a) perspective view of the 3-D model of the filter. a=19.05 mm, b=9.525 mm (b) side view of the filter with important dimensions, in this design: $l_1=l_7$, $l_2=l_6$, $l_3=l_5$, $d_0=d_7$, $d_1=d_6$, $d_2=d_5$, $d_3=d_4$.

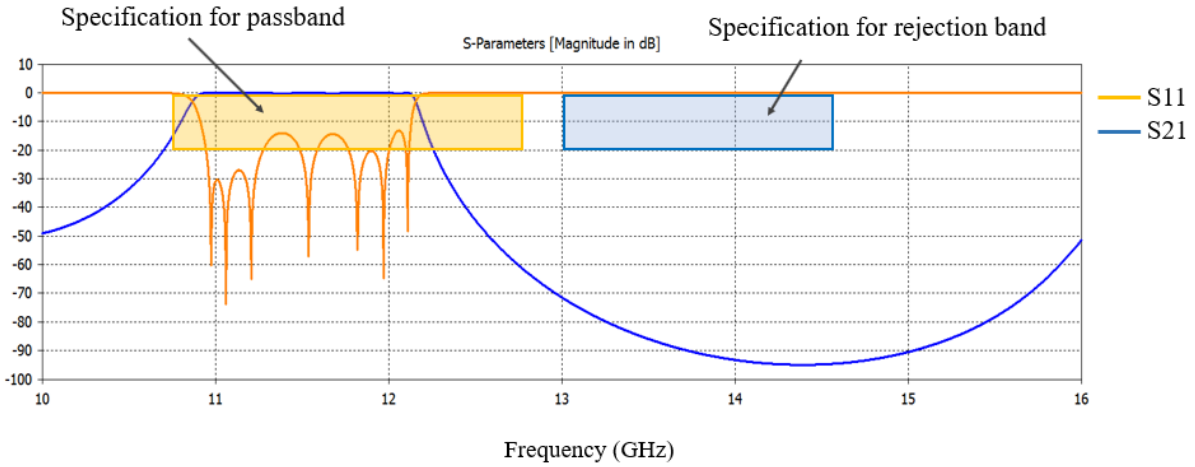

Fig. A.6 Simulated responses using initial dimensions

The best result after using local optimisation is shown in Fig. A.7. By optimising the filter with initial dimensions using SMEAFO method, each EM simulation costs around 2 min and the convergence happens before 1000 EM simulations. The optimised dimensions are given in Table-A.3. The S-parameter responses after SMEAFO optimisation can meet all requirements and are given in Fig. A.8.

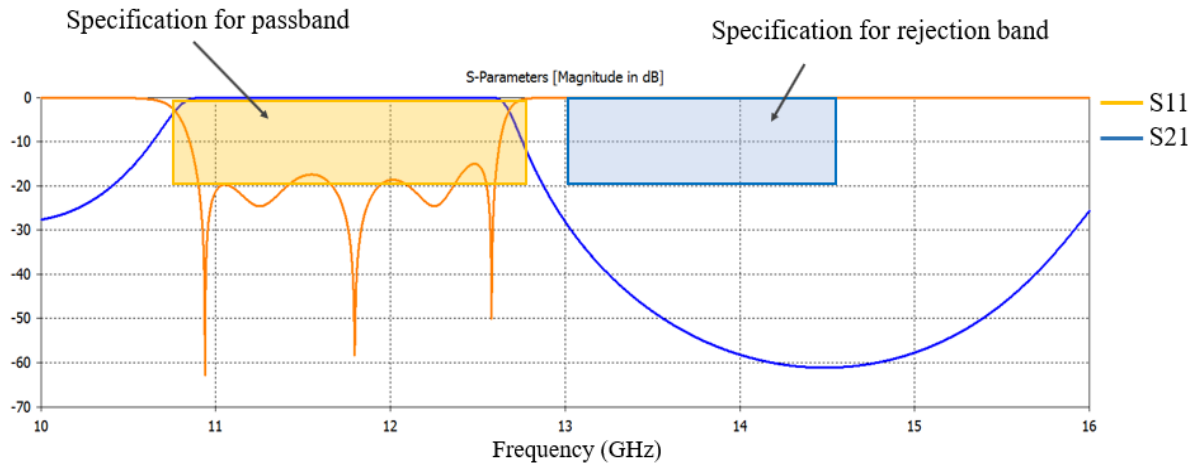

Fig. A.7 Simulated responses after using local optimisation

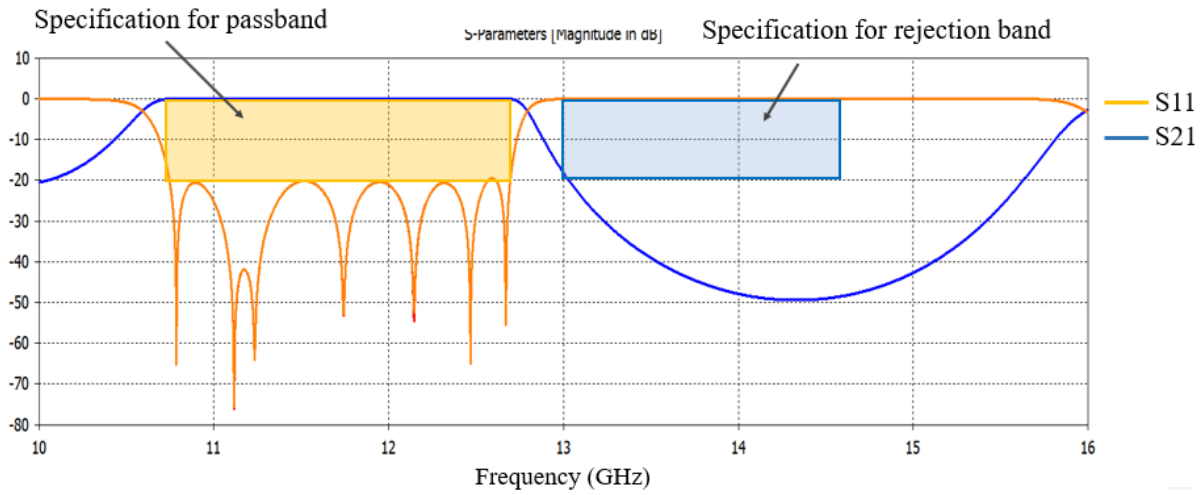

Fig. A.8 Simulated responses after optimised using SMAEFO method

Table-A.3 Initial dimensions and optimised dimension for example 2 (all dimensions are in millimetres)

Variables	l_1	l_2	l_3	l_4	d_0	d_1	d_2	d_3
Initial dimensions	23.189	21.434	20.732	20.636	5.398	3.205	2.091	1.907
Optimised dimensions (local optimisation)	23.512	22.036	21.176	21.054	6.955	4.976	3.575	3.349
Optimised dimensions (SMEAFO method)	23.333	21.980	21.301	21.192	6.747	5.097	4.072	3.749

Example 3: A diplexer composed of a T-junction and two channel filters

Microwave diplexers and multiplexers are frequency selective components that are employed to combine or separate signals of different frequency bands in multiport networks with specified frequency selectivity and isolation requirements [4]. As shown in Fig. A.9, a multiplexer conventionally consists of a common junction and a set of channel filters [5]. A diplexer has the simplest topology of the multiplexer. It is a passive three-port device that connects two ports operating at different frequencies to a common port, while the signals on those two ports can co-exist on the common port without interfering with each other.

A diplexer operating on 9-16 GHz has been designed to demonstrate the potential of surrogate model-assisted evolutionary algorithm (SMEA) for the optimisation of complex diplexer design. This diplexer is a wide-band design and specified to work at the frequency bands of 10.7-12.75 GHz and 13-14.5 GHz. The full specifications of the diplexer are given in Table-A.4.

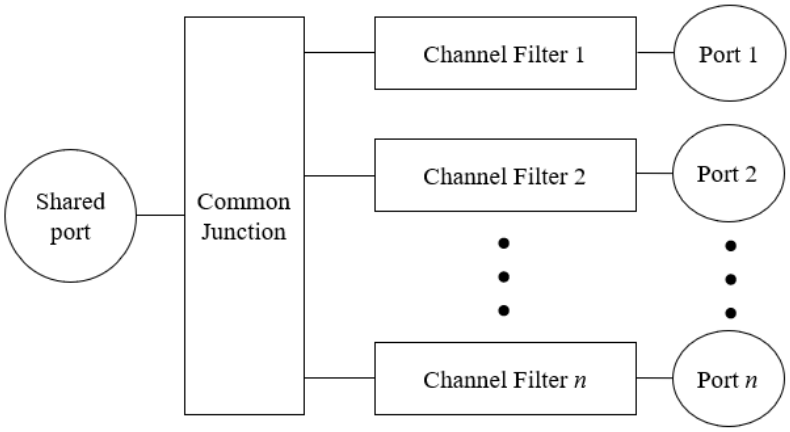

Fig. A.9 Structure of a traditional multiplexer with *n* channels

Table-A.4: Specification of the wide-band diplexer

	Frequency band	specification	
Low guard band	10-10.3 GHz	Rejection	Better than 20 dB
Channel 1	10.7-12.75 GHz	Return loss	Better than 20 dB
		Isolation	Better than 20 dB
Channel 2	13-14.5 GHz	Return loss	Better than 20 dB
		Isolation	Better than 20 dB
high guard band	15-16 GHz	Rejection	Better than 20 dB

To achieve the specifications, this diplexer is designed to have 7 resonators for the channel filter 1 and 6 resonators for the channel filter 2 while these two channels are connected by a T-junction. A prediction of the responses using coupling matrix synthesis is given in Fig. A.10. This diplexer is a complex design in terms of two aspect: (i) it consists of 13 resonators which means more than 26 variables are needed to be optimised; (ii) the passbands for each channel are extreme broadband, which makes the prediction of initial dimensions inaccurate and extremely hard; (iii) the guard band is very narrow and specifications are demanding, thus full-wave EM model with high accuracy is required [6]. These difficulties make the optimisation of the diplexer structure computationally expensive and even impossible to be achieved by most conventional optimisation process. A design synthesis for diplexer composed of a T-junction and two channel filters presented in [7] is employed in this example. This is achieved by firstly designing two bandpass filters to meet the specification of each channel separately. Then two channel filters are connected with a T-junction structure and the whole structure is optimised. The filter with 7 resonators designed to meet specifications of channel 1 is presented in Example 2. The 6^{th} order Chebyshev filter for channel 2 is also designed and optimised using SMEAFO method. Both bandpass filters

are achieved by using capacitive iris and are presented in Fig. A.11. The specifications for the diplexer optimisation problem can be formulated as:

$\max(|S_{11}|) \leq$ -20 dB, 10.7-12.75 GHz, $\max(|S_{11}|) \leq$ -20 dB, 13-14.5 GHz

$\max(|S_{21}|) \leq$ -20 dB, 13-14.5 GHz, $\max(|S_{21}|) \leq$ -20 dB, 10-10.3 GHz

$\max(|S_{31}|) \leq$ -20 dB, 10.7-12.75 GHz, $\max(|S_{31}|) \leq$ -20 dB, 15-16 GHz

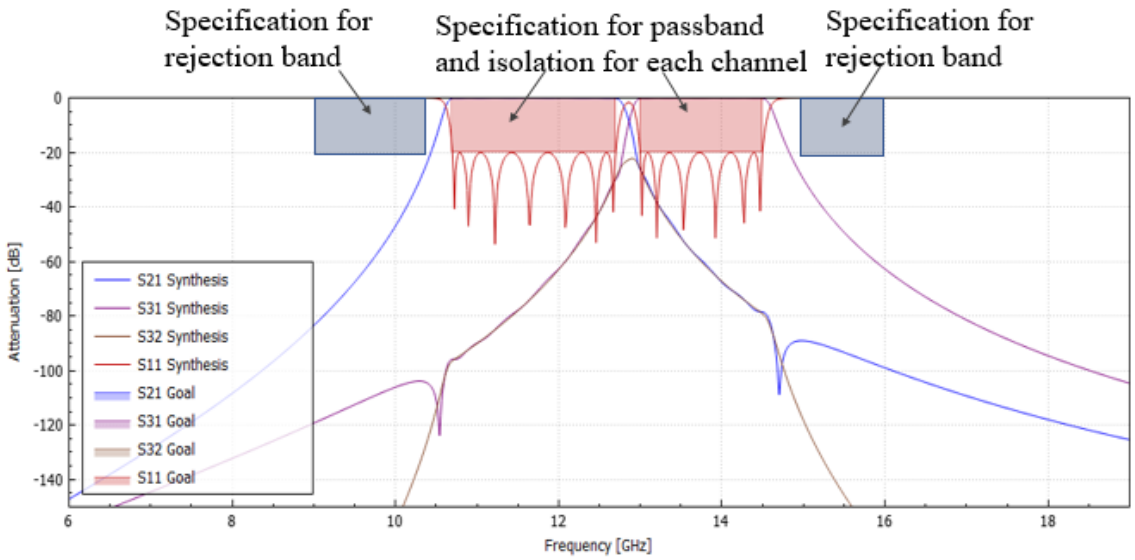

Fig. A.10 Prediction of the responses for the diplexer using coupling matrix synthesis

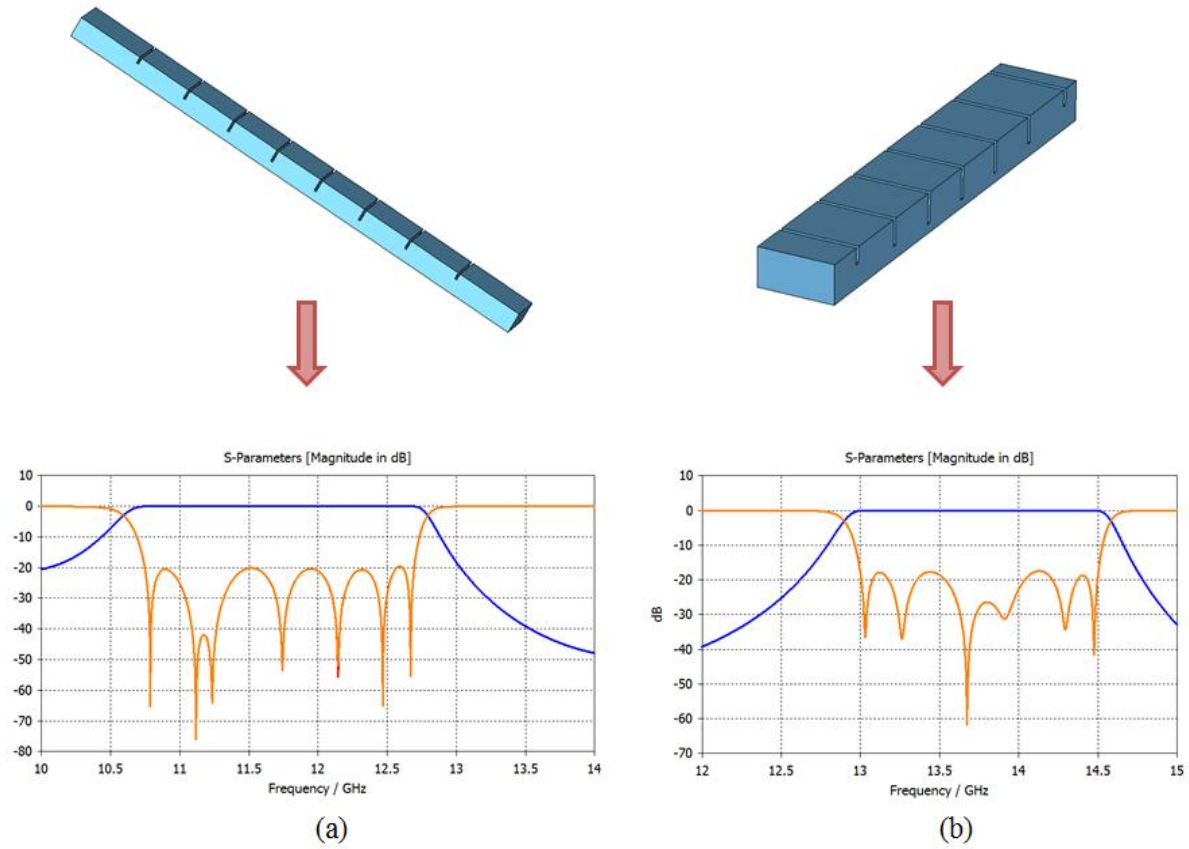

Fig. A.11 Bandpass filters designed to fulfil the specifications for each channel. (a) A 7th order waveguide presented in example 2, this is used as the channel filter to achieve the first passband. (b) A 6th order waveguide filter designed to meet the specification of the second passband. The design of this filter is also optimised using SMEAFO method.

After the design of both channel filters, a T-junction is used to connect the two bandpass filters together in the diplexer. Firstly, we design an original three-port junction shown in Fig. A.12 (a), which provides a compact solution for rectangular waveguide diplexers. This T-junction is then adjusted into a compact form shown in Fig. A.12 (b), under the circumstances that the dimensions for the length of the waveguide for the T-junction (i.e. w_1 or w_2 shown in Fig. A.12 (a)) are less than 0.

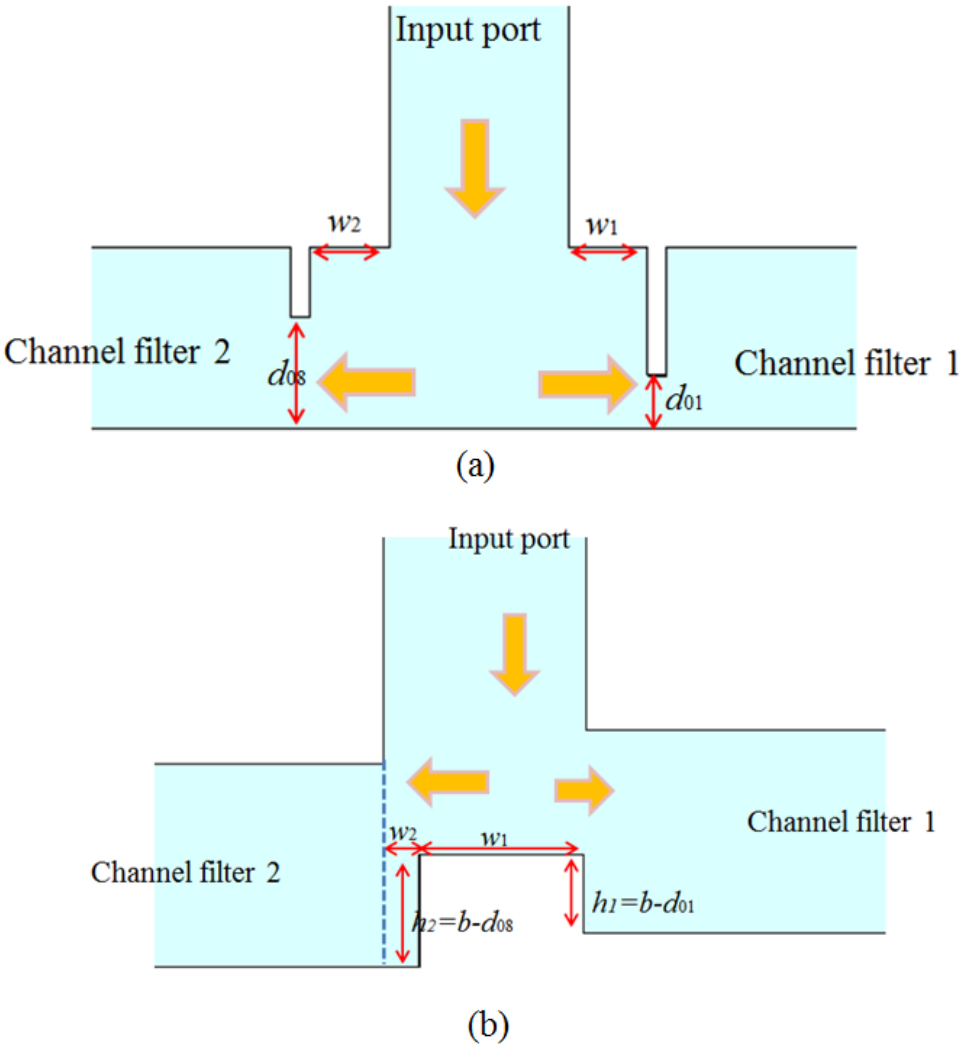

Fig. A.12 T-junction design. (a) Normal T-junction design coupled with channel filters by capacitive iris. d_{01}/ d_{08} represent the dimension of coupling iris between the T-junction and resonator 1/resonator 8. (b) Compact design of the T-junction when channel filters are directly coupled to input port.

In the final step, the whole diplexer structure that combines the T-junction with two channel filters is optimised in EM full-wave model using SMEAFO method. Fig. A.13 gives the details for the diplexer structure to be optimised.

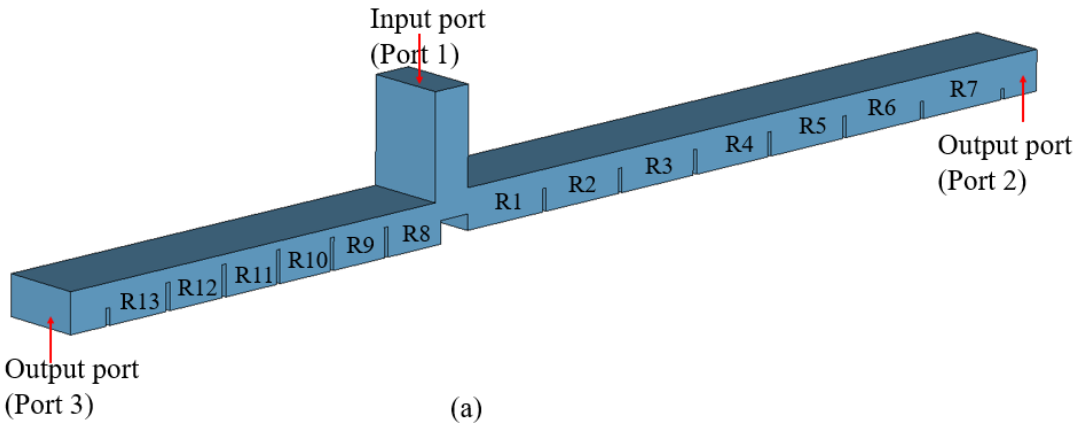

(a)

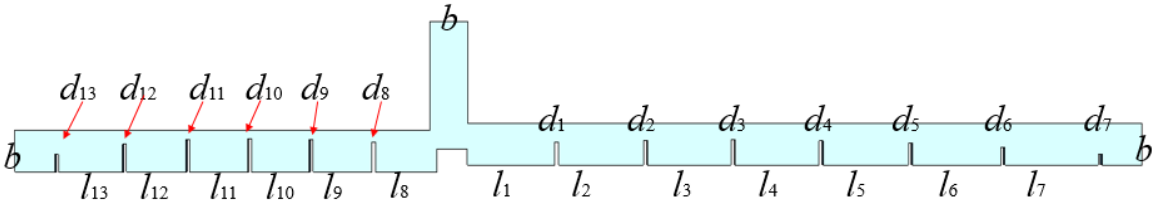

(b)

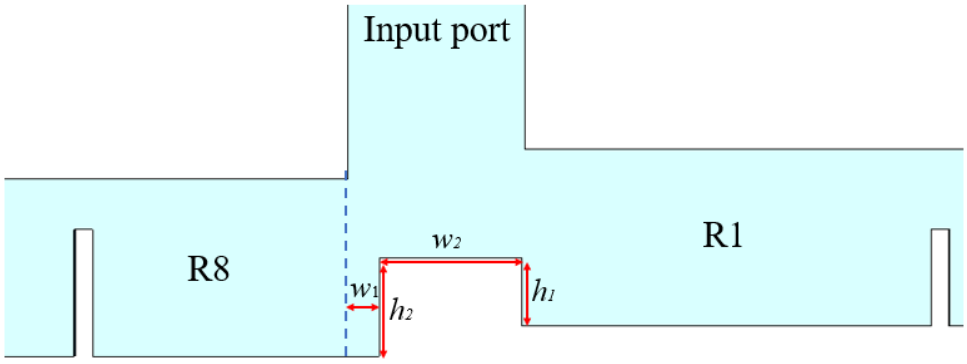

(c)

Fig. A.13 Structure of the diplexer (a) perspective view, R1-R13 represent the resonator 1 to resonator 13. (b) side view of the diplexer, variables for the resonators are marked on the figure. l_n represents the length of the *n* th resonator, d_n represents the width of coupling iris between the *n* th resonator and next resonator or port. (c) zoom in view of the T-junction.

After the optimisation using SMEA method, the optimised dimension is shown in Table- A.5 and the optimised responses in given in Fig. A.14. Although the best optimised results are not able to meet all the specifications, good overall performance for the diplexer is achieved and the potential of applying SMEA method on diplexer optimisations is demonstrated.

Table-A.5 Dimension for the diplexer after optimisation (all dimensions in millimetres)

	d_1	d_2	d_3	d_4	d_5	d_6	d_7	d_8
optimised	4.305	3.864	3.776	3.916	4.407	5.340	7.023	2.764
	d_9	d_{10}	d_{11}	d_{12}	d_{13}	l_1	l_2	l_3
optimised	2.039	1.913	2.122	3.151	5.538	22.006	21.231	21.112
	l_4	l_5	l_6	l_7	l_8	l_9	l_{10}	l_{11}
optimised	21.131	21.493	22.240	23.300	15.146	14.566	14.456	14.513
	l_{12}	l_{13}	h_1	h_2	w_1	w_2		
optimised	14.850	16.026	5.262	3.672	1.698	7.693		

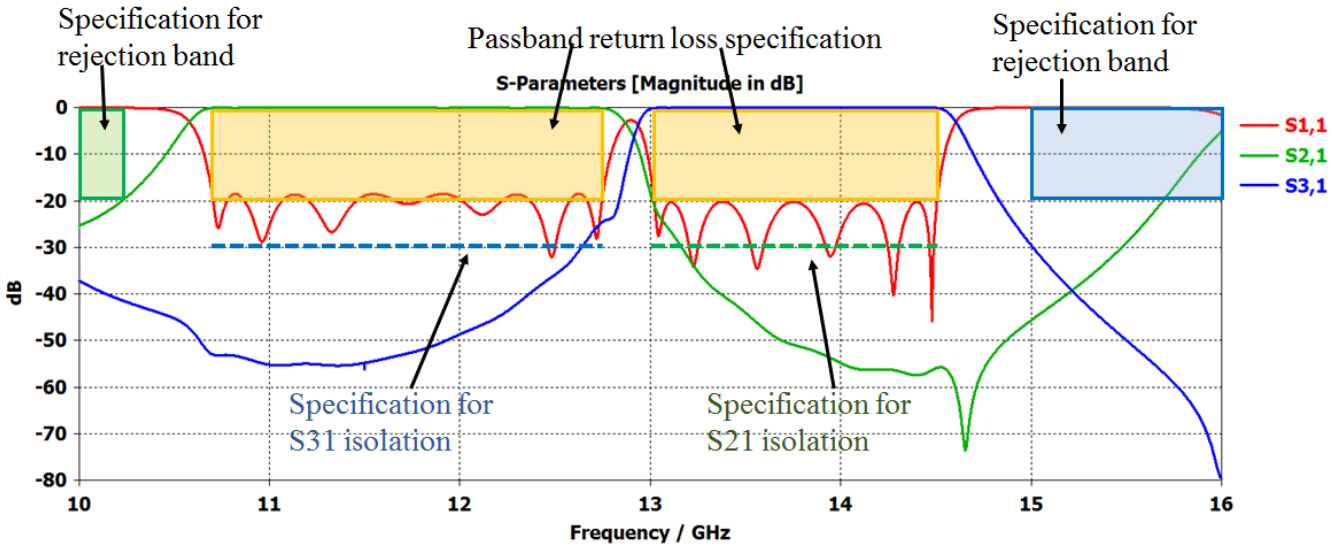

Fig. A.14 Responses of the diplexer after final optimisation.

References:

[1] J. Hong and M. J. Lancaster, *Microstrip Filters for RF/Microwave Applications*. New York: Wiley, 2001.

[2] B. Liu, H. Yang, and M. J. Lancaster, "Global optimization of microwave filters based on a surrogate model-assisted evolutionary algorithm," *IEEE Transactions on Microwave Theory and Techniques*, vol. 65, no. 6, pp. 1976–1985, 2017.

[3] H. Yang, Y. Dhayalan, X. Shang, M. J. Lancaster, *et al.*, "WR-3 waveguide filter based on high precision CNC milling and SU-8 photoresist technology," *IEEE Transactions on Terahertz Science and Technology*, vol. 8, no. 1, pp. 100-107, Jan. 2018.

[4] P. Zhao and K. L. Wu, "An iterative and analytical approach to optimal synthesis of a multiplexer with a star junction, " *IEEE Trans. Microw. Theory Techn.*, vol.62, no.12, pp.3362-3369, Dec.2014.

[5] R. J. Cameron, C. M. Kudsia, R.R. Mansour, *Microwave Filters for Communication Systems: Fundamentals, Design and Applications.* Hoboken, NJ, USA: Wiley, 2007.

[6] S. Bastioli, L. Marcaccioli and R. Sorrentino, "An Original Resonant YJunction for Compact Waveguide Diplexers," Microwave Symposium Digest, 2009. MTT '09. IEEE MTT-S International

[7] Y. Rong, H.-W. Yao, K. A. Zaki, T. G. Dolan, "Millimeter-wave Ka-band H-plane diplexers and multiplexers," *IEEE Transactions on Microwave Theory and Techniques*, vol. 47, no. 12, Dec. 1999.

Appendix II

Publications

1. **H. Yang**, Y. Dhayalan, X. Shang, M. J. Lancaster, *et al.*, "WR-3 waveguide filter based on high precision CNC milling and SU-8 photoresist technology," *IEEE Transactions on Terahertz Science and Technology*, vol. 8, no. 1, pp. 100-107, Jan. 2018.
2. B. Liu, **H. Yang** and M. J. Lancaster, "Global Optimization of Microwave Filters Based on a Surrogate Model-Assisted Evolutionary Algorithm," *IEEE Transaction on Microwave Theory and Techniques* vol. 65. no. 6. pp. 1976-1985. Jun. 2017.
3. X. Shang, **H. Yang**, D. Glynn and M. J. Lancaster, "Submillimeter-wave waveguide filters fabricated by SU-8 process and laser micromachining," *IET Microwaves, Antennas & Propagation*, vol. 11, no. 14, pp. 2027-2034, Nov. 2017.
4. B. Liu, **H. Yang** and Michael J. Lancaster, "Synthesis of Coupling Matrix for Diplexers Based on a Self-Adaptive Differential Evolution Algorithm," in *IEEE Transactions on Microwave Theory and Techniques*, vol. 66, no. 2, pp. 813-821, Feb. 2018.
5. X. Shang, **H. Yang**, Y. Dhayalan, M. J. Lancaster, H. Wang and P. G. Huggard, "SU-8 micromachined cross-coupled waveguide cavity filter for sideband rejection above 300 GHz," *2017 10th UK-Europe-China Workshop on Millimetre Waves and Terahertz Technologies (UCMMT)*, Liverpool, 2017, pp. 1-2.

WR-3 Waveguide Bandpass Filters Fabricated Using High Precision CNC Machining and SU-8 Photoresist Technology

Hao Yang, Yuvaraj Dhayalan, Xiaobang Shang, *Member, IEEE*, Michael J. Lancaster, *Senior Member, IEEE*, Bo Liu, *Senior Member, IEEE*, Hui Wang, Manju Henry, and Peter G. Huggard, *Senior Member, IEEE*

***Abstract*—This paper presents two WR-3 band (220–325 GHz) filters, one fabricated in metal using high precision computer numerically controlled milling and the other made with metallized SU-8 photoresist technology. Both are based on three coupled resonators, and are designed for a 287.3–295.9-GHz passband, and a 30-dB rejection between 317.7 and 325.9 GHz. The first filter is an extracted pole filter coupled by irises, and is precision milled using the split-block approach. The second filter is composed of three silver-coated SU-8 layers, each 432 μm thick. The filter structures are specially chosen to take advantage of the fabrication processes. When fabrication tolerances are accounted for, very good agreement between measurements and simulations are obtained, with median passband insertion losses of 0.41 and 0.45 dB for the metal and SU-8 devices, respectively. These two filters are potential replacements of frequency selective surface filters used in heterodyne radiometers for unwanted sideband rejection.**

***Index Terms*—Micromachining, SU-8, terahertz components, waveguide filter.**

I. Introduction

MULTICHANNEL air and spaceborne sounders are employed for spectroscopic characterization of the Earth's atmosphere [1]. These instruments perform molecular spectroscopy at millimeter and submillimeter wavelengths in relatively narrow frequency channels. Within the instrument, linearly polarized signals are frequency demultiplexed by a quasi-optical feed chain using frequency selective surfaces (FSSs). FSSs are also used to prevent the signals in the unwanted sideband from reaching the double sideband heterodyne mixers [2]. As the atmospheric signals are weak, the sideband rejecting FSS needs to have a very low insertion loss and a high isolation between two adjacent channels which are close to each other in frequency [3]. For instance, the FSS reported in [3] transmits 316.5–325.5-GHz radiation with a maximum insertion loss of 0.6 dB and achieves greater than 30-dB rejection from 349.5 to 358.5 GHz. To achieve this specification, a transmission zero is required and we believe this paper describes the first filter to achieve this at these high frequencies.

Waveguide technology is potentially an attractive alternative to FSS for sideband selection, due to its low loss and the possibility to construct lower volume filters. For waveguide components in general, device dimensions decrease as frequency increases. This means a reduction in size and mass of components, but also a tighter dimensional tolerance is required during fabrication. Different micromachining techniques, such as computer numerically controlled (CNC) milling [4]–[6], Si deep reactive ion etching (DRIE) [7]–[9], lithographic micromachining technique [10], and SU-8 photoresist technology [11]–[13], have been developed and employed to achieve high-dimensional accuracy in the fabrication of high-frequency waveguide filters. Laser micromachining [14] and 3-D printing [14] have also been utilized for high-frequency filters by the authors using different designs at about 100 GHz. This paper is complementary showing how alternative technologies cope, at higher frequencies, for a filter with demanding specifications.

CNC milling is a traditional way of fabricating metal waveguide components, especially at lower frequencies. Waveguide components fabricated by CNC milling with excellent performance have been reported. Authors in [4] and [5] describe fourth-order W-band filters. In [4], the filter is measured to have 0.5-dB insertion loss and a 4.53% (4.20 GHz) bandwidth, and in [5], the filter is measured to have 0.6-dB insertion loss and a 10% (10 GHz) bandwidth. For the 220–325-GHz WR-3 band, waveguide features and tolerances decrease by a factor of around 3. Fabricating waveguide filters at such a frequency requires an expensive, high precision CNC mill. Filter design flexibility is also limited by tool sizes and depth to diameter aspect ratios [5]. However, the limits of conventional CNC milling are still being pushed: examples of WR-3 band CNC milled filter

Manuscript received September 19, 2017; accepted November 6, 2017. Date of publication December 7, 2017; date of current version January 9, 2018. This work was supported by the U.K. Engineering and Physical Science Research Council under Contract EP/M016269/1. *(Corresponding author: Hao Yang.)*

H. Yang, Y. Dhayalan, and M. J. Lancaster are with the Department of Electronic, Electrical and Systems Engineering, University of Birmingham, Birmingham B15 2TT, U.K. (e-mail: hxy297@bham.ac.uk; yuvaraj@gmail.com; m.j.lancaster@bham.ac.uk).

X. Shang was with the Department of Electronic, Electrical and Systems Engineering, University of Birmingham, Birmingham B15 2TT, U.K. He is now with the National Physical Laboratory, Teddington TW11 0LW, U.K. (e-mail: xiaobang.shang@npl.co.uk).

B. Liu is with the School of Electrical, Electronic, and System Engineering, University of Birmingham, Birmingham B15 2TT, U.K., and also with the Department of Computing, Wrexham Glyndwr University, Wrexham LL11 2AW, U.K. (e-mail: liubo168@gmail.com).

H. Wang, M. Henry, and P. G. Huggard are with the Space Science and Technology Department, Rutherford Appleton Laboratory, Oxfordshire OX11 0QX, U.K. (e-mail: hui.wang@stfc.ac.uk; manju.henry@stfc.ac.uk; peter.huggard@stfc.ac.uk).

Color versions of one or more of the figures in this paper are available online at http://ieeexplore.ieee.org.

Digital Object Identifier 10.1109/TTHZ.2017.2775441

can be found in [6], where two fourth-order bandpass filters are presented, one with measured 0.7-dB insertion loss and 8.77% (22.6 GHz) bandwidth and another with measured 0.5-dB insertion loss and 9.83% (25.2 GHz) bandwidth. In this paper, we present a WR-3 band CNC milled extracted pole filter with an improved performance, which is designed specifically for sideband rejection.

SU-8 photoresist is a promising technology for manufacturing millimeter and submillimeter waveguide components, and is used for the second filter discussed in this paper. SU-8 is a photolithographically patterned, epoxy-based, resin that is resistant to organic solvents once cured, and can have a thickness ranging from 0.5 μm to 1 mm [15]. There are several advantages of using SU-8 micromachining over CNC machining. For example, SU-8 can achieve a similar high-dimensional accuracy with potentially lower cost. It may also allow sharper internal corners and higher corner radius to depth ratios. Meanwhile, the SU-8 process is a batch fabrication which allows repeatability between devices as well as production of several devices in a single fabrication run [15]. Compared with DRIE, standard photolithography processes are used with SU-8 with better surface roughness on the sidewalls of waveguide structures [15]. SU-8 photoresist technology has been employed to demonstrate filters in the WR-10 [11], WR-3 [12], and WR-1.5 bands [13]. In this paper, a new WR-3 band waveguide filter is designed for the SU-8 process to meet a specification similar to the FSS filter described above.

For both the CNC and the SU-8 filters presented and compared below, the specifications in [3] were adjusted to cope with the available measurement capability. Both filters have transmission zeros with the CNC filter having a conventional design; however, the SU8 filter is a completely new design topology to produce the transmission zero. Frequencies have been scaled down by a factor of 1.1, so that the new passband is 287.3–295.9 GHz and the stopband attenuation specification becomes 30 dB between 317.7 and 325.9 GHz.

Structural details and design methods of the two filters are presented in Sections II and III, which is followed by a description of the fabrication process in Section IV. Measurements and discussions are presented in Section V, and conclusions are given in Section VI.

II. Design of CNC Milled Extracted Pole Filter

The CNC filter design is shown in Fig. 1. It is based on three coupled resonators operating at TE_{101} mode and an extracted pole resonator [16]. The material conductivity is assumed to be that of gold (i.e., $4.10 \times 10^7 \mathrm{S/m}$). A third-order waveguide cavity filter which has a Chebyshev response was designed first, using the synthesis technique described in [17], to have a center frequency of 291.6 GHz, a bandwidth of 3% (8.6 GHz), and a return loss in the passband of $\geq$20 dB. For this structure, an iris between the test ports and the first/last resonators controls the external coupling (Q_e); the iris between resonators 1 and 2 (or resonators 2 and 3) controls the coupling coefficient k_{12} (or k_{23}). To meet this specification, the external Q and coupling coefficients are calculated to be $Q_{e1} = Q_{e3} = 28.87$,

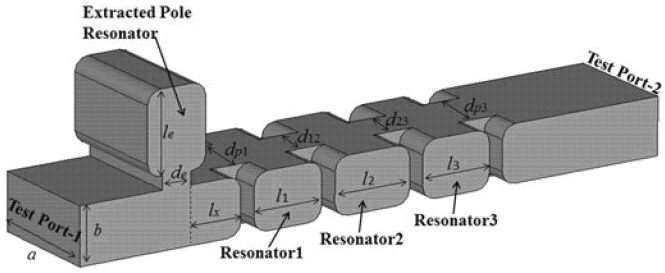

Fig. 1. Diagram of extracted pole filter structure. $a = 864$, $b = 432$, $\mathrm{l}_1 = \mathrm{l}_3 = 510$, $l_2 = 517$, $l_e = 619$, $l_x = 383$, $d_e = 205$, $d_{p1} = d_{p3} = 432$, and $d_{12} = d_{23} = 309$ (unit: μm).

$k_{12} = k_{23} = 0.030$. To meet the upper stopband specification, a steep roll-off is needed on the high frequency side of the passband. It has been shown [16] that the selectivity of a conventional waveguide filter can be improved by using inductively coupled stopband cavities connected to the broad wall of the waveguide [18]. In [19], the advantages of this extracted pole technique have been demonstrated. A single extracted pole resonator, added to the third-order waveguide filter using the method of authors in [20] and [21], provides a transmission zero in the rejection band and achieves a very high cut-off rate into the upper sideband.

In order to be compatible with CNC milling process, the corners of the resonators have a radius of 0.10 mm (see Fig. 1) to permit fabrication with a 0.20-mm end mill. Meanwhile, the minimum dimension in the *E*-plane must also be larger than 0.20 mm. After initial design of the structure using the coupling matrix approach [17], full-wave simulation and optimization for this filter are carried out by CST Microwave Studio (version 2016) using the Trust Region Framework algorithm. The cavity dimensions achieved after optimization are shown in Fig. 1. To give an idea of scale, the total length of the filter structure is 4 mm.

In order to test the filter, a CNC machined block which contains the filter is designed. The input and output waveguides have both been extended by 8 mm in order to accommodate standard waveguide flanges and screws. A 20-mm length of straight WR-3 waveguide is included as a measurement reference in the same block as the waveguide filter. Standard UG-387 waveguide flanges were machined in the block. By utilizing an *E*-plane split-block technique, the transmission loss is minimized as no surface current flows across the contact plane. The simulation results after optimization for *S*-parameters are shown in Fig. 2. The predicted passband insertion loss for the extracted pole filter (4 mm filter structure) is below 0.4 dB and the rejection in the unwanted sideband is above 30 dB. Passband reflectivity, S_{11}, is below -20 dB.

III. Design of SU-8 Micromachined Filter

The SU-8 photoresist filter is designed [16] to meet the same specifications. It exploits the stacked metalized layer approach associated with SU-8 [22]. The filter has three coupled resonators and a cross-coupling between the first and third resonators and is shown in Fig. 3. With this topology and by setting the frequency of the transmission zero at

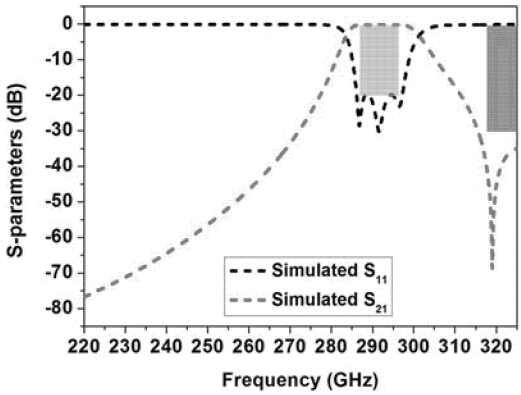

Fig. 2. Simulated *S*-parameters for the CNC milled extracted pole filter. Passband and stopband specifications are shown in gray and red, respectively.

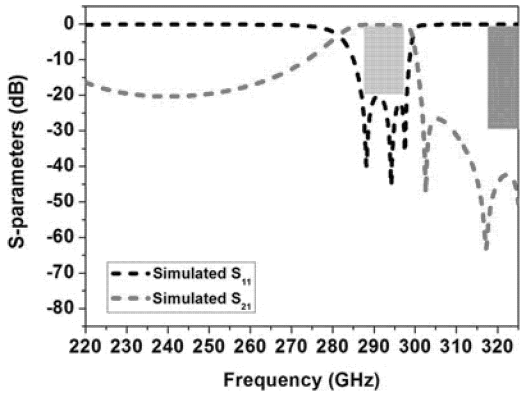

Fig. 4. Simulated *S*-parameters for the SU-8 micromachined filter. Passband and stopband specifications are shown in gray and red, respectively.

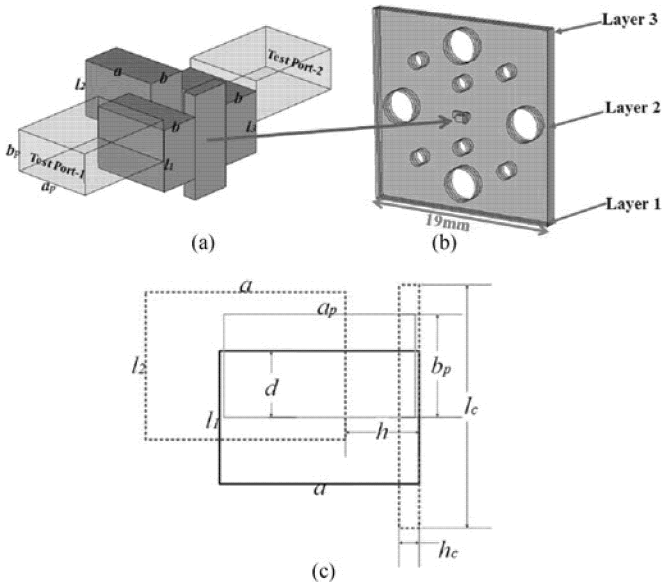

Fig. 3. Diagram of WR-3 band filter formed of three SU-8 layers with the same thickness of 432 μm. (a) Diagram of the filter structure. Dimensions of the test ports are: $a_p = 864$ μm, $b_p = 432$ μm. Dimensions of the resonators are: $a = 876$ μm, $b = 432$ μm, $l_1 = l_3 = 647$ μm, and $l_2 = 589$ μm. (b) Illustration of the whole filter device including dowel holes and screw clearance holes designed to match the UG-387 waveguide flange. (c) Perspective front view of the filter structure. The blue rectangle represents the input/output of test port. The black rectangle represents the first (or third) resonator, whereas the cavities in the second layer are represented by red rectangles. $d = 327$ μm, $h = 578$ μm, $l_c = 1100$ μm, and $h_c = 143$ μm.

317.7 GHz, which is the lower boundary of the upper stopband, external Q and coupling coefficients are calculated as: $Q_{e1} = Q_{e3} = 27.65$, $k_{12} = k_{23} = 0.031$, $k_{13} = 0.006$, $k_{11} = k_{33} = 0.002$, $k_{22} = -0.006$. Each of the silver-coated SU-8 layers has a thickness of 432 μm and contains one resonator. As shown in Fig. 3(a), the value of the SU-8 layer thickness determines the WR-3 waveguide resonator height, b. Since the central resonator couplings k_{12} and k_{23} are equal, layers 1 and 3 are identical and the whole structure is symmetrical. Rather than controlling the coupling through a conventional iris, the relative positions of the resonators are shifted to obtain the desired coupling coefficients. In other words, the horizontal displacement h, shown in Fig. 3(c), determinates k_{12} and k_{23}, whereas the offset d between the test port and first/third resonators controls the external coupling. The cross coupling between first and third resonators is accomplished by a slot in the middle layer. The frequency of the resulting transmission zero is controlled by the width of this cross-coupling slot, h_c. The above geometric design parameters, shown in Fig. 3, are optimized by the SMEAFO method [23] using CST Microwave Studio (version 2016). Fig. 3 provides the detailed dimensions of this filter after optimization.

The filter is designed to be inserted between standard UG-387 waveguide flanges for measurement. As shown in Fig. 3(b), holes to accommodate the flange dowels, thereby accurately aligning the different SU-8 layers, are incorporated in the design. Larger clearance holes for the waveguide flange screws are also introduced.

The optimized *S*-parameter response of the filter is shown in Fig. 4. The predicted passband insertion loss is below 0.4 dB and the rejection in the unwanted sideband is better than 35 dB. Passband reflectivity, S_{11}, is below -20 dB. The simulations predict two unexpected transmission zeros, one located between passband and upper stopband at 302.5 GHz and another at 326.2 GHz, just above the waveguide band's upper edge. These zeros are caused by unwanted cancellation effect of the signals transmitted by different paths from the input to the output due to the special structure of the design. That is, apart from cross coupling accomplished by the slot on the middle layer, there is an additional coupling path between resonators 1 and 3.

IV. Fabrication Details

The extracted pole waveguide filter was fabricated at the Rutherford Appleton Laboratory using a high-precision Kern milling machine and tungsten carbide cutters with diameters down to 0.20 mm. The block material was copper alloy which was then coated with a thin film of gold (around 3 μm) by electroplating. As mentioned above, the internal corners of the filter had a radius of 0.2 mm. Fig. 5 shows a photograph of the split plane of the CNC machined block with its four resonators.

The fabricated layers of the SU-8 filter are shown in Fig. 6(a). The process details for the SU-8 filter can be found in [13], [24],

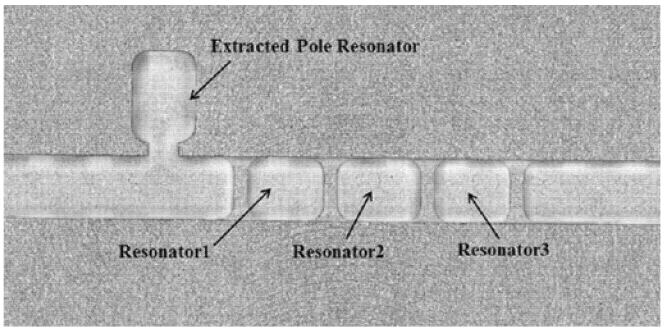

Fig. 5. Photograph of the internal cavities of the fabricated CNC milled extracted pole filter.

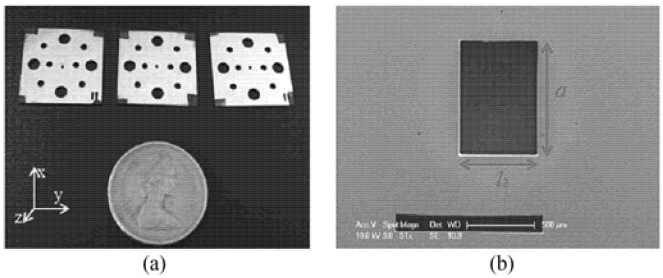

Fig. 6. (a) Photograph of the three silver-coated SU-8 layers, 20 × 20 mm for each layer with a thickness of 0.432 mm. (b) Scanning electron microscope image of the cavity structure for the second SU-8 layer.

and [25]. In summary, a single-side-polished 100-mm-diameter 1-mm-thick silicon wafer was used as a base for forming the SU-8. OmniCoat from MicroChem was used as a 1.5-μm-thick sacrificial layer between SU-8 and silicon. This thickness of OmniCoat was built up from five 300-nm-thick layers. Each was formed from precursor spun at 350 r/min for 10 s and then at 700 r/min for 20 s. The coating was soft baked by placing the wafer on a hot plate at 200 °C for 120 s. It was then cooled on a flat copper plate at room temperature for 300 s.

SU-8 50 negative photoresist from MicroChem was then spin coated onto the OmniCoat. The thickness of the SU-8 layer is calculated by measuring the mass of the coating [13]. A mass of 5.20 g on a 100-mm-diameter wafer corresponds to a thickness of 432 μm. The coated wafer is left on a leveled copper plate at room temperature for 1 h for self-planarization. Then it was soft baked at 65 and 85 °C for 40 and 240 min, respectively. In order to reduce the thermal stresses during soft bake, the temperature was increased at 5 °C/min from room temperature during heating. During cooling, the hotplate and wafer cooled naturally to room temperature after switching off the power. UV photolithography was carried out in Cannon PLA-510 mask aligner. The resist was exposed for 4 cycles of 40 s, with a 2-min interval between each cycle to allow the resist to stabilize. A PL 360 filter was placed over the chrome mask during UV exposure, which effectively blocked UV radiation with a wavelength below the 365-nm i-line [26]. The exposed wafers were baked at 70 °C for 30 min, which helps the acid-assisted cross linking of the exposed structures. After this bake, the SU-8/Si wafer was developed for 15 min in MicroChem EC at room temperature with constant magnetic

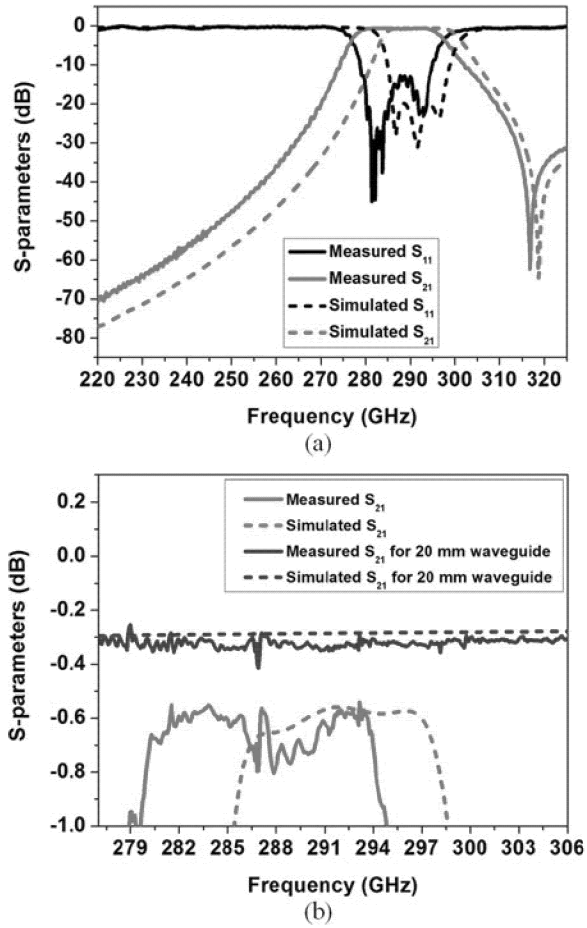

Fig. 7. Comparison of the simulated and measured results of the filter produced by CNC milling. (a) Response over whole WR-3 band. (b) Expanded view of S_{21} showing the passband. The simulations are performed assuming a material conductivity corresponding to that of bulk gold.

stirring. The patterned SU-8 layers were released by dissolving the sacrificial layer in tetramethylammonium hydroxide-based MFCD26 solution from MicroChem at room temperature for 5 h. The released SU-8 pieces were cleaned with propan-2-ol and dried by nitrogen gas. Layers of 30 nm of chromium, and subsequently 1500 nm of silver, were deposited by sputtering and thermal evaporation, respectively. This was done on both sides of the patterned SU-8 layers without breaking the vacuum. A purpose-built sample-tilted-rotating rig allowed the metal to reach the inner walls of the waveguides and cavities.

V. Measurement and Discussion

The *S*-parameter measurements for the CNC milled extracted pole filter were carried out using a Keysight PNA network analyzer with a pair of VDI (Virginia Diodes, Inc.) WR-3.4 extension heads. For the measurement, the CNC machined block was fixed between the waveguide flanges of two frequency extension heads. The insertion loss for the 20-mm length of WR-3 waveguide in the same block was also measured. The results are shown in Fig. 7. The filter has an average passband insertion loss of around 0.65 dB and greater than 30-dB rejection in the upper stopband. As shown in Fig. 7(b), the insertion loss for

TABLE I
COMPARISON BETWEEN DESIGNED AND MEASURED RESONATOR DIMENSIONS FOR THE CNC MILLED EXTRACTED POLE FILTER

	Designed (μm)	Measured (μm)
Cavity #	$a \times b \times l$	$a \times b \times l$
Resonator 1	$864 \times 432 \times 510$	$874 \times 438 \times 521$
Resonator 2	$864 \times 432 \times 567$	$874 \times 438 \times 574$
Resonator 3	$864 \times 432 \times 510$	$874 \times 438 \times 519$

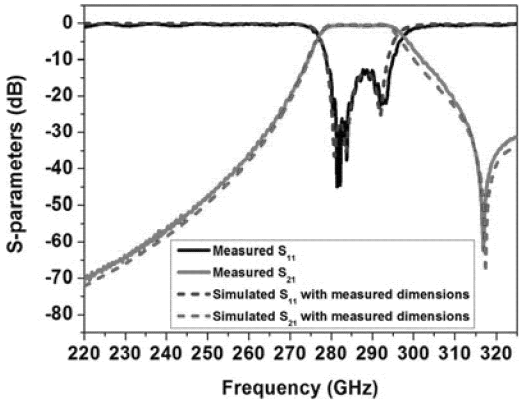

Fig. 8. Simulated response of the CNC milled extracted pole filter with measured dimensions shown in Table I.

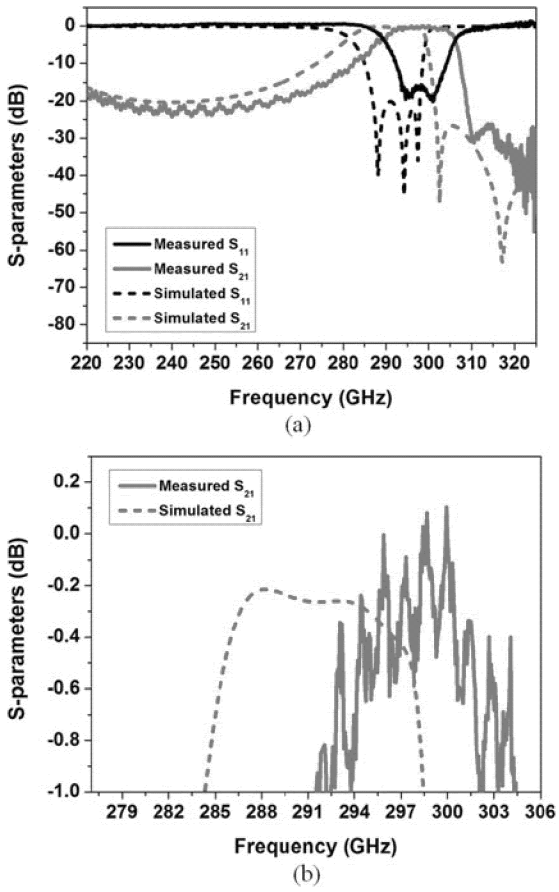

Fig. 9. Comparison of the simulated results and measured results of the filter based on SU-8 photoresist technology. (a) Response over whole WR-3 band. (b) Expanded view of S_{21} over passband. The simulations are performed in CST assuming a material conductivity equal to that of silver.

TABLE II
COMPARISON BETWEEN DESIGNED AND MEASURED RESONATOR DIMENSIONS FOR THE SU-8 FILTER

	Designed (μm)	Measured (μm)	
		Side 1	Side 2
Cavity #	$a \times l$	$a \times l$	$a \times l$
Resonator 1	876×647	863×623	869×638
Resonator 2	876×589	861×576	874×584
Resonator 3	876×647	855×630	873×641

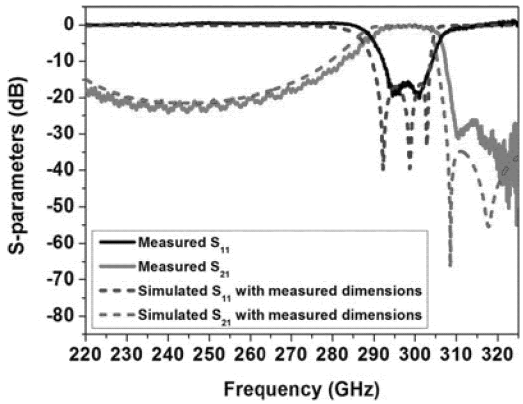

Fig. 10. Simulated response of the SU-8 filter with measured dimensions in Table II.

TABLE III
COMPARISON OF MEASUREMENTS BETWEEN CNC MILLED EXTRACTED POLE FILTER AND SU-8 MICROMACHINED FILTER

	CNC extracted pole filter	SU-8 filter
Passband insertion loss	0.41 dB	0.45 dB
Passband frequency shift	-5 GHz	7 GHz
Stopband attenuation	>32 dB	>33 dB
Size of filter device	20 mm $\times$ 20 mm $\times$ 4 mm	19 mm $\times$ 19 mm $\times$ 0.432 mm (three layers)

20 mm of waveguide is measured to be 0.3 dB, giving the waveguide a loss of 0.015 dB/mm. Allowing for a total of 16 mm of waveguide connecting the filter to the flanges, the loss of the 4-mm-long filter structure is thus 0.41 dB.

The measurements are in very good agreement with simulations except that center frequency of the filter is shifted downwards by around 5 GHz. This frequency shift is mainly due to larger-than-designed dimensions of resonators, which have been measured with results shown in Table I. Generally dimensions are within a few micrometers of designed values, except for the width of the waveguide which is about 15 μm larger than assumed in the simulations. When the filter is resimulated with CST using the measured dimensions, excellent agreement with measurements is obtained as shown in Fig. 8.

For the SU-8 filter, the measurement is performed on an Agilent E8361A network analyzer using a short-open-load-thru calibration. The SU-8 filter is placed between two waveguide flanges of the network analyzer and the layers aligned by the high precision dowels on the waveguide flanges.

TABLE IV
COMPARISON OF RECENTLY PUBLISHED WAVEGUIDE BANDPASS FILTER OPERATING IN FREQUENCY RANGE FROM WR-3 TO WR-1.5 BAND

Waveguide band	f_0 (GHz)	*FBW*	Micromachining techniques	Filter response	*n*	*IL* (dB)	*RL* (dB)	Reference (year)
WR-3	257.7	8.77%	CNC (*H*-plane split)	Quasi-elliptical, one TZ at lower stopband and one upper stopband	4	0.7	>14	[6] (2017)
WR-3	256.3	9.83%	CNC (*H*-plane split)	Quasi-elliptical, one TZ at lower stopband and one upper stopband	4	0.5	>15	[6] (2017)
WR-3	309.35	4.4%	SU-8 (three layers)	Chebyshev, one TZ at lower stopband	3	0.4	>15	[12] (2013)
WR-3	286.6	5.58%	CNC (*E*-plane split)	Chebyshev, one TZ at upper stopband	3	0.41	>14	This work
WR-3	298.6	5.36%	SU-8 (three layers)	Chebyshev, three TZs at upper stopband	3	0.45	>16	This work
WR-1.5	570	8.77%	DRIE (two pieces)	Chebyshev, no TZ	3	0.9	>10	[9] (2012)
WR-1.5	671	7.91%	SU-8 (three layers)	Chebyshev, one TZ at lower stopband	3	0.65	>11	[13] (2013)

Note: f_0: center frequency of the filter; *FBW*: fractional bandwidth; TZ: transmission zero; *n*: filter order; *IL*: passband insertion loss; *RL*: passband return loss.

The measured results for the SU-8 filter are shown in Fig. 9. It can be observed from Fig. 9(b) that there are significant ripples in the measured S_{21} response. A different network analyzer was used in these measurements to those of the CNC filter and the ripple is attributed to a poor match in the receiver head which has a transmit-only module at Port 2. This problem is discussed in detail in [27]. The measured insertion loss is around 0.45 dB in the passband and a larger than 30-dB rejection within the upper stopband. However, the center frequency of this filter is shifted upward by around 7 GHz from the simulation. Because the layer thickness determines the resonator height *b*, simulations show that the center frequency of the filter does not strongly depend on the layer thickness. So, the difference in center frequency of the filter between measurement and simulation may be due to inaccurate dimensions in the layer plane. The dimensions of the SU-8 filter cavities were measured using a scanning electron microscope. The image in Fig. 6(b) shows the cavity within the second layer and Table II shows the measured resonator dimensions. Measured dimensions in the plane are around 1% smaller than designed values on one side of the SU-8 layer and 3% smaller on the other side, which means that the frequency shift may be caused by both changed dimensions and nonvertical sidewalls. After inserting the measured dimensions in CST simulations, a much improved agreement with measurements is obtained, as shown in Fig. 10.

Table III shows a comparison of measurements on the CNC extracted pole filer and the SU-8 micromachined filter. Both filters comfortably achieve the requirements of a lower than 0.6-dB passband insertion loss, with measured values of 0.41 and 0.45 dB for the metal and SU-8 devices, respectively. The requirements for over 30-dB stopband attenuation are also achieved. The CNC milled extracted pole filter offers a better low frequency rejection, whereas the SU-8 device provides a steeper roll-off on this high frequency side of the passband and a smaller overall volume.

Table IV shows the comparison between waveguide filters reported in open literature and two filters described here. These filters operate in the frequency range from WR-3 band to WR-1.5 band. A comparison of some WR-10 band waveguide filters can be found in [14]. All of the filters summarized in Table IV are based on coupled rectangular resonant cavities, but fabricated using different micromachining techniques. Care must be taken with the comparisons as the filters have different specifications.

VI. CONCLUSION

A CNC milled extracted pole waveguide filter and a SU-8 micromachined filter working in WR-3 band have been designed to best exploit the characteristics of the fabrication processes. It is the first demonstration that a CNC milled filter with a steep rejection characteristic beyond 300 GHz and a SU-8 micromachined filter with novel cross-coupling topology working at WR-3 band. The measured performance of the filters is in very good agreement with the numerical predictions once the latter have been corrected for the small errors in manufacturing. The two filters show no significant difference in performance despite the two alternative fabrication processes and designs. Both filters achieve an insertion loss of below 0.5 dB in a ~10-GHz-wide passband and a rejection of more than 30 dB in the stopband. Either of these two micromachined waveguide filters can therefore be potential replacements of FSS filters used in spaceborne radiometers for unwanted sideband rejection.

REFERENCES

[1] R. J. Martin and D. H. Martin, "Quasi-optical antennas for radiometric remote sensing," *Electron. Commun. Eng. J.*, vol. 8, pp. 37–48, Feb. 1996.

[2] R. Cahill *et al.*, "Low loss FSS for channel demultiplexing and image band rejection filtering," in *Proc. 24th ESTEC Antenna Workshop Innov. Periodic Antennas Photon. Bandgap Fractal Freq. Sel. Surf.*, The Netherlands, May 2001, pp. 103–108, European Space Agency.

[3] R. Dickie *et al.*, "Submillimeter wave frequency selective surface with polarization independent spectral responses," *IEEE Trans. Antennas Propag.*, vol. 57, no. 7, pp. 1985–1994, Jul. 2009.

[4] X. Liao, L. Wan, Y. Yin, and Y. Zhang, "W-band low-loss bandpass filter using rectangular resonant cavities," *IET Microw. Antennas Propag.*, vol. 8, no. 15, pp. 1440–1444, Sep. 2014.

[5] C. A. Leal-Sevillano, J. R. Montejo-Garai, J. A. Ruiz-Cruz, and J. M. Rebollar, "Low-loss elliptical response filter at 100 GHz," *IEEE Microw. Wireless Compon. Lett.*, vol. 22, no. 9, pp. 459–461, Sep. 2012.

[6] J. Q. Ding *et al.*, "WR-3 band quasi-elliptical waveguide filters using higher order mode resonances," *IEEE Trans. THz Sci. Technol.*, vol. 7, no. 3, pp. 302–309, May 2017.

[7] H. V. Jansen, M. J. de Boer, S. Unnikrishnan, M. C. Louwerse, and M. C. Elwenspoek, "Black silicon method X: A review on high speed and selective plasma etching of silicon with profile control: An in-depth comparison between Bosch and cryostat DRIE processes as a roadmap to next generation equipment," *J. Micromech. Microeng.*, vol. 19, no. 3, pp. 033 001-1–033 001-41, Feb. 2009.

[8] J. Y. Li, B. Pan, C. Lugo, M. Tentzeris, and J. Papapolymerou, "Design and characterization of a W-band micromachined cavity filter including a novel integrated transition from CPW feeding lines," *IEEE Trans. Microw. Theory Techn.*, vol. 55, no. 12, pp. 2902–2910, Dec. 2007.
[9] K. M. K. H. Leong *et al.*, "WR1.5 silicon micromachined waveguide components and active circuit integration methodology," *IEEE Trans. Microw. Theory Techn.*, vol. 60, no. 4, pp. 998–1005, Apr. 2012.
[10] J. R. Stanec and N. S. Barker, "Fabrication and integration of micromachined submillimeter-wave circuits," *IEEE Microw. Wireless Compon. Lett.*, vol. 21, no. 8, pp. 409–411, Aug. 2011.
[11] X. Shang, M. Ke, Y. Wang, and M. J. Lancaster, "Micromachined W-band waveguide and filter with two embedded H-plane bends," *IET Microw. Antennas Propag.*, vol. 5, no. 3, pp. 334–339, Feb. 2011.
[12] Q. Chen, X. Shang, Y. Tian, J. Xu, and M. J. Lancaster, "SU-8 micromachined WR-3 band waveguide bandpass filter with low insertion loss," *Electron Lett.*, vol. 49, no. 7, pp. 480–482, Mar. 2013.
[13] X. Shang, Y. Tian, M. J. Lancaster, and S. Singh, "A SU8 micromachined WR-1.5 band waveguide filter," *IEEE Microw. Wireless Compon. Lett.*, vol. 23, no. 6, pp. 300–302, Jun. 2013.
[14] X. Shang *et al.*, "W-band waveguide filters fabricated by laser micromachining and 3-D printing," *IEEE Trans. Microw. Theory Techn.*, vol. 64, no. 8, pp. 2572–2580, Aug. 2016.
[15] C. H. Smith, A. Sklavonuos, and N. S. Barker, "SU-8 micromachining of millimeter and submillimeter waveguide circuits," in *IEEE MTT-S Int. Microw. Symp. Dig.*, Boston, MA, USA, 2009, pp. 961–964.
[16] J. Bornemann, "A new class of E-plane integrated millimeter-wave filters," in *IEEE MTT-S Int. Microw. Symp. Dig.*, Long Beach, CA, USA, vol. 2, 1989, pp. 599–602.
[17] J. Hong and M. J. Lancaster, *Microstrip Filters for RF/Microwave Applications*. New York, NY, USA: Wiley, 2001.
[18] R. R. Mansour and G. Woods, "Design of millimeter-wave extracted-pole filters with asymmetrical frequency characteristics," in *IEEE MTT-S Int. Microw. Symp. Dig.*, Boston, MA, USA, vol. 2, 1991, pp. 659–663.
[19] J. D. Rhodes and R. J. Cameron, "General extracted pole synthesis technique with applications to low-loss TE_{011} mode filters," *IEEE Trans. Microw. Theory Techn.*, vol. 28, no. 9, pp. 1018–1028, Sep. 1980.
[20] Y. Yang, M. Yu, and Q. Wu, "Advanced synthesis technique for unified extracted pole filters," *IEEE Trans. Microw. Theory Techn.*, vol. 64, no. 12, pp. 4463–4472, Dec. 2016.
[21] J. R. Montejo-Garai *et al.*, "Compact low-cost diplexer with elliptic filter response for Ka-band satellite applications," in *Proc. 2015 Int. Workshop Microw. Filters*, 2015, pp. 1–3.
[22] C. H. Smith III, H. Xu, and N. S. Barker, "Development of a multilayer SU-8 process for terahertz frequency waveguide blocks," in *IEEE MTT-S Int. Microw. Symp. Dig.*, 2005, pp. 439–442.
[23] B. Liu, H. Yang, and M. J. Lancaster, "Global optimization of microwave filters based on a surrogate model-assisted evolutionary algorithm," *IEEE Trans. Microw. Theory Techn.*, vol. 65, no. 6, pp. 1976–1985, Jun. 2017.
[24] J. D. Williams and W. Wang, "Study on the postbaking process and the effects on UV lithography of high aspect ratio SU-8 microstructures," *J. Microlithogr. Microfab. Microsyst.*, vol. 3, pp. 563–568, 2004.
[25] X. Shang, M. Ke, Y. Wang, and M. J. Lancaster, "WR-3 band waveguides and filters fabricated using SU8 photoresist micromachining technology," *IEEE Trans. THz Sci. Technol.*, vol. 2, no. 6, pp. 629–637, Oct. 2012.
[26] D. Glynn *et al.*, "Submillimetre rectangular waveguides based on SU-8 photoresist micromachining technology," in *Proc. 2016 46th Eur. Microw. Conf.*, London, U.K., 2016, pp. 1346–1349.
[27] Y. Wang, M. J. Lancaster, M. Ke, and X. Shang, "Measurements of micromachined waveguide devices at WR-3 band using a T/R-T module based network analyzer," in *Proc. 77th ARFTG Microw. Meas. Conf.*, Baltimore, MD, USA, 2011, pp. 1–4.

Hao Yang was born in Wuhan, China, in 1991. He received the B.Eng. degree in electronics and information engineering from the Huazhong University of Science and Technology, Wuhan, in 2014, and the B.Eng. degree in electronic and electrical engineering from the University of Birmingham, Birmingham, U.K., in 2014, where he is currently working toward the Ph.D. degree.

His current research interests include terahertz frequency filters and mutiplexers.

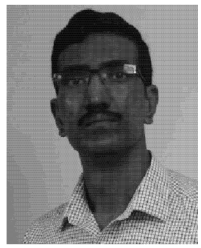

Yuvaraj Dhayalan received the M.Sc. degree in materials science from the College of Engineering, Anna University, Chennai, India, in 2004, and the Ph.D. degree from the Indian Institute of Science, Bangalore, India, in 2010.

He has been with the University of Birmingham, Birmingham, U.K., as a Research Fellow since 2015. His research interests are in thin film, nanoscale devices, microfabrication, and nanofabrication.

Xiaobang Shang (M'13) was born in Hubei, China, in 1986. He received the B.Eng. degree (first class) in electronic and communication engineering from the University of Birmingham, Birmingham, U.K., in 2008, the B.Eng. degree in electronics and information engineering from Huazhong University of Science and Technology, Wuhan, China, in 2008, and the Ph.D. degree in microwave engineering from the University of Birmingham, in 2011. His doctoral research concerned micromachined terahertz waveguide circuits and synthesis of multiband filters.

He is currently a Senior Research Scientist with the National Physical Laboratory (NPL), U.K. Prior to joining the NPL, he was a Research Fellow with the University of Birmingham. His current main research interests include microwave measurements, microwave filters and multiplexers, and micromachining techniques.

Dr. Shang was the recipient of the ARFTG Microwave Measurement Student Fellowship Award in 2009 and the co-recipient of the Tatsuo Itoh Award in 2017.

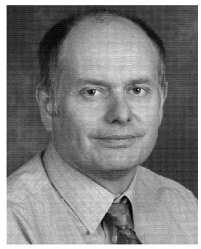

Michael J. Lancaster (SM'04) was born in U.K., in 1958. He received the Graduation degree in physics and Ph.D. dergree for research into nonlinear underwater acoustics from Bath University, Bath, U.K., in 1980 and 1984, respectively.

After leaving Bath University, he joined the Surface Acoustic Wave (SAW) Group, Department of Engineering Science, Oxford University, as a Research Fellow. His research was in the design of new, novel SAW devices, including RF filters and filter banks. In 1987, he became a Lecturer with the Department of Electronic and Electrical Engineering, University of Birmingham, Birmingham, U.K., lecturing in electromagnetic theory and microwave engineering. Shortly after he joined the department, he began the study of the science and applications of high-temperature superconductors, working mainly at microwave frequencies. He was promoted to the Head of the Department of Electronic, Electrical and Systems Engineering in 2003. He has authored or coauthored 2 books and more than 200 papers in refereed journals. His research interests include microwave filters and antennas, as well as the high frequency properties and applications of a number of novel and diverse materials. This includes micromachining as applied to terahertz communications devices and systems.

Dr. Lancaster is a Fellow of the Institution of Engineering and Technology and the U.K. Institute of Physics. He is a Chartered Engineer and a Chartered Physicist. He has served on the IEEE Microwaves and Theory and Techniques Society International Microwave Symposium Technical Committees.

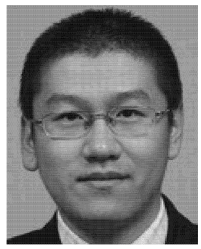

Bo Liu (M'15–SM'17) received the B.S. degree from Tsinghua University, Beijing, China, in 2008, and the Ph.D. degree from the MICAS Laboratories, University of Leuven (KU Leuven), Leuven, Belgium, in 2012.

From 2012 to 2013, he was a Humboldt Research Fellow and was with the Technical University of Dortmund, Dorthmund, Germany. In 2013, he was appointed a Lecturer with Wrexham Glyndwr University, Wrexham, U.K., where he was promoted to a Reader in computer-aided design in 2016. He has authored or coauthored 1 book and more than 40 papers in international journals, edited books, and conference proceedings. His research interests include design automation methodologies of analog/RF integrated circuits, microwave devices, microelectromechanical systems, evolutionary computation and machine learning.

Dr. Liu is an Honorary Fellow of the University of Birmingham, Birmingham, U.K.

Hui Wang received the M.Sc. and Ph.D. degrees in astrophysics and space instrumentation from the University Pierre and Marie Curie, Paris, France, in 2005 and 2009, respectively.

She joined the Millimetre Wave Technology Group, STFC Rutherford Appleton Laboratory, Oxfordshire, U.K., in 2009, where she is currently leading mixer device development within the group. Her current research interests include millimeter-wave and terahertz devices, primarily heterodyne frequency mixers and harmonic up-conversion multipliers, in support of earth observation and astronomy remote sounding experiments.

Manju Henry received the Master's and Ph.D. degrees in electronic engineering from the Cochin University of Science and Technology, Kerala, India, in 1998 and 2002, respectively.

After receiving the Ph.D. degree, she had done five years of postdoctoral studies with the Institute of High Frequency and Microwave Techniques, Karlsruhe Institute of Technology, the former FZK, Karlsruhe, Germany, and at the University of Surrey, Guildford, U.K. She joined the Millimetre Wave Technology Group, STFC Rutherford Appleton Laboratory, Oxfordshire, U.K., in 2007. After joining the group, she had undertaken key technical and management roles in several European Union/European Space Agency programs. She is currently involved in a wide range of tasks that include millimeter-wave passive system design for atmospheric sounding and astronomy, active system development for meteorological remote sounding, and security imaging.

Peter G. Huggard (M'11–SM'12) received the B.A. (Mod) degree in experimental physics and Ph.D. degree from the University of Dublin, Trinity College, Dublin, Ireland, in 1986 and 1991, respectively.

Since 2000, he has been a member of the Millimetre Wave Technology Group, UK's STFC Rutherford Appleton Laboratory, Oxfordshire, U.K. His current research interests include developing filters, sources and detectors for gigahertz and terahertz radiation.

Global Optimization of Microwave Filters Based on a Surrogate Model-Assisted Evolutionary Algorithm

Bo Liu, *Member, IEEE*, Hao Yang, and Michael J. Lancaster, *Senior Member, IEEE*

***Abstract*— Local optimization is a routine approach for full-wave optimization of microwave filters. For filter optimization problems with numerous local optima or where the initial design is not near to the optimal region, the success rate of the routine method may not be high. Traditional global optimization techniques have a high success rate for such problems, but are often prohibitively computationally expensive considering the cost of full-wave electromagnetic simulations. To address the above challenge, a new method, called surrogate model-assisted evolutionary algorithm for filter optimization (SMEAFO), is proposed. In SMEAFO, considering the characteristics of filter design landscapes, Gaussian process surrogate modeling, differential evolution operators, and Gaussian local search are organized in a particular way to balance the exploration ability and the surrogate model quality, so as to obtain high-quality results in an efficient manner. The performance of SMEAFO is demonstrated by two real-world design cases (a waveguide filter and a microstrip filter), which do not appear to be solvable by popular local optimization techniques. Experiments show that SMEAFO obtains high-quality designs comparable with global optimization techniques but within a reasonable amount of time. Moreover, SMEAFO is not restricted by certain types of filters or responses. The SMEAFO-based filter design optimization tool can be downloaded from http://fde.cadescenter.com.**

***Index Terms*— Design optimization, design tools, evolutionary computation, Gaussian process (GP), metamodeling, microwave filters.**

I. Introduction

MICROWAVE filter design can be formulated as an optimization problem. Among various optimization methods, evolutionary algorithms (EAs) are being widely used for microwave design optimization due to their high global optimization ability, free of a good initial design, wide applicability, and robustness [1]–[3]. Moreover, they are embedded in most commercial electromagnetic (EM) simulation tools, such as CST Microwave Studio. However, EAs are seldom applied to microwave filter design, because full-wave EM simulations are often needed to obtain accurate performance evaluation, which are computationally expensive. Considering thousands to tens of thousands of EM simulations needed for a standard EA to get the optimum, the filter design optimization time can be unbearable (e.g., several months).

To obtain an optimal design in a reasonable timeframe, local optimization from an initial design has become a routine approach for filter design optimization during the last decade. Derivative-based local optimization methods (e.g., sequential quadratic programming [4]) and derivative free local optimization methods (e.g., the Nelder–Mead simplex method [5]) are widely applied. Because the quality of the initial design is essential for the success of local optimization, a lot of research has been done aiming to find a reasonably good initial design efficiently. Available methods mainly include employing equivalent circuit [6], low-fidelity EM model [7] for a preliminary relatively low-cost optimization, and coupling matrix fitting [8].

To further improve the efficiency of local optimization, the space mapping technique [9] is widely used. Several important improvements have been made to enhance the reliability and the efficiency of traditional space mapping, such as introducing the human design intuition [10], altering an EM model by embedding suitable tuning elements (port tuning) [11], and the multilevel method [12]. The port tuning method has shown great success in commercial applications for planar filters. Methods based on integrating human design intuition and port tuning have obtained optimal designs for some filters whose initial designs are not near the optimal region. Adjoint sensitivity is also introduced to replace traditional gradient-based local optimization techniques, and shows great speed improvement [13].

Although many filters have been successfully designed using the available techniques, and some of them even only need a few high-fidelity EM simulations, available methods still face severe challenges when the initial design is not near the optimal region and/or the filter design landscape has many local optima (not smooth enough) [10]. Unfortunately, this happens to many microwave filter design problems, and this problem is the target of this paper. Clearly, traditional space mapping and adjoint sensitivity techniques are difficult to provide a generic solution to this issue, because their main goal is to improve the efficiency of local optimization rather than improve the optimization capacity (i.e., jumping out of

Manuscript received July 5, 2016; revised October 25, 2016; accepted December 24, 2016. Date of publication March 2, 2017; date of current version June 2, 2017. This work was supported by the U.K. Engineering and Physical Science Research Council under Project EP/M016269/1.

B. Liu is with the School of Electrical, Electronic, and System Engineering, University of Birmingham, Edgbaston, Birmingham B15 2TT, U.K., and also with the Department of Computing, Wrexham Glyndwr University, Wrexham LL11 2AW, U.K. (e-mail: b.liu.3@bham.ac.uk; liubo168@gmail.com).

H. Yang and M. J. Lancaster are with the School of Electrical, Electronic, and System Engineering, University of Birmingham, Edgbaston, Birmingham B15 2TT, U.K. (e-mail: hxy297@student.bham.ac.uk; m.j.lancaster@bham.ac.uk).

Color versions of one or more of the figures in this paper are available online at http://ieeexplore.ieee.org.

Digital Object Identifier 10.1109/TMTT.2017.2661739

local optima). In recent years, some novel methods have been proposed to improve the optimization capacity while keeping the efficiency improvement, but they often concentrate on a certain type of filter or response [6].

Also, with the rapid improvement of computing power and numerical analysis techniques, high-fidelity EM simulation of many microwave filters can be completed within 20 min. Although directly employing EAs is still prohibitively computationally expensive, developing *widely applicable* methods with *largely improved optimization ability* compared with local optimization, but using *a practical timeframe* (e.g., within several days) for the targeted problem is of great importance to complement the state of the arts.

An alternative is surrogate model-assisted EAs (SAEAs), which introduce surrogate modeling to EAs. In the context of filter optimization, a surrogate model is a computationally cheap mathematical model approximating the output of EM simulations, which is often constructed by statistical learning techniques and is widely used in space mapping. By coupling surrogate models with an EA, some of the EM simulations can be replaced by the surrogate model predictions, and the computational cost can, therefore, be reduced significantly. SAEA is attracting increasing attention in the computational intelligence field, and various new SAEAs have been proposed.

However, most of the available SAEAs are not suitable for filter optimization. Besides the efficiency issue, microwave filter optimization has two difficulties:

1) A filter is a narrowband device, and the optimal region is often very narrow.
2) There often exist numerous local optima in the landscape, especially for high-order filters.

Because of different tradeoffs between the exploration ability and the surrogate model quality, most available SAEAs can get either the optimal solution, but need more than necessary EM simulations causing very long optimization time or spend reasonable time but miss the optimal solution. The reasons will be described in Section III-A.

To address this challenge, a new method is proposed, called SAEA for filter optimization (SMEAFO). The main innovation of SMEAFO is the new SAEA framework balancing the exploration ability and the surrogate model quality considering the characteristics of filter design landscape. SMEAFO targets at filter optimization problems with numerous local optima and/or where the initial design is far from the optimal region, aiming to the following:

1) achieve comparable results with standard EAs (often have very high success rate and are considered as the best in terms of solution quality);
2) obtain significant speed improvement compared with standard EAs and complete the optimization in a reasonable timeframe (several hours to several days) for problems with less than 20 min per EM simulation;
3) general enough for most kinds of filters without considering specific properties of the targeted filter.

The remainder of this paper is organized as follows. Section II introduces the basic techniques. Section III introduces the SMEAFO algorithm, including its main ideas, design of each algorithmic component, its general framework, and parameter settings. Section IV presents a waveguide filter and a microstrip filter that do not appear to be solvable by available popular local optimization techniques to show the performance of SMEAFO. Comparisons with the standard differential evolution (DE) algorithm are also provided. The concluding remarks are presented in Section V.

II. Basic Techniques

A. Gaussian Process Surrogate Modeling

Among various surrogate modeling methods, Gaussian process (GP) machine learning [14] is selected for SMEAFO. The main reason is that the prediction uncertainty of GP has a sound mathematical background, which is able to take advantage of prescreening methods [15] for surrogate model-based optimization. A brief introduction is as follows. More details are in [14].

Given a set of observations $x = (x^1, \ldots, x^n)$ and $y = (y^1, \ldots, y^n)$, GP predicts a function value $y(x)$ at some design point x by modeling $y(x)$ as a Gaussian distributed stochastic variable with mean μ and variance σ^2. If the function is continuous, the function values of two points x^i and x^j should be close if they are highly correlated. In this paper, we use the Gaussian correlation function to describe the correlation between two variables

$$\text{corr}(x^i, x^j) = \exp\left(-\sum_{l=1}^{d} \theta_l |x_l^i - x_l^j|^2\right) \tag{1}$$

where d is the dimension of x and θ_l is the correlation parameter, which determines how fast the correlation decreases when x^i moves in the l-direction. The values of μ, σ, and θ are determined by maximizing the likelihood function that $y = y^i$ at $x = x^i (i = 1, \ldots, n)$. The optimal values of μ and σ can be found by setting the derivatives of the likelihood function to 0 and solve the equations, which are as follows:

$$\hat{\mu} = (I^T R^{-1} y)^{-1} I^T R^{-1} y \tag{2}$$

$$\hat{\sigma^2} = (y - I\hat{\mu})^T R^{-1} (y - I\hat{\mu}) n^{-1} \tag{3}$$

where I is an $n \times 1$ vector with all elements having the value of one and R is the correlation matrix

$$R_{i,j} = \text{corr}(x^i, x^j), \quad i, j = 1, 2, \ldots, n. \tag{4}$$

Using the GP model, the function value $y(x^*)$ at a new point x^* can be predicted as (x^* should be included in the correlation matrix)

$$\hat{y}(x^*) = \hat{\mu} + r^T R^{-1} (y - I\hat{\mu}) \tag{5}$$

where

$$r = [\text{corr}(x^*, x^1), \text{corr}(x^*, x^2), \ldots, \text{corr}(x^*, x^n)]^T. \tag{6}$$

The measurement of the uncertainty of the prediction (mean square error), which is used to access the model accuracy, can be described as

$$\hat{s^2}(x^*) = \hat{\sigma^2}[I - r^T R^{-1} r + (I - r^T R^{-1} r)^2 (I^T R^{-1} I)^{-1}]. \tag{7}$$

To make use of the prediction uncertainty to assist SAEA, the lower confidence bound prescreening [15], [16] is selected. We consider the minimization of $y(x)$ in this paper. Given the predictive distribution $N(\hat{y}(x), s^2(x))$ for $y(x)$, a lower confidence bound prescreening of $y(x)$ can be defined as [16]

$$y_{lcb}(x) = \hat{y}(x) - \omega s(x) \qquad \omega \in [0, 3] \tag{8}$$

where ω is a constant, which is often set to two to balance the exploration and exploitation ability [15].

In this paper, we use the ooDACE toolbox [17] to implement the GP surrogate model.

B. Differential Evolution

In SMEAFO, the DE algorithm [18] is selected as the global search engine. DE outperforms many EAs for continuous optimization problems [18] and also shows advantages for EM design optimization problems among various EAs [19]. DE is an iterative method. In each iteration, the mutation operator is firstly applied to generate a population of mutant vectors. A crossover operator is then applied to the mutant vectors to generate a new population. Finally, selection takes place and the corresponding candidate solutions from the old population and the new population compete to comprise the population for the next iteration.

In DE, mutation is the main approach to explore the design space. There are a few different DE mutation strategies trading off the convergence speed and the population diversity (implying higher global exploration ability) in different manners. Arguably, the three DE mutation strategies that are widely used in engineering design optimization are as follows.

1) *Mutation Strategy 1*: DE/best/1

$$v^i = x^{\text{best}} + F \cdot (x^{r_1} - x^{r_2}) \tag{9}$$

where x^{best} is the best individual in P (the current population) and x^{r_1} and x^{r_2} are two different solutions randomly selected from P and are also different from x^{best}. v^i is the ith mutant vector in the population after mutation. $F \in (0, 2]$ is a control parameter, often called the scaling factor [18].

2) *Mutation Strategy 2*: DE/rand/1

$$v^i = x^{r_3} + F \cdot (x^{r_1} - x^{r_2}). \tag{10}$$

Compared with DE/best/1, x^{best} is replaced by a randomly selected solution x^{r_3} that is also different from x^{r_1} and x^{r_2}.

3) *Mutation Strategy 3*: DE/current-to-best/1[1]

$$v^i = x^i + F \cdot (x^{\text{best}} - x^i) + F \cdot (x^{r_1} - x^{r_2}) \tag{11}$$

where x^i is the ith vector in the current population.

Crossover is then applied to the population of mutant vectors to produce the child population U, which works as follows.

1) Randomly select a variable index $j_{\text{rand}} \in \{1, \ldots, d\}$.

[1]This mutation strategy is also referred to as DE/target-to-best/1.

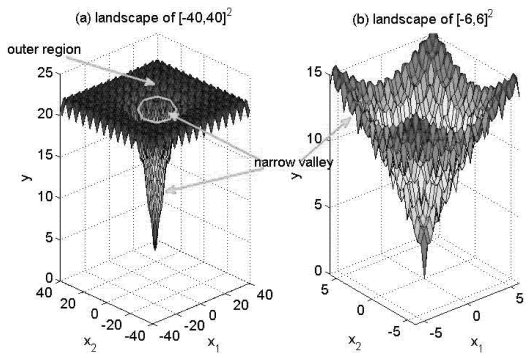

Fig. 1. Illustrative figure of filter design landscape: the Ackley function [21] is used.

2) For each $j = 1$ to d, generate a uniformly distributed random number rand from $(0, 1)$ and set

$$u^i_j = \begin{cases} v^i_j, & \text{if } (\text{rand} \le \text{CR}) | j = j_{\text{rand}} \\ x^i_j, & \text{otherwise} \end{cases} \tag{12}$$

where $\text{CR} \in [0, 1]$ is a constant called the crossover rate.

Following that, the selection operation decides on the population of the next iteration, which is often based on a one-to-one greedy selection between P and U.

C. Gaussian Local Search

Gaussian local search is a verified effective method for elaborate search in a local area [20]. Gaussian local search is often used for enhancing local search ability of EAs. In SMEAFO, the following implementation is used:

$$xg^i_j = \begin{cases} x^i_j + N(0, \sigma^{\text{gls}}_j), & \text{if rand} \le \frac{1}{d} \\ x^i_j, & \text{otherwise;} \\ & j = 1, 2, \ldots, d \end{cases} \tag{13}$$

where $N(0, \sigma^{\text{gls}}_j)$ is a Gaussian distributed random number with a standard deviation of σ^{gls}_j and rand is a uniformly distributed random number from $(0, 1)$.

III. SMEAFO Algorithm

A. Challenges and Main Ideas of SMEAFO

The SMEAFO algorithm is an SAEA. Integrating a surrogate model into global optimization is much more difficult than integrating it into space mapping because there is no information of the optimal region. Recall the two major difficulties for filter optimization described in Section I (an illustrative figure is Fig. 1): 1) the optimal region is located in a (very) narrow valley of the design space and 2) there are often numerous local optima. The SAEA, therefore, should have sufficient exploration ability to jump out of local optima in the outer region so as to find the narrow valley and to jump out of local optima within it. Although this is often achievable for a modern standard EA, SAEAs may not have the same exploration ability due to the surrogate model prediction uncertainty, i.e., some optimal designs may be predicted wrong and then the SAEA search is guided to wrong directions.

High exploration ability indicates getting access to diverse candidate designs. To make a good prediction of them, more training data points through EM simulations are necessary to maintain the surrogate model quality, which decreases the efficiency. Finding an appropriate balance between the exploration ability and the efficiency for filter design landscape is the main challenge of SMEAFO.

The required exploration ability in the filter optimization process is different from time to time. Instead of using a fixed SAEA with a certain exploration ability, it is natural to divide it into the *exploration phase* aiming to find a near optimal region and the *exploitation phase* aiming to obtain the final optimal design from near-optimal designs. The latter phase requires less exploration ability (indicating more space for efficiency) without sacrificing the solution quality. Various methods can be used for the exploitation phase, and space mapping is compatible. Because space mapping is sometimes sensitive to the surrogate model type and settings [7], a surrogate model-assisted Gaussian local search method is used in SMEAFO for the sake of generality. Now the major challenge is the exploration phase providing both sufficient exploration ability and efficiency.

To balance the exploration ability and the efficiency, available SAEAs can be mainly classified into "conservative" SAEAs and "active" SAEAs. Conservative SAEAs [22], [23] emphasize the exploration ability. These methods begin with a standard EA for certain iterations aiming to collect training data points that are able to build a reasonably good global surrogate model and then iteratively improve the solution quality and the surrogate model quality in the consecutive search. Thus, the exploration ability can benefit a lot at the cost of a considerable computing overhead for standard EA-based iterations. When applied to filter optimization, much of this computing overhead is wasted because they are collecting training data points for modeling the outer region instead of the narrow valley where the optimal design is located.

Active SAEAs, in contrast, emphasize the efficiency [15]. These methods perform exact expensive evaluations to the "optimal" solutions predicted by the existing surrogate model, despite that its quality may not be good enough. The number of expensive exact evaluations is therefore highly reduced, but the exploration ability becomes a weakness. Prescreening methods [16], [24] are used to assist jumping out of local optima, but they cannot fully solve the problem. In [15], tests on the Ackley benchmark problem (with a narrow valley and many local optima) [21] (Fig. 1) show that such SAEAs are not able to jump out of local optima. Hence, the exploration ability is insufficient for filter optimization.

The exploration phase of SMEAFO follows the idea of active SAEAs to avoid consuming considerable EM simulations to nonoptimal regions. To largely improve the exploration ability compared with existing active SAEAs, two questions are focused: 1) what is the search method to obtain sufficient exploration ability? and 2) how to build surrogate models of sufficient quality using as few samples as possible (for the sake of efficiency) in order to support the exploration ability? This is achieved by the combination of a novel surrogate model assisted search method with specific DE mutation and training sample selection methods, which will be detailed in Section III-B.

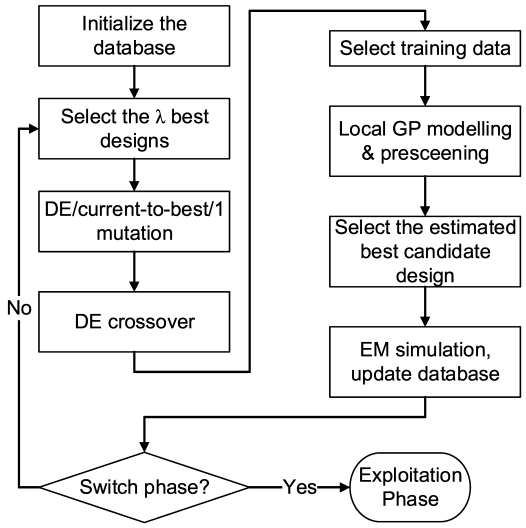

Fig. 2. Flow diagram of the exploration phase.

B. Design of the Exploration Phase

The general framework of the exploration phase is shown in Fig. 2, which consists of the following steps.

- Step 1: Sample λ (often small) candidate designs, perform EM simulations of all of them, and let them form the initial database.
- Step 2: Select the λ best designs from the database based on the objective function values to form a population P.
- Step 3: Apply the DE/current-to-best/1 mutation (11) and the crossover operator (12) on P to generate λ child solutions.
- Step 4: For each child solution, select training data points and construct a local GP surrogate model.
- Step 5: Prescreen the λ child solutions generated in Step 3 using the lower confidence bound method. Estimate the best child solution based on the lower confidence bound values.
- Step 6: Perform EM simulation to the estimated best child solution from Step 5. Add this design and its performance (EM simulation result) to the database. Go back to Step 2 until switching to the exploitation phase.

A main difference compared with available active SAEAs is that a standard EA process is not adopted; instead, only the predicted best candidate design is simulated and the current best λ candidate designs are used as the new population in each iteration. This new SAEA framework improves the locations of training data points. It is well known that the number of training data points affects the quality of the surrogate model, while their locations are often overlooked. With the same number of training data points, it is intuitive that using training data points located near the points waiting to be predicted (child population in Step 3) can obtain surrogate model(s) with better quality. This is implemented in Steps 2–6.

From Step 2 to Step 6, in each iteration, the λ current best candidate solutions construct the parent population (it is reasonable to assume that the search focuses on the promising region) and the best candidate design based on prescreening in the child population is selected to replace the worst one in the parent population. Hence, only at most one candidate is changed in the parent population in each iteration, so the best candidate in the child solutions in several consecutive iterations may not be far from each other (they will then be simulated and are used as training data points). Therefore, the training data points describing the current promising region can be much denser compared with those generated by a standard EA population updating mechanism, which may spread in different regions of the design space, while there may not be sufficient training data points around the candidate solutions to be prescreened.

Using the database with improved sample locations for surrogate modeling, a consecutive critical problem is selecting samples from it which will be used as the training data points. Most SAEAs build a single surrogate model for predicting the child population. For example, a certain number of evaluated promising solutions (ranked by fitness function values) [15] or latest solutions are used to build a model for the child population. But such methods are not suitable for the targeted problem because of the two design landscape characteristics of microwave filters (Section III-A). In particular, due to the narrow valley where the optimal design is located, a promising point that is located near it may be predicted to be not promising when many training data points are in the outer nonoptimal region. The reason is that the hyperparameters in (1) are highly likely to be poorly estimated in likelihood function optimization when the number of training data points near it is insufficient. Therefore, in SMEAFO, a local GP surrogate model is built for each child solution using τ nearest samples (based on Euclidean distance). This means that λ separate local GP models are built in each iteration.

With improved surrogate model quality, appropriate search operators should be selected to provide neither insufficient nor excessive population diversity, which directly determine the exploration ability. Intuitively, DE/best/1 (9) may not have sufficient population diversity, because the added diversity into the current best design is not large. Note that although there exist SAEAs with DE/best/1 showing success [25], the optima of the test problems are not located in a narrow valley. In contrast, DE/rand/1 (10) may introduce too much population diversity. DE/current-to-best/1 (11) is in the middle. Pilot experiments on the Ackley benchmark problem [21] are carried out. Results show that DE/current-to-best/1 just gets an appropriate balance of the population diversity and the surrogate model quality (almost 100% getting very near to the global optimum) with the new GP model-assisted search framework, while DE/rand/1 performs the worst because excessive diversity suffers the surrogate model quality.

It has to be noted that the above particular surrogate model-assisted search method, the training data selection method for GP modeling (building a separate GP model for each child solution), and the above DE mutation operator (DE/current-to-best/1) must be used together.

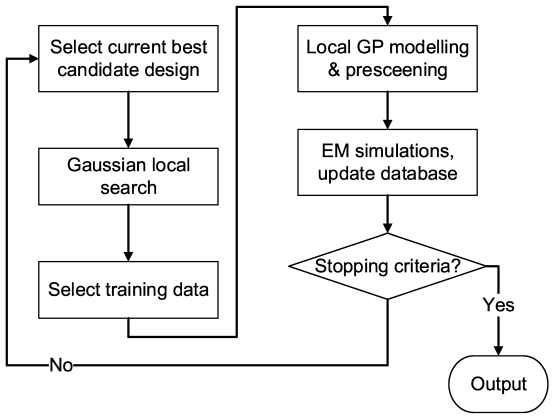

Fig. 3. Flow diagram of the exploitation phase.

Pilot experiments on real-world filters show that when any of the factors is altered, the algorithm often fails to find the narrow valley or the performance becomes unstable.

Note that the lower confidence bound method also contributes to the algorithm performance. In Step 5, instead of the predicted value of the GP model, the lower confidence bound value (8) is used for ranking. The use of lower confidence bound can balance the search between present promising regions [i.e., with low $\hat{y}(x)$ values in (8)] and less explored regions [i.e., with high $s(x)$ values], so as to improve the ability of an SAEA to jump out of local optima. Reference [15] provides more details.

For initial population generation (Step 1), each candidate solution is calculated by (14) if an initial design is available; otherwise, it is generated randomly within the design space

$$x_j = x_j^{\text{init}} + N(0, \sigma_{\text{init}}), \quad j = 1, 2, \ldots, d \tag{14}$$

where x^{init} is the initial design and σ_{init} is the standard deviation of the added Gaussian distributed random number. The value of σ_{init} is roughly estimated according to the response of the initial design. Pilot experiments show that the initial population is far from optimal no matter if using (14) or random generation due to the landscape characteristics of microwave filters and the quality of the initial designs. Note that SMEAFO performs global optimization and a poor initial population is not a problem and is even assumed.

C. Design of the Exploitation Phase

The general framework of the exploitation phase is shown in Fig. 3, which consists of the following steps.

Step 1: Perform Gaussian local search from the current best design in the database to generate d (number of design variables) solutions.

Step 2: For each solution from Step 1, select training data points using the method in Section III-B and construct a local GP surrogate model.

Step 3: Prescreen the d solutions generated in Step 1 using the lower confidence bound method. For each of them, if the lower confidence bound value is better than the current best design, perform an

EM simulation to it. Add this design and its performance (the EM simulation result) to the database.

Step 4: If a preset stopping criterion (e.g., computing budget) is met, output the best solution from the database; otherwise, go back to Step 1.

The goal of the exploitation phase is to obtain the final optimal design from a near optimal design based on a surrogate-based local search method with largely reduced exploration ability. Although heuristic local search methods themselves are not complex, a common challenge is the adaptation of critical parameters, including the starting condition and the scale of exploitation [26].

Note that there is no clear threshold to divide exploration and exploitation in a search process because "near optimal" is an empirical definition [26]. However, an appropriate definition of the starting condition of the exploitation phase is important for SMEAFO. Early starting of this phase may make the algorithm trapped in a local optimum, while late starting decreases the efficiency. In SMEAFO, we use the average standard deviation of the current population P, σ_P, to reflect the population diversity or progress of SMEAFO. Often, the value of σ_P first increases (exploring the design space) and then decreases (converge to the optimal area) in an SMEAFO run. We set 10% of the maximum σ_P in the exploration phase as the threshold to start the exploitation phase.

For the sake of generality, a verified effective method for elaborate search, Gaussian local search (Section II-C), is used in this phase. σ_{gls} is a critical parameter of Gaussian local search and is problem dependent. However, with the help of the exploration phase, it is set self-adaptively as

$$\sigma_j^{\text{gls}} = 0.5 \times \text{std}(\text{PB}_j), \quad j = 1, 2, \ldots, d \tag{15}$$

where PB is the best d candidate designs in the database and std is the standard deviation. This indicates that 95.4% (2σ value) of the candidate designs generated by Gaussian local search are within the standard deviation of the best d available candidate designs, which are already in a small region. This is in line with the basic idea of this phase (performing local exploitation around the current best design). With the update of PB, the σ^{gls} is self-adapted. Experiments on mathematical benchmark problems and eight real-world filter design problems verified empirical settings of σ_P and the self-adaptive setting of σ^{gls}.

Considering the surrogate model quality, because this phase performs local search, the database provided by the exploration phase is a good starting pool of training data points. The training data pool is also updated adaptively by Step 3 supporting the consecutive local search. The lower confidence bound value is used in Step 3 to avoid missing potentially optimal solutions, which also provides more samples around the optimal region.

D. Parameter Settings

Besides the self-adaptive parameters and the threshold value to start the exploitation phase (they are no longer parameters), remaining parameters are the DE parameters (λ, F, and CR), the number of training data points (τ) for each solution waiting to be prescreened (Step 4 in the exploration phase and Step 2 in the exploitation phase), and σ_{init} (Step 1 in the exploration phase).

The DE parameters have clear setting rules. Following [18], we suggest $F = 0.8$, CR $= 0.8$, and $\lambda = 50$. We suggest $\tau = 8 \times d$. This is based on the empirical rule in [24] and [25] for online surrogate modeling, and pilot experiments show a success. Note that in all the test problems, the same set of the above parameters is used. σ_{init} is a rough estimation of the scale to be added to the initial design if it exists. If the response of the initial design is far from anticipated, a larger σ_{init} can be used; otherwise, a smaller one may be used. This parameter is not sensitive for most filter design cases because no optimal solution is expected in the initial population. For some very challenging cases, using a smaller value is recommended to prevent the valley from becoming too narrow, so as to improve the solution quality and efficiency. The use of (14) is because using information from the initial design (although may have low quality) is better than random initialization.

IV. Experimental Results and Comparisons

SMEAFO has been tested by eight real-world filter design problems (five waveguide filters, one hairpin filter, one microstrip filter, and one diplexer). The initial designs are obtained by equivalent circuits or coupling matrix fitting [27]. The number of design variables varies from 5 to 22. The number of orders varies from 3 to 16. SMEAFO obtains high-quality results to all of them taking from 10 h to four days. We have not successfully solved six out of eight problems by popular local optimization-based methods.

In this section, two examples are used to demonstrate SMEAFO for different kinds of filter optimization problems with different challenges. The first one is a waveguide filter, and the initial design is obtained by coupling matrix fitting. Unfortunately, the initial response is far from the design specifications. The second one is a microstrip filter. The initial design is obtained by an equivalent circuit optimization, and the initial response is reasonably good. However, this seemingly easy problem is, in fact, difficult because the design landscape is very rugged, making local search methods fail to jump out of local optima in the narrow valley.

For the first example, ten runs of SMEAFO with independent random numbers (including initialization) are carried out to test the robustness of SMEAFO and the results are analyzed statistically. A comparison with standard DE is also carried out. Because the advantages of the DE algorithm compared with some other popular EAs (e.g., genetic algorithm and particle swarm optimization) in microwave engineering have been demonstrated in [28], such comparisons will not be repeated here. For the second example, only a single run of SMEAFO is carried out because standard DE is not affordable in terms of the computing overhead. The ability to handle larger search space is especially interesting for filter optimization because this is a major challenge of filter landscapes (Section I). This example has 12 design variables, which is relatively large for filter optimization, and we further intentionally expand the search ranges of each design variable

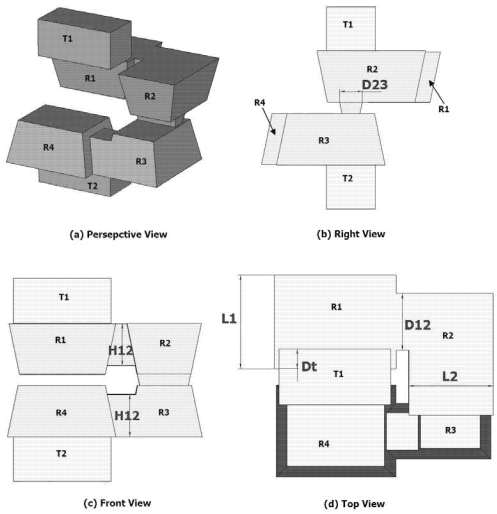

Fig. 4. Waveguide filter: T1, input test port, T2: output test port, and R1–R4: resonators.

TABLE I

RANGES OF THE SIX DESIGN VARIABLES (ALL SIZES IN MILLIMETERS) FOR EXAMPLE 1

$Variables$	$D12$	$D23$	Dt	$H12$	$L1$	$L2$
Lower bound	0.2	0.1	0.05	0.05	0.5	0.5
Upper bound	0.6	0.3	0.3	0.43	0.9	0.9

to make the optimal valley even narrower, so as to verify the capability of SMEAFO on an extreme case.

Both examples are constrained optimization problems. The penalty function method [29] is used to handle the constraints, and the penalty coefficient is set to 50. The examples are run on a PC with Intel 3.5-GHz Core i7 CPU and 8-GB RAM under Windows operating system. CST is used as the EM simulator. No parallel computation is applied in these experiments. All the time consumptions in the experiments are clock time.

A. Example 1

The first example is a WR-3 band (220–325 GHz) waveguide filter, which is composed of four coupled resonators operating in the TE101 mode. The filter has a Chebyshev response [30] (Fig. 4). Because of the fabrication methods in this frequency range, the filters can be complex in construction and difficult to design. The ranges of design variables are in Table I. The design specifications are that the passband is from 296 to 304 GHz (8-GHz passband centered at 300 GHz) and the $\max(|S_{11}|)$ within the passband should be at least less than -20 dB and is as smaller as possible. The stopbands are from 280 to 292 GHz and from 308 to 320 GHz, where the $\max(|S_{11}|)$ should be better than -1 dB. Therefore, the optimization problem is formulated as

$$\begin{aligned} &\text{minimize } \max(|S_{11}|), \quad 296 \text{ GHz–}304 \text{ GHz} \\ &\text{s.t. } \min(|S_{11}|) \geq -1\text{dB}, \quad 280 \text{ GHz–}292 \text{ GHz} \\ &\min(|S_{11}|) \geq -1\text{dB}, \quad 308 \text{ GHz–}320 \text{ GHz}. \end{aligned} \tag{16}$$

The initial design is obtained by coupling matrix fitting and is shown in Table II with a performance in Fig. 5(a). It can

TABLE II

INITIAL SOLUTION AND AN OPTIMIZED SOLUTION (ALL SIZES IN MILLIMETERS) FOR EXAMPLE 1

Variables	$D12$	$D23$	Dt	$H12$	L	$L2$
Initial design	0.42	0.19	0.15	0.369	0.725	0.66
SMEAFO optimized design	0.442	0.257	0.168	0.296	0.735	0.658

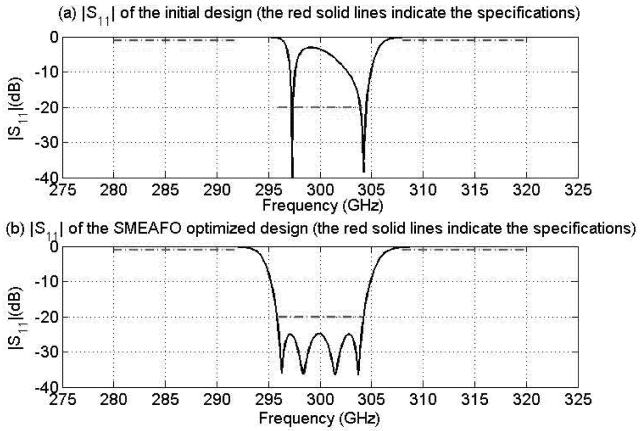

Fig. 5. Response of the waveguide filter.

TABLE III

OPTIMIZED RESULTS USING DIFFERENT METHODS FOR EXAMPLE 1

Methods	$max(\lvert S_{11}\rvert)$: 296–$304GHz$	$min(\lvert S_{11}\rvert)$: 280–$292GHz$	$min(\lvert S_{11}\rvert)$: 308–$320GHz$	time
Nelder-Mead simplex	–3.26 dB	–0.20 dB	–0.05 dB	9.2 hours
sequential quadratic programming	–4.22e-5 dB	–1.7e-3 dB	–0.84 dB	1.9 hours
DE	–22.86 dB	–0.08 dB	–0.17 dB	691.2 hours
SMEAFO	–24.85 dB	–0.12 dB	–0.25 dB	20.6 hours

be seen that this response is far from the specifications. The Nelder–Mead simplex method [5] and the sequential quadratic programming method [4] are first used. These two methods are well-known local optimization methods, and many space mapping techniques are based on these two search engines. The implementation is based on MATLAB optimization toolbox functions fminsearch and fminimax. Each EM simulation costs about 2 min. The results are shown in Table III. It can be seen that both of them fail to find the narrow valley where the optimal design is located. It is not a surprise because the poor response of the initial design indicates that it is not near the optimal region, which is a major challenge for local optimization methods when facing filter design landscapes.

Ten runs with independent random numbers (including ten different initial populations) are carried out for SMEAFO to demonstrate the performance and the robustness. Because the initial response is far from the specifications and considering the ranges of the design variables, we set σ_{init} to 0.1. When the generated values by (14) are not within the ranges of the design variables, they are set to the nearest bound. As was said in Section III-D, the value of σ_{init} is a rough estimation

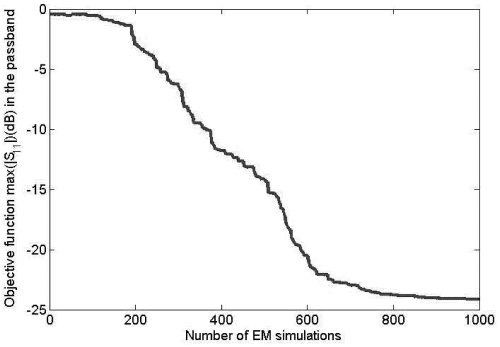

Fig. 6. SMEAFO convergence trend for Example 1 (average of ten runs).

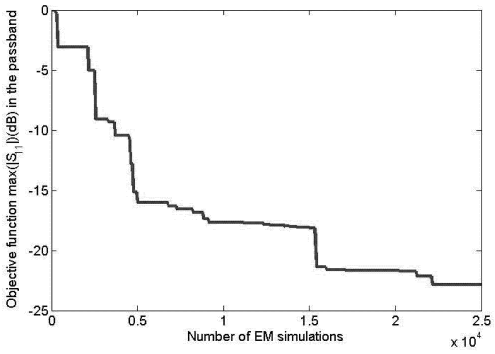

Fig. 7. DE convergence trend for Example 1.

and is not sensitive. The computing budget is 1000 EM simulations, but in most runs, convergence happens before 800 EM simulations. In all the ten runs using SMEAFO, the constraints are satisfied and the average objective function value is −24.14 dB. The best value is −26.90 dB, the worst value is −17.72 dB, and the standard deviation is 3.37. Eight out of ten runs obtain $\max(|S_{11}|)$ (296–304 GHz) smaller than −24 dB. A medium one is provided in Tables II (optimized design variables) and III and Fig. 5(b) (performance). The convergence trend is shown in Fig. 6. It can be seen that the design quality is satisfactory using less than 600 EM simulations on average.

DE is also carried out using the initial population of the SMEAFO run provided in Tables II and III with the same related algorithm parameters of SMEAFO. The computing budget is set to 25 000 EM simulations. The obtained result is −22.86 dB. Hence, SMEAFO obtains more than 33 times speed improvement compared with standard DE for this example, making the unbearable time to be very practical (one month to one day) and obtaining an even better result. The convergence trend of DE is shown in Fig. 7. Comparing the two convergence trends, some observations can be made.

On average, the exploitation phase of SMEAFO starts from about 540 EM simulations with the starting performance of about −17 dB (according to the rule defined in Section III-C). The observations are as follows.

1) DE completes the exploration using about 8500 EM simulations (obtaining −17 dB), while SMEAFO uses about 540 EM simulations, obtaining about 16 times speed improvement.
2) DE then costs 16 500 EM simulations to improve the result from near-optimal designs to the final optimized design because of the rugged landscape in the valley, while the exploitation phase of SMEAFO costs about 250 EM simulations to get a better solution, achieving about 66 times speed improvement. This verifies the effectiveness of main ideas of SMEAFO in both phases.

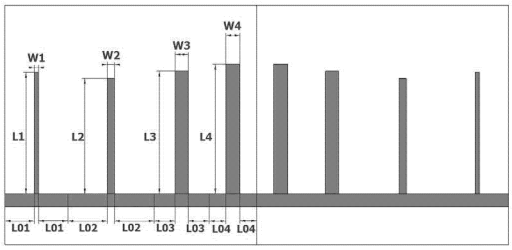

Fig. 8. Microstrip filter: front view.

TABLE IV
RANGES OF THE 12 DESIGN VARIABLES (ALL SIZES IN MILLIMETERS) FOR EXAMPLE 2

$Variables$	$W1$	$W2$	$W3$	$W4$	$L01$	$L02$
Lower bound	0.5	0.5	0.5	0.5	2	2
Upper bound	3.5	3.5	3.5	3.5	8	8
$Variables$	$L03$	$L04$	$L1$	$L2$	$L3$	$L4$
Lower bound	2	2	7	7	7	7
Upper bound	8	8	18	18	18	18

B. Example 2

The second example is an eighth-order microstrip filter working from 3.3 to 7.3 GHz, which is shown in Fig. 8. The ranges of design variables are in Table IV. As mentioned above, they are intentionally expanded to test SMEAFO in an extreme condition. The design specifications are that the passband is from 4 to 7 GHz and the stopbands are from 3.3 to 3.92 GHz and from 7.08 to 7.3 GHz. Therefore, the optimization problem is defined as follows:

$$\begin{aligned} &\text{minimize } \max(|S_{11}|), \quad 4 \text{ GHz–7 GHz} \\ &\text{s.t. } \min(|S_{11}|) \geq -3\text{dB}, \quad 3.3 \text{ GHz–3.92 GHz} \\ &\min(|S_{11}|) \geq -3\text{dB}, \quad 7.08 \text{ GHz–7.3 GHz}. \end{aligned} \tag{17}$$

An equivalent circuit model is available, which is used for a first optimization to get the initial design, in which the simulation is performed by ADS circuit simulator (not Momentum). Because each ADS circuit simulation only costs a few seconds, standard DE is used. The optimized design variables (initial design for full-wave optimization) are shown in Table V with a performance in Fig. 9(a). It can be seen that the response of the optimized design using the equivalent circuit model is excellent in terms of circuit simulation, and when simulating it with the full-wave EM model, the response seems to be good as a starting point and only a slight move from the initial design is needed. However, this "correct slight move" is difficult.

TABLE V
INITIAL SOLUTION AND AN OPTIMIZED SOLUTION (ALL SIZES IN MILLIMETERS) FOR EXAMPLE 2

$Variables$	$W1$	$W2$	$W3$	$W4$	$L01$	$L02$
Initial design	0.591	0.746	1.476	1.324	4.440	5.408
$Variables$	$L03$	$L04$	$L1$	$L2$	$L3$	$L4$
Initial design	2.742	2.595	16.531	15.42	16.748	17.708
$Variables$	$W1$	$W2$	$W3$	$W4$	$L01$	$L02$
SMEAFO optimized design	0.549	0.953	1.727	1.887	3.885	5.245
$Variables$	$L03$	$L04$	$L1$	$L2$	$L3$	$L4$
SMEAFO optimized design	2.771	2.219	16.111	15.321	16.273	17.206

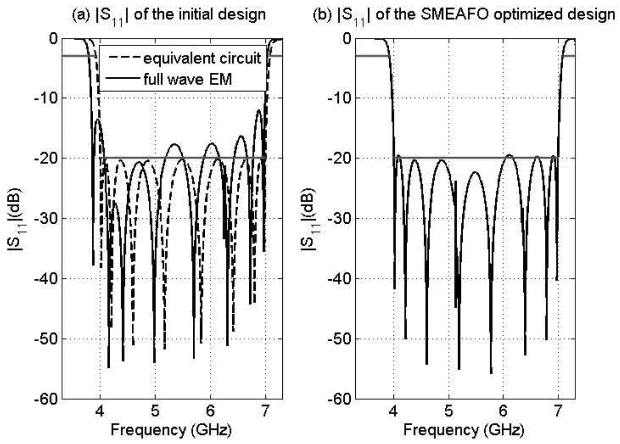

Fig. 9. Response of the microstrip filter.

TABLE VI
OPTIMIZED RESULTS USING DIFFERENT METHODS FOR EXAMPLE 2

Methods	$max(\|S_{11}\|)$: 4–7GHz	$min(\|S_{11}\|)$: 3.3–3.92GHz	$min(\|S_{11}\|)$: 7.08–7.3GHz	time
Nelder-Mead simplex	–6.29 dB	–2.81 dB	–3.00 dB	47.2 hours
sequential quadratic programming	–2.42 dB	–22.40 dB	–0.20 dB	77 hours
SMEAFO	–19.48 dB	–2.93 dB	–2.96 dB	96.9 hours

The Nelder–Mead simplex method and the sequential quadratic programming method are first applied. Note that these local optimization methods are not affected by the expanded search ranges, as a good starting point is available. For this example, each EM simulation costs about 3–6 min. The results are shown in Table VI. It can be seen that Nelder–Mead simplex fails to jump out of local optima, although the initial design is near the narrow valley, while sequential quadratic programming goes out of the narrow valley and is trapped in a local optimum in the outer region. Simulation data indicates that in all the eight test problems, this problem has the most rugged landscape.

Then, SMEAFO is carried out. Because of the intentionally set large ranges of the design variables, σ_{init} is set to 0.25. As was said in Section III-D, the value of σ_{init} is a rough estimation and is not sensitive. The computing budget is 1250 EM simulations. The results are shown in Tables V (optimized design variables) and VI and Fig. 9(b) (performance). The convergence trend is shown in Fig. 10. It can be seen that SMEAFO obtains a satisfactory result for this very challenging problem in terms of the ruggedness of the landscape and the narrowness of the optimal valley. This example shows that for problems that space mapping seems to be the suitable method, there are exceptions and SMEAFO can be a supplement for these exceptions.

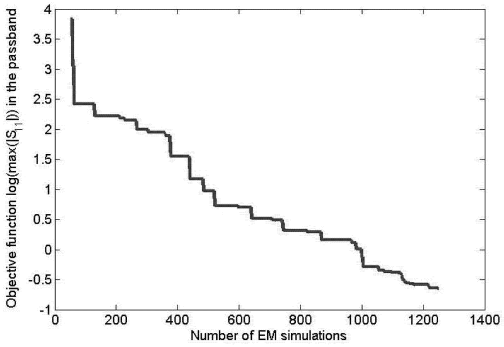

Fig. 10. SMEAFO convergence trend for Example 2.

Experiments on our real-world filter design test cases show that most hard filter optimization can be finished within 700 EM simulations using SMEAFO obtaining satisfactory results. For most test cases, the optimization time is one to two days. Note that SMEAFO is designed for filter optimization problems that may be difficult to solve by existing local optimization methods (space mapping-based methods without problem specific tuning often at most obtain the same solution quality compared with direct local search), comparing speed with such methods is therefore not relevant. Rather, an excellent result in a reasonable timeframe for hard problems is the goal of SMEAFO.

V. CONCLUSION

In this paper, the SMEAFO algorithm has been proposed. SMEAFO is aimed to serve as a widely applicable method (i.e., not restricted by filter types/responses) targeted at microwave filter optimization problems that are difficult to be solved by popular local optimization methods, while at the same time are not affordable to be solved by standard global optimization methods, so as to complement the state of the arts. Experiments show that SMEAFO can provide optimal filter designs that are comparable with the DE algorithm, which is expected to provide very high-quality design, but uses a reasonable timeframe and is several orders faster than DE. These results are achieved by our novel SAEA designed for filter landscapes, including the two-phase structure, the novel surrogate model-assisted search methods, and the training data selection method in each phase. In addition, SMEAFO with a lower fidelity EM model can be used to support space mapping, providing a good initial design and a database with lower fidelity model evaluation results. The SMEAFO-based filter design optimization tool can be downloaded from http://fde.cadescenter.com. Future works include developing parallelized SMEAFO.

ACKNOWLEDGMENT

The authors would like to thank Prof. S. Koziel, Reykjavik University, Iceland, for valuable discussions.

REFERENCES

[1] M. Fakhfakh, E. Tlelo-Cuautle, and P. Siarry, *Computational Intelligence in Analog and Mixed-Signal (AMS) and Radio-Frequency (RF) Circuit Design*. Berlin, Germany: Springer, 2015.

[2] A. Deb, J. S. Roy, and B. Gupta, "Performance comparison of differential evolution, particle swarm optimization and genetic algorithm in the design of circularly polarized microstrip antennas," *IEEE Trans. Antennas Propag.*, vol. 62, no. 8, pp. 3920–3928, Aug. 2014.

[3] N. He, D. Xu, and L. Huang, "The application of particle swarm optimization to passive and hybrid active power filter design," *IEEE Trans. Ind. Electron.*, vol. 56, no. 8, pp. 2841–2851, Aug. 2009.

[4] P. T. Boggs and J. W. Tolle, "Sequential quadratic programming," *Acta Numer.*, vol. 4, pp. 1–51, Jan. 1995.

[5] J. C. Lagarias, J. A. Reeds, M. H. Wright, and P. E. Wright, "Convergence properties of the Nelder–Mead simplex method in low dimensions," *SIAM J. Optim.*, vol. 9, no. 1, pp. 112–147, 1998.

[6] M. Sans, J. Selga, A. Rodríguez, J. Bonache, V. E. Boria, and F. Martín, "Design of planar wideband bandpass filters from specifications using a two-step aggressive space mapping (ASM) optimization algorithm," *IEEE Trans. Microw. Theory Techn.*, vol. 62, no. 12, pp. 3341–3350, Dec. 2014.

[7] S. Koziel, S. Ogurtsov, J. W. Bandler, and Q. S. Cheng, "Reliable space-mapping optimization integrated with EM-based adjoint sensitivities," *IEEE Trans. Microw. Theory Techn.*, vol. 61, no. 10, pp. 3493–3502, Oct. 2013.

[8] X. Shang, Y. Wang, G. L. Nicholson, and M. J. Lancaster, "Design of multiple-passband filters using coupling matrix optimisation," *IET Microw., Antennas Propag.*, vol. 6, no. 1, pp. 24–30, 2012.

[9] J. W. Bandler, R. M. Biernacki, S. H. Chen, P. A. Grobelny, and R. H. Hemmers, "Space mapping technique for electromagnetic optimization," *IEEE Trans. Microw. Theory Techn.*, vol. 42, no. 12, pp. 2536–2544, Dec. 1994.

[10] C. Zhang, F. Feng, V.-M.-R. Gongal-Reddy, Q. J. Zhang, and J. W. Bandler, "Cognition-driven formulation of space mapping for equal-ripple optimization of microwave filters," *IEEE Trans. Microw. Theory Techn.*, vol. 63, no. 7, pp. 2154–2165, Jul. 2015.

[11] Q. S. Cheng, J. W. Bandler, and S. Koziel, "Space mapping design framework exploiting tuning elements," *IEEE Trans. Microw. Theory Techn.*, vol. 58, no. 1, pp. 136–144, Jan. 2010.

[12] R. Ben Ayed, J. Gong, S. Brisset, F. Gillon, and P. Brochet, "Three-level output space mapping strategy for electromagnetic design optimization," *IEEE Trans. Magn.*, vol. 48, no. 2, pp. 671–674, Feb. 2012.

[13] M. A. E. Sabbagh, M. H. Bakr, and J. W. Bandler, "Adjoint higher order sensitivities for fast full-wave optimization of microwave filters," *IEEE Trans. Microw. Theory Techn.*, vol. 54, no. 8, pp. 3339–3351, Aug. 2006.

[14] T. J. Santner, B. J. Williams, and W. I. Notz, *The Design and Analysis of Computer Experiments*. Berlin, Germany: Springer, 2013.

[15] M. T. M. Emmerich, K. C. Giannakoglou, and B. Naujoks, "Single- and multiobjective evolutionary optimization assisted by Gaussian random field metamodels," *IEEE Trans. Evol. Comput.*, vol. 10, no. 4, pp. 421–439, Aug. 2006.

[16] J. E. Dennis and V. Torczon, "Managing approximation models in optimization," in *Multidisciplinary Design Optimization: State of the Art*. Hampton, VA, USA: SIAM, 1997, pp. 330–347.

[17] I. Couckuyt, A. Forrester, D. Gorissen, F. De Turck, and T. Dhaene, "Blind Kriging: Implementation and performance analysis," *Adv. Eng. Softw.*, vol. 49, pp. 1–13, Jul. 2012.

[18] K. Price, R. M. Storn, and J. A. Lampinen, *Differential Evolution: A Practical Approach to Global Optimization*. New York, NY, USA: Springer-Verlag, 2005.

[19] A. Hoorfar, "Evolutionary programming in electromagnetic optimization: A review," *IEEE Trans. Antennas Propag.*, vol. 55, no. 3, pp. 523–537, Mar. 2007.

[20] X. Yao, Y. Liu, and G. Lin, "Evolutionary programming made faster," *IEEE Trans. Evol. Comput.*, vol. 3, no. 2, pp. 82–102, Jul. 1999.

[21] M. Jamil and X.-S. Yang, "A literature survey of benchmark functions for global optimisation problems," *Int. J. Math. Model. Numer. Optim.*, vol. 4, no. 2, pp. 150–194, 2013.

[22] D. Lim, Y. Jin, Y. S. Ong, and B. Sendhoff, "Generalizing surrogate-assisted evolutionary computation," *IEEE Trans. Evol. Comput.*, vol. 14, no. 3, pp. 329–355, Jun. 2010.

[23] Z. Zhou, Y. S. Ong, P. B. Nair, A. J. Keane, and K. Y. Lum, "Combining global and local surrogate models to accelerate evolutionary optimization," *IEEE Trans. Syst., Man, Cybern. C, Appl. Rev.*, vol. 37, no. 1, pp. 66–76, Jan. 2007.

[24] D. R. Jones, M. Schonlau, and W. J. Welch, "Efficient global optimization of expensive black-box functions," *J. Global Optim.*, vol. 13, no. 4, pp. 455–492, 1998.

[25] B. Liu, D. Zhao, P. Reynaert, and G. G. E. Gielen, "Synthesis of integrated passive components for high-frequency RF ICs based on evolutionary computation and machine learning techniques," *IEEE Trans. Comput.-Aided Des. Integr. Circuits Syst.*, vol. 30, no. 10, pp. 1458–1468, Oct. 2011.

[26] C. C. Coello, G. B. Lamont, and D. A. Van Veldhuizen, *Evolutionary Algorithms for Solving Multi-Objective Problems*. Springer, 2007.

[27] J.-S. G. Hong and M. J. Lancaster, *Microstrip Filters for RF/Microwave Applications*, vol. 167. Hoboken, NJ, USA: Wiley, 2004.

[28] P. Rocca, G. Oliveri, and A. Massa, "Differential evolution as applied to electromagnetics," *IEEE Antennas Propag. Mag.*, vol. 53, no. 1, pp. 38–49, Feb. 2011.

[29] D. M. Himmelblau, *Applied Nonlinear Programming*. New York, NY, USA: McGraw-Hill, 1972.

[30] X. Shang, M. Ke, Y. Wang, and M. J. Lancaster, "WR-3 band waveguides and filters fabricated using SU8 photoresist micromachining technology," *IEEE Trans. THz Sci. Technol.*, vol. 2, no. 6, pp. 629–637, Nov. 2012.

Bo Liu (M'15) received the B.S. degree from Tsinghua University, Beijing, China, in 2008, and the Ph.D. degree from MICAS Laboratories, University of Leuven, Leuven, Belgium, in 2012.

From 2012 to 2013, he was a Humboldt Research Fellow with the Technical University of Dortmund, Dortmund, Germany. In 2013, he joined Wrexham Glyndwr University, Wrexham, U.K., as a Lecturer, where he became a Reader of computer-aided design in 2016. He is currently an Honorary Fellow with the University of Birmingham, Edgbaston, Birmingham, U.K. He has authored or co-authored 1 book and more than 40 papers in international journals, edited books, and conference proceedings. His current research interests include design automation methodologies of analog/RF integrated circuits, microwave devices, MEMS, evolutionary computation, and machine learning.

Hao Yang was born in Wuhan, China, in 1991. He received the B.Eng. degree in electronics and information engineering from the Huazhong University of Science and Technology, Wuhan, in 2014, and the B.Eng. degree in electronic and electrical engineering from the University of Birmingham, Edgbaston, Birmingham, U.K., in 2014, where he is currently pursuing the Ph.D. degree.

His current research interests include terahertz frequency filters and mutiplexers.

Michael J. Lancaster (SM'04) was born in West Yorkshire, U.K., in 1958. He received the bachelor's degree in physics and Ph.D. degree (with a focus on nonlinear underwater acoustics) from the University of Bath, Bath, U.K., in 1980 and 1984, respectively.

He was a Research Fellow with the Surface Acoustic Wave (SAW) Group, Department of Engineering Science, Oxford University, Oxford, U.K., where he was involved in the design of new, novel SAW devices, including RF filters and filter banks. In 1987, he became a Lecturer in electromagnetic theory and microwave engineering with the Department of Electronic and Electrical Engineering, University of Birmingham, Edgbaston, Birmingham, U.K., where he was involved in the study of the science and applications of high-temperature superconductors, mainly at microwave frequencies, and became the Head of the Department of Electronic, Electrical, and Systems Engineering in 2003. He has authored 2 books and over 190 papers in refereed journals. His current research interests include microwave filters and antennas, high-frequency properties and applications of a number of novel and diverse materials, and micromachining as applied to terahertz communications devices and systems.

Prof. Lancaster is a Fellow of the IET and the Institute of Physics, U.K. He is a Chartered Engineer and a Chartered Physicist. He has served on the IEEE MTT-S IMS Technical Committees.

Synthesis of Coupling Matrix for Diplexers Based on a Self-Adaptive Differential Evolution Algorithm

Bo Liu, *Senior Member, IEEE*, Hao Yang, and Michael J. Lancaster, *Senior Member, IEEE*

***Abstract*— Diplexer coupling matrix synthesis often involves both analytical methods and optimization techniques. At present, general purpose optimization algorithms are used, but they need strong supporting information (e.g., high-quality starting points and very narrow search ranges) from analytical methods, which is not available or too complex to be obtained in many cases. Aiming to obtain the desired coupling matrix with highly reduced supporting information to relieve the pressure of analytical methods, a new optimization algorithm, called self-adaptive differential evolution for coupling matrix synthesis (SADEC), is proposed. Considering the landscape characteristics of diplexer coupling matrix synthesis problems, a new self-adaptive multipopulation search framework and a self-adaptive algorithm parameter control strategy are proposed and organized in a particular way. The performance of SADEC is demonstrated by two all-resonator-based narrowband diplexers using large search ranges only with the requirement of matching the diplexer topology and no *ad hoc* analysis is included. Experiments and comparisons show the high performance of SADEC and clear advantages compared with the state-of-the-art global optimization methods. SADEC is also applicable to filter coupling matrix synthesis and is downloadable.**

***Index Terms*— Coupling matrix, coupling matrix synthesis, differential evolution (DE), diplexer.**

I. Introduction

THE coupling matrix model is often employed in modern filter and diplexer design [1]. Because of the direct connection between the coupling matrix and the geometric parameters of the physical design, the coupling matrix is a widely used tool to obtain the initial geometric design parameters before 3-D full-wave electromagnetic (EM) simulation-based design optimization. Bandler *et al.* [2] and Liu *et al.* [3] show that both the local optimization and global optimization-based EM simulation-driven design optimization methods can benefit from a good initial design for complex filters and diplexers. Therefore, the high-quality synthesis of a coupling matrix is essential.

Manuscript received July 4, 2017; revised September 19, 2017; accepted September 30, 2017. Date of publication January 3, 2018; date of current version February 5, 2018. This work was supported by the U.K. Engineering and Physical Science Research Council under Project EP/M016269/1. *(Corresponding author: Bo Liu.)*

B. Liu is with the School of Electrical, Electronic and System Engineering, University of Birmingham, Birmingham B15 2TT, U.K., and also with the School of Applied Science, Computing and Engineering, Wrexham Glyndwr University, Wrexham LL11 2AW, U.K. (e-mail: b.liu.3@bham.ac.uk; liubo168@gmail.com).

H. Yang and M. J. Lancaster are with the School of Electrical, Electronic and System Engineering, University of Birmingham, Birmingham B15 2TT, U.K. (e-mail: hxy297@student.bham.ac.uk; m.j.lancaster@bham.ac.uk).

Color versions of one or more of the figures in this paper are available online at http://ieeexplore.ieee.org.

Digital Object Identifier 10.1109/TMTT.2017.2772855

Coupling matrix synthesis methods can be mainly classified into three categories: analytical methods [4]–[6], optimization-based methods [7]–[9], and hybrid analytical and optimization methods [10], [11]. In analytical methods, the appropriate coupling coefficient and external quality factor values are analytically calculated based on the properties of the microwave device. They are theoretically sound and with guaranteed good results. Optimization-based methods, on the other hand, obtain the appropriate coupling matrix through a black-box optimization process. Except for the selection of cost functions [9], [12], [13], much less theoretical analysis is involved, providing the advantages of ease of use and being general.

However, as the complexity of the response and topology increases, especially for multiport devices, both kinds of methods face challenges: the analytical methods can become intricate and sometimes impossible to realize [14] and the optimization methods may have a low success rate even with fine tuning of the cost function and the search range [9], [15]. Traditional genetic algorithms or genetic algorithm-based memetic/hybrid algorithms and state-of-the-art global optimization algorithms (e.g., differential evolution (DE) [16] and particle swarm optimization (PSO) [17]) are tested in our pilot experiments. The success rate is low for various diplexer coupling matrix synthesis problems.

Therefore, the hybrid analytical and optimization-based methods are attracting much attention. In such methods, an optimization engine is employed, but the optimization problem is highly simplified based on analytical methods, such as a high-quality starting point [11], a well-organized synthesis process [10], or highly reduced search ranges [18]. Due to such strong supporting information, the optimization algorithm does not need to be strong. At present, the widely used methods are general purpose optimization methods, such as Nelder–Mead simplex method [19], sequential quadratic programming [20], and evolutionary algorithms (EAs), which are widely used in microwave engineering [21]–[24].

However, the main application area of hybrid analytical and optimization-based methods is filter synthesis. To the best of our knowledge, for more complex topologies, such as the all-resonator-based diplexer, which is a new and promising component in satellite communication systems, there are a few matured coupling matrix synthesis methods. When applying the above hybrid method for diplexer synthesis, it is not easy to obtain a good enough starting point or the search range is not narrow enough in many cases, causing optimization not to be successful [15]. Hence, developing a strong optimization mechanism for complex coupling matrix synthesis, which

can considerably relieve the pressure of the prior analytical analysis, is important to complement the state of the art for coupling matrix synthesis for multiport devices.

Aiming to fill this gap, an optimization method for coupling matrix synthesis for diplexers, called self-adaptive DE for coupling matrix synthesis (SADEC), is proposed. The main innovations include a new self-adaptive multipopulation search framework and a self-adaptive DE algorithm parameter control strategy. Both of them are designed to tackle the landscape characteristics of the targeted problem. SADEC aims as follows.

1) To obtain highly optimal solutions for diplexer coupling matrix synthesis with a high success rate.
2) Do not rely on good initial values, highly reduced search ranges, or other specific properties of the targeted design cases.

We believe that if these two goals are met, diplexer coupling matrix synthesis with weak, easy to obtain, or highly reduced supporting information from analytical methods is expected to be successful in most cases. General purpose optimization techniques (e.g., sequential quadratic programming and PSO), which show difficulty for the targeted problem, can therefore be replaced.

The remainder of this paper is organized as follows. Section II introduces the basic techniques, including a brief introduction of the coupling matrix method and the standard DE algorithm. Section III introduces the SADEC algorithm, including its main ideas, the design of the new algorithm framework and algorithmic components and parameter setting. Section IV demonstrates SADEC by two all-resonator-based diplexers. Large search ranges only with the requirement of matching the diplexer topology are used. Comparisons with standard DE and PSO are also provided. The concluding remarks are provided in Section V.

II. Basic Techniques

A. Coupling Matrix Method for Diplexer Design

The S-parameter design specifications of a diplexer can be calculated using the scaled external quality factors q_{ei} and the general matrix $[A]$ using the following equations [18]:

$$S_{11} = \pm\left(1 - \frac{2}{q_{e1}}[A]^{-1}_{1,1}\right)$$
$$S_{i1} = 2\frac{1}{\sqrt{q_{e1}q_{ei}}}[A]^{-1}_{i,1}, \quad i = 2, \ldots, n \tag{1}$$

where n is the number of ports. The general matrix $[A]$ can be expressed as

$$[A] = [q] + p[U] - j[m] \tag{2}$$

where $[q]$ is an $n \times n$ matrix with all entries zero, except for $q_{ii} = (1/q_{ei}), i = 1, 2, \ldots, n$ (i stands for the index of a resonator connected to an external port), $[U]$ is an $n \times n$ identity matrix, p is the complex lowpass frequency variable, and $[m]$ is the general normalized coupling matrix, which is what SADEC targets at.

B. Differential Evolution Algorithm

The DE algorithm [16] is the fundamentals of SADEC. DE is a population-based global optimization algorithm, which outperforms many EAs for continuous optimization problems [16] and is widely used in the EM design optimization domain. Nevertheless, DE is not the only choice, other popular EAs (e.g., PSO and evolution strategy) may also be improved following similar ideas in this paper.

DE is an iterative method. In each iteration, the mutation operator is first applied to generate a population of mutant vectors. A crossover operator is then applied to the mutant vectors to generate a new population. Finally, selection takes place and the corresponding candidate solutions from the old population and the new population compete to comprise the population for the next iteration.

In the tth iteration, the ith candidate solution in the population, P, can be represented as

$$x^i(t) = \left[x^i_1, x^i_2, \ldots, x^i_d\right] \tag{3}$$

where d is the number of design variables.

In DE, mutation is the main approach to explore the design space. There are a few different DE mutation strategies trading off the convergence speed and the population diversity in different manners. Arguably, the most widely used one is DE/rand/1 [16], which is as follows:

$$v^i(t+1) = x^{r_1}(t) + F \cdot (x^{r_2}(t) - x^{r_3}(t)) \tag{4}$$

where x^{r_1}, x^{r_2}, and x^{r_3} are three different solutions randomly selected from the current population, P. v^i is the ith mutant vector in the population after mutation. $F \in (0, 2]$ is a control parameter, called the scaling factor.

Crossover is then applied to the population of mutant vectors to produce the child population U, which works as follows.

1) Randomly select a variable index $j_{\text{rand}} \in \{1, \ldots, d\}$.
2) For each $j = 1$ to d, generate a uniformly distributed random number rand from $(0, 1)$ and set

$$u^i_j(t+1) = \begin{cases} v^i_j(t+1), & \text{if } (\text{rand} \le \text{CR}) | j = j_{\text{rand}} \\ x^i_j(t), & \text{otherwise} \end{cases} \tag{5}$$

where CR $\in [0, 1]$ is a constant called the crossover rate.

Following that, the selection operation decides on the population of the next iteration, which is often based on a one-to-one greedy selection between P and U. Considering a minimization problem, the selection operator is

$$x^i(t+1) = \begin{cases} u^i(t+1), & \text{if } f(u^i(t+1)) < f(x^i(t)) \\ x^i(t), & \text{otherwise.} \end{cases} \tag{6}$$

III. SADEC Algorithm

A. Challenges and Motivations

Aiming to propose a general method for diplexer coupling matrix synthesis, case-specific information is not included

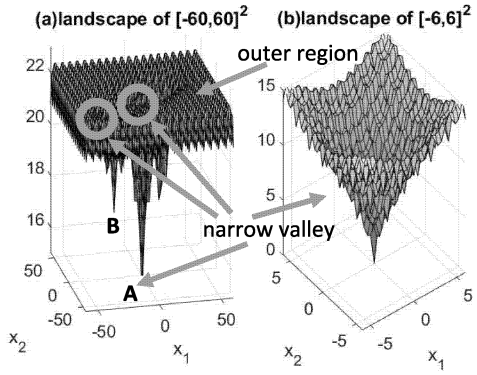

Fig. 1. Illustrative figure of diplexer coupling matrix synthesis problem landscape (the Ackley benchmark test function [25] is used for illustration).

in the cost function. Our cost function only involves violation of S-parameter constraints, such as $\max\{\max(|S_{11}|) - (-20 \text{ dB}), 0\}$ for the constraint of $\max|S_{11}| < -20$ dB in the passband(s). The cost function is defined as the sum of normalized S-parameter constraint violations. For normalization, the violation of each constraint for each candidate solution is divided by the maximum constraint violation so far for the corresponding constraint. Examples are shown in Section IV. Transmission and reflection zeros are not used due to generality consideration. Transmission zeros do not always exist. We also found that for some complex synthesis problems, there are many solutions with very close transmission and/or reflection zeros compared with the desired ones, but the S-parameter response is far away from the specifications.

Using the above cost function, by studying various diplexer coupling matrix synthesis problems (e.g., sampling and sweeping), Fig. 1 (illustrative figure) shows the characteristics of the landscape. It can be seen that: 1) if without an *ad hoc* selection of the search range, the optimal regions locate in several narrow valleys of the search space and the outer region is flat. This characteristic is understandable because most diplexers are narrowband, and resonance only happens in very particular design parameters; 2) the optimal regions are separated because these narrow valleys are not connected with each other; 3) the best solution in most of the narrow valleys is only a local optimum (point B in Fig. 1), which is not useful (an example is shown in Section IV-A); and 4) even in a narrow valley, the landscape is multimodal (has local optima).

EAs are stochastic optimization methods and there is always a balance between the exploration ability and the probability to find the correct search direction [26]. In a stochastic search process, if the diversity of possible movements is limited, it is easy to get trapped in a local optimum. When the diversity of possible movements increases, the capacity of exploring unknown space is promoted, but the probability to find the correct search direction decreases considerably. The characteristics of the targeted landscape require the optimization algorithm having a good exploration ability because it is multimodal. However, it also requires the algorithm having a high capacity to find the correct search direction because the optima locate in narrow valleys. In addition, most of the narrow valleys only provide local optima even if they are visited. Therefore, it is not a surprise that modern EAs, such as standard DE and PSO, have a very low success rate. Our pilot experiments show that standard DE and PSO have difficulty in converging at the global optimum and may converge at a local optimum (i.e., point B in Fig. 1).

In the computational intelligence field, various improved DE and PSO are proposed [27] and many of them focus on jumping out of local optima. Their general idea is to promote the exploration ability. However, these methods do not seem suitable for the targeted problem. These methods target at highly multimodal problems, but their optimal regions are not narrow and not separated [25]. Hence, finding the correct search direction is not a main consideration for those methods, but it is an important challenge for the coupling matrix synthesis problem. Arguably, the benchmark test problem with the narrowest optimal region used in the computational intelligence field is the Ackley function [25], while our experiments show that the optimal region of the targeted problem is much narrower than that of the Ackley function. Therefore, promoting exploration ability makes the optimization algorithm be trapped in the outer region when synthesizing diplexer coupling matrix, which is verified by our pilot experiments. For example, several popular improved DE even cannot detect the narrow valleys.

To the best of our knowledge, there are few works focusing on identifying the correct search direction for the targeted landscape. Therefore, the goal of the SADEC algorithm is to increase the probability of finding and preserving the correct search direction while maintaining its exploration ability. SADEC is based on DE and its design is described in Sections III-B and III-C.

B. Self-Adaptive Parameter Control Strategy

There are four key algorithmic parameters in DE, which are the population size (NP), the mutation strategy, the scaling factor (F), and the CR. The selection of them has a significant influence on the performance of DE for complex optimization problems [28], [29]. The mutation strategy and the scaling factor control the exploration of the decision space. In particular, the mutation strategy can be considered as the choice of the search direction, while the scaling factor can be considered as the step length. An example is the DE/rand/1 mutation (4). Selecting different kinds of mutation strategies and scaling factor leads to different capabilities of exploration. Besides, by increasing the size of the population, the exploration ability is promoted. As described above, the probability of finding the correct search direction is therefore decreased. According to (5), the crossover operator decides how many decision variables in expectation are changed in a population member. Thus, it decides to what extent that the visited search patterns (or search directions) can be changed/preserved.

A central question then becomes how to control these parameters so as to promote the probability of finding and preserving the correct search directions while maintaining the exploration ability. As described in Section III-A, there

are almost no guidelines for the landscapes of the targeted problem. Hence, empirical tests using various coupling matrix synthesis problems with different complexities are carried out and the following observations are obtained: 1) the inventor of DE suggests that the population size NP should be around $5 \times D$ to $10 \times D$ [16]. Our experiments show that when using the DE/rand/1 mutation with a reasonable scaling factor, NP = $5 \times D$ always provides enough exploration ability and 2) when using DE mutation strategies with higher exploration ability than DE/rand/1 (e.g., DE/rand/2 [16]), the probability of visiting the narrow valleys decreases. Given the settings of NP = $5 \times D$ and the DE/rand/1 mutation, the control of F and CR is discussed in the following.

Considering the characteristics of the targeted landscape, large F is needed to explore the decision space so as to get access to the narrow valleys. Small F is also needed to perform local exploitation in the narrow valley. Price *et al.* [16] suggest that F should not be smaller than 0.4, while a widely used parameter study Gämperle *et al.* [30] argue that the lower bound of F is problem dependent. Both studies suggest that if F is larger than 1.0, the convergence speed will decrease. Price *et al.* [16] and Gämperle *et al.* [30] recommend to use $F = 0.5$ and $F = 0.6$ as a default value, respectively. Considering above, SADEC uses the following method to decide the scaling factor:

$$F_{\text{temp}} = \text{norm}(0.5, 0.25)$$
$$F^i(t) = \begin{cases} 1, & \text{if } F_{\text{temp}} > 1 \\ 0.1, & \text{if } F_{\text{temp}} < 0.1 \\ F_{\text{temp}}, & \text{otherwise} \end{cases} \tag{7}$$

where norm(0.5, 0.25) is a Gaussian distributed random number with a mean of 0.5 and a standard deviation of 0.25.

It can be seen that: 1) because of the Gaussian distribution, there is about 68% probability, the generated F is between 0.25 and 0.75 (near the recommended default values). For about 27% probability, F is between 0.1 and 0.25 or between 0.75 and 1 (emphasizes exploration or exploitation in particular) and 2) for each candidate solution in each iteration, there is a separate F. In this way, different kinds of candidate designs have the opportunity to use various kinds of F (i.e., step size) in an appropriate range to either perform exploration or exploitation.

In terms of CR control strategy, various DE parameter studies show different recommendations [16], [30], [31]. Unfortunately, none of them works in our pilot tests using diplexer coupling matrix synthesis problems. In our empirical study, using various candidate solutions (x) and their mutant vectors (v) in the optimization process, a number of child candidates (u) are generated for a certain CR value. The number of successful crossovers, for which, u is better than x, can be observed. Two main observations include: 1) for different candidate solutions, there is not a universal workable CR value and the fit CR values can be very different and 2) in many cases, the workable CR value for a candidate solution spans in a narrow range (e.g., 0.4–0.5). This explains why a fixed setting rule of CR cannot work for the targeted problem. Therefore, a possible way is to explore random CR values and inherit the workable ones, which is shown as follows:

$$\text{CR}_{\text{temp}} = 0.1 + \text{rand}_1 \times 0.8$$
$$\text{CR}^i(t) = \begin{cases} \text{CR}_{\text{temp}}, & \text{if } \text{rand}_2 < 0.1 \\ \text{CR}^i(t-1), & \text{otherwise} \end{cases} \tag{8}$$

where rand is a uniformly distributed random number between 0 and 1. $\text{CR}(1) = 0.9$, which is based on the suggested default value in [16].

It can be seen that for 10% probability, CR can be any value between 0.1 and 0.9 (the possible range suggested by [16]); Otherwise, CR is inherited from the last iteration. Note that each candidate solution in the optimization process has its own CR value. Pilot experiments show that there is a considerable probability that a feasible CR for a certain candidate solution is sampled and inherited in the optimization process. Comparisons with several widely used self-adaptive setting rules (see [32]) show that this control method has the highest success rate.

C. Self-Adaptive Multipopulation Search Framework

Despite employing the above self-adaptive parameter control mechanism, obtaining the appropriate F and CR values cannot be guaranteed. Sometimes, the optimization converges to narrow valleys that only contain local optima (such as point B in Fig. 1). In almost all of the local optima that we have encountered, some resonance happens in undesired frequency ranges, while the others are correct. Hence, a new operator, called self-adaptive return operator, is activated when the optimization is judged to be trapped in local optima, which can often be observed in earlier iterations if it happens. The judgment of being trapped in local optima is based on two conditions: 1) the maximum standard deviation of decision variables in the current population is smaller than a predefined threshold δ and 2) the number of reflection zeros in any passband is incorrect. Using the return operator, the optimization returns to the original initial population, and the F and CR will be resampled based on (7) and (8) and the optimization process will restart. The effectiveness of this operator is shown by various test cases, and an example is shown in Section IV-B.

Uhm *et al.* [7] shows that the choice of initial population has an effect on the final result for coupling matrix synthesis problems. Our pilot experiments show a similar observation that some initial populations have a higher probability to obtain the desired global optimum than others using the same process in Section III-B. Hence, a multipopulation framework is proposed to increase the success rate.

Two populations are used. For one of them (P), the initialization is based on random sampling. The initialization of the other one ($\bar{P}$) is the opposite population of P, which is composed by

$$\bar{x}^i(1) = a + b - x^i(1) \tag{9}$$

where $x^i(1)$ is the ith candidate solution in initial P, $\bar{x}^i(1)$ is the corresponding candidate solution in initial $\bar{P}$, and $[a, b]^d$ is the search range. Experiments show that in many cases, if the optimization is not successful when using P as the initial

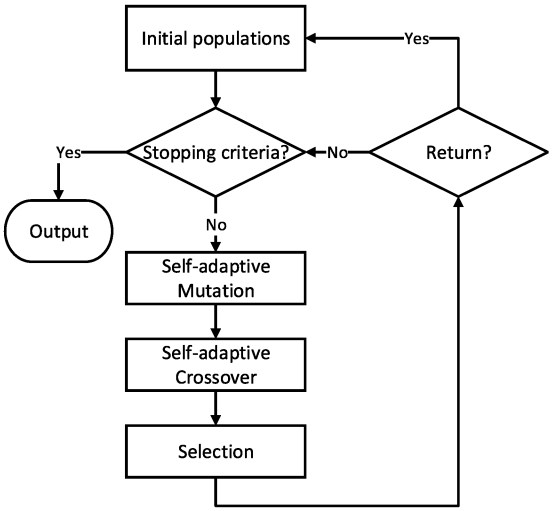

Fig. 2. Flow diagram of SADEC.

population, using $\bar{P}$ as the initial population has much larger success rate than using another randomly sampled population. This is understandable because $\bar{P}$ is often the best complement of P, covering search patterns that do not exist in P as much as possible.

D. General Framework of the SADEC Algorithm

The flow diagram of the SADEC algorithm is shown in Fig. 2, which consists the following steps.

Step 1: Initialize P and $\bar{P}$ using the method in Section III-C. Initialize NP to be $5 \times D$. Initialize CR to be 0.9 for the crossover of the first iteration.

Step 2: Check if the stopping criteria (e.g., a certain number of iterations) are met. If yes, output the result; otherwise, go to Step 3.

Step 3: Apply the DE/rand/1 mutation (4) on P and $\bar{P}$ to generate mutant vectors V_p and $V_{\bar{p}}$. Use (7) to generate F values for the composing of each mutant vector.

Step 4: Apply the crossover operator (5) on V_p and $V_{\bar{p}}$ to generate U_p and $U_{\bar{p}}$. If it is in the first iteration, CR $= 0.9$; otherwise, use (8) to generate CR for each crossover.

Step 5: Apply the selection operator (6) to generate P and $\bar{P}$ for the next iteration.

Step 6: Check if the return criteria for P or $\bar{P}$ are met. If yes, return to the corresponding initial population(s) and go to Step 2; otherwise, go to Step 3.

The only user defined algorithmic parameter in SADEC is δ when judging whether the population is trapped in a local optimum or not, which is the threshold of the maximum standard deviation of the decision variables in the current population. This threshold should be small enough making sure that the difference between the members of the current population is small, indicating that convergence happens. Clearly, this parameter is not sensitive if it is small enough, and the worst case is wasting function evaluations when the search stucks in a narrow valley that only contains a local optimum. Considering the search range of (normalized) coupling matrix optimization problems, which is often around $[-1, 1]$, a recommended setting is $\delta = 0.01$.

IV. Numerical Results and Comparisons

SADEC has been tested by coupling matrix synthesis problems of seven real-world all-resonator-based diplexers. SADEC obtains high-quality results with very high success rate to all of them. In this section, two examples are used to demonstrate different operators in SADEC. To the best of our knowledge, there are no general global optimization-based methods to solve them. The two diplexers have Chebyshev response, but SADEC is applicable to any response (e.g., Butterworth response) that can be generated by a coupling matrix. In both examples, the sum of normalized constraint violations is set as the cost function to be minimized. Because we are working with normalized values, practical diplexers can in principle be made at any frequency with any type of resonator [1]. Hence, we only concentrate on the normalized coupling matrix in the following.

For both examples, 20 runs are carried out for SADEC, standard DE, and PSO and the results are compared statistically. DE and PSO are the state-of-the-art global optimization methods, which have both strong global exploration and local exploitation ability. The stopping criterion for SADEC is that the maximum number of activating the return operator is 3 and the maximum number of iterations after each activation (if there is) is 1000. If the return operator is not activated, the maximum number of iterations is 1000. The stopping criterion for DE and PSO is also 1000 iterations. In all the runs for the three methods, the convergence happens before 1000, either stucks in a local optimum or obtains a successful result.

For the parameter setting of standard DE, the population size is the same as SADEC, the same DE/rand/1 mutation is used. As suggested by [16] and [33], $F = 0.5$, CR $= 0.9$ are used. PSO is implemented using the MATLAB Global Optimization Toolbox. The star topology is used. As suggested by [34], the cognitive coefficient and the social coefficient are both set to 2. According to [35], when the swarm size is larger than 50, PSO is not sensitive to the size of the population. Similar to DE, to improve the probability of finding the correct search direction, larger swarm size should not be used. Hence, the swarm size is set to 50. There are various methods to set the inertia weight. Our experiments show that using a constant inertia weight of 0.4 shows the best performance, which is used for comparison.

The examples are run on a PC with Intel 3.5-GHz Core (TM) i7 CPU and 8-GB RAM under Windows operating system. Since each function evaluation costs around 1 s, computational time is not a problem. Each SADEC run often costs about 40 min to 1 h, while each DE and PSO runs often costs about 20 min. In the SADEC optimization, the number of cost function calls, for example, 1 is around 1660 and that, for example, 2 is around 2870. In each cost function evaluation, 4000 frequencies are swept.

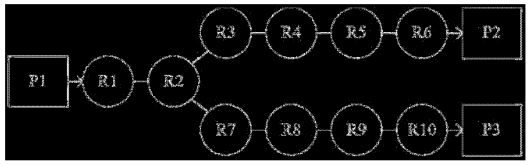

Fig. 3. Topology of example 1.

A. Example 1

The first example is a 10-resonator diplexer with a symmetrical Chebyshev response [36] (Fig. 3), which is a moderate test case among all the problems. This is a novel all-resonator-based diplexer topology that eliminates the need of additional common junction such as T-junction or power splitter. It is especially suitable for applications that need reduced size and volume of the circuit. A full description is in [36]. Due to the symmetry of the response and topology, the total number of variables in the coupling matrix is reduced to 9 [36]. The external quality factors can be straightforwardly calculated, which are $q_{e1} = 1.943$ and $q_{e2} = q_{e3} = 3.886$. The ranges of the design variables are in Table I. The design variables are the coupling matrix elements m_{ij} defined in (2). It can be seen that the search range is decided without any careful selection and no additional information is provided to SADEC. The design specifications over the normalized frequency are: two passbands (PB_1 and PB_2) are with the same bandwidth of 0.5 centered at -0.75 and 0.75 and the $\max(|S_{11}|)$ within the passband should be at least less than -20 dB. The normalized stopbands for channel 1 (PB_{1L} and PB_{1R}) are from -2 to 0.25 and from 1.25 to 2, where the $\max(|S_{21}|)$ should be less than -20 dB. The normalized stopbands for channel 2 (PB_{2L} and PB_{2R}) are from -2 to -1.25 and from -0.25 to 2, where the $\max(|S_{31}|)$ should be less than -20 dB. The design specifications are

$$\begin{aligned} \text{PB}_1 &\le -20 \text{ dB} \\ \text{PB}_2 &\le -20 \text{ dB} \\ \text{PB}_{1L} &\le -20 \text{ dB} \\ \text{PB}_{1R} &\le -20 \text{ dB} \\ \text{PB}_{2L} &\le -20 \text{ dB} \\ \text{PB}_{2R} &\le -20 \text{ dB} \end{aligned} \tag{10}$$

where

$$\begin{aligned} \text{PB}_1 &= \max(|S_{11}|), 0.5 \text{ to } 1 \\ \text{PB}_2 &= \max(|S_{11}|), -1 \text{ to } -0.5 \\ \text{PB}_{1L} &= \max(|S_{21}|), -2 \text{ to } 0.25 \\ \text{PB}_{1R} &= \max(|S_{21}|), 1.25 \text{ to } 2 \\ \text{PB}_{2L} &= \max(|S_{31}|), -2 \text{ to } -0.75 \\ \text{PB}_{2R} &= \max(|S_{31}|), -0.25 \text{ to } 2 \end{aligned} \tag{11}$$

where the numbers in (11) are normalized frequencies.

TABLE I
RANGES OF THE NINE DECISION VARIABLES FOR EXAMPLE 1

Variables	m_{12}	m_{23}	m_{34}	m_{45}	m_{56}
Lower bound	0	0	0	0	0
Upper bound	1	1	1	1	1
Variables	m_{33}	m_{44}	m_{55}	m_{66}	
Lower bound	0	0	0	0	
Upper bound	1	1	1	1	

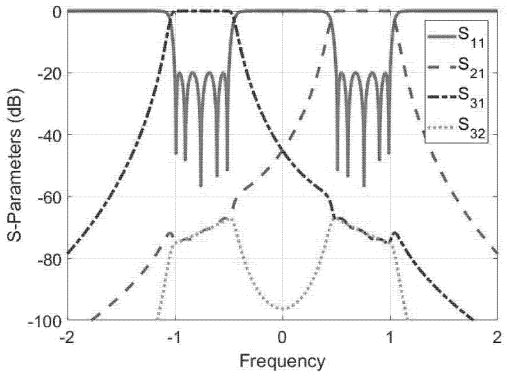

Fig. 4. Example 1: response of a typical optimized solution by SADEC.

TABLE II
TYPICAL OPTIMAL RESULT FOR EXAMPLE 1

Variables	m_{12}	m_{23}	m_{34}	m_{45}	m_{56}
Values	0.8204	0.2856	0.1625	0.1598	0.2170
Variables	m_{33}	m_{44}	m_{55}	m_{66}	
Values	0.7004	0.7442	0.7478	0.7487	

The cost function is defined as

$$\begin{aligned} f_1 = &\frac{\max(\text{PB}_1 - (-20), 0)}{M_{\text{PB}_1}} + \frac{\max(\text{PB}_2 - (-20), 0)}{M_{\text{PB}_2}} \\ &+ \frac{\max(\text{PB}_{1L} - (-20), 0)}{M_{\text{PB}_{1L}}} + \frac{\max(\text{PB}_{1R} - (-20), 0)}{M_{\text{PB}_{1R}}} \\ &+ \frac{\max(\text{PB}_{2L} - (-20), 0)}{M_{\text{PB}_{2L}}} + \frac{\max(\text{PB}_{2R} - (-20), 0)}{M_{\text{PB}_{2R}}} \end{aligned} \tag{12}$$

where M_{PB_1} is the $\max\{\max(\text{PB}_1 - (-20), 0)\}$ so far (i.e., the maximum violation of the $\text{PB}_1 \le -20$-dB constraint, found so far), so do the others.

A typical response of SADEC is shown in Fig. 4, and the corresponding optimal design variables are shown in Table II. Other normalized coupling coefficients are: $m_{27} = m_{23}$, $m_{78} = m_{34}$, $m_{89} = m_{45}$, $m_{9,10} = m_{56}$, $m_{77} = -m_{33}$, $m_{88} = -m_{44}$, $m_{99} = -m_{55}$, and $m_{10,10} = -m_{66}$. Plugging in the optimal values to (2) and then to (1), the response can be obtained. The average optimized responses of SADEC, standard DE, and PSO are shown in Table III. It can be seen that SADEC obtains successful results and is much better than DE and PSO in terms of optimization quality for this example.

The most important criterion for comparison is the success rate. In a diplexer design flow, the coupling matrix synthesis provides an initial design for 3-D EM simulation-driven design

TABLE III
OPTIMIZED RESULTS USING DIFFERENT METHODS FOR EXAMPLE 1 (AVERAGE OF 20 RUNS, IN DECIBEL)

Methods	PB_1	PB_2	PB_{1L}	PB_{1R}	PB_{2L}	PB_{2R}
SADEC	–19.92	–19.92	–27.64	–23.15	–23.36	–27.40
DE	–14.97	–14.97	–27.23	–20.22	–23.36	–27.40
PSO	–5.29	–5.25	–20.00	–19.97	–19.98	–20.00

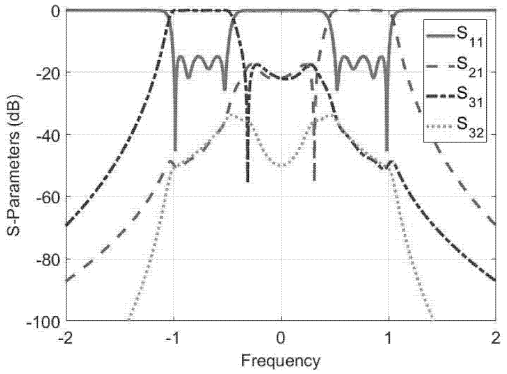

Fig. 5. Local optimum (example 1).

optimization, rather than the final design. Hence, we define a successful result based on the following rules: 1) the reflection zeros are located in proper frequency ranges and the number is correct. A poor example is shown in Fig. 5. We consider that it is a local optimum, because performing various kinds of local optimization (e.g., sequential quadratic programming) from this starting point cannot find a better solution. When it comes to 3-D EM simulation-driven local optimization, experiments show that using such a starting point often cannot obtain a successful final design and 2) the S-parameter design specifications are (almost) satisfied.

Using the above rules, the success rate of SADEC is 20/20, while those for DE and PSO are 4/20 and 1/20, respectively. Most DE and PSO runs obtain solutions like Fig. 5 (like point B in Fig. 1). For SADEC, in 17/20 runs, the return operator is not activated to either P or $\bar{P}$, which means that successful results are obtained directly using the self-adaptive parameter control strategy starting from both P and $\bar{P}$. In the other three runs, the return operator is only activated for once and successful results are obtained. This verifies the considerable improvement of the capacity of finding and preserving correct search directions compared to standard DE, thanks to the algorithm parameter control strategy in Section III-B.

B. Example 2

The second example is a 12-resonator diplexer with a cross-coupling topology shown in [18] (Fig. 6). This topology allows the design of diplexers with sharp rejection in the guard band and is especially suitable for applications that require a reduced guard bandwidth. A full description is in [18]. A cross coupling between resonators 2 and 5 is introduced in a quadruplet to provide a pair of transmission zeros for both channels. Using the symmetry characteristics of the diplexer, the total number of variables is reduced to 12 [18]. The ranges

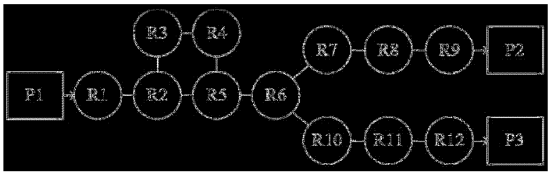

Fig. 6. Topology of example 2.

of design variables are in Table IV. Again, the search range is decided without any careful selection and no additional information is provided to SADEC. The design specifications over the normalized frequency are: two passbands (PB_1 and PB_2) are with the same bandwidth of 0.5 centered at -0.75 and 0.75 and the $\max(|S_{11}|)$ within the passband should be at least less than -20 dB. The constraints for the middle guard bands (PB_{1M} and PB_{2M}) (-0.3 to 0.3) of channels 1 and 2 are that $\max(|S_{21}|)$ and $\max(|S_{31}|)$ should be less than -40 dB due to the introduction of transmission zeros. The $\max(|S_{21}|)$ for the right stopband of channel 1 (PB_{1R}) (1.2 to 2) and $\max(|S_{31}|)$ for the left stopband of channel 2 (PB_{2L}) (-2 to -1.2) should be less than -20 dB. Therefore, the optimization problem is formulated as

$$\begin{aligned} \mathrm{PB}_1 &\le -20 \text{ dB} \\ \mathrm{PB}_2 &\le -20 \text{ dB} \\ \mathrm{PB}_{1M} &\le -40 \text{ dB} \\ \mathrm{PB}_{2M} &\le -40 \text{ dB} \\ \mathrm{PB}_{1R} &\le -20 \text{ dB} \\ \mathrm{PB}_{2L} &\le -20 \text{ dB} \end{aligned} \tag{13}$$

where

$$\begin{aligned} \mathrm{PB}_1 &= \max(|S_{11}|), 0.5 \text{ to } 1 \\ \mathrm{PB}_2 &= \max(|S_{11}|), -1 \text{ to } -0.5 \\ \mathrm{PB}_{1M} &= \max(|S_{21}|), -0.3 \text{ to } 0.3 \\ \mathrm{PB}_{2M} &= \max(|S_{31}|), -0.3 \text{ to } 0.3 \\ \mathrm{PB}_{1R} &= \max(|S_{21}|), 1.2 \text{ to } 2 \\ \mathrm{PB}_{2L} &= \max(|S_{31}|), -2 \text{ to } -1.2 \end{aligned} \tag{14}$$

where the numbers in (14) are normalized frequencies.

The cost function is defined as

$$\begin{aligned} f_2 = &\frac{\max(\mathrm{PB}_1 - (-20), 0)}{M_{\mathrm{PB}_1}} + \frac{\max(\mathrm{PB}_2 - (-20), 0)}{M_{\mathrm{PB}_2}} \\ &+ \frac{\max(\mathrm{PB}_{1M} - (-40), 0)}{M_{\mathrm{PB}_{1M}}} + \frac{\max(\mathrm{PB}_{2M} - (-40), 0)}{M_{\mathrm{PB}_{2M}}} \\ &+ \frac{\max(\mathrm{PB}_{1R} - (-20), 0)}{M_{\mathrm{PB}_{1R}}} + \frac{\max(\mathrm{PB}_{2L} - (-20), 0)}{M_{\mathrm{PB}_{2L}}} \end{aligned} \tag{15}$$

where M_{PB_1} is the $\max\{\max(\mathrm{PB}_1 - (-20), 0)\}$ so far (i.e., the maximum violation of the $\mathrm{PB}_1 \le -20$-dB constraint, found so far), so do the others.

A typical response of SADEC is shown in Fig. 7, and the corresponding optimal design variables are shown in Table V. Other normalized coupling coefficients are: $m_{6,10} = m_{67}$, $m_{10,11} = m_{78}$, $m_{11,12} = m_{89}$, $m_{10,10} = -m_{77}$, $m_{11,11} = -m_{88}$, and $m_{12,12} = -m_{99}$. The average optimized responses

TABLE IV
RANGES OF THE 12 DECISION VARIABLES FOR EXAMPLE 2

$Variables$	m_{12}	m_{23}	m_{34}	m_{45}	m_{56}	m_{67}
Lower bound	0	0	0	0	0	0
Upper bound	1	1	1	1	1	1
$Variables$	m_{78}	m_{89}	m_{77}	m_{88}	m_{99}	m_{25}
Lower bound	0	0	0	0	0	0
Upper bound	1	1	1	1	1	1

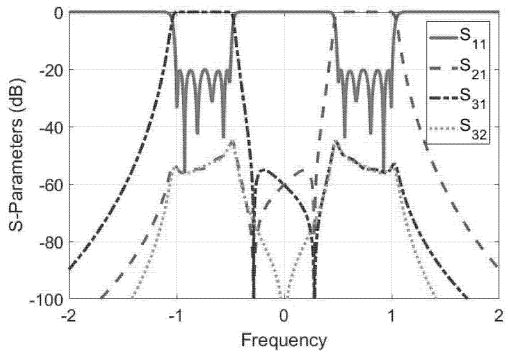

Fig. 7. Example 2: response of a typical optimized solution by SADEC.

TABLE V
TYPICAL OPTIMAL RESULT FOR EXAMPLE 2

$Variables$	m_{12}	m_{23}	m_{34}	m_{45}	m_{56}	m_{67}
Values	0.8278	0.3519	0.5786	0.2450	0.7609	0.2087
$Variables$	m_{78}	m_{89}	m_{77}	m_{88}	m_{99}	m_{25}
Values	0.1558	0.2142	0.7395	0.7495	0.7501	0.1955

TABLE VI
OPTIMIZED RESULTS USING DIFFERENT METHODS FOR EXAMPLE 2 (AVERAGE OF 20 RUNS, IN DECIBEL)

Methods	PB_1	PB_2	PB_{1M}	PB_{2M}	PB_{1R}	PB_{2L}
SADEC	–19.82	–19.83	–32.88	–46.92	–47.14	–32.61
DE	–9.05	–9.05	–26.41	–38.41	–38.39	–26.23
PSO	–3.19	–3.17	–19.94	–39.69	–39.71	–19.92

of SADEC, standard DE, and PSO are shown in Table VI. It can be seen that SADEC obtains successful results and is much better than DE and PSO in terms of optimization quality for this example.

In this example, the success rate of SADEC is 20/20, while those for DE and PSO are 0/20 and 0/20, respectively. In 11/20 runs, the return operator is not activated to either P or $\bar{P}$ in SADEC. Among these 11 runs, successful results are obtained from either P or $\bar{P}$ in 10 of them (only starting from P or $\bar{P}$ obtains successful results); for the other one run, successful results are obtained from both P and $\bar{P}$. This verifies that using two opposite populations, P and $\bar{P}$, in initialization establishes an effective complementation. Among the other 9 runs, the return operator is only activated for once in 7 of them; among 2/9 runs, the return operator is activated for twice and successful results are obtained. These nine runs verify the effectiveness of the return operator to avoid converging into a narrow valley that only contains local optima.

It is intuitive that with the increase of the number of decision variables, the valley that contains the global optimum is narrower and narrower with respect to the decision space. This causes any optimization algorithm, including SADEC, to have difficulty in detecting the narrow valley. We found that for coupling matrix synthesis problems with more than 25 design variables, the success rate of SADEC is low if using large search ranges only with the requirement of matching the topology (e.g., $[-1, 1]^{25}$). In such cases, the support from analytical methods that reasonably narrow down the search ranges is needed. Note that SADEC does not aim to replace the analytical methods; instead, it aims to provide a much stronger optimizer than the existing general purpose optimizers applied in hybrid analytical and optimization-based coupling matrix synthesis methods.

V. CONCLUSION

In this paper, the SADEC algorithm for diplexer coupling matrix synthesis has been proposed. SADEC aims at filling the gap that strong supporting information (e.g., high-quality starting points and narrow enough search ranges) from analytical methods is essential for the success of diplexer coupling matrix synthesis when employing available general purpose optimizers. SADEC focuses on proposing a stronger optimization mechanism especially for the targeted problem, which only requires weak, easy to obtain, or highly reduced supporting information in most cases. Experiments show that SADEC is able to obtain highly optimized coupling matrix solutions with very high success rate even without *ad hoc* supporting information for various diplexers. Much better solution quality and success rate are shown compared with the state-of-the-art global optimization methods, DE and PSO. These results are achieved by our self-adaptive parameter control strategy and self-adaptive multipopulation search framework. Future works include developing software tools using SADEC and coupling matrix synthesis for multiplexers.

ACKNOWLEDGMENT

The authors would like to thank Dr. X. Shang, University of Birmingham, Birmingham, U.K., for valuable discussions.

REFERENCES

[1] J.-S. G. Hong and M. J. Lancaster, *Microstrip Filters for RF/Microwave Applications*, vol. 167. Hoboken, NJ, USA: Wiley, 2004.
[2] J. W. Bandler, R. M. Biernacki, S. H. Chen, P. A. Grobelny, and R. H. Hemmers, "Space mapping technique for electromagnetic optimization," *IEEE Trans. Microw. Theory Techn.*, vol. 42, no. 12, pp. 2536–2544, Dec. 1994.
[3] B. Liu, H. Yang, and M. J. Lancaster, "Global optimization of microwave filters based on a surrogate model-assisted evolutionary algorithm," *IEEE Trans. Microw. Theory Techn.*, vol. 65, no. 6, pp. 1976–1985, Jun. 2017.
[4] A. Atia, A. Williams, and R. Newcomb, "Narrow-band multiple-coupled cavity synthesis," *IEEE Trans. Circuits Syst.*, vol. CAS-21, no. 5, pp. 649–655, Sep. 1974.
[5] R. J. Cameron, "General coupling matrix synthesis methods for Chebyshev filtering functions," *IEEE Trans. Microw. Theory Techn.*, vol. 47, no. 4, pp. 433–442, Apr. 1999.
[6] S. Tamiazzo and G. Macchiarella, "Synthesis of cross-coupled filters with frequency-dependent couplings," *IEEE Trans. Microw. Theory Techn.*, vol. 65, no. 3, pp. 775–782, Mar. 2017.

[7] M. Uhm, S. Nam, and J. Kim, "Synthesis of resonator filters with arbitrary topology using hybrid method," *IEEE Trans. Microw. Theory Techn.*, vol. 55, no. 10, pp. 2157–2167, Oct. 2007.

[8] G. L. Nicholson and M. J. Lancaster, "Coupling matrix synthesis of cross-coupled microwave filters using a hybrid optimisation algorithm," *IET Microw., Antennas Propag.*, vol. 3, no. 6, pp. 950–958, Sep. 2009.

[9] X. Shang, Y. Wang, G. Nicholson, and M. J. Lancaster, "Design of multiple-passband filters using coupling matrix optimisation," *IET Microw., Antennas Propag.*, vol. 6, no. 1, pp. 24–30, Jan. 2012.

[10] L. Szydlowski, A. Lamecki, and M. Mrozowski, "A novel coupling matrix synthesis technique for generalized Chebyshev filters with resonant source–load connection," *IEEE Trans. Microw. Theory Techn.*, vol. 61, no. 10, pp. 3568–3577, Oct. 2013.

[11] D. A. Tubail and T. F. Skaik, "Synthesis of coupled resonator-based multiplexers with generalised structures using coupling matrix optimisation," *Electron. Lett.*, vol. 51, no. 23, pp. 1891–1893, Nov. 2015.

[12] M. Mokhtaari, J. Bornemann, K. Rambabu, and S. Amari, "Coupling-matrix design of dual and triple passband filters," *IEEE Trans. Microw. Theory Techn.*, vol. 54, no. 11, pp. 3940–3946, Nov. 2006.

[13] A. Lamecki, P. Kozakowski, and M. Mrozowski, "Fast synthesis of coupled-resonator filters," *IEEE Microw. Wireless Compon. Lett.*, vol. 14, no. 4, pp. 174–176, Apr. 2004.

[14] W. A. Atia, K. A. Zaki, and A. E. Atia, "Synthesis of general topology multiple coupled resonator filters by optimization," in *IEEE MTT-S Int. Microw. Symp. Dig.*, vol. 2. Jun. 1998, pp. 821–824.

[15] W. Xia, "Diplexers and multiplexers design by using coupling matrix optimisation," Ph.D. dissertation, School Electron., Elect. Syst. Eng., Univ. Birmingham, Birmingham, U.K., 2015.

[16] K. Price, R. Storn, and J. Lampinen, *Differential Evolution: A Practical Approach to Global Optimization*. New York, NY, USA: Springer-Verlag, 2005.

[17] J. Kennedy, "Particle swarm optimization," in *Encyclopedia of Machine Learning*. Boston, MA, USA: Springer, 2011, pp. 760–766.

[18] X. Shang, Y. Wang, W. Xia, and M. J. Lancaster, "Novel multiplexer topologies based on all-resonator structures," *IEEE Trans. Microw. Theory Techn.*, vol. 61, no. 11, pp. 3838–3845, Nov. 2013.

[19] J. C. Lagarias, J. A. Reeds, M. H. Wright, and P. E. Wright, "Convergence properties of the Nelder–Mead simplex method in low dimensions," *SIAM J. Optim.*, vol. 9, no. 1, pp. 112–147, 1998.

[20] P. T. Boggs and J. W. Tolle, "Sequential quadratic programming," *Acta Numer.*, vol. 4, pp. 1–51, Jan. 1995.

[21] Ł. Januszkiewicz, P. Di Barba, and S. Hausman, "Field-based optimal placement of antennas for body-worn wireless sensors," *Sensors*, vol. 16, no. 5, p. 713, May 2016.

[22] Ł. Januszkiewicz, P. Di Barba, and S. Hausman, "Automated identification of human-body model parameters," *Int. J. Appl. Electromagn. Mech.*, vol. 51, no. s1, pp. S41–S47, Apr. 2016.

[23] U. Singh, H. Kumar, and T. S. Kamal, "Design of Yagi-Uda antenna using biogeography based optimization," *IET Microw., Antennas Propag.*, vol. 58, no. 10, pp. 3375–3379, Oct. 2010.

[24] B. Liu, D. Zhao, P. Reynaert, and G. G. E. Gielen, "GASPAD: A general and efficient mm-wave integrated circuit synthesis method based on surrogate model assisted evolutionary algorithm," *IEEE Trans. Comput.-Aided Design Integr.*, vol. 33, no. 2, pp. 169–182, Feb. 2014.

[25] M. Jamil and X.-S. Yang, "A literature survey of benchmark functions for global optimisation problems," *Int. J. Math. Model. Numer. Optim.*, vol. 4, no. 2, pp. 150–194, Feb. 2013.

[26] E. Mezura-Montes, J. Velázquez-Reyes, and C. A. C. Coello, "A comparative study of differential evolution variants for global optimization," in *Proc. 8th Annu. Conf. Genetic Evol. Comput.*, 2006, pp. 485–492.

[27] S. Das and P. N. Suganthan, "Differential evolution: A survey of the state-of-the-art," *IEEE Trans. Evol. Comput.*, vol. 15, no. 1, pp. 4–31, Feb. 2011.

[28] Y. Wang, Z. Cai, and Q. Zhang, "Differential evolution with composite trial vector generation strategies and control parameters," *IEEE Trans. Evol. Comput.*, vol. 15, no. 1, pp. 55–66, Feb. 2011.

[29] J. Brest, S. Greiner, B. Boskovic, M. Mernik, and V. Zumer, "Self-adapting control parameters in differential evolution: A comparative study on numerical benchmark problems," *IEEE Trans. Evol. Comput.*, vol. 10, no. 6, pp. 646–657, Dec. 2006.

[30] R. Gämperle, S. D. Müller, and P. Koumoutsakos, "A parameter study for differential evolution," in *Advances in Intelligent Systems, Fuzzy Systems, Evolutionary Computation*. New York, NY, USA: Springer, 2002, pp. 293–298.

[31] J. Ronkkonen, S. Kukkonen, and K. V. Price, "Real-parameter optimization with differential evolution," in *Proc. IEEE Congr. Evol. Comput.*, vol. 1. Sep. 2005, pp. 506–513.

[32] A. K. Qin, V. L. Huang, and P. N. Suganthan, "Differential evolution algorithm with strategy adaptation for global numerical optimization," *IEEE Trans. Evol. Comput.*, vol. 13, no. 2, pp. 1785–1791, Apr. 2005.

[33] J. Vesterstrom and R. Thomsen, "A comparative study of differential evolution, particle swarm optimization, and evolutionary algorithms on numerical benchmark problems," in *Proc. Congr. Evol. Comput.*, vol. 2. Jun. 2004, pp. 1980–1987.

[34] J. Kenndy and R. Eberhart, "Particle swarm optimization," in *Proc. Int. Conf. Neural Netw.*, vol. 4. Nov./Dec. 1995, pp. 1942–1948.

[35] R. C. Eberhart, Y. Shi, and J. Kennedy, *Swarm Intelligence*. Amsterdam, The Netherlands: Elsevier, 2001.

[36] W. Xia, X. Shang, and M. J. Lancaster, "Responses comparisons for coupled-resonator based diplexers," in *Proc. 3rd Annu. Seminar Passive RF Microw. Compon.*, Mar. 2012, pp. 67–75.

Bo Liu (M'15–SM'17) received the B.S. degree from Tsinghua University, Beijing, China, in 2008, and the Ph.D. degree from the MICAS Laboratories, University of Leuven, Leuven, Belgium, in 2012.

From 2012 to 2013, he was a Humboldt Research Fellow and was with the Technical University of Dortmund, Dortmund, Germany. In 2013, he was a Lecturer with Wrexham Glyndwr University, Wrexham, U.K., where he was a Reader in computer-aided design in 2016. He is currently an Honorary Fellow with the University of Birmingham, Birmingham, U.K. He has authored or co-authored 1 book and more than 40 papers in international journals, edited books, and conference proceedings. His current research interests include the design automation methodologies of analog/RF integrated circuits, microwave devices, MEMS, evolutionary computation, and machine learning.

Hao Yang was born in Wuhan, China, in 1991. He received the B.Eng. degree in electronic and electrical engineering from the University of Birmingham, Birmingham, U.K., in 2014, and the B.Eng. degree in electronics and information engineering from the Huazhong University of Science and Technology, Wuhan, China, in 2014. He is currently pursuing the Ph.D. degree in electronic and electrical engineering at the University of Birmingham.

His current research interests include terahertz frequency filters and mutiplexers.

Michael J. Lancaster (SM'04) was born in West Yorkshire, U.K., in 1958. He received the bachelor's degree in physics and Ph.D. degree with a focus on nonlinear underwater acoustics from Bath University, Bath, U.K., in 1980 and 1984, respectively.

He joined the Surface Acoustic Wave (SAW) Group, Department of Engineering Science, Oxford University, Oxford, U.K., as a Research Fellow. He was involved in the design of new novel SAW devices, including RF filters and filter banks. In 1987, he was a Lecturer of electromagnetic theory and microwave engineering with the Department of Electronic and Electrical Engineering, University of Birmingham, Birmingham, U.K., where he was focused on the study of the science and applications of high-temperature superconductors, particularly in microwave frequencies. He was the Head of the Department of Electronic, Electrical and Systems Engineering in 2003. He has authored 2 books and over 190 papers in refereed journals. His current research interests include microwave filters and antennas, as well as the high-frequency properties and the applications of a number of novel and diverse materials, including micromachining as applied to terahertz communications devices and systems.

Prof. Lancaster is a Fellow of the IET and the U.K. Institute of Physics. He is a Chartered Engineer and Chartered Physicist. He has served on the IEEE MTT-S IMS Technical Committee.